

POSITION AND TEMPERATURE MEASUREMENTS OF A SINGLE ATOM
VIA RESONANT FLUORESCENCE

by

RICHARD WAGNER JR.

A DISSERTATION

Presented to the Department of Physics
and the Graduate School of the University of Oregon
in partial fulfillment of the requirements
for the degree of
Doctor of Philosophy

June 2019

DISSERTATION APPROVAL PAGE

Student: Richard Wagner Jr.

Title: Position and Temperature Measurements of a Single Atom via Resonant Fluorescence

This dissertation has been accepted and approved in partial fulfillment of the requirements for the Doctor of Philosophy degree in the Department of Physics by:

Michael Raymer	Chair
Daniel A Steck	Advisor
Benjamín J. Alemán	
George Nazin	Institutional Representative

and

Janet Woodruff-Borden	Dean of the Graduate School
-----------------------	-----------------------------

Original approval signatures are on file with the University of Oregon Graduate School.

Degree awarded June 2019

© 2019 Richard Wagner Jr.

This work is licensed under a Creative Commons
Attribution-NonCommercial-NoDerivs (United States) License.



This work may be shared freely with attribution to the author and institution. It may not be edited or used for any commercial purpose.

DISSERTATION ABSTRACT

Richard Wagner Jr.

Doctor of Philosophy

Department of Physics

June 2019

Title: Position and Temperature Measurements of a Single Atom via Resonant Fluorescence

The magneto-optical trap (MOT) has been an important tool in quantum optics research for three decades. MOTs allow for hundreds of thousands to millions of atoms to be cooled to micro-Kelvin temperatures for use in a wide variety of experiments. For nearly as long, MOTs with just a single atom have been of some interest to the research community. We have developed an algorithm, based on Bayesian statistics, to carefully measure small numbers of atoms in a MOT.

Many techniques have been developed to measure the temperature of atoms in a MOT, including some that can translate to single atoms. We propose a new technique to measure the temperature of a single atom without releasing the atom from the MOT. Temporal modulations in a spatially dependent magnetic field encode information about the position of an atom through associated variation in its fluorescence rate. Measuring this variation reveals the atom's position distribution and therefore its temperature. The technique is examined for a variety of MOT parameters. Measurements with the technique are an order of magnitude larger than predicted by theory and potential routes for future study are offered.

CURRICULUM VITAE

NAME OF AUTHOR: Richard Wagner Jr.

GRADUATE AND UNDERGRADUATE SCHOOLS ATTENDED:

University of Oregon, Eugene, OR
Miami University, Oxford, OH

DEGREES AWARDED:

Doctor of Philosophy in Physics, 2019, University of Oregon
Master of Science in Physics, 2016, University of Oregon
Bachelor of Science in Physics, 2009, Miami University

PROFESSIONAL EXPERIENCE:

Graduate Research Fellow, Department of Physics, University of Oregon, Eugene OR, Fall 2012, AY 2012-2013, Winter & Spring 2014, Fall 2015, Fall 2016, Spring 2016, Fall 2017, Spring 2016, AY 2017-2018

Science Literacy Program Fellow, University of Oregon, Eugene OR, Winter & Spring 2012, Fall 2014

Graduate Teaching Fellow, Department of Physics, University of Oregon, Eugene OR, AY 2009-2010, AY 2019-2011, Winter & Spring 2015, Winter 2016, Winter 2017

Adjunct Instructor, Lane Community College, Eugene OR, AY 2016-2017, AY 2017-2018

GRANTS, AWARDS AND HONORS:

Science Literacy Program Fellow, University of Oregon, Winter & Spring 2012, Fall 2014

Astronaut Scholar, Astronaut Scholarship Foundation, 9/2008

Provost's Academic Achievement Award, Miami University Office of the Provost, 9/2008

PUBLICATIONS:

Richard Wagner and James P. Clemens. Fidelity of quantum teleportation based on spatially and temporally resolved spontaneous emission. *Journal of the Optical Society of America B*, 27(6):A73-A80, 2010.

N. Souther, R. Wagner, P. Harnish, M. Briel, and S. Bali. Measurements of light shifts in cold atoms using Raman pump-probe spectroscopy. *Laser Physics Letters*, 7(4):321-327, 2010.

Richard Wagner and James P. Clemens. Performance of a quantum teleportation protocol based on collective spontaneous emission. *Journal of the Optical Society of America B*, 26(3):541-548, 2009.

Richard Wagner Jr. and James P. Clemens. Performance of a quantum teleportation protocol based on temporally resolve photodetection of collective spontaneous emission. *Physical Review A*, 79:042322, 2009.

For Mom and Dad.

Thank you.

TABLE OF CONTENTS

Chapter		Page
I.	INTRODUCTION	1
	1.1. Single Atom MOTs	2
	1.2. MOT Temperature Measurements	4
	1.3. Optical Trap Oscillations	7
	1.4. Dissertation Outline	8
II.	ATOM OPTICS AND MAGNETO-OPTICAL TRAPS	9
	2.1. A Single Atom	9
	2.2. Atoms and Light	11
	2.3. Atoms and Magnetic Fields	21
	2.4. The $F_g = 0 \rightarrow F_e = 1$ Atom	25
	2.5. Magneto-Optical Traps	35
III.	EXPERIMENTAL SETUP	44
	3.1. Vacuum	44
	3.2. Lasers	53
	3.3. Magnetic Fields	66
	3.4. Photon Collection	80
IV.	OUR SINGLE ATOM MOT	90
	4.1. Detecting A Single Atom MOT	91
	4.2. Bayesian Algorithm	100
V.	ATOMIC FORCES IN A MOT	114
	5.1. 3D and ^{87}Rb Hamiltonians	114
	5.2. Matching Simulation to Experiments	123

Chapter	Page
5.3. 3D and ^{87}Rb Calculations	128
5.4. Escape Channels	134
5.5. Recovering Potential	143
 VI. POSITION AND TEMPERATURE MEASUREMENTS	 146
6.1. Theory	146
6.2. Analysis of Photon Arrivals	156
6.3. Measurements	165
6.4. Multiple Atom Fluorescence Amplitudes	184
6.5. Parametric Resonances	185
6.6. Non-Sinusoidal Waveforms	198
 VII. CONCLUSIONS	 203
 APPENDICES	
A. HOW A $F_G = 0 \rightarrow F_E = 1$ ATOM BECOMES A V-ATOM	208
B. DUAL POLARIZER NOISE REDUCTION	212
C. MOT COIL WATER COOLING RATE	215
D. BAYESIAN EVOLUTION DERIVATION	222
E. GAUSSIAN SAMPLED OSCILLATION AMPLITUDE	225
F. PARAMETRIC RESONANCE DERIVATION	229
 REFERENCES CITED	 233

LIST OF FIGURES

Figure	Page
1.1. The magneto-optical trap	2
2.1. ^{87}Rb D ₂ Transition Level Diagram	22
2.2. $F_g = 0 \rightarrow F_e = 1$ Atom Level Diagrams	26
2.3. Optical molasses beam arrangement	32
2.4. V-atom forces	32
2.5. Magneto-Optical Trap Level Diagram	36
2.6. Atom with Mutlple Ground States	41
2.7. Sisyphus Cooling	42
3.1. Experimental Diagram of Vacuum Chamber	46
3.2. Installed LIAD system	49
3.3. LED circuit for LIAD setup	49
3.4. (Re)baking the vacuum chamber	52
3.5. Beam Path of MOT Trapping Lasers	54
3.6. Beam Path of MOT Repumping Lasers	54
3.7. Pyramid MOT Mirrors	56
3.8. MOT Frequency Controlling Beam Path	61
3.9. ^{87}Rb D-2 line spectrum	62
3.10. Fiber Polarization Mount	65
3.11. Permanent Magnet Magnetic Field Calculation Methods	68
3.12. Permanent Magnet Quadrupole Field	69
3.13. Single Atom MOT Magnetic Field Designs	70

Figure	Page
3.14. Plumbing Diagram for water cooling the MOT coils	74
3.15. Water Cooled Coils Protection Circuit	75
3.16. MOT Coils Current Monitoring Circuit	77
3.17. Helmholtz Coil Layout	78
3.18. Single Photon Collect Lens System	81
3.19. BNC-Header Adaptor for DE2 FPGA	84
3.20. FPGA implementation for counting photons	85
3.21. FPGA implementation for timing photons	86
3.22. APD Protection Mechanisms	88
4.1. Sample Photon Collection Data	92
4.2. Histograms of sample photon collection data	95
4.3. Variances of sample photon collection data	98
4.4. Atom counting with CCD camera	99
4.5. Sample data for bayesian fluorescence number estimation	104
4.6. Bayesian algorithm flow chart	111
5.1. Excited state populations for ^{87}Rb and V-atom	130
5.2. 1D forces on ^{87}Rb and V-atom	133
5.3. 3D MOT forces for an assortment of beam phases	135
5.4. 3D MOT phase dependence	142
6.1. Sampled oscillation spectrum	159
6.2. Assorted measured spectra	166
6.3. Single-atom temperatures with release-recapture method	168
6.4. Fluorescence amplitude scaling with current amplitude	168
6.5. Simulated 1D modulation slopes	170

Figure	Page
6.6. Fluorescence amplitude spectrum	174
6.7. Lorentzian fluorescence amplitude spectrum	176
6.8. Fluorescence amplitude scaling with field gradient	177
6.9. Simulated fluorescence amplitude scaling with field gradient	178
6.10. Fluorescence amplitude as a function of laser detuning	180
6.11. Fluorescence amplitude with background magnetic fields	182
6.12. Spectra of multiple atoms in a MOT.	185
6.13. Images of Single Atom Parametric Resonance	189
6.14. Light Distribution for Parametric Oscillating Atom	191
6.15. Fitted Light Distributions for Parametric Oscillating Atoms	193
6.16. Light intensity loss due to parametric oscillations	195
6.17. Power spectra for different waveforms	199
B.1. Laser power control with polarizers	213
C.1. Water cooling channel dimensions	219

LIST OF TABLES

Table	Page
3.1. Permanent Ring Magnet Parameters	67
3.2. Helmholtz Coil Field Gradients	79
3.3. Photon Collection Lens System Collection Efficiency	83
5.1. Repumping field and populations of ^{87}Rb D_2 energy levels	115
5.2. MOT Beam Circular Polarizations	120
6.1. High-gradient MOT parametric resonance conditions	187
6.2. Variance compared to amplitude for common waveforms	201
C.1. Water-cooled MOT coil parameters	218

CHAPTER I

INTRODUCTION

The magneto-optical trap (MOT) has become one of the bedrocks for research on the quantum behavior of atoms. The MOT can produce millions of atoms with temperatures on the order of microkelvins. Such small temperatures are necessary to limit atomic motion for studying their classical and quantum dynamics. The magneto-optical trap uses multiple laser fields whose frequencies are often a few MHz smaller (red-detuned) than an atomic resonance of the atomic species being trapped. The light is lower in frequency so that atoms moving towards the laser source sees a Doppler shift moving the light from that laser closer to resonance. This Doppler shift makes the atom more likely to absorb photons from the laser (due the reduced detuning), resulting in radiation pressure that pushes the atom in the propagation direction of the light. With $D + 1$ lasers for a MOT in D -dimensions, this can result in a cooling force as the lasers damp the motion of the atoms. This process creates what is often referred to as *optical molasses* and was originally conceived in the 1970s [1, 2] and experimental verified in the following decade [3].

Doppler cooling is only responsible for cooling atoms; it does not trap them. In addition to the laser fields, a MOT requires a (quadrupole) magnetic field which produces a spatially dependent Zeeman shift of atomic energy levels. The Zeeman shifts provide in an additional preferential excitation of the atoms by the laser, creating a restoring force that traps atoms near the location where the magnetic field vanishes. Together with optical molasses, the quadrupole fields impart a force on the atom which causes it behave as a damped harmonic oscillator. There are a number of configurations for a magneto-optical trap, but this work focuses on the trap shown in Figure 1.1. Here, three pairs of counter-propagating lasers push the

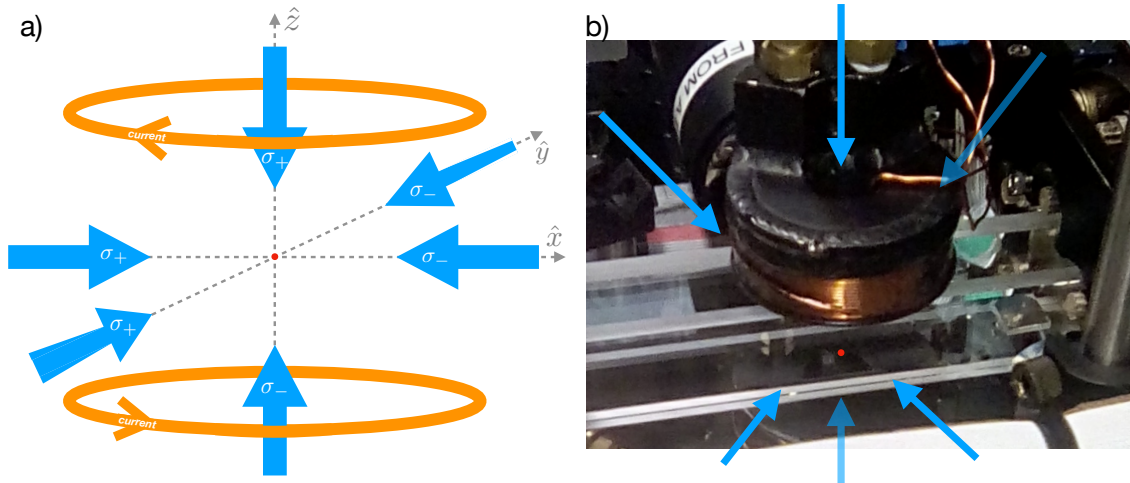


FIGURE 1.1. The magneto-optical trap. a) Schematic drawing. b) Photograph of our MOT setup around the experiment vacuum cell. For both images, blue arrows show the six-counter propagating MOT beams (with their appropriate polarizations in the schematic drawing). Orange loops are anti-Helmholtz coils that generate the linear magnetic field near the origin. The MOT loads at the origin (red dot).

atom towards their intersection point and the magnetic field is generated by a pair of anti-Helmholtz coils—coaxial coils with currents traveling in opposite directions. At the midpoint between the two coils on their central axis, the magnetic field vanishes, establishing the equilibrium position for the atom.

1.1 Single Atom MOTs

Not long after the first MOTs were developed [4], they were extended to allow capture of small numbers of atoms, primarily by greatly increasing the strength of the confining magnetic field. This produced traps on order of tens of atoms [5] and quickly down to individual atoms [6]. Since then, single- or few-atom MOTs have largely been used as efficient sources of single atoms for loading into other optical systems [7]. These systems include cavity QED experiments [8, 9], which allow for strong coupling between the atom and cavity optical field modes; optical dipole traps

[10, 11], which generally have tighter confinement of atomic motion than MOTs and are far-detuned from atomic excitation; and one-dimensional optical lattices [12, 13], which allow for targeted experimental interaction with multiple atoms. There have been a broad field of research looking at atomic counting and MOT characterization with single (and low-numer) MOTs [14, 15]. Other uses of single atom MOTs have included studies of cross-atomic-species cold-atom interactions [16, 17], rare-isotope separation [18, 19], and detailed studies of the high-gradient MOT loading and loss mechanisms [20, 21].

Besides these studies of loading and loss mechanisms, there is little experimental research on the dynamics of a few atoms in a magneto-optical trap. Additionally, these have investigated loss rates statistically as opposed to the dynamics which causes atomic loss in the traps. For few-atom MOTs, these losses are due to collisions between atoms in the MOT resulting in atoms exiting the trap [15]. Some atomic collisions coincide with atomic energy transitions that provide enough kinetic energy for the atoms to escape the MOT [22]. The only experiments that have looked at the dynamics of a *single atom* in a magneto-optical trap examined correlations between photons emitted by the atom [23, 24]. These works reveal temporal-correlations that reflect both internal atomic dynamics (Rabi oscillations) and external dynamics (position-dependent electric field intensity and polarization) over several orders of magnitude.

The work discussed in this dissertation adds to this little-explored topic by looking at position-dependent oscillations of the atom in a MOT magnetic field. The fluorescence rate of an atom depends on the detuning from resonance of the exciting laser field. Because of the linear magnetic field of the quadrupole, the Zeeman shifted energy levels have detunings that vary spatially. Modulating this magnetic field

introduces oscillations in the detuning and thus the rate of fluorescence from the atom. Measuring the fluorescence oscillations can produce a time-averaged position distribution for the atom in the MOT. The position distribution of the atom is very closely related to its potential energy, which can be used, via the equipartition theorem [25–27], to measure the atomic temperature. Therefore, this work functions as an in-situ temperature measurement of the atom in addition to examining the averaged motion of the atom in the MOT.

1.2 MOT Temperature Measurements

There are already a few established methods for measuring atomic temperatures in a MOT. Some of the methods, like the method proposed here, compare measurements of the atom(s) in the MOT to models of the MOT in order to extract potential energy information about the atom. Others methods more directly measure the temperature through the atomic kinetic energy, but these methods are lossy, requiring releasing the atom(s) from the MOT and reloading new atoms for experiments.

One such lossy method is the release-recapture method which was used to estimate the MOT temperature in the first successful MOT publication [4]. This method turns off the trapping fields in order to allow the trapped atoms to expand from the trap ballistically. Turning the trap on again, after a given amount of time, recaptures just a fraction of the atoms. Comparing trap-off times with recapture fraction gives an estimate of average atomic velocity, and hence temperature in the MOT. In addition to measuring the temperature of traps with large numbers of atoms, this technique has been used to measure the temperature of a single atom both in a MOT and in a dipole trap [16, 28, 29].

The time of flight technique releases atoms from a MOT and allows them to fall under gravity through a near-resonant laser field [30]. As the atoms pass through the field, the light they scatter is measured. Observing how this fluorescence changes as a function of time from release (atoms moving directly downward initially pass through the laser before atoms that were initially moving directly upward) gives an estimate of the average velocity of the atoms, and hence their temperature. This technique can be used for other systems including atoms in an optical lattice [31]. Other configurations of the time of flight technique use an additional laser beam to push the atoms in some direction where the probe beam has been located [30]. Pushing the atoms vertically upward takes advantage of converting kinetic energy to gravitation potential energy in order to measure a maximum height for the MOT atoms to reach, giving a measure of their initial kinetic energy. Pushing the atoms horizontally lets gravity drag the atoms downward, under the probe beam, to measure a travel distance for the atoms—and therefore a maximum horizontal velocity distribution.

Modified time-of-flight techniques have been used to measure the temperature of single atom [29], although due to the difficulty of imaging scatter from a single atom, they are less commonly used than release-recapture methods. For the single-atom measurement, instead of detecting the light of an atom as it passes through a nearby beam, the position of the atom is detected on a CCD after a resonant imaging pulse. Repeating the test provides information of the spatial distribution of the atom after release, allowing velocity and temperature to be estimated for an atom initially inside the MOT.

Another lossy method adiabatically reduces the optical potential in which an atom resides [16, 28, 32]. Measuring the probability that the atom remains in the trap at a given potential energy gives an estimate of its kinetic energy. This

method is similar in concept to evaporative cooling techniques used, as an example, in Bose-Einstein condensates [33]. While evaporative cooling is used to decrease the temperature and increase the density of an atomic cloud, the adiabatic lowering technique just probes the temperatures of a small number of atoms. For temperature measurements, this technique is mostly used in dipole traps where the potential can be easily reduced by lowering the intensity of the trapping laser [4, 16, 34].

One method that preserves the number of atoms in the MOT looks at the frequency spectrum of photons emitted by the atoms. The motion of atoms in the trap will broaden the wavelength of the emitted light via the Doppler effect. Measuring this broadening allows for an estimate of the velocity of the atoms [35]. This is also used in measuring the temperature of trapped ions [36]. Ion traps can also make use of quantized motion to measure spectra and temperature [36]. Spectra from ions (including single ions [37]) reveal sidebands of resonance peaks. The number and relative intensities of the sidebands are related to the average vibrational mode of the ion in the trap, and hence to temperature. This technique can also be used to measure temperatures of neutral atoms in optical lattices [38].

Another number-preserving method takes advantage of the harmonic-oscillator model of the MOT and the equipartition theorem. This method uses an external force (created either an oscillating, external uniform magnetic field [26] or additional laser beam [27]) to drive oscillations in the center of mass of the MOT. Measuring the amplitude responses at different frequencies gives the natural frequency, and thus the spring constant, of the restoring force in the MOT. With a measurement of the RMS radius of the MOT via pictures of it, the average potential energy of the atoms is revealed. As a temperature estimate, this method is similar to our proposed technique

as it measures temperature via external oscillations, but this method is not applicable to single-atom MOTs where there is not a well defined size of the atomic cloud.

1.3 Optical Trap Oscillations

In addition to measuring MOT spring constants with oscillations, oscillations of laser fields have been used to measure properties of particles in other forms of optical traps. For beads in an optical dipole trap (see Section 2.2.4), oscillating the power of the laser which confines the atom can excite resonances in the bead [39]. As with the MOT spring measurements above, Imaging the bead's motion with these oscillations reveals the trapping strength on the bead. Similar experiments have probed the trapping potential for atoms in an optical lattice, in which the interference of multiple laser fields creates a periodic lattice of positions where atoms are trapped [40, 41]. Here, modulations of the lattice's trapping beam power also modulates the trapping potential for the atoms. Measuring the populations of atoms still present in the lattice after being driven at various frequencies can reveal the vibrational states of the lattice [40]. Additionally, the modulations can be seen in changes in power measured from beams diffracted by the atoms arranged in the lattice [41].

For these two purely optical traps, a magnetic field is not necessary, requiring that modulations be driven by oscillations in laser power. Attempting to detect oscillations in fluorescence from the trapped particles, then, would be difficult as the signal would be swamped by oscillations in background fluorescence levels. Instead, these experiments (save for the diffraction experiment in [41]) directly imaged the particles in the trap with a camera to observe oscillations. This can be challenging for a single atom, although our experiment does reveal similar oscillations for the single atom when imaged with a CCD camera (see section 6.5). Without modulating

the beam power, as in our experiment, we instead detect oscillations directly through measurements of photon arrivals from an atom.

1.4 Dissertation Outline

The layout of this dissertation is as follows. Chapter II has a theoretical description of the interaction between atoms, light and magnetic fields, building to a description of the functioning of a MOT. Chapter III describes the experimental apparatus, focusing on relevant changes made for the single-atom experiments described in later Chapters. Chapter IV discusses our single-atom MOT and examines a new technique for monitoring and controlling experiments based on a single atom. Chapter V expands on the theory in Chapter II to look more closely at the behavior of atoms with the complete electronic structure of the D_2 transition for rubidium. Chapter VI looks at position and temperature measurement experiments performed on our single atoms. Finally, Chapter VII draws conclusions for our experiment and briefly lays out the path forward for future investigation.

CHAPTER II

ATOM OPTICS AND MAGNETO-OPTICAL TRAPS

In this Chapter, the interaction of atoms with light and magnetic fields is sketched using a standard semiclassical picture in which the atom's internally energy is quantized but its external motion and external fields are treated classically. Calculations are done in one-dimension with the atom is treated as having a single ground state and a small number of excited states when appropriate. Details of the calculation are given with an eye toward the three-dimensional picture in Chapter V with a full D₂ transition of ⁸⁷Rb. After examining atomic interactions with electric and magnetic fields individually, an atom inside a magneto-optical trap is discussed.

2.1 A Single Atom

Until the broader discussion of magneto-optical traps in Section 2.5, the atom will be treated as a qubit with energy separation $\hbar\omega_0$. Under this assumption, the atomic Hamiltonian should have the form

$$\hat{H}_A = \hbar\omega_0 |e\rangle\langle e| \quad (2.1)$$

with the quantum state of the atom in the form

$$|\psi\rangle = c_e|e\rangle + c_g|g\rangle \quad (2.2)$$

where $|e\rangle$ and $|g\rangle$ are the atomic excited and ground states, respectively. In this definition, the ground state energy is defined to be zero. Rather than working with the atomic wavefunction, later calculations are simplified by using the atomic density

operator [42]. defined by

$$\rho = |\psi\rangle\langle\psi| = \begin{bmatrix} |c_e|^2 & c_e c_g^* \\ c_g c_e^* & |c_g|^2 \end{bmatrix} = \begin{bmatrix} \rho_{e,e} & \rho_{e,g} \\ \rho_{g,e} & \rho_{g,g} \end{bmatrix}. \quad (2.3)$$

s In the Schrödinger picture, the density operator evolves under the equation

$$\begin{aligned} \frac{d}{dt}\rho &= \left(\frac{d}{dt}|\psi\rangle\right)\langle\psi| + |\psi\rangle\left(\frac{d}{dt}\langle\psi|\right) \\ &= -\frac{i}{\hbar}\hat{H}|\psi\rangle\langle\psi| + \frac{i}{\hbar}|\psi\rangle\langle\psi|\hat{H} \\ \frac{d}{dt}\rho &= -\frac{i}{\hbar}[\hat{H},\rho]. \end{aligned} \quad (2.4)$$

Note that this equation is identical to the time evolution of an operator in the Heisenberg picture. The use of density matrices must be implemented to look at mixed states—quantum states which cannot be simple written as a linear superposition of eigenstates of a Hamiltonian [43]. Such states appear, for example, in analysis of entanglement [44], teleportation [45], and when looking at quantum trajectories [46, 47]. The density operator also is beneficial as operator expectation values are calculated simply by tracing the atomic states over the product of the operator applied to the atomic density operator as

$$\langle\hat{A}\rangle = \text{Tr}[\hat{A}\rho] = \sum_n \langle n|\hat{A}\rho|n\rangle \quad (2.5)$$

where $|n\rangle$ form a complete basis to describe eigenstates of the system.

For analysis of an atom in the MOT, the use of the density operator is important in modeling spontaneous emission of photons from the atom through the Lindblad

superoperator [48] defined as

$$\mathcal{L}[\hat{\sigma}]\rho = \hat{\sigma}\rho\hat{\sigma}^\dagger - \frac{1}{2}(\hat{\sigma}^\dagger\hat{\sigma}\rho + \rho\hat{\sigma}^\dagger\hat{\sigma}) \quad (2.6)$$

where $\hat{\sigma} = |g\rangle\langle e|$ and $\hat{\sigma}^\dagger = |e\rangle\langle g|$ are the atomic raising and lowering operators respectively. For the two level atom, the superoperator simplifies to

$$\mathcal{L}[\hat{\sigma}]\rho = \rho_{e,e}|g\rangle\langle g| - \frac{1}{2}(|e\rangle\langle e|\rho + \rho|e\rangle\langle e|). \quad (2.7)$$

Including this operator, the evolution of an atom which undergoes spontaneous emission follows

$$\frac{d}{dt}\rho = -\frac{i}{\hbar}[\hat{H}_A, \rho] + \Gamma\mathcal{L}[\hat{\sigma}]\rho, \quad (2.8)$$

where Γ is the decay rate of the atom.

2.2 Atoms and Light

A few simplifying assumptions are made to analyze the interaction of an atom with light, following the methodology of [48]. The light, for now, is treated as a linearly polarized electric field of a single mode. The atom is treated as small enough that the spatial variation of the electric field can be ignored. Thus the light field has the form

$$\vec{E}(t) = \hat{e}E_0 \cos(\omega t + \phi), \quad (2.9)$$

where ω is the frequency of the light, assumed to be close to the transition frequency of the atom, ω_0 , and \hat{e} is the polarization direction of the light. These assumptions are sufficient for finding a form for the interaction Hamiltonian between an atom and

light, but removing some of these assumptions leads to interesting results, which are discussed when appropriate.

2.2.1 Interaction Hamiltonian

The interaction between the atom and electric field is treated as a dipole interaction with an atomic dipole operator

$$\hat{d} = \langle e | \vec{d} | g \rangle (\hat{\sigma}^\dagger + \hat{\sigma}), \quad (2.10)$$

where $\vec{d} = e\vec{r}$ is the dipole moment of the atom (\vec{r} is the position operator for the atom's electron). This definition of \hat{d} derives from treating the electron position operator as that of a harmonic oscillator, where \hat{r} is proportional to the sum of the oscillator raising and lowering operators [49], which here correspond to atomic raising and lowering operators, $\hat{\sigma}^\dagger$ and $\hat{\sigma}$. The expectation value of the dipole operator is

$$\langle \hat{d} \rangle = \langle e | \vec{d} | g \rangle (\langle \hat{\sigma}^\dagger \rangle + \langle \hat{\sigma} \rangle). \quad (2.11)$$

With the atom treated as a dipole, we can find an interaction Hamiltonian by comparison to the energy of an electric dipole interacting with a field. This provides an interaction Hamiltonian

$$\hat{H}_{\text{AF}} = -\vec{E} \cdot \hat{d}. \quad (2.12)$$

In the absence of the electric field, the excited state population evolves as $e^{-i\omega_0 t}$ and $\langle \hat{\sigma} \rangle$ evolves in this same way. With this, the dipole operator can be written in the form

$$\hat{d} = \hat{d}^- - \hat{d}^+ \quad (2.13)$$

with $\hat{d}^- \equiv \langle e|\vec{d}|g\rangle\hat{\sigma}^\dagger \sim e^{i\omega_0 t}$ and $\hat{d}^+ \equiv \langle e|\vec{d}|g\rangle\hat{\sigma} \sim e^{-i\omega_0 t}$. Writing the electric field in terms of complex exponentials gives

$$\vec{E}(t) = \hat{\epsilon} \frac{E_0}{2} [e^{+i\omega t + \phi} + e^{-i\omega t - \phi}] \equiv \vec{E}^- + \vec{E}^+ \quad (2.14)$$

and is used to write the interaction Hamiltonian as

$$H_{AF} = - \left(\hat{d}^- \cdot \vec{E}^- + \hat{d}^- \cdot \vec{E}^+ + \hat{d}^+ \cdot \vec{E}^- + \hat{d}^+ \cdot \vec{E}^+ \right). \quad (2.15)$$

In terms of the exponentials, these four terms are proportional to $e^{i(\omega_0 + \omega)t}$, $e^{i(\omega_0 - \omega)t}$, $e^{-i(\omega_0 - \omega)t}$ and $e^{-i(\omega_0 + \omega)t}$ respectively. In the limit where the frequency of light is very close to that of the atomic energy, the terms with the frequency differences oscillate much more slowly than the terms with their sum (the first and last term). The rotating wave approximation ignores these quickly oscillating terms, so that the interaction Hamiltonian becomes

$$H_{AF} = -\hat{d}^- \cdot \vec{E}^+ - \hat{d}^+ \cdot \vec{E}^-. \quad (2.16)$$

Written in terms of atomic raising and lowering operators, the Hamiltonian is

$$H_{AF} = \frac{\hbar}{2} (\Omega^* \hat{\sigma} e^{-i\omega t} + \Omega \hat{\sigma}^\dagger e^{+i\omega t}), \quad (2.17)$$

where

$$\Omega = \frac{\langle g|\hat{\epsilon} \cdot \vec{d}|e\rangle E_0 e^{-i\phi}}{\hbar} \quad (2.18)$$

is named the Rabi frequency. The excited state population for any two level system at rest and interacting with a non-resonant electric field will oscillate with this frequency [42, 50, 51].

In an alternate view of the rotating wave approximation, the electric field is quantized as a harmonic oscillator. Under this view, the (single frequency, polarization and mode) electric field follows

$$\vec{E} \propto \vec{f}(\vec{r})\hat{a} + \vec{f}^*(\vec{r})\hat{a}^\dagger, \quad (2.19)$$

where $\vec{f}(\vec{r})$ are the spatial mode functions of the field, and \hat{a}^\dagger is the photon creation operator for this mode (expanding to a general electric field requires summing over this term for each frequency, mode, and polarization). With this picture, the interaction Hamiltonian is

$$\hat{H}_{\text{AF}} \propto \hat{a}\hat{\sigma} + \hat{a}\hat{\sigma}^\dagger + \hat{a}^\dagger\hat{\sigma} + \hat{a}^\dagger\hat{\sigma}^\dagger. \quad (2.20)$$

The first term of this equation removes a photon from the field and lowers the atom from excited to ground state. The last term adds a photon to the field and raises the atom into the excited state. Both of these are non-energy conserving and can be dropped¹. These two terms are the same as the quickly rotating terms which were dropped previously.

¹These terms, while ignorable here, can be viewed as atomic interaction with the quantum vacuum [52]. This interaction leads to phenomenon such as the Casimir-Polder affect [53] and the Lamb shift [42, 54].

2.2.2 Optical Bloch Equations

The evolution of the atomic wavefunction in the Schrödinger picture is

$$\frac{d}{dt}|\psi\rangle = -\frac{i}{\hbar}(H_A + H_{AF})|\psi\rangle \quad (2.21)$$

which produces equations

$$\begin{aligned} \dot{c}_g &= -\frac{i\Omega e^{i\omega t}}{2}c_e \\ \dot{c}_e &= -i\omega_0 c_e + \frac{i\Omega^* e^{i\omega t}}{2}c_g. \end{aligned} \quad (2.22)$$

These can be simplified in a rotating frame where c_e is transformed to $\tilde{c}_e e^{-i\omega t}$ to produce

$$\begin{aligned} \dot{c}_g &= -\frac{i\Omega}{2}c_e \\ \dot{c}_e &= -i(\omega_0 - \omega)c_e + \frac{i\Omega^*}{2}c_g \end{aligned} \quad (2.23)$$

(note, here I've dropped the \tilde{c}_e notation). Eventually moving to this frame is what motivated writing the dipole operator in terms of complex exponentials in Equation 2.13. These same equations could have been derived from an atomic Hamiltonian of the form

$$\hat{H}_A = -\hbar\Delta |e\rangle\langle e| \quad (2.24)$$

and interaction Hamiltonian

$$\hat{H}_{AF} = \frac{\hbar}{2}(\Omega^* \hat{\sigma} + \Omega \hat{\sigma}^\dagger), \quad (2.25)$$

where $\Delta = \omega - \omega_0$ is the detuning of the electric field from the atomic resonance frequency. These are the forms of the atomic and interaction Hamiltonians that will be used throughout this text.

From these forms, the time evolution of the atomic density operator, calculated from Equation 2.8, produces the optical bloch equations [42]

$$\begin{aligned}
\dot{\rho}_{e,e} &= -\Gamma\rho_{e,e} - \frac{i}{2}(\Omega\rho_{g,e} - \Omega^*\rho_{e,g}) \\
\dot{\rho}_{e,g} &= -\left(\frac{\Gamma}{2} + i\Delta\right)\rho_{e,g} - \frac{i\Omega}{2}(\rho_{g,g} - \rho_{e,e}) \\
\dot{\rho}_{g,e} &= -\left(\frac{\Gamma}{2} - i\Delta\right)\rho_{g,e} + \frac{i\Omega^*}{2}(\rho_{g,g} - \rho_{e,e}) \\
\dot{\rho}_{g,g} &= \Gamma\rho_{e,e} + \frac{i}{2}(\Omega\rho_{g,e} - \Omega^*\rho_{e,g}).
\end{aligned} \tag{2.26}$$

In the steady state, these have analytic solutions

$$\begin{aligned}
\rho_{e,e}^{SS} &= \frac{|\Omega|^2/\Gamma^2}{1+(2\Delta/\Gamma)^2+2|\Omega|^2/\Gamma^2} \\
\rho_{e,g}^{SS} &= -\frac{i\Omega}{\Gamma} \frac{1+2i\Delta/\Gamma}{1+(2\Delta/\Gamma)^2+2|\Omega|^2/\Gamma^2} \\
\rho_{g,e}^{SS} &= \frac{i\Omega^*}{\Gamma} \frac{1-2i\Delta/\Gamma}{1+(2\Delta/\Gamma)^2+2|\Omega|^2/\Gamma^2} \\
\rho_{g,g}^{SS} &= \frac{1+(2\Delta/\Gamma)^2}{1+(2\Delta/\Gamma)^2+2|\Omega|^2/\Gamma^2}.
\end{aligned} \tag{2.27}$$

Recall that $\rho_{e,e}$ is the population of the excited state $\rho_{e,e} = |c_e|^2$ from Equation 2.2.

With this definition, the rate that an atom scatters photons is

$$R = \Gamma\rho_{e,e}. \tag{2.28}$$

2.2.3 Radiation Pressure

The force acting on an atom is the time evolution of the atom's (classical) momentum \vec{p} . Following the Heisenberg picture, this is

$$\vec{F} = \frac{i}{\hbar} [\hat{H}, \vec{p}] = -\vec{\nabla} \hat{H}. \quad (2.29)$$

To look at the force of light on the atoms, we use the Hamiltonian 2.25. This gives

$$\vec{F} = -\frac{\hbar}{2} \left(\vec{\nabla} \Omega^* \hat{\sigma} + \vec{\nabla} \Omega \hat{\sigma}^\dagger \right). \quad (2.30)$$

From the definition of the Rabi frequency in Equation 2.18, $\Omega \propto E_0 e^{i\phi}$, where E_0 is the field magnitude and ϕ is its phase. Both of these can depend on space, but for now consider the electric field to be a plane wave propagating in the $+\hat{z}$ direction so that the electric field strength has the form

$$E_0(\vec{r}) = E_0 e^{+ikz}. \quad (2.31)$$

Using this in Equation 2.30 gives a straightforward equation for the force

$$\begin{aligned} \vec{F} &= -\frac{\hbar}{2} \left(\frac{2dE_0}{\hbar} \vec{\nabla} e^{-ikz} \hat{\sigma} + \frac{2dE_0}{\hbar} \vec{\nabla} e^{+ikz} \hat{\sigma}^\dagger \right) \\ &= -\frac{\hbar}{2} \left(-ik\hat{z} \frac{2dE_0 e^{-ikz}}{\hbar} \hat{\sigma} + ik\hat{z} \frac{2dE_0 e^{+ikz}}{\hbar} \hat{\sigma}^\dagger \right) \\ \vec{F} &= -\frac{ik\hbar}{2} (-\Omega^* \hat{\sigma} + \Omega \hat{\sigma}^\dagger) \hat{z}. \end{aligned} \quad (2.32)$$

Taking the expectation value of the force gives

$$\begin{aligned}\langle \vec{F} \rangle &= -\frac{ik\hbar}{2} \text{Tr} [(-\Omega^* \hat{\sigma} + \Omega \hat{\sigma}^\dagger) \rho] \hat{z} \\ &= -\frac{ik\hbar}{2} (-\Omega^* \rho_{e,g} + \Omega \rho_{g,e}) \hat{z}\end{aligned}\tag{2.33}$$

after using Equation 2.5. The evolution for the excited state population from the optical bloch equations in 2.26 can be solved in steady state to get

$$\Gamma \rho_{e,e}^{SS} = -\frac{i}{2} (-\Omega^* \rho_{e,g}^{SS} + \Omega \rho_{g,e}^{SS}).$$

Comparing this to the expectation value for the force, the steady-state force on the atoms is

$$\langle \vec{F} \rangle^{SS} = \hbar k \Gamma \rho_{e,e}^{SS} \hat{z}.\tag{2.34}$$

This is an insightful equation as $\Gamma \rho_{e,e}$ is just the scatter-rate of photons by the atom as in Equation 2.28, and $\hbar k \hat{z}$ is the momentum carried by each photon. Thus the force felt by atom is just the average rate it absorbs momentum from scattered photons. The momentum change from emitting photons goes to zero in the limit of many absorption-emission events as the emissions have random directions. This force due to absorbed photon momentum is commonly referred to as radiation pressure.

In addition to being the basis for optical molasses (see Section 2.4.1 below), radiation pressure has been used experimentally to launch atoms in atomic clocks [55, 56], cool micromechanical resonators [57, 58], and even macroscopic objects such as the first solar sail successfully flown by the Japan Aerospace Exploration Agency [59, 60].

2.2.4 Dipole Traps

Returning to Equation 2.30, if the assumption is made that the electric field magnitude, rather than the phase, depends on space, the equation for force can be written as

$$\begin{aligned}
\vec{F} &= -\frac{\hbar}{2} \left(\frac{2de^{-i\phi}}{\hbar} \vec{\nabla} E_0 \hat{\sigma} + \frac{2de^{i\phi}}{\hbar} \vec{\nabla} E_0 \hat{\sigma}^\dagger \right) \\
&= -\frac{\hbar}{2} \left(\frac{2dE_0 e^{-i\phi}}{\hbar} \frac{\vec{\nabla} E_0}{E_0} \hat{\sigma} + \frac{2dE_0 e^{i\phi}}{\hbar} \frac{\vec{\nabla} E_0}{E_0} \hat{\sigma}^\dagger \right) \\
&= -\frac{\hbar}{2} \left(\Omega^* \vec{\nabla} \log[E_0] \hat{\sigma} + \Omega \vec{\nabla} \log[E_0] \hat{\sigma}^\dagger \right). \tag{2.35}
\end{aligned}$$

As done previously, the expectation value for the force is

$$\langle \vec{F} \rangle = -\frac{\hbar}{2} \vec{\nabla} \log[E_0] (\Omega^* \rho_{e,g} + \Omega \rho_{g,e}). \tag{2.36}$$

This equation is real, as the sum of the complex terms produces just $2\text{Re}[\Omega \rho_{g,e}]$.

From the steady state Bloch equations, this is

$$(\Omega^* \rho_{e,g}^{ss} + \Omega \rho_{g,e}^{ss}) = \frac{4\Delta |\Omega|^2 / \Gamma^2}{1 + (2\Delta/\Gamma)^2 + 2|\Omega|^2 / \Gamma^2} \tag{2.37}$$

where, again, Δ is the detuning of the electric field from the atomic energy, Ω is the Rabi frequency and Γ is the atomic decay rate. Here, it is convenient to introduce a saturation parameter defined as

$$s = \frac{2|\Omega|^2 / \Gamma^2}{1 + (2\Delta/\Gamma)^2} \tag{2.38}$$

so that

$$(\Omega^* \rho_{e,g}^{ss} + \Omega \rho_{g,e}^{ss}) = \frac{2\Delta s}{1+s}. \quad (2.39)$$

Then, the force becomes

$$\langle \vec{F} \rangle = -\frac{\hbar\Delta s}{1+s} \vec{\nabla} \log[E_0]. \quad (2.40)$$

The definition of s is proportional to the field intensity, which goes as E_0^2 . As field intensity is a more common parameter for experiments than field magnitude (the (integrated) electric field intensity of a laser is proportional to beam power), writing $\vec{\nabla} \log[E_0]$ in terms of the saturation parameter comes from

$$\vec{\nabla} s = 2s \vec{\nabla} \log[E_0]. \quad (2.41)$$

This produces a force equation just in terms of the saturation parameter

$$\langle \vec{F} \rangle = -\frac{\hbar\Delta \vec{\nabla} s}{2(1+s)} = -\frac{\hbar\Delta}{2} \vec{\nabla} \log[1+s]. \quad (2.42)$$

For large detunings where there is little excitation of the atom by the field, $s \ll 1$.

This simplifies the force to

$$\langle \vec{F} \rangle \approx -\frac{\hbar\Delta \vec{\nabla} s}{2(1+s)} = -\frac{\hbar\Delta}{2} \vec{\nabla} s, \quad (2.43)$$

so that the force on the atom is directed towards regions of high intensity (large s).

A common field where the beam intensity depends on position is a pair of tightly focused gaussian beams. This field has electric field intensity [61]

$$I(\vec{r}) = \frac{2P}{\pi w_0^2 [1 + (z/z_0)^2]} \exp \left[\frac{-2(x^2 + y^2)}{w_0^2 (1 + (z/z_0)^2)} \right] \quad (2.44)$$

where P is the total beam power, w_0 is the beam waist, the beam radius at its focus, and z_0 is the Rayleigh range of the beam, which gives a measure of the length of the focus size along the beam axis and is defined as the distance where the beam radius grows from its minimum by a factor of $\sqrt{2}$. For this field, the force is given by

$$\langle \vec{F} \rangle = \frac{2\hbar\Delta s}{w_0^2 [1 + (z/z_0)^2]} \left[x\hat{x} + y\hat{y} + \left(\frac{w_0^2}{z_0^2} - \frac{2(x^2 + y^2)}{z_0^2 [1 + (z/z_0)^2]} \right) z\hat{z} \right]. \quad (2.45)$$

With the laser detuned below resonance, $\Delta < 0$, this is clearly a restoring force. This specific arrangement of focused gaussian beams is often called a dipole trap.

2.3 Atoms and Magnetic Fields

The interaction of an atom with a magnetic field is a magnetic dipole interaction based on the total angular momentum of the atom, including the orbital angular momentum \vec{L} , spin \vec{S} and nuclear angular momentum \vec{I} . The combination of these give the hyperfine structure of the atom, quantized with

$$\vec{F} = \vec{L} + \vec{S} + \vec{I}. \quad (2.46)$$

The D_2 transition of ^{87}Rb , on which our MOT is based, has transitions between the $5^2S_{1/2}$ ground state and the $5^2P_{3/2}$ excited states. Both of these states have $S = 1/2$. The ground state has $L = 1/2$ and the excited state has $L = 3/2$. Together with ^{87}Rb 's nuclear spin of $I = 1/2$, the excited state can have total angular momentum F with values between 0 and 3, and the ground state can have values of either 0 or 1 [62]. This is shown in the level diagram of Figure 2.1. The frequency splitting between the hyperfine levels is on the order of 10^2 MHz while energy shifts due to the magnetic field (Zeeman shifts) of the MOT is on the order of MHz. With such

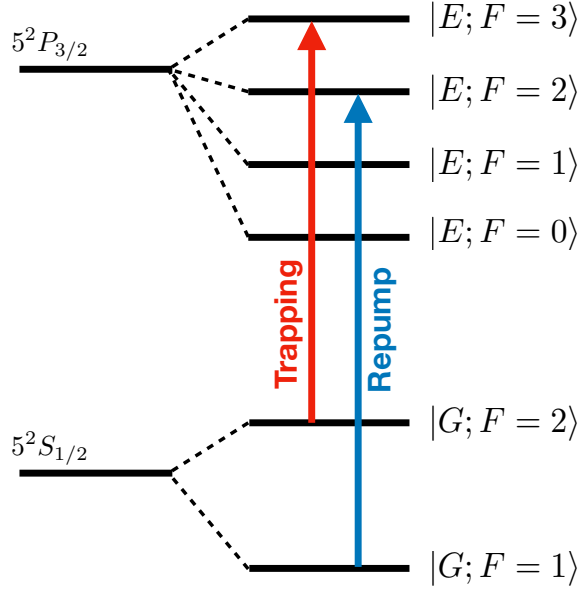


FIGURE 2.1. ^{87}Rb D₂ Transition Level Diagram. Labeled at the transitions address for our MOT.

a small shift of the levels due to the magnetic field, the total angular momentum \vec{F} is a fair quantum number to use to study the interaction between the atom and the magnetic field [62]. Here, we'll treat the $|G; F = 2\rangle$ and $|E; F = 3\rangle$ levels as the only two levels of our atom. A fuller picture of the hyperfine atom is discussed in Chapter V.

The atom is treated as a magnetic dipole that is aligned with its angular momentum

$$\vec{\mu} = \mu_B g_F \vec{F}, \quad (2.47)$$

where μ_B is the Bohr magneton.

Much like the electric dipole interacting with the electric field of light, the interaction between the magnetic dipole and magnetic field is then [63]

$$\hat{H}_z = -\vec{\mu} \cdot \vec{B}. \quad (2.48)$$

Working in one dimension, assuming that \vec{B} lies along the z-axis, the interaction simplifies to

$$\hat{H}_z = -\mu_B g_F \hat{F}_z B_z$$

when the z-axis is also the angular momentum quantization axis of the atom. \hat{F}_z is the projection operator of the atomic angular momentum along the quantization axis. Writing this explicitly gives

$$\hat{H}_z = -\mu_B B_z \sum_{s=e,g} \sum_F \sum_{m_F} g_F m_F |s; F, m_F\rangle \langle s; F, m_F| \quad (2.49)$$

where s is the excited or ground state of the atom. From this, it is clear that the magnetic field is responsible for shifts of the energy levels of atoms, the Zeeman shifts [64].

The quantities g_F are Landé g-factors [62]. They result from perturbative approximations made when the shift in atomic energy levels due to the magnetic field is much smaller than the hyperfine splitting. In this case, the total atomic angular momentum \vec{F} , as defined in 2.46, serves as a good quantum number. In ^{87}Rb , the hyperfine splitting is on the order of gigahertz for the ground states and hundreds of MHz for the excited states. The Zeeman splitting (per Gauss) is on the order of 1MHz/G. With magnetic fields in the MOT on the order of tens of Gauss, this condition is met, which is good since all For ^{87}Rb 's D_2 transition, all excited states have $g_{F_e} = 2/3$ and the ground states have $g_{F_g=2} = 1/2$ and $g_{F_g} = -1/2$ [62].

When a 3D model of the atom is discussed in Chapter V, this assumption about the magnetic interaction will remain true—the atom's quantization axis will align with the magnetic field direction at every location in space. This will require rotation of the lab frame to align the z-axis of the lab frame with the magnetic field. This is

the largest complication of the 3D model as the polarization directions for each of the six MOT beams must be correctly written in a circular and linear polarization basis. This rotation is discussed in Section 5.1.3.

2.3.1 Magnetic Trapping

A particle with a magnetic dipole momentum $\vec{\mu}$ in a magnetic field will have a potential energy $U = -\vec{\mu} \cdot \vec{B}$. If this energy is spatially varying, the particle will experience a magnetic force

$$\vec{F} = \vec{\nabla}(\vec{\mu} \cdot \vec{B}) \quad (2.50)$$

As done above (and as will be assumed while discussing the MOT), when the dipole moment is aligned with the field the interaction energy is $U = \mu |\vec{B}|$. Under these circumstances, the force is then

$$\vec{F} = -\mu \vec{\nabla} |\vec{B}|, \quad (2.51)$$

so that the force is zero where the magnetic field strength vanishes. This force must also apply to an atom with magnetic dipole moment [65, 66] and is critical to evaporative cooling for Bose-Einstein condensates [67].

As done for radiation pressure, the force is examined quantum mechanically by Equation 2.29 with the Hamiltonian 2.49. An atom in the steady state experiences a force

$$\langle \vec{F} \rangle = \mu_B \left(\frac{\partial B_z}{\partial z} \hat{z} \right) \sum_{s=e,g} \sum_F \sum_{m_F} g_F m_F |c_{s,m_F}^{ss}|^2, \quad (2.52)$$

where the energy level populations are written as their wavefunction coefficients rather than density operator elements (strictly for simplification of subscripts). The

relationship to the classical magnetic force of 2.51 is a bit unclear as it appears uniform. However, the steady state populations have spatial dependence (see Figures 5.1 for a graph of the populations as a function of position), which allows for magnetic trapping.

For a linear magnetic field $\vec{B} = -B'_z z \hat{z}$, as will be discussed for the MOT, the force is

$$\vec{F} = -\mu_B B'_z \hat{z} \sum_{s=e,g} \sum_F \sum_{m_F} g_F m_F |c_{s,m_F}^{ss}|^2. \quad (2.53)$$

For states where $g_F > 0$, when $z < 0$ (so that $B > 0$), the energy levels with $m_F < 0$ will be preferentially populated as their energies will be reduced by Zeeman shifting. This results in the double sum producing a negative value, given an overall force in the positive z-direction. When $z > 0$, the $m_F > 0$ energy levels are preferentially populated and produce a force in the negative z-direction. Thus, the overall force is to locate the atom near $z = 0$, just as in the classical case. This results holds true when $g_F < 0$, with the preferential population switching positive and negative values for m_F .

It is important to note here that this magnetic trapping is distinct from the magnetic confinement discussed in Section 2.5.1. The trapping here results from the minimization of the magnetic dipole energy. The confinement trapping results from spatially preferential photon absorption due energy level Zeeman splitting.

2.4 The $F_g = 0 \rightarrow F_e = 1$ Atom

For the remainder of this Chapter, the focus will be on a $F_g = 0 \rightarrow F_e = 1$ atom, that is one having no ground state angular momentum and an excited state with a total angular momentum of 1. With the angular momentum formalism in Equation

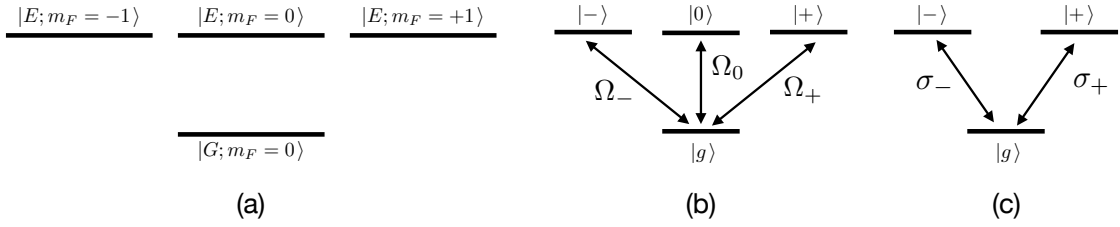


FIGURE 2.2. $F_g = 0 \rightarrow F_e = 1$ Atom Level Diagrams. (a) Full labeling for states of the atom. (b) Simplified naming conventions used in the text. The electric fields coupling excited and ground states are labeled with their Rabi frequencies as give in Equation 2.56. (c) V-atom reduction when there is no electric field to excite the $|0\rangle$ state.

2.46, this could correspond to a spin-1/2 atom ($S = 1/2$), orbital angular momentum $L = 1/2$ and no nuclear spin ($I = 0$). With no nuclear spin, the angular momentum vector $\vec{J} = \vec{L} + \vec{S}$ is often used rather than \vec{F} , but \vec{F} used here for more directed comparison to the full atomic energy levels discussed in Chapter V. The level diagram for such an atom is shown in Figure 2.2a.

For this atom, the levels will be labeled as shown in Figure 2.2b. The atom has density operator

$$\rho = \begin{bmatrix} \rho_{--} & \rho_{-0} & \rho_{-+} & \rho_{-g} \\ \rho_{0-} & \rho_{00} & \rho_{0+} & \rho_{0g} \\ \rho_{+-} & \rho_{+0} & \rho_{++} & \rho_{+g} \\ \rho_{g-} & \rho_{g0} & \rho_{g+} & \rho_{gg} \end{bmatrix}. \quad (2.54)$$

Each excited states has its own raising operator defined, the three being defined as

$$\begin{aligned} \sigma_-^\dagger &= |- \rangle \langle g|, \\ \sigma_0^\dagger &= |0 \rangle \langle g|, \quad \text{and} \\ \sigma_+^\dagger &= |+ \rangle \langle g|. \end{aligned} \quad (2.55)$$

The excited and ground states are coupled via electric fields \vec{E}_+ , \vec{E}_0 and \vec{E}_- , named relative to the excited states they couple (note this names are opposite the naming conventions in Equation 5.9). These fields are circularly polarized or linearly polarized. Following the derivation of Equation 2.25, this leads to an atom-field coupling Hamiltonian

$$\hat{H}_{\text{AF}} = -\frac{\hbar}{2} \left(\Omega_-^* \hat{\sigma}_- + \Omega_- \hat{\sigma}_-^\dagger \right) - \frac{\hbar}{2} \left(\Omega_0^* \hat{\sigma}_0 + \Omega_0 \hat{\sigma}_0^\dagger \right) - \frac{\hbar}{2} \left(\Omega_+^* \hat{\sigma}_+ + \Omega_+ \hat{\sigma}_+^\dagger \right). \quad (2.56)$$

It is also assumed that the electric fields are all detuned from resonance ω_0 by some amount. Following the derivation in 2.24, the atomic Hamiltonian can be written as

$$\hat{H}_A = -\hbar\Delta_+ |+\rangle\langle+| - \hbar\Delta_0 |0\rangle\langle 0| - \hbar\Delta_- |-\rangle\langle-|. \quad (2.57)$$

The magnetic field Hamiltonian is given directly from Equation 2.49 and for the $F_g = 0 \rightarrow F_e = 1$ atom is

$$\hat{H}_z = \mu_B g_F B_z (|+\rangle\langle+| - |-\rangle\langle-|), \quad (2.58)$$

as evident from the m_F values shown in Figure 2.2a. Defining $\Delta_B = \mu_B g_F B_z / \hbar$, this can be written as

$$\hat{H}_z = \hbar\Delta_B |+\rangle\langle+| - \hbar\Delta_B |-\rangle\langle-|. \quad (2.59)$$

Each of the excited states can spontaneously decay and it assumed this occurs at the same rate, Γ , for each state. The evolution of the atomic density operator follows the equation

$$\frac{d}{dt}\rho = -\frac{i}{\hbar} \left[\hat{H}_A + \hat{H}_{\text{AF}} + \hat{H}_z, \rho \right] + \Gamma \mathcal{L}[\hat{\sigma}_-] \rho + \Gamma \mathcal{L}[\hat{\sigma}_0] \rho + \Gamma \mathcal{L}[\hat{\sigma}_+] \rho \quad (2.60)$$

based on the density operator evolution definition of 2.8. The form of the Lindblad superoperator of Equation 2.7 reveals that spontaneous emission from one excited state of the atom depends only on the populations of that excited state. With these separate decay paths, the impact on the evolution of the state of the atom from each state is independent as written above. The time evolution of each density operator element $\rho_{i,j}$ is listed in Appendix A.2.

Our magneto-optical trap consists of pairs of counter-propagating, circularly polarized lasers, as shown in Figure 2.5. The counter-propagating beams have the same circular polarization in their reference frame, but in the reference frame of an atom (with the beams moving towards it from different directions) the two beams have opposite polarizations, corresponding to only the \vec{E}_- and \vec{E}_+ electric fields. Matching the model to our experiment sets $\vec{E}_0 \rightarrow 0$. As discussed in Appendix A, doing this effectively simplifies the atom to the V-atom, shown in Figure 2.2c. Without the linear field component to excite the $|0\rangle$ state, the x'x' population of this state will decay quickly to zero and can be ignored. The remainder of this Chapter will assume this simplification of the atomic structure.

The equations of motion for the internal structure of the V-atom are given in equations A.4. In these equations, for simplicity, the excited state energies Zeeman energy shifts are left out. They can be returned to the solutions by allowing $\Delta_{\pm} \rightarrow \Delta_{\pm} \pm \Delta_B$. These solutions are not particularly enlightening other than it is nice that there is an analytic solution and we can use the two-level atom steady-state solution to check their validity. To do this, remove one electric field by letting $\Omega_{\mp} \rightarrow 0$ and $\Delta_{\mp} \rightarrow 0$, then the population in the $|\pm\rangle$ state is

$$\rho_{\pm,\pm}^{ss} = \frac{|\tilde{\Omega}_{\pm}|^2}{1 + 4\delta_{\pm}^2 + 2|\tilde{\Omega}_{\pm}|^2} \quad (2.61)$$

where, as defined in Appendix A, $\tilde{\Omega}_{\pm} = \Omega_{\pm}/\Gamma$ and $\delta_{\pm} = \Delta_{\pm}/\Gamma$. These agree with the population of the excited state from the two-level atom optical Bloch equations 2.27, as they should: as was the case for the $|0\rangle$ state, when there is no field coupling an excited state to the ground state, that excited state can be ignored as its population will decay to zero. Thus, with only one laser, the atom should behave as a two-level atom excited by just one field and the solutions should agree exactly with the optical Bloch equations.

The quantity $\tilde{\Omega} = \Omega/\Gamma$ is often written in terms of the ratio of the electric field intensity relative to a saturation intensity as

$$\frac{I}{I_{\text{sat}}} = 2 \left| \tilde{\Omega} \right|^2 = \frac{2 |\Omega|^2}{\Gamma^2}. \quad (2.62)$$

This is the saturation parameter, Equation 2.38, with $\Delta = 0$. For the electric field with amplitude E_0 , the intensity of the field is $I = \epsilon_0 c E_0^2/2$. Together with the definition of Ω in Equation 2.18, the saturation intensity is

$$I_{\text{sat}} = \frac{\epsilon_0 c \hbar^2 \Gamma^2}{4 \left| \langle g | \hat{\epsilon} \cdot \vec{d} | e \rangle \right|^2}. \quad (2.63)$$

This is referred to as the saturation intensity, as when $I \gg I_{\text{sat}}$ (i.e. $|\Omega| \gg \Gamma$), the two-level atom excited state population in Equation 2.27 saturates to 1/2. This quantity clearly has different values for different electric field polarizations $\hat{\epsilon}$ (the denominator will be changed). When the saturation intensity is referred to throughout this text, it is in reference to circular polarized light exciting MOT trapping transition which has a value 1.669mW/cm² for the atomic species of rubidium used in our experiments [62].

2.4.1 Optical Molasses

The idea of radiation pressure can be extended further to look at the effects of identical counter-propagating plane waves interacting with an atom. These two fields are defined as

$$\begin{aligned} E_+(\vec{r}) &= E_0 e^{-ikz} & \text{and} \\ E_-(\vec{r}) &= E_0 e^{+ikz}. \end{aligned} \tag{2.64}$$

These are defined so the field propagating in the negative z -direction excites only the σ_+ transition and the field propagating in the positive z -direction excites only the σ_- transition, as shown in 2.3. For each of these beams, atoms moving against their propagation direction should see the frequency of the light shifted to a higher frequency due to the Doppler effect. An atom with velocity v then sees each beam having velocity

$$\begin{aligned} \omega_+ &= \omega + kv \\ \omega_- &= \omega - kv, \end{aligned} \tag{2.65}$$

where ω is the rest frequency of the light. The atom then sees light that is detuned from the resonant frequency ω_0 by

$$\begin{aligned} \Delta_+ &= \omega_+ - \omega_0 = (\omega - \omega_0) + kv = \Delta_L + kv \\ \Delta_- &= \omega_- - \omega_0 = (\omega - \omega_0) - kv = \Delta_L - kv, \end{aligned} \tag{2.66}$$

where Δ_L is the (red) detuning of the laser from the atomic resonance. Following the atomic force derivation in Section 2.2.3, the force operator is

$$\vec{F} = -\frac{ik\hbar}{2} (\Omega_+^* \hat{\sigma}_+ - \Omega_+ \hat{\sigma}_+^\dagger) \hat{z} - \frac{ik\hbar}{2} (-\Omega_-^* \hat{\sigma}_- + \Omega_- \hat{\sigma}_-^\dagger) \hat{z}, \tag{2.67}$$

which calculated in steady-state gives

$$F^{ss}(v) = [-\hbar k \Gamma \rho(v)_{+,+} + \hbar k \Gamma \rho(v)_{-,-}] \hat{z}, \quad (2.68)$$

where the density operator elements are written to note that they explicitly depend on the velocity of the atom through the Doppler shifted detuning of the lasers. Allowing $\Omega_+ = \Omega_- = \Gamma/\sqrt{2}$ and $\Delta_L = -\Gamma$, the force (in units of $\hbar k \Gamma$) is plotted as a function of velocity (in units of $|\Delta_L|/k$) in Figure 2.4a in red.

This result is easy to explain. An atom moving towards one of the fields, sees a Doppler-shifted beam (at higher frequency) that is closer to resonance than the beam it is travel along with. A smaller detuning (recall, $\Delta_L < 0$) allows the opposing beam to more easily excite the atom. This is shown with the different length arrows coupling the ground and excited states in the level diagram of Figure 2.3. The photons absorbed from the in-tune beam apply a larger force than the opposing beam, giving a net force pushing the away in the opposite direction of its motion. With counter-propagating beams, each beam slows atoms moving towards it. This gives an overall decrease in speed, and thus temperature of the atom. This arrangement of lasers is known as optical molasses and are a well studied method to cool atoms [1–3].

For the D₂ transition of ⁸⁷Rb, the force scale is 3.2×10^{-20} N and the velocity scale is 4.7 m/s in Figure 2.4a. A speed of 4.7 m/s corresponds to an atomic temperature of 78mK [62]. Typically MOT temperatures are order of 10 μ K, corresponding to velocities of order 10 cm/s (This difference in expected and measured temperatures is discussed in Section 2.5.3). The graph of Figure 2.4b rescales the axes to 10^{-22} N and cm/s. Clearly from this graph, in the range of velocities for atoms in the MOT, the force is very close to linear. Expanding Equation 2.68 to first order in v gives a

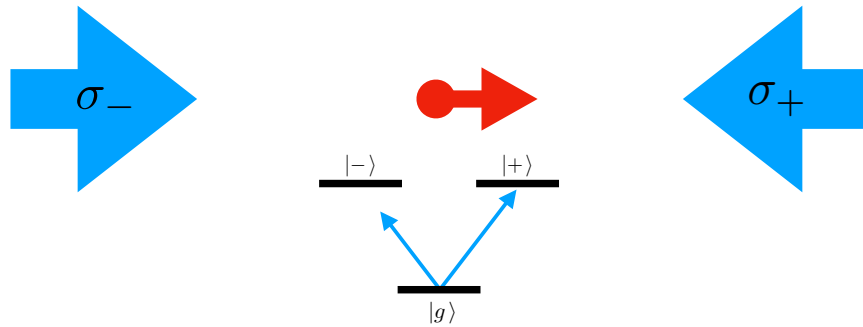


FIGURE 2.3. Optical molasses beam arrangement. An atom moving towards a beam see its frequency shifted closer to resonance.

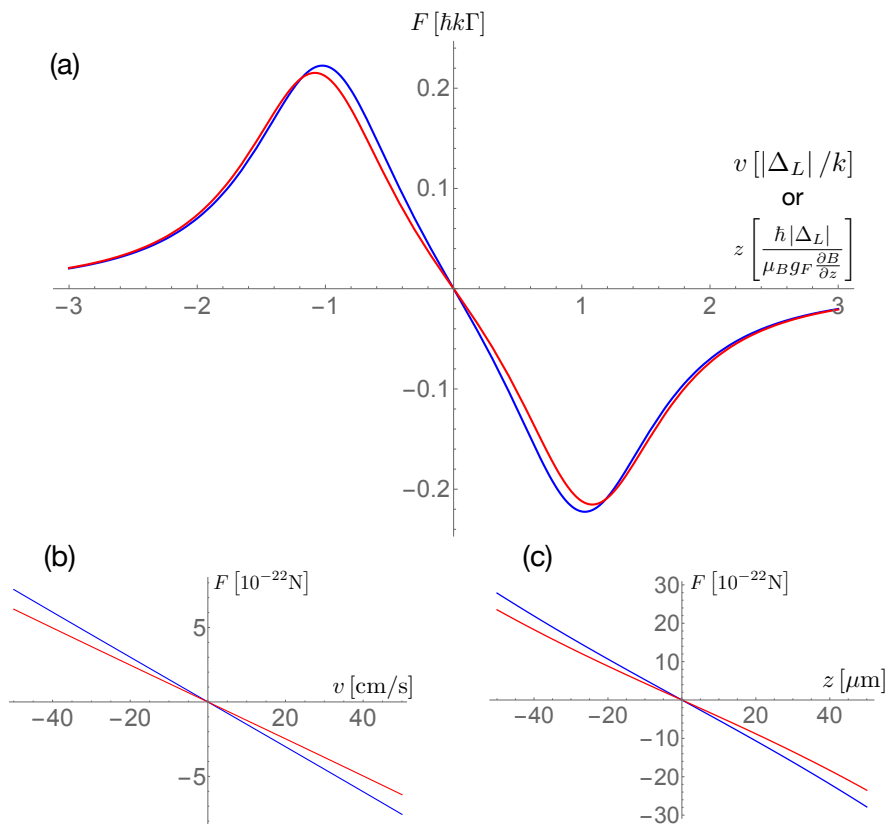


FIGURE 2.4. V-atom forces. (a) The red curve shows forces of a 1-dimensional V-atom and the blue curve shows the force on the extended two-level atom. Graph shown is for both atom in optical molasses as a function of velocity or atom in a MOT as a function of position. Peaks occur where Doppler shift (molasses) or Zeeman shift (MOT) match the laser detuning, Δ_L . (b) Damping force for velocities in range of atoms in a MOT. (c) Restoring force for positions on scale of atomic motion in a MOT.

damping force $\vec{F}(v) = \vec{F}_0 \hat{z} - \beta v \hat{z}$ where

$$F_0 = \frac{\hbar k \Gamma \left(|\tilde{\Omega}_p|^2 - |\tilde{\Omega}_m|^2 \right)}{1 + 4\delta_L^2 + 2|\tilde{\Omega}_m|^2 + 2|\tilde{\Omega}_p|^2} \quad (2.69)$$

and

$$\beta = 8\hbar k^2 |\delta_L| \times \left\{ \frac{(|\tilde{\Omega}_m|^2 + |\tilde{\Omega}_p|^2)(|\tilde{\Omega}_m|^2 - |\tilde{\Omega}_p|^2)^2 + 4(|\tilde{\Omega}_m|^2 + |\tilde{\Omega}_p|^2)^2}{[1 + 4\delta_L^2 + 2|\tilde{\Omega}_m|^2 + 2|\tilde{\Omega}_p|^2][16\delta_L^2 + (2 + |\tilde{\Omega}_m|^2 + |\tilde{\Omega}_p|^2)^2]} + \frac{4(|\tilde{\Omega}_m|^2 + |\tilde{\Omega}_p|^2)(1 + 4\delta_L^2) + 16|\tilde{\Omega}_m|^2|\tilde{\Omega}_p|^2}{[1 + 4\delta_L^2 + 2|\tilde{\Omega}_m|^2 + 2|\tilde{\Omega}_p|^2][16\delta_L^2 + (2 + |\tilde{\Omega}_m|^2 + |\tilde{\Omega}_p|^2)^2]} \right\}. \quad (2.70)$$

The sign of this constant force F_0 depends just on the two field's intensities (recall, the Rabi frequencies are proportional to the field strength). So, this constant force is just an overall force caused by one beam having more power, and thus pushing harder, on the atom. For most cases, this is dropped by balancing the beams, as plotted in Figure 2.4a. In this case, the damping force reduces to $\vec{F} = -\beta_{\text{V-atom}} v \hat{z}$ with

$$\beta_{\text{V-atom}} = - \frac{16k^2 \hbar |\delta_L| |\tilde{\Omega}|^2}{\left[1 + 4|\tilde{\Omega}|^2 + 4\delta_L^2 \right] \left[1 + 4\delta_L^2 + 2|\tilde{\Omega}|^2 + |\tilde{\Omega}|^4 \right]}. \quad (2.71)$$

A common alternative derivation of this damping is done by using the two-level atom result for $\rho_{e,e}^{ss}$ in Equation 2.27 for *both* excited state populations in Equation 2.68. This is taking the two equations of 2.61 and treating them both as accurate, while they are in only true in the presence of just one excitation field. With these, and making sure to use the the appropriate detunings from Equation 2.66, as done in [25, 48], the atomic damping force is

$$F = \left[-\hbar k \Gamma \rho_{e,e}^{SS} (\Delta_L + kv) + \hbar k \Gamma \rho_{e,e}^{SS} (\Delta_L - kv) \right] \hat{z}.$$

The results of this extended two-level atom is shown in Figure 2.4 as the blue curves. This calculation does not rely on oppositely polarized fields. Two fields with linear polarization will work for the extended two-level model.

The extended two-level method overestimates the force from one beam. It assumes too large of an excited state population, as it ignores effects on the atomic population due the opposite beam. With the V-atom, an individual excited state population is reduced from its two-level atom population, as some of that population is shifted into the other excited state. At large speeds, the agreement between methods is better. In this case, the fast-moving atoms are much closer to resonance with one of the beams, allowing it to dominate the atomic state. The V-atom then behaves much like the two-level atom at large speeds. In the small speed range, the force calculated by [25, p. 88] for the extended two-level atom is

$$\vec{F}(v) = -\frac{16\hbar k^2 |\delta_L| |\tilde{\Omega}|^2}{\left[1 + 2|\tilde{\Omega}|^2 + 4\delta_L^2\right]^2} v \hat{z}. \quad (2.72)$$

Compared to the V-atom in the Equation 2.71, the damping coefficient β for the extended two-level atom is slightly larger.

While the damping of the motion should drive the atom to rest, this damping force is balanced by the random emission of photons by the atom. Each photon absorption, which damps the motion is followed by an emission, which gives the atom a momentum bump of magnitude $\hbar k$ in the opposite direction of the photon direction. With a detuning $\Delta = -\Gamma/2$, to maximum β for both models in equations 2.71 and 2.72, analyzing the diffusion of the atomic velocity distribution [2, 25] results in a minimum atomic energy of

$$U_{min} = \frac{\hbar\Gamma}{4}. \quad (2.73)$$

With the 1D equipartition theorem, this results in what is called the Doppler temperature, the lower limit on temperatures for atoms in an optical molasses.

$$T_D = \frac{\hbar\Gamma}{2k_B}. \quad (2.74)$$

2.5 Magneto-Optical Traps

As noted above, atoms in optical molasses are still free to diffuse [68] without being confined to any one location. Confining the atom to make an actual trap can be done with magnetic fields.

2.5.1 Magnetic Confinement

Placing an atom into a region with a spatially varying magnetic field will give the excited states of the atoms a spatially varying Zeeman shift. In particular, adding a linear magnetic field with gradient $-B'_z$ (here, assume $B'_z > 0$) shifts the excited state energies (for the V-atom) by

$$\Delta_B = \frac{\mu_B g_F}{\hbar} (-B'_z z), \quad (2.75)$$

following the convention from Equation 2.59. The spatial energy shifts of the $|\pm\rangle$ states are shown in Figure 2.5. From this Figure, an atom located at $z > 0$ has its $|+\rangle$ excited state energy shifted down in energy. This reduces the detuning of the laser from resonance, Δ_L (shown in Figure by the thin, red line), improving the atomic interaction with σ_+ light. With σ_+ light traveling from the $z > 0$ direction, photons absorbed from that field push the atom back toward $z = 0$. The same analysis holds true for an atom located at $z < 0$ with the $|-\rangle$ level and the σ_- field. This results

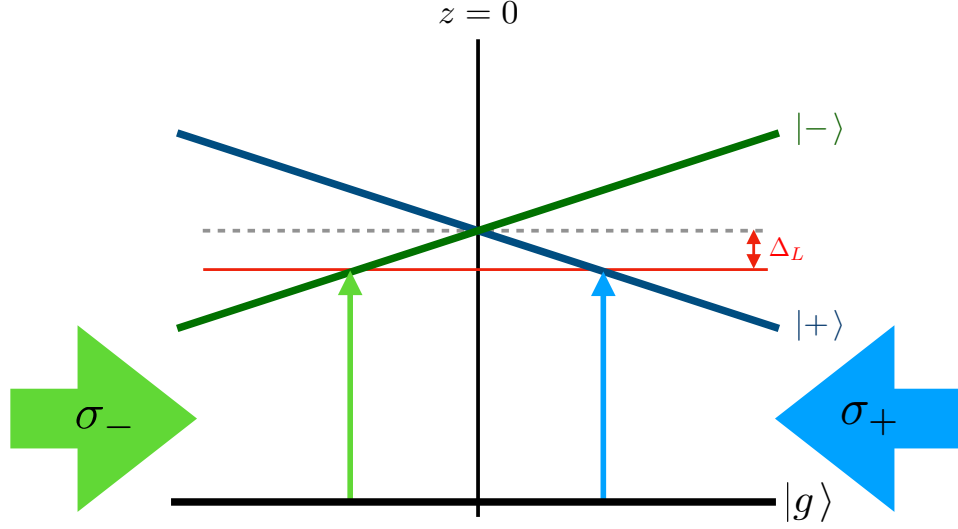


FIGURE 2.5. Magneto-Optical Trap Level Diagram. An atom displaced from $z = 0$ has one excited state energy Zeeman shifted closer to frequency of the red detuned laser. Correctly matching the polarization of a laser to the direction of the magnetic field applies a restoring force on the atom towards $z = 0$.

in the magnetic field imposing a restoring force from the lasers onto the atom. This behavior is the position-space analog to damping in optical molasses.

This interaction is quantified following similar steps to those in Section 2.4.1.

The detuning of the atoms from resonance follow the equations

$$\begin{aligned}\Delta_+ &= \omega_+ - \omega_0 = \omega - (\omega_0 - \Delta_B) = \Delta_L + \Delta_B \\ \Delta_- &= \omega_- - \omega_0 = \omega - (\omega_0 + \Delta_B) = \Delta_L - \Delta_B,\end{aligned}\tag{2.76}$$

where it is important to note that the energy differences here are the result in shifts of the excited state frequencies, rather than shifts in the laser frequencies as was the case for optical molasses. The force on an atom is then

$$F^{ss}(z) = [-\hbar k \Gamma \rho(z)_{+,+} + \hbar k \Gamma \rho(z)_{-,-}] \hat{z},\tag{2.77}$$

where the explicit dependence on position comes from the detuning energy shifts in Equation 2.76. This equation has exactly the form of Equation 2.68 in position-space rather than velocity space. The graph of this function will be the same as the red curve in the graph of Figure 2.4a with the horizontal axis being position in units of $\hbar\Delta_L/\mu_B g_F B'_z$. This graph agrees with the restoring force interpretation presented above. A change of sign for the magnetic field ($\vec{B}(z) = +B'_z z \hat{z}$) requires flipping the polarization of the two beams to create a trap again.

Typical MOT parameters, for our single-atom MOT, have $B'_z \approx 241$ G/cm. Following the g_F derivation in [62] to use $g_F \approx 1.33$, the distance scale is $135\mu\text{m}$. Atoms in our MOT have typical displacements from the center of the MOT on the order of $10\mu\text{m}$, again allowing examination of small position displacements (“small” being defined so atomic Zeeman shifts are much smaller than the detuning of the laser). A graph of this is shown Figure 2.4c. Again, this force is very close to linear so that we can expand the equation to get a restoring force $\vec{F} = \vec{F}_0 \hat{z} - \kappa z \hat{z}$ with the same value for F_0 as Equation 2.69 and

$$\kappa = 8k\mu_B g_F B'_z |\delta_L| \times \left\{ \frac{(|\tilde{\Omega}_m|^2 + |\tilde{\Omega}_p|^2)(|\tilde{\Omega}_m|^2 - |\tilde{\Omega}_p|^2)^2 + 4(|\tilde{\Omega}_m|^2 + |\tilde{\Omega}_p|^2)^2}{[1 + 4\delta_L^2 + 2|\tilde{\Omega}_m|^2 + 2|\tilde{\Omega}_p|^2][16\delta_L^2 + (2 + |\tilde{\Omega}_m|^2 + |\tilde{\Omega}_p|^2)^2]} + \frac{4(|\tilde{\Omega}_m|^2 + |\tilde{\Omega}_p|^2)(1 + 4\delta_L^2) + 16|\tilde{\Omega}_m|^2|\tilde{\Omega}_p|^2}{[1 + 4\delta_L^2 + 2|\tilde{\Omega}_m|^2 + 2|\tilde{\Omega}_p|^2][16\delta_L^2 + (2 + |\tilde{\Omega}_m|^2 + |\tilde{\Omega}_p|^2)^2]} \right\}. \quad (2.78)$$

Returning briefly to the purely magnetic trapping of Section 2.3.1, the magnetic trapping force of Equation 2.53 for the V-atom was

$$\vec{F}_{\text{Mag. Trap}}^{ss} = -\mu_B g_F B'_z [\rho(z)_{+,+} - \rho(z)_{-,-}] \hat{z}. \quad (2.79)$$

This force is identical in form to Equation 2.77 but with scaling $\mu_B g_F B'_z z$. For the typically MOT parameters above, the magnetic trapping force is of order 10^{-23} . This

is orders of magnitude smaller than the MOT force scaling $\hbar k \Gamma$, which is of order 10^{-20} .

As seen with the $|0\rangle$ energy level, without electric fields to excited the atom, those excited states will not be populated. Without these fields, then, the V-atom will have no magnetic trapping as $F_g = 0$. For the full ^{87}Rb atom, however, the ground states do have angular momentum. Thus, there can still be magnetic trapping for ^{87}Rb without near-resonant electric fields. In addition, the $|F_g = 1, mg\rangle$ states have $g_F = -1/2$, which results in atoms in this ground state being repelled from the minimum of the magnetic field magnitude rather than trapped [63, 69].

For the magnetic confinement equation, in the case where $\Omega_- \neq \Omega_+$, the F_0 term is non-zero and shifts the “center” of the MOT – the position where the restoring force is zero. A similar effect occurs with a background magnetic field $\vec{B}_0 = B_0 \hat{z}$ to give a total field of

$$\vec{B}(z) = -B'_z z \hat{z} + B_0 \hat{z}. \quad (2.80)$$

This shifts the location where $\vec{B} = 0$, again moving the center of the MOT and modifying the force equation

$$\vec{F} = \vec{F}_{z,0} - \kappa \left(z + \frac{B_0}{B'_z} \right) \hat{z}. \quad (2.81)$$

From Equation 2.78, κ can be written as $\kappa = \tilde{\kappa} B'_z$. Then the force equation becomes

$$\vec{F} = \vec{F}_{z,0} - \kappa z \hat{z} - B_0 \tilde{\kappa} \hat{z}. \quad (2.82)$$

Therefore, a non-zero background field of magnitude $B_0 = F_{z,0}/\tilde{\kappa}$ can cancel the offsetting force due to beam imbalance to return a purely linear restoring force $\vec{F} = -\kappa z \hat{z}$. This can also be used to cancel gravitational forces on the MOT.

Comparing the equation for restoring constant κ to Equation 2.70, the optical molasses damping constant, we have

$$\kappa = \beta \frac{\mu_B g_F B'_z}{\hbar k}, \quad (2.83)$$

which is the same as the equation for the extended two-level atom [25]. Therefore, the extended two-level atom solution has the same overly strong assumptions for the restoring force strength as it does for the damping force.

Taking the case with balanced electric fields, the restoring force becomes $F = -\kappa_{V\text{-atom}} z$ with

$$\kappa_{V\text{-atom}} = \frac{16k\mu_B g_F B'_z |\delta_L| |\tilde{\Omega}|^2}{\left[1 + 4|\tilde{\Omega}|^2 + 4\delta_L^2\right] \left[1 + 4\delta_L^2 + 2|\tilde{\Omega}|^2 + |\tilde{\Omega}|^4\right]}. \quad (2.84)$$

2.5.2 Finally, a MOT

Combing the effects of the atomic motion-based Doppler shift creating a damping force and the magnetic field creating a spatially dependent restoring force, the force on an atom in the MOT is that of a damped, harmonic oscillator

$$F = -\beta z - \kappa v. \quad (2.85)$$

Here, the F_0 forces from MOT beam imbalance have been suppressed.

With such a force, an atom in a MOT should behave as in a harmonic potential, $U = \frac{1}{2}\kappa z^2$. As above, the damping of the atomic motion by the MOT lasers will not force the atom to rest because of the random emission of photons. Thus the atom should have an average energy due to motion that has the form $\langle U \rangle = \frac{1}{2}\kappa\langle z^2 \rangle$. With the equipartition theorem [25], in one dimension the atomic position should follow

$$\langle z^2 \rangle = \frac{k_B T}{\kappa}. \quad (2.86)$$

With this relation, measurements of the size of a magneto-optical trap can give a measure of the trap's temperature as done in many of the temperature techniques discussed in Chapter I. Early MOT experiments expected temperatures close to the Doppler temperature, Equation 2.74, but experiments measured clearly lower temperatures [30, 70].

2.5.3 Sub-Doppler Cooling

Atomic temperatures below the Doppler temperature are a result of polarization changes seen by the atom moving in an optical molasses [64, 71]. In both cases, this enhanced cooling only appears for atoms with multiple ground states, such as the one shown in Figure 2.6, so we're getting a bit ahead of ourselves for the discussion in Chapter V. For optical molasses with counter-propagating *linearly* polarized electric fields, alluded to in the discussion of the extended two-level atom in Section 2.4.1, the sub-Doppler cooling mechanism is named the Sisyphus effect.

In this linear field arrangement, the polarizations for the two counter-propagating fields created by MOT beams are at right angles. Their interference creates two potentials, which underpin the force of Equation 2.29, that the atoms move through.



FIGURE 2.6. Atom with Mutliple Ground States

One potential oscillates as $\sin(kx)$ where k is the wavenumber of the light and corresponds to the σ_+ polarized light. The other potential oscillates as $\sin(kx + \pi)$ and corresponds to the σ_- polarized light.

Atoms primarily interacting with the σ_+ light, such as atoms oscillating between the outer two levels on the right side of Figure 2.6, will follow that light's potential energy curve, increasing and decreasing speed as it moves. This is shown as the leftmost atom (black dot) in Figure 2.7. However, on occasion, when the atom is at the peak of the potential, with the smallest kinetic energy, the atom can absorb a σ_- photon (center atom in Figure 2.7). When it does so, it moves onto the σ_- curve, which is at its lowest point in the potential energy curve (shown as the arrow for the center atom). The kinetic energy of the atom here does not change (except for a small change due to photon emission recoil), but it now is at a potential energy minimum (rightmost atom in the Figure). Repeating this process lowers the overall mechanical energy of the atom and results in temperatures lower than predicted by Doppler cooling.

For optical molasses with circular polarizations, such as the MOT described in 2.5, the sub-Doppler cooling mechanism arises from an additional enhanced

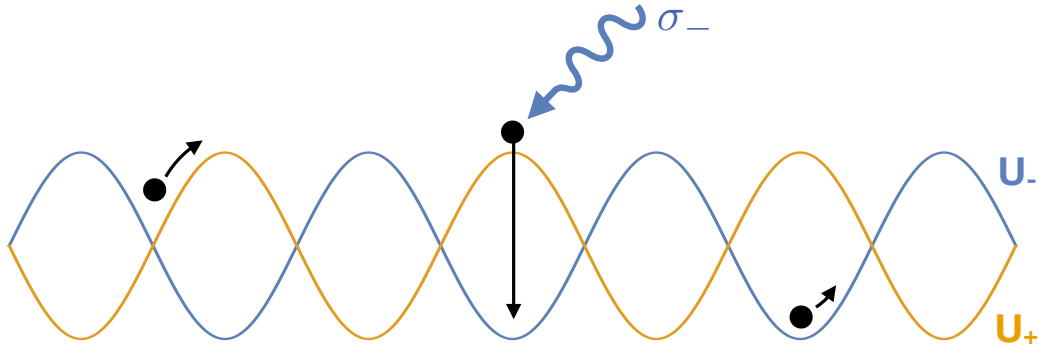


FIGURE 2.7. Sisyphus Cooling. Atoms (left) interacting with only σ_+ light follow the potential energy curve U_+ . If an atom (center) absorbs a σ_- photon while at the top of the U_+ curve, it will drop to the U_- curve (right), losing mechanical energy in the process.

scattering rate from a beam that an atom is moving towards. In this arrangement, the light's linear polarization direction rotates around the beams' propagation axis. In the reference frame of the atom seeing a fixed polarization direction, the changing electric field direction appears as a magnetic field that Zeeman shifts the atom's energy levels. This shifting induces pumping between different ground states of the atom leading to preferential excitation by the light field the atom is moving towards [71, 72]. This preferential interaction slows the atoms more quickly than Doppler theory predicts giving a lower atomic speed and temperature. As our MOT is based on circular beams, this is the sub-Doppler cooling mechanism expected for our MOT.

This cooling, polarization gradient cooling, only occurs with atoms that have multiple ground states. The V-atom has just one by construction, while the full ^{87}Rb atom has many. The added cooling from polarization gradient cooling is clearly demonstrated in the much larger slope, due to enhanced restoring constant κ , near the origin of Figure 5.2 for the full atom (blue) as opposed to the V-atom (red). Evoking the equipartition theorem to calculate the temperature still holds for the

sub-Doppler cooling, although there is not an analytic solution for κ for the full ^{87}Rb atom in a MOT. In any case, measuring temperature via the equipartition theorem, as was developed for Equation 2.86, the temperature is inversely proportional to κ . The evidently larger value for κ for the ^{87}Rb atom then reveals the cooler-than-Doppler temperature.

These two sub-Doppler cooling mechanisms do not rely on the presence of the magnetic field for the MOT. They originate entirely from the counter-propagating electric fields and thus also appear for atoms in an optical molasses. The magnetic field for the MOT is, again, strictly responsible for the position-dependent trapping of the atoms near $z = 0$.

CHAPTER III

EXPERIMENTAL SETUP

This chapter will discuss the experimental apparatus for the experiments discussed in chapters IV and VI. The experiment design implements a dual-MOT setup in which one MOT is singularly used to increase load rates into the second MOT through radiation pressure. The second MOT is where our experiments are performed. For moving from a many-atom MOT to a single-atom MOT, changes were made primarily to the second MOT.

In this chapter, the vacuum chamber and laser system will be first discussed. These systems were designed and built by prior students and are discussed in detail in their theses [73–76]. The systems are discussed in brief, focusing on changes made to the system in order to allow for single-atom trapping. Larger changes made to the experimental apparatus are discussed after, looking at high-gradient magnetic field systems and a single-photon detection apparatus.

3.1 Vacuum

Our vacuum chamber is segmented into two chambers, a “high pressure” chamber and a “low pressure” chamber, as shown in Figure 3.1. The “high” and “low” designations refer to their relative pressures as both sides fall into the ultra-high vacuum (UHV) regime. The high pressure chamber originally had a pressure of $\sim 10^{-8}$ torr and the low pressure chamber had a pressure of $\sim 10^{-10}$ torr [73]. The high pressure chamber contains the first MOT and the low pressure chamber contains the second MOT. An important feature of the low pressure chamber is an 8” long,

30mm square rectangular cell made of fused silica. This glass cell is installed to stick outward along the long axis of the optical table, giving broad optical access.

The two chambers are connected by a differential pumping tube. The diameter of this narrow, tapered tube grows at an angle of about 3° from the high pressure chamber to the low pressure chamber [75]. The narrowness of the tube reduces the probability for atoms to transit its length between chambers. The taper allows the atomic beam of atoms to expand as it is sent between the first MOT and the second MOT (see Section 3.2 for a discussion of the two MOT design).

As a way to improve the chances to capture just a single atom, we decided to reduce the already low background pressure. This was done by closing the valve leading to the rubidium source for the past many years. The background vapor has gradually adsorbed onto the inner chamber or filtered out through an ion pump (Varian VacIon Plus Starcell 75), lowering the background pressure below levels measurable by the pump (10^{-8} torr). The loading rate of MOTs with a small number of atoms can be used to estimate the background pressure of atoms using the loading rate of single atoms [6, 77]. Our permanent magnet MOT discussed in Section 3.3.1, with lasers detuned by about -2Γ (Γ is the natural line width of Rubidium 87, about 5.75 MHz [62]), has a loading rate of 0.0058 atoms/sec. This suggests the main vacuum chamber has a pressure on the order of 10^{-15} torr and background rubidium density of 40 atoms/cm³.

After an unplanned rebaking of the vacuum system (see Section 3.1.2) the background pressure was kept low by severely limiting the initial atomic rubidium vapor. In the initial build for a large MOT, the system was flooded with rubidium vapor by heating a 1 g rubidium source contained in the system [73]. After the rebake, the rubidium source was reopened via valve and vapor was allowed to reenter

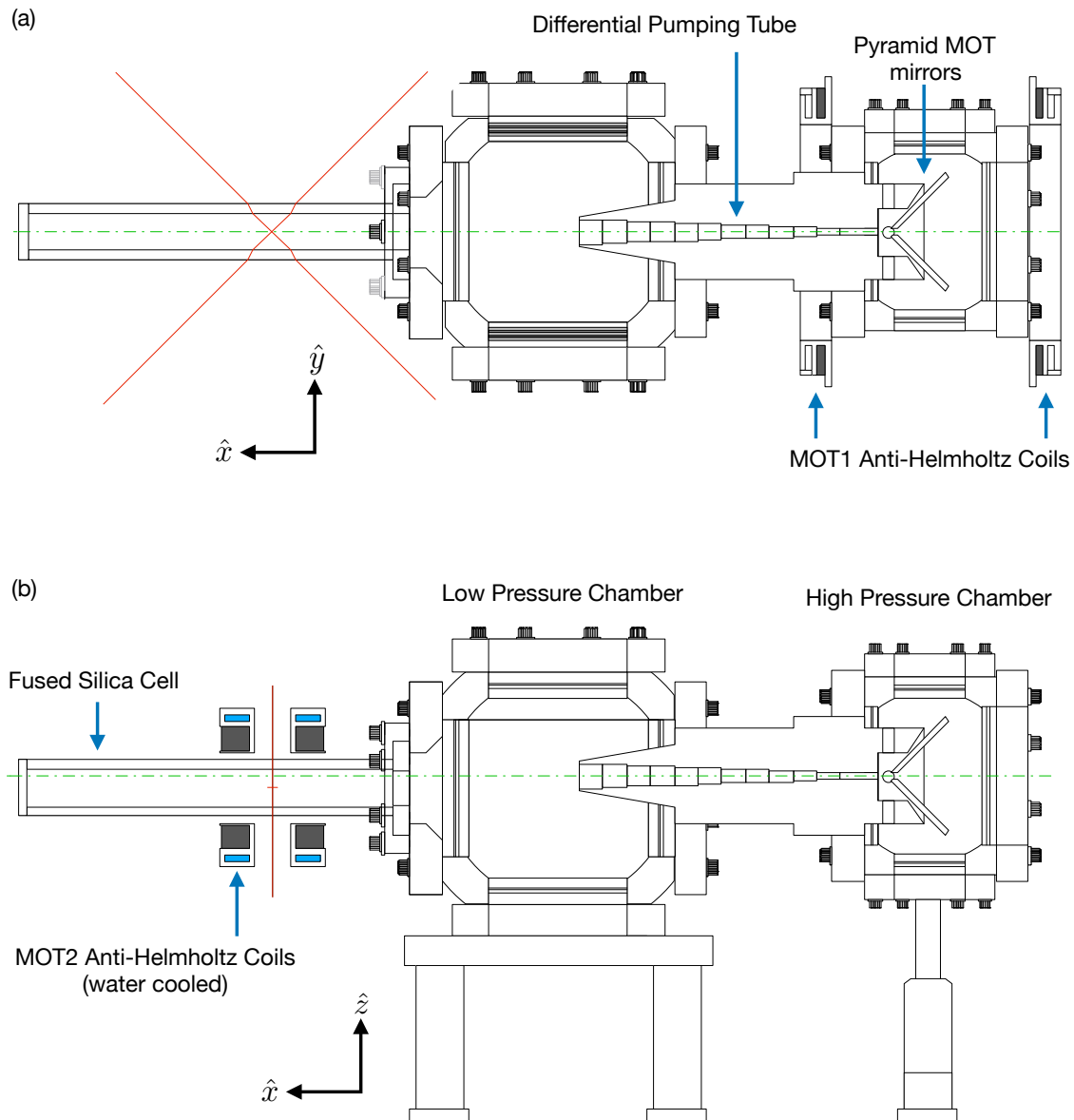


FIGURE 3.1. Experimental Diagram of Vacuum Chamber. (a) Top-down view. (b) Side view. The two chambers are joined by a differential pumping tube. The high pressure chamber contains MOT 1. The low pressure chamber contains MOT 2 within the fused-silica cell and is where experiments are done. The red dash-dot line shows the beam path of the MOT 1 laser through the chamber. The solid-red lines show the beam paths for the second MOT. Only vacuum chamber elements important for the discussion in chapters IV and VI are shown. Missing from this diagram are pumps and titanium getters, the rubidium source, and mirrors for a high powered fiber laser [73].

the vacuum. Without heating the source, only a small amount of rubidium enters the system and allowed us to capture single atoms again.

3.1.1 Light Induced Atomic Desorption

Significantly lowering the background vapor of rubidium helps the chances to capture just one atom, but it also limits the chances to capture any atoms. To briefly improve loading rates, we implemented a light- induce atomic desorption (LIAD) system.

Shining bright, off-resonant light into a vacuum chamber whose walls have been coated with rubidium can desorb the rubidium from the walls to increase the vapor pressure in the chamber [11, 78]. This has been observed for not just rubidium but other atomic vapors [79–81] and even for molecules [82]. For many surfaces, this desorption has been explained as the light breaking ionic bonding between alkali atoms and silicon-oxygen chains in the surface [82]. This effect has also been observed to occur for atoms adsorbed onto stainless steel, although the physical mechanism for this is less well understood [81, 83].

A number of groups have used LIAD to increase atomic counts in MOTs [11, 81, 84, 85]. LIAD as a method to load traps has the benefit of allow for a low background vapor pressure but still allow for quick loading of the trap by temporarily increasing the vapor pressure. A low vapor pressure is important for single-atom MOTs to limit loading rates from the background and to increase MOT lifetimes by limit background atom collisions. A MOT loaded with LIAD demonstrates those effects [86, 87].

We built and implemented an LIAD system based on the work of [81] using three 1W blue power LEDs (Newark P/N 51R2234). These were arranged symmetrically around a used copper vacuum gasket and the gasket was mounted outside of the first

MOT access window as shown in Figure 3.2. The LEDs were powered with the circuit shown in Figure 3.3. The double transistor design was implemented to use a high current PNP transistor (Mouser P/N 511-BD238) we had on hand. The addition of the NPN transistor functions as NOT gate to reverse TTL logic appropriately for the PNP transistor. The parallel resistor design is for safe power dissipation while the circuit is running.

For a many-atom MOT, our LIAD setup gives an atom number increase in the second MOT of around 10%. This is significantly below what was seen in [81] as that experiment loaded the MOT directly from the desorbed gas. Our tests did not measure the atom number increase in a MOT loaded directly from the desorbed gas (our first MOT), but from a MOT that was loaded by this (potentially) enlarged MOT. Our experimental setup doesn't allow for measurement of the atom number in the first MOT. A LIAD setup is not used near the second MOT as the bright lights of the LIAD could damage the single-photon counting avalanche photodiode used to detect single atoms in the second MOT.

3.1.2 Table-Top Bakeout

An unplanned breaking of the vacuum system (do not push on the fused-silica cell!) required a rebaking of the system to achieve UHV pressures. The baking process vaporizes gasses which have deposited onto the vacuum chamber and allow them to be removed from the vacuum via pump. Because the system should still be relatively clean even after filling with air, a lower temperature bake was done compared to the original construction [73]. When the system was originally built, a power failure also broke vacuum near the end of the bake. An additional final bake, to only 150°C, done

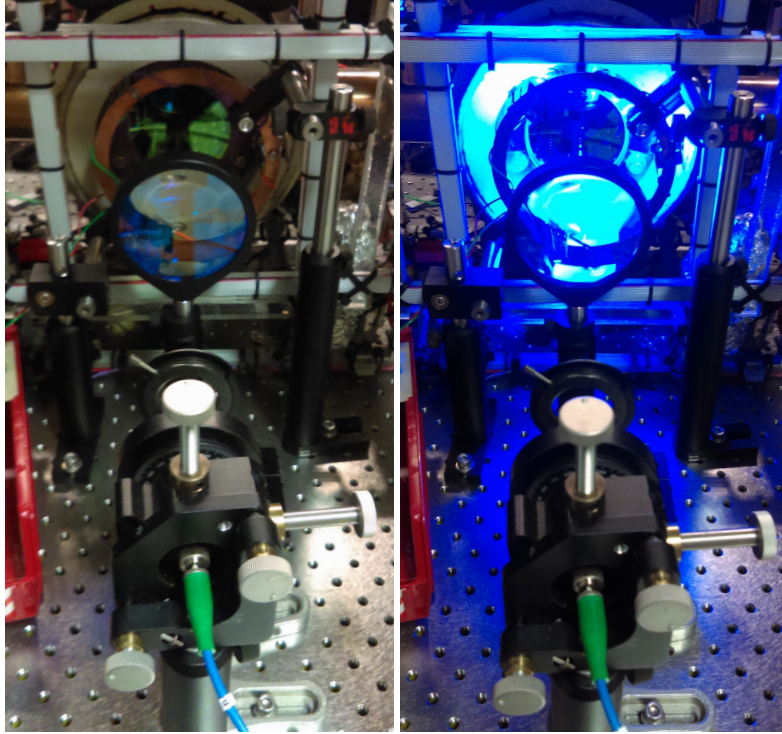


FIGURE 3.2. Installed LIAD system. Three blue LEDs are attached to the reverse of the copper coil seen in left image, which is also the dark, black ring in the right image. The fiber in the foreground carries trapping and repump light for MOT 1.

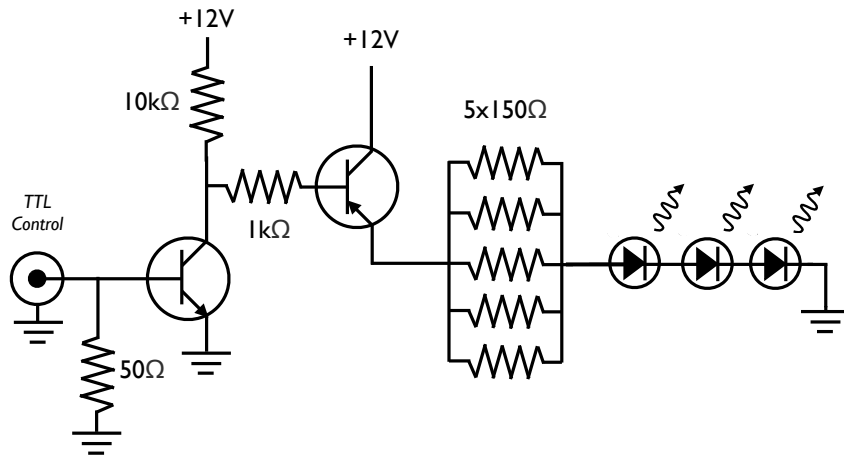


FIGURE 3.3. LED circuit for LIAD setup

over night was sufficient to return to UHV pressures. For this rebake, a similar low temperature bake was sufficient to return to UHV pressures.

Because the vacuum chamber was already in place on the optical table and positions of experimental equipment were set relative to it, we decided to attempt a bake of the chamber in place instead of moving it away from the table. This was done following the “many heater” method described by Birnbaum [88]. After removing sensitive experimental equipment around the vacuum system, heater tape (P/N Omega SRT101-060 and similar) was wrapped around various vacuum chamber parts and thermocouples were positioned around the chamber. Around the tip of most of the thermocouples, a short sleeve of fiberglass (harvested from around broken heater tapes) was placed to electrically insulate the exposed ends of the thermocouples from being grounded to the vacuum chamber. The thermocouples were positioned so that temperature gradients were easy to detect. For example, a series of thermocouples were located at the window of the first MOT, one on each side of the differential pumping tube, and one on each side of the (newly replaced) fused-silica cell. This allows us to monitor the temperature gradient along the full length of the chamber, making sure a relatively even temperature was kept along that axis.

After positioning the heater tapes and thermocouples, the chamber was covered in many layers of aluminum foil. Windows were covered by wrapping oil-free aluminum foil (All Foils UHV aluminum foil) around the window flange and its bolts, creating a heightened ring of foil around the rim of the window, as shown in Figure 3.4a. More foil was then placed over the ring and ends were stretched to wrap around the chamber holding the foil over the top of the window in place and leaving a gap of air between the foil and the window. This was to prevent foil scratching the glass and provide an insulating pocket of air to keep high temperatures. Around the fused-

silica cell, foil wrapped fire bricks were stacked to a few inches below the cell. A single heater tape was laid over the top of the firebricks under the cell. Four very long pieces of UHV aluminum foil were folded into long, stiff strips which were bent into arches that stretched over the cell and tucked under the bricks on each side of the cell. Similar long, folded pieces of UHV foil were wrapped between the arches, building the framework of an oven around the cell (affectionately referred to as The Barn). This is shown in Figure 3.4b. A layer of UHV foil was wrapped around the sides of The Barn and folded onto the top and a layer of UHV foil was wrapped over the top. The UHV foil covering windows and the rest of the vacuum chamber, including ion pumps and pump hoses, were wrapped in many layers of kitchen quality aluminum foil. The fully wrapped vacuum chamber is shown in Figure 3.4c.

The vacuum chamber was heated slowly with the heater tapes to temperatures around 120°C over a few days. The 2nd vacuum chamber temperature increase was particularly slow due to its size and limited surface area where heating tape could be wrapped, which slowed the process considerably as the entire system was attempted to be kept close to the same temperature. The ion pumps were heated much higher than the other portions of the chamber (to 180°C and 170°C for the larger and smaller ion pump respectively). This was to clean off material that had built up inside the ion pumps. The small ion pump had not worked for years as collected material had shorted the high voltage difference across the pump. Particularly warm or cool spots of the chamber were adjusted by removing and adding aluminum foil, respectively. To help visualize the temperatures, the thermocouple values were plotted spatially in three dimensions with their locations corresponding to the (ideal) position of the thermocouples. A few additional temperatures were estimated based on the temperature measurements of nearby thermocouples. Lines between these

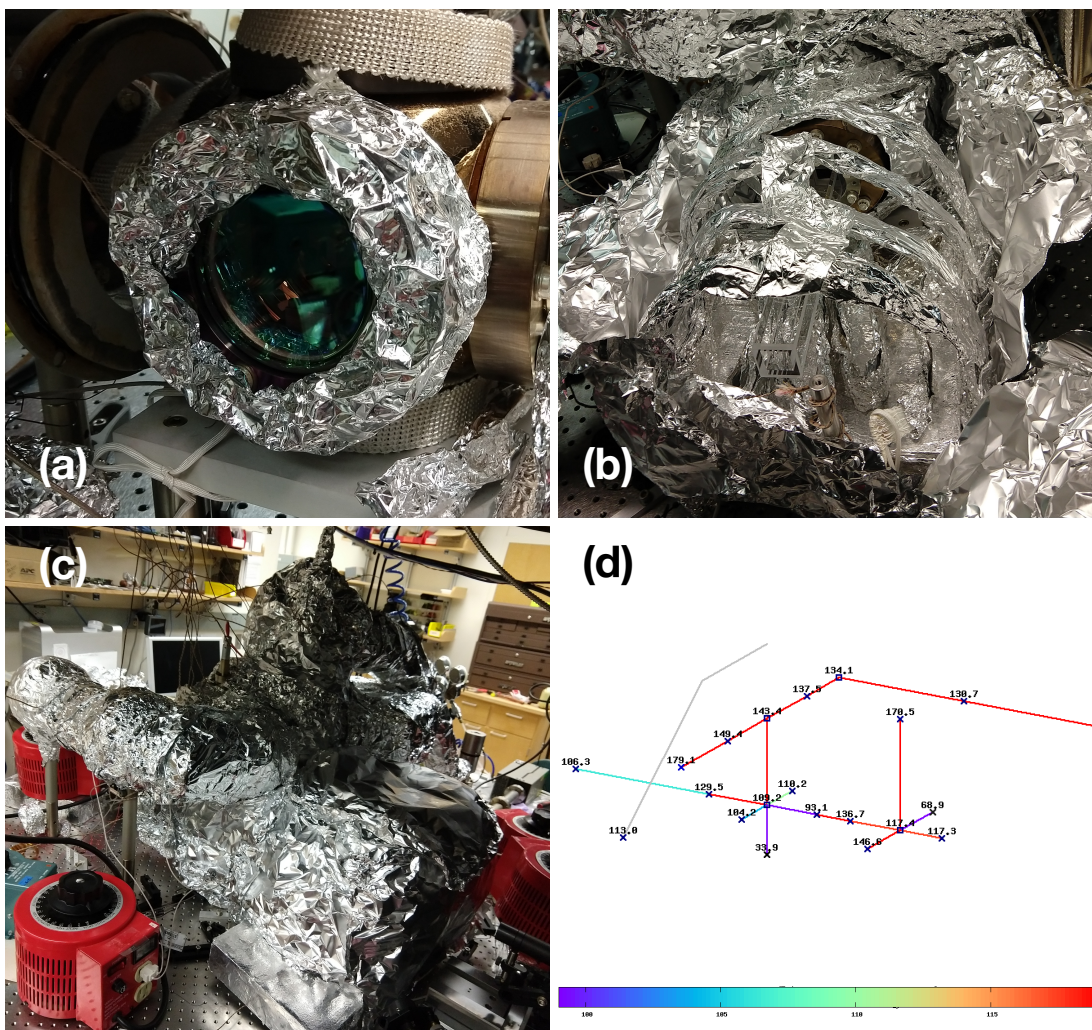


FIGURE 3.4. (Re)baking the vacuum chamber. (a) Protected window coverings. (b) Oven constructed around the fused-silica cell. (c) Entire vacuum system wrapped and baking. (d) Positional temperature monitoring graph.

points were colored as relative temperature of the extreme points from an estimate of the temperature at the center of the large MOT chamber. One such of these graphs is shown in Figure 3.4d. The graph was particularly helpful in visualizing the temperatures and potential strong gradients in the system. This graph, along with graphs of the individual thermocouple temperatures over time, were used to adjust the various heater tape voltages to bring the chamber up to temperature.

Prior to baking but after replacing the fused silica cell and pumping out the system, the lowest pressure measured by the turbo pump (BOC Edwards P/N EXT 70H 24V) was 3.2×10^{-8} torr. After baking, the pressure had reduced to 6.4×10^{-9} torr. This is comparable to a final pressure of 8.3×10^{-9} torr achieved during the initial baking of the system. This difference is primarily due to a small leak in the home-made gasket for mounting the fused-silica cell that was present during the initial bake. Tightening the flange for the cell closed the leak after ending the bake sealed it, but limited the pressure during the bake. No such leak was present before or after the rebake. Pressure readings with the ion pumps measured post-baking pressures of $< 4 \times 10^{-10}$ torr and 3×10^{-9} torr on the low- and high-pressure sides of the chamber, respectively.

3.2 Lasers

The laser system for our MOT has been largely unchanged from previous experiments [76]. All of the lasers for the experiment are homemade external-cavity diode lasers with outputs of around 100 mW near 780 nm, the transition wavelength for ^{87}Rb .

The main MOT trapping laser consists of a master laser injection locked to two slave lasers, discussed in detail in [76]. The beam path for the MOT trapping laser

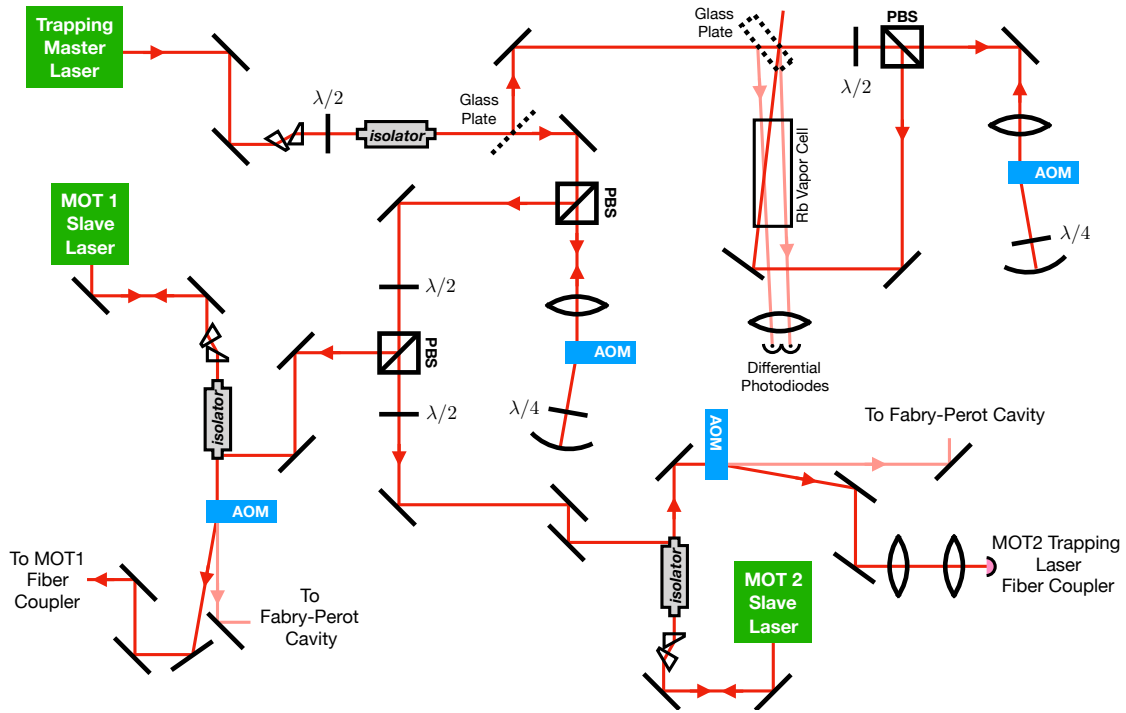


FIGURE 3.5. Beam Path of MOT Trapping Lasers

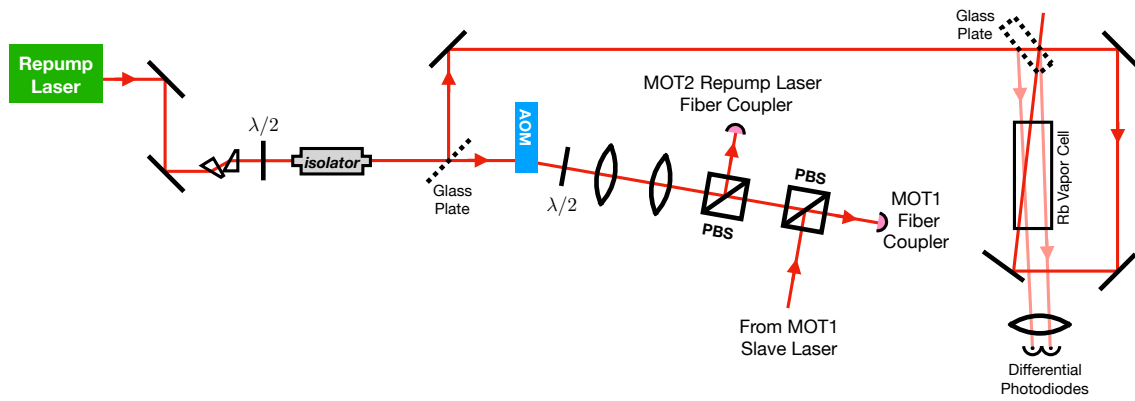


FIGURE 3.6. Beam Path of MOT Repumping Lasers

is shown in Figure 3.5. The two slave lasers reproduce the frequency of the input light and effectively increase the total MOT laser power. A portion of the light from a slave laser is sent to a Fabry-Perot cavity. Monitoring the output of the cavity verifies successful injection of the maser laser as only a single peak will appear in the cavity signal. The remainder of the slave lasers' outputs are coupled to optical fibers for use in the MOTs. One slave laser is used to operate each of the two MOTs.

The repumping beam, needing much less power than the trapping laser, does not seed slave lasers. This beam is split and directly coupled into two fibers, one for each MOT. The beam path for the repump trapping laser is shown in Figure 3.6.

3.2.1 MOT 1 Laser

For the first MOT, light from the repump laser and light from one of the slave lasers are combined via a beamsplitter before being coupled into a 5 μm core diameter optical fiber (Oz Optics P/Ns PMJ3A3A-850-5/125-3-x-1, where x corresponds to various fiber lengths). The fiber emits light freely into space (there is no collimation lens) before reaching a 3-inch lens which collimates the now greatly expanded beam. The fiber and lens are visible in pictures of the LIAD, Figure 3.2. The now collimated light travels into the vacuum chamber through a large window on the right side of the high pressure chamber as marked with the green dash-dot line shown in the MOT chamber diagram (Figure 3.1). Inside the chamber, the beam reaches a set of "pyramid mirrors" to form the MOT.

The pyramid mirrors are shown in Figure 3.7. These are a set of four Pyrex pieces coated to reflect light at 780nm and are each aligned at 45° degree inclines. As the collimated light reaches the pyramid mirrors, it is reflected perpendicular to the original beam. As shown in Figure 3.7a, the reflected beams counter-propagate from

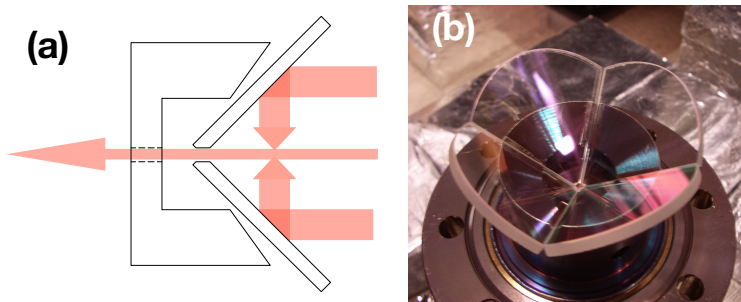


FIGURE 3.7. Pyramid MOT Mirrors. (a) Diagram of arrangement of pyramid MOT mirrors with beam behavior shown. (b) Picture of built pyramid MOT mirrors.

opposing mirrors. The four sets of beams reflected from the pyramid mirrors, together with large anti-Helmholtz coils mounted on the exterior of the vacuum chamber form a 2-dimensional MOT at the center of the pyramid. They are trapped on the plane that is perpendicular to the MOT 1 beam axis.

As shown in Figure 3.7, the mirror pieces are cut to leave a hole at their center to allow atoms to escape from the 2-dimensional MOT [89, 90]. The hole aligns with the small-diameter opening of the differential pumping tube. The portion of the MOT light that travels directly along the center of the pyramid will travel through hole and along the differential pumping tube. This is shown as the green dash-dot line in Figure 3.1. Before entering the tube, this light intersect the 2-dimensional MOT. The light applies radiation pressure (see Section 2.2.3) to the cooled atoms and pushes them along its path, through the differential pumping tube and into the high pressure chamber. The fused-silica cell is attached opposite the differential pumping tube so that the light, and atoms, traveling through the tube will continue on along the length of the cell.

The second MOT's center is located about 5-3/8" from the end of the fused-silica cell and is positioned a quarter inch below the beam path for the first MOT

laser through the differential pumping tube. The atoms pushed by this light travel approximately the full length of the cell while still inside the beam [74]. However, some atoms sink out of this path and can fall into the range of the second MOT. This drooping is caused by gravity and atomic motion perpendicular to the beam axis (this motion is the same that necessitates the taper in the differential pumping tube). Thus, we can load atoms into the second MOT from the first by capturing atoms dropping out of the beam. We have seen that using the first MOT to load the second MOT increases the loading rate of the permanent magnet MOT (see Section 3.3.1) by a factor of 4.

No changes were made to the first MOT laser in preparation for single-atom experiments.

3.2.2 MOT 2 Laser

Unlike the MOT 1 laser, the trapping and repump beams for the second MOT are coupled into separate fibers. These two fibers are the inputs of a fiber beam splitter array (custom design from Canadian Instrumentation and Research) which combines the two inputs and splits the light to 6 fibers, the 6 fibers for our MOT. The fiber array was designed so that each output beam received equal power, but is not perfect. The lowest power beam has around two-thirds of the power of the highest power beam. The output beams, as used in the experiment, are matched so counterpropagating beams have about equal power to limit effects of beam imbalances (see Section 2.4.1). An imbalance ratio between counterpropagating beams is defined as

$$w = \frac{P_+ - P_-}{P_+ + P_-}, \quad (3.1)$$

where P_+ and P_- are the powers in the higher powered beam and the lower powered beam respectively [91, 92]. This definition is convenient as $P_+ = \langle P \rangle(1 + w)$ and $P_- = \langle P \rangle(1 - w)$ where $\langle P \rangle$ is the average power of the counterpropagating beams. With this definition, the MOT beam pairs have imbalance ratios of $w = 0.0367$, $w = 0.0034$ and $w = 0.115$. The largest imbalance ratio was chosen for the two beams traveling vertically up and down, along the axis of the MOT anti-Helmholtz coils. This large beam imbalance has implications for the discussion in Chapter VI and is resolved as in 3.2.4.

Originally, the six fibers are connected to a stack of components that contain a fiber collimator (Thorlabs P/N F810FC-780) and a quarter-wave plate (Casix P/N WPL1225-lambda/4-780nm-M) [73]. The collimators produce a 6.6 mm diameter beam (the $1/e^2$ power diameter) and the wave plates convert the linearly polarized input light to circular light. The waveplate is mounted on the face of a 0.594" diameter aluminum tube. The tube (and thus waveplates) are rotated around the collimator to give correct light polarization to create the MOT.

Four of the fibers launch light parallel to the surface of our optical table, intersecting the fused silica cell at 45° . Because the beams enter non-normal to the cell, the beams experience a shift in propagation direction due to refraction. The fiber launchers are positioned on the table to account for this, resulting in opposing beams that counterpropagate as desired. These beam paths are the red lines shown in Figure 3.1a. The final two beams are the vertical beams discussed above. These beams intersect normal to the cell and do not experience refraction. These are the red lines seen in Figure 3.1b.

Two changes were required for the second MOT lasers when moving to the single atom experiments. Changing the anti-Helmholz coils to permanent magnets required

repositioning the fiber launcher that was below the experimental cell. This launcher was moved to propagate light parallel to the table and reflect vertically off an extra pyramid mirror. The reflection reversed the polarization of the light, so the wave plate in the fiber launcher had to be adjusted to account for this.

The second change added 25 cm irises (Thorlabs P/N IN25) between the fiber launcher and experimental cell. The irises are closed to typical diameters of 3 mm. The irises allowed us to reduce the diameter of the MOT beams, which has three benefits. One, the clipped beams reduce the total amount of light reaching the experimental cell. This reduced background scattered light during an experiment - an important feature as single-atom detection is done by photon counting (Section 3.4). Second, the smaller beams reduce the loading rate of the MOT. Although the size of the trapping region of the MOT is dominated by the magnetic-field gradient of the anti-Helmholtz coils, the counterpropagating beams outside this region create an optical molasses which slows atoms without trapping them [1–3]. These slowed atoms can wander into the trapping region, which increases the loading rate of the MOT. Lastly, clipping the beams with irises, as opposed to replacing the collimator with one that produces a small diameter beam, allows easy adjustment of the beam size without altering the beam intensity at the center of the MOT. Atoms in the MOT should be trapped very close to the intersection of the centers of the six beams. Clipping the tails of beams will not affect the intensity at center, keeping the parameters affecting atomic fluorescence and motion the same, while allowing us to change the loading rates and reduce the photon background.

3.2.3 Trapping Beam Detuning Control

The beam paths for the trapping and repump lasers was shown in figures 3.5 and 3.6, but a detailed description of them was left for prior students' dissertations, particularly that of Tao Li [75]. However, due to the importance of laser detuning to MOT performance, a detailed view of the frequency control elements for the two MOT beams is below.

The frequency of the MOT trapping beam is controlled by the the beam diagram shown in Figure 3.8. This diagram shows only pieces of the overall beam path (Figure 3.5) that are necessary for frequency control. Most notably absent is a split in the beam path at point 3 to seed both slave lasers. The slave lasers only affect the beam power before going to a final AOM and then the fiber couplers. The output frequency of the laser is locked via a home designed lock-in amplifier [75] whose input comes from a doppler-free spectral measurement of the hyperfine structure of rubidium via saturation absorption [93]. In this method, two lasers counter propagate through an atomic sample. Close to resonance, atoms moving in opposite directions absorb photons from opposite beams. This is very similar to the enhanced absorption from beams that lead to the optical molasses in Section 2.4.1, although here the beam polarization is linear. Measuring the output from each beam would reveal an absorption signal that is doppler broadened. because of atomic motion. However, if one beam has a much higher power, atoms whose speed is nearly zero will interact much more strongly with that beam. These atoms will be *saturated* (see Equation 2.63 and its discussion) by the stronger beam and will absorb little light from the weaker beam. A photodiode signal from the weaker beam would not show absorb at frequencies very close to the atomic resonances of the atom. Measuring this signal,

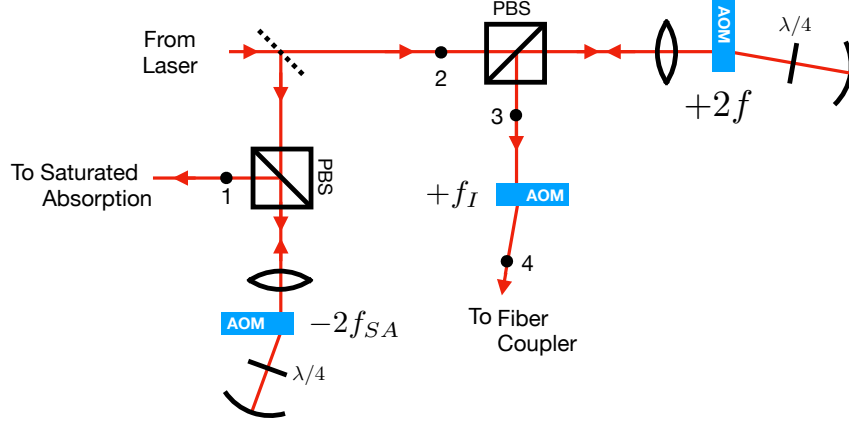


FIGURE 3.8. MOT Frequency Controlling Beam Path. Numerically labeled points along the beam path are reference points for the discussion in the text.

and subtracting away the doppler signal from an identical unsaturated beam, can reveal a non-doppler broadened spectrum for the atomic sample.

One such spectrum is shown in Figure 3.9 and is measured (effectively) at the beam path point 1 as shown in Figure 3.8. The spectrum shows 6 peaks, only three of which correspond directly to hyperfine transitions of the D_2 line of ^{87}Rb . These peaks are the peaks labeled A, D, and F in the spectrum and correspond to optical transitions. Peak A corresponds to the transitions $|F_g = 2\rangle \rightarrow |F_e = 3\rangle$, which is the MOT trapping transition. Peak D corresponds to the $|F_g = 2\rangle \rightarrow |F_e = 2\rangle$ transition. And peak F corresponds to the $|F_g = 2\rangle \rightarrow |F_e = 1\rangle$ transition. Using the $|F_g = 2\rangle \rightarrow |F_e = 3\rangle$ transition as a reference frequency, the peaks are located at the frequencies given in the spectrum (frequencies from Steck [62]). The other three peaks are “crossover” peaks originating from moving atoms whose speeds causes resonant light frequencies for one atomic transition to become doppler shifted into resonance with a different transition. In this case, the frequency of these peaks are the average of the two different resonant transitions, as shown in the spectrum [48].

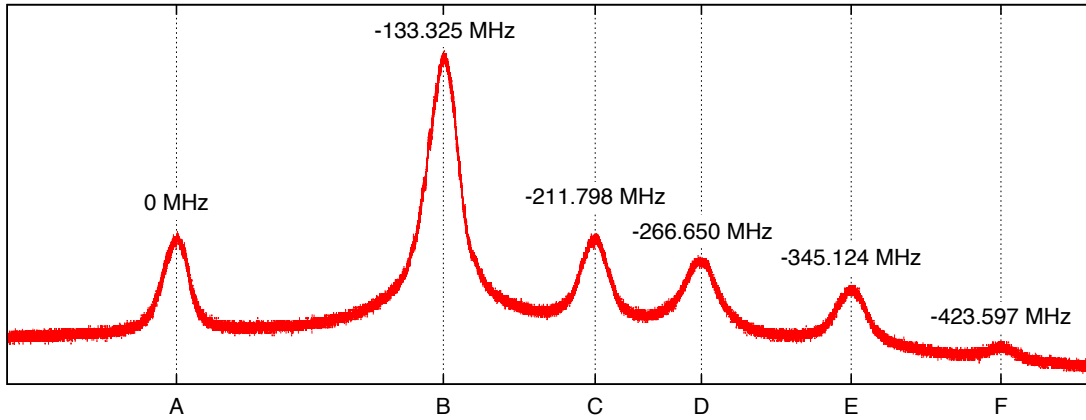


FIGURE 3.9. ^{87}Rb D-2 line spectrum. This spectrum shows decays to the $|F_g = 2\rangle$ state. Frequencies listed are peak locations relative to the decay energy from the $|F_e = 3\rangle$ state, peak A.

The laser is locked to peak B in Figure 3.9, giving the light at the point 1 in Figure 3.8 a frequency of $\Delta = -133.326$ MHz, where the frequency is referenced to the $|F_g = 2\rangle \rightarrow |F_e = 3\rangle$ transition. Prior to reaching this point, the beam double passes through an acousto-optic modulator (AOM), the AOM at the bottom left of Figure 3.9. Because the lasers are locked via lock-in detection, their measurement requires an added modulation. Adding the modulation directly the output laser is not feasible as a MOT needs very stable laser frequencies. Instead, this AOM has its input frequency modulated between 143 MHz and 147 MHz at a rate of 200 kHz. Taking the average of the two input frequencies as a single frequency of the AOM, f_{SA} , the laser has a frequency of $\Delta = -133.326$ MHz $- 2f_{SA}$ before entering this AOM. The AOMs can be used to give either a positive or negative shift in frequency depending on angle of entry of the laser beam. For the remainder of this discussion, these positive or negative shifts are taken by adding or subtracting the frequencies

input into an AOM. This frequency is the same frequency at position 2 in Figure 3.8 and must be the frequency of the light as it leaves the laser.

The portion of the light that is not used for frequency locking double passes through an AOM with a single frequency. This AOM, unlike the other two in this setup, has a tunable frequency using our home build experimental control system ZOINKS [94]. If this AOM has a frequency f , after double passing through it, the light has frequency $\Delta = -133.326 \text{ MHz} - 2f_{SA} + 2f$. This is the light frequency at position 3. This is also the position where the light is split into two paths, and each path is injection locked to a slave laser. This is not shown in the figure as it only increases beam power. The two light paths, after being split, both follow the rest of the path to point 4 shown in Figure 3.8, although they go to different AOMs with the same set frequency.

After having the power increased by the slave laser and before entering the 6-way fiber splitter array, the light (for both MOTs) passes through a final AOM whose use is to control the overall beam intensity and shutter the beam when it is not wanted in the experiment. This AOM has a frequency f_I , giving a final laser frequency of

$$\Delta = -133.326 \text{ MHz} - 2f_{SA} + 2f + f_I, \quad (3.2)$$

where again Δ is the detuning of the light from the $|F_g = 2\rangle \rightarrow |F_e = 3\rangle$ transition, as this was the reference frequency in Figure 3.9. This is the frequency at position 4 of Figure 3.8 and is the frequency of the light that creates our the MOT.

Taking typical values of $f_{SA} = 72.5 \text{ MHz}$ and $f_I = 79.782 \text{ MHz}$, the detuning follows

$$\Delta = -198.544 \text{ MHz} + 2f$$

The AOMs used have a frequency range of 80 MHz to 100 MHz giving usable a MOT laser detuning in the range of about -36 MHz to +2MHz. The MOT is typically ran with detuning between -2Γ and $-\Gamma$.

The repump beam for the magneto-optical trap has a much simpler frequency control setup. There is only one AOM involved in shifting the frequency, as seen in Figure 3.6. The repump beam is locked to the same cross-over peak as the trapping beam. This peak is detuned from resonance of the $|F_g = 1\rangle \rightarrow |F_e = 2\rangle$ transition by -78.474 MHz. There are no frequency changes made between the repump laser output and the repump saturation absorption setup, so that the laser output is detuned this same amount. Before traveling to fiber couplers, the beam travels through a single AOM that applies a shift of $+f_R$ to the beam. This provides a repump beam detuning of

$$\Delta_R = -78.474 \text{ MHz} + f_R \quad (3.3)$$

where Δ_R is the detuning from the $|F_g = 1\rangle \rightarrow |F_e = 2\rangle$ repumping transition.

3.2.4 *Recircularizing and Balancing the MOT2 beams*

The fiber array for the MOT2 lasers are (linear) polarization maintaining fibers. As our design for the MOT requires circular polarization, previous experiments mounted quarter-wave plates to the output fiber launcher for each of the six beams for the 2nd MOT [73]. As noted Section 3.2.2, the power output of these beams was not particularly well balanced. This imbalance shifts the loading location of the MOT, which was not desirable for our position measurements of a single atom. To

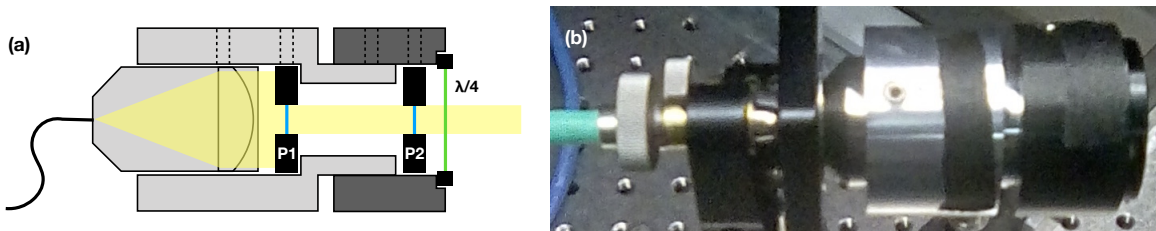


FIGURE 3.10. Fiber Polarization Mount. (a) Schematic drawing of entire mount. One polarizer (P1) is mounted to be aligned with the polarization axis of the fiber. The quarter-wave plate is glued in place aligned with the fast axis of the 2nd polarizer (P2). (b) Picture of built mount. The colors of each piece roughly correspond to the colors in image (a). Black tape covers set screws which hold the polarizations in place. They are to prevent accidental unmounting of the polarizers while adjusting the mounts.

resolve this, the quarter-wave plate mount was modified to allow for control of the power output of each beam as shown in Figure 3.10.

A new mount was made that holds a 1/2" sheet polarizer (Laser Components P/N 11006083) mounted in a modified 1/2" to 1" optics adaptor (Thorlabs P/N AD1T). This polarizer is labeled P1 in the Figure 3.10a. On top of this, the original quarter-wave plate mount was installed after being modified to hold a second 1/2" polarizer (labeled P2) inside of it (the quarter-wave plate is glued on the output face of the mount, just as noted in Section 3.2.2). The 2nd polarizer is aligned so that its fast axis aligns with the axis of the quarter-wave plate, allowing for any light that travels through the polarizer to be circularized by the quarter-wave plate. The first polarizer is aligned to the polarization axis of the fiber and acts as a filter to limit polarization angle noise in the fiber. Rotating the 2nd mount, with the 2nd polarizer and quarter-wave plate, adjusts the power output through the mount without changing the circularization of the beam. The entire two-polarizer-quarter-wave-plate mount system is shown in Figure 3.10.

The power output through a polarizer goes as the cosine² of the angle between the input light polarization and the polarizer axis (see Appendix B). While this is parameter we hope to use to control individual MOT beam power, any fluctuations in the polarization angle of the input light will cause fluctuations in the beam power. We measured polarization angle fluctuations of around $\delta_n = 2^\circ$ from the light through the optical fibers for the 2nd MOT. For beams where we want very little (if any) attenuation (the angle being close to 0), this noise is not a problem, but for fibers where large attenuation was needed to balance the beam power, this can cause large power fluctuations. As shown in Appendix B, aligning the first polarizer to the ideal axis of the fiber, limits power fluctuations output through the three-optic system to order δ_n^2 , compared to order δ_n when only a single polarizer is used.

3.3 Magnetic Fields

Extending the lab's previous experiments [95, 96] to the single atom regime required increasing the field gradient to trap single atoms. We accomplished this in two ways, first with a matched pair of permanent magnetic rings to create a quadrupole magnetic field. This did successfully allow us to trap single atoms, but the permanent magnetic field was not ideal for experimenting, so we designed and built a high-current, water cooled pair of electro-magnets.

3.3.1 *Permanent Magnet Anti-Helmholtz Coils*

The first attempt to greatly increase the anti-Helmholtz magnetic field gradient used a pair of matched permanent ring magnets with their magnetic poles on the

Property	Value
Inner Radius, R_1	0.5in
Outer Radius, R_2	1in
Magnet Thickness, L	0.25in
Magnet Separation, s	2.25in
Maximum Magnetic Field, B_{max}	1468G

TABLE 3.1. Permanent Ring Magnet Parameters

flat-faces of the magnets. (K&J Magnetics P/N RY0X04). The measurements of the magnets are in Table 3.1

With the origin at the center of the (hole in the) magnet and the z-axis running on the central axis of the magnet (coordinate system shown in Figure 3.11), the field along the z-axis is given by

$$\begin{aligned}
B_z(z) = B_{z,max} & \left[\frac{L}{\sqrt{(\frac{L}{2})^2 + R_2^2}} - \frac{L}{\sqrt{(\frac{L}{2})^2 + R_1^2}} \right]^{-1} \times \\
& \left(\frac{(z - \frac{L}{2})}{\sqrt{(z - \frac{L}{2})^2 + R_1^2}} - \frac{(z - \frac{L}{2})}{\sqrt{(z - \frac{L}{2})^2 + R_2^2}} + \right. \\
& \left. - \frac{(z + \frac{L}{2})}{\sqrt{(z + \frac{L}{2})^2 + R_1^2}} + \frac{(z + \frac{L}{2})}{\sqrt{(z + \frac{L}{2})^2 + R_2^2}} \right), \tag{3.4}
\end{aligned}$$

where $B_{z,max}$ is the magnetic field z-component at the origin, R_1 and R_2 are the inner and outer radii of the ring magnet, and L is the thickness of the magnet.

This can be derived one of two ways. First, by integrating the magnetic field of a magnetic dipole oriented in the \hat{z} direction [97] over the volume of the permanent magnet (Figure 3.11a). This integral, in cylindrical coordinates, is:

$$B_z(z) = \frac{\mu_0 m}{2} \int_{R_1}^{R_2} \rho d\rho \int_{-L/2}^{L/2} dz' \left(\frac{2(z - z')^2 - \rho^2}{[(z - z')^2 + \rho^2]^{5/2}} \right).$$

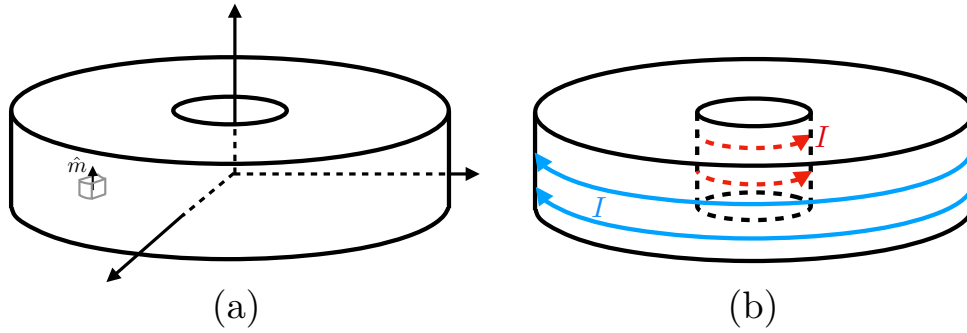


FIGURE 3.11. Permanent Magnet Magnetic Field Calculation Methods. (a) Calculation method that integrates a magnetic dipole field over the volume of the magnet. (b) Calculation method that treats the permanent magnet as opposite-direction sheets of current on the inner and outer walls of the magnet.

The second method is to assume the magnetic is made up of a sheet of current with height L and radius R_1 , and a second sheet of current with height L and radius R_2 with the same current magnitude but in the opposite direction of the inner-sheet (Figure 3.11b). Both of these derivation methods require replacing the unknown magnetization, \hat{m} , or unknown current, I , the appropriate equation involving the magnetic field at the origin, $B_{z,max}$.

The paired permanent magnets, separated by distance s , have a total field

$$B_{tot}(z) = B_z(z + s/2) - B_z(z - s/2) \quad (3.5)$$

The $\pm s/2$ terms shift the magnets by half the separation, redefining the origin to be at the mid-point between the magnets. This quadrupole field using the permanent magnet measurements in Table 3.1 is plotted in Figure 3.12 along with measured values for the magnetic field for our magnets. Near the center of the coils, the total

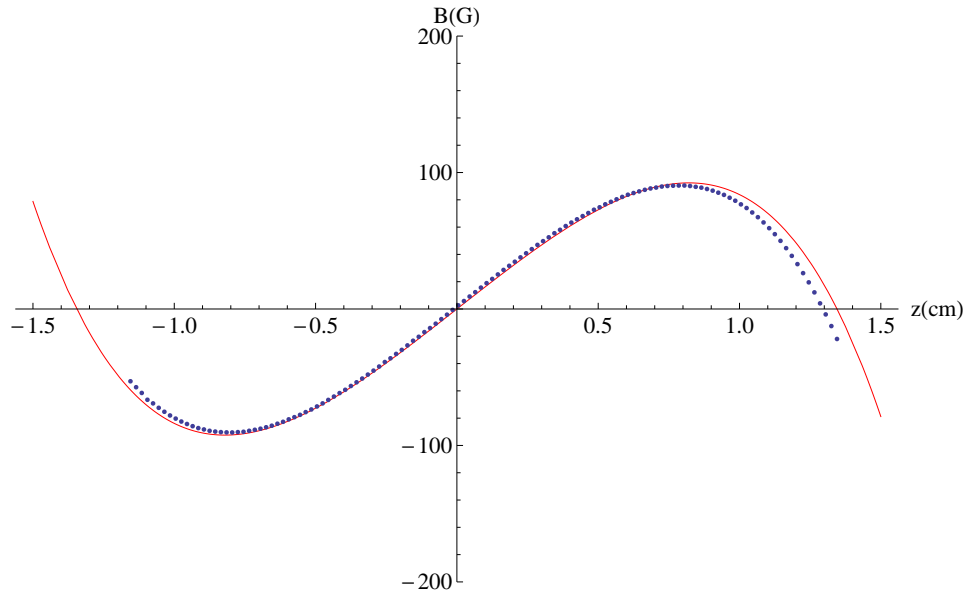


FIGURE 3.12. Permanent Magnet Quadrupole Field

magnetic field is nearly linear² with a (theoretical) gradient of $B'_z = 163$ G/cm and a measured gradient of $B'_z = 165$ G/cm.

The permanent magnet MOT was mounted around the experimental cell cased in laser-cut acrylic. A first design shown in 3.13a used clear acrylic (McMaster-Carr P/N 8560K354) and did allow for our first trap of single atoms, but the design suffered from noise issues. Reflections of the lasers off the experimental cell scattered off the acrylic and to the avalanche-photodiode used to detect single atoms. The design also could flex, which changed the scatter and shifted background fluorescence levels. A second design used black acrylic (McMaster-Carr P/N 8505K92). Stiffer supports solved the flexing issue and built in Wood's horns [98, 99] solved scatter issues. The horns were made by bending and clamping closed metal tubing (McMaster-Carr P/N

² $B_{tot}(z)$ of Equation 3.5 is an odd function and the magnitude of the z^3 component of the field within $100\mu\text{m}$ of the center is an order of magnitude smaller than the linear component using the magnet parameters in Table 3.1. These justify a linear assumption.

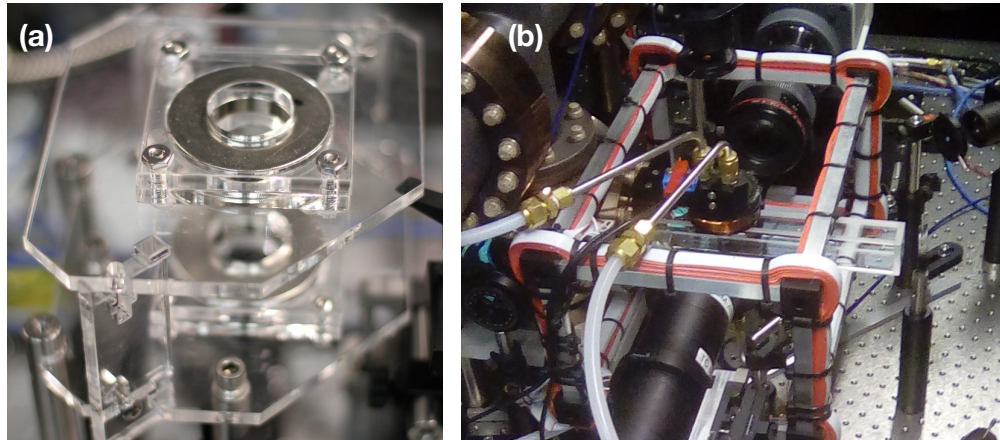


FIGURE 3.13. Single Atom MOT Magnetic Field Designs. (a) First design with permanent magnets. (b) Water-cooled electromagnets installed in the experiment.

5177K69 and P/N 8955K141). The inside of the tubes were painted black (Krylon Black indoor/outdoor primer).

3.3.2 Electromagnetic Anti-Helmholtz Coils

Electromagnetic anti-Helmholtz coils are preferred for our experiment as they can be easily turned off to do away with external magnetic fields. They were designed to closely match the fields of the permanent magnets. These installed MOT coils are shown in 1.1b and in 3.13b.

The MOT coils were designed looking at two factors – the magnetic field gradient at the center of the coils and the power dissipated in the coils. Both of these are predominately set by the current in the coils and by their shape. For two single loops of wire with radius r and resistivity ρ that are separated by a distance s , the magnetic field gradient at the midpoint between them and the power dissipation by them are

given by the equations

$$\left. \frac{\partial B}{\partial z} \right|_{z=0} = -\frac{3\mu_0 I}{2} \frac{r^2 s}{[(s/2)^2 + r^2]^{5/2}} \quad (3.6)$$

$$P = 4\pi r \rho I^2. \quad (3.7)$$

The magnetic field equation can be found from Ampere's Law and the power equation comes from the power dissipated by two resistors in series (having the coils in series is preferable for our experiment so that the current in each is the same). Clearly, the magnetic field gradient scales linearly with current in the coils, while the power scales as a square of the current. Reducing the size of the coils, through decreasing the radius of the coils, increases the magnetic field gradient and it will reduce the power dissipated, both things we wanted to occur. Numerically calculating field gradients and power use with multiple loops of wire with different radii and separation between coils was used to decide on general design for the coils.

Additionally, the thickness of the wires had be taking into account two ways. First, the thickness controlled the radius of the next layer of wires outward from the center of a single coil. Second, the loops were assumed to be closely packed together, with each outward layer of coils nestled in the "gap" between two coils of this previous layer. This negatively affects the design by increase the separation of the coils and by reducing the number of vertical stacks of wire in each even numbered layer of wires. It improves the design by reducing the radius of the wires for every subsequent outward layer, reducing the overall size of the coil of wires, and it makes wrapping the coil of wires easier as the wires will naturally fall into this gap when wrapped tightly.

The final design examined various gauges of wire, the number of outward layers of wire and the number of vertically stacks of wire. The calculations lead to a design with 270 individual loops of 20 gauge wire, arranged with 20 outward layers arranged with 14/13 vertical stacks of wire in odd/even outward layers. The inner-most radius of the loops of wire was 0.5” and the separation of the two facing sides of the coils was 4cm. Relative to input current, this design should produce a magnetic field gradient of $B'_z/I = 27.4$ G/A·cm and each coil should have a resistance of 2.2 Ω . When measured after being built, the designed coils created a gradient of $B'_z/I = 26.88$ G/A·cm and their combined resistance is 4.75 Ω .

The coils are powered with a Kepco ATE75-15 power supply which can output up to 15 A. The power supply is programmed using a PC-12 adaptor allowing for external current control and in fast mode, which allows fast altering of the current and voltage output [100]. Running the experiment in fast mode is desired for trapping only single atoms (see Section 4.1) and for making our position measurements (see Section 6.2). Setting a voltage between 0 V and 1 V across pins 15 and 30 of the PC-12 will set the output of the power supply between 0 A and 15 A.

3.3.3 Water Cooling

Because of the high power dissipation of the electromagnets, their mounting brackets were designed to allow water cooling to occur on the surfaces of the brackets opposite the experimental chamber, as shown with blue rectangles in Figure 3.1b. Each coil has a 1/8” tall and half-inch wide channel inside the coil. Each channel runs 300° around the coil with a water intake and output on either end. Water lines are connected to 3/8” Swagelok brass tube fittings (Portland Valve Fitting P/N B-600-6). The water lines are made of rigid polyethylene tubing (McMaster-Carr

P/N 50375K47) as visible in Figure 3.13b. The water lines are attached to a water chiller (Neslab RTE-100) which can pump about 3 gallons/minute. The water chiller has a 1.3 gallon tank and can cool up to 350 W when operated at 20°C. The water temperature is typically set around 15°C. This temperature is chosen to improve cooling of the coils, according to Equation C.10, and so that touching the below-room temperature coils will be cool to the touch to verify they are being chilled correctly. The water chiller does not seem to have standard pipe fittings, so we adapted 1/4" compression tube fittings (brass sleeve fitting McMaster-Carr P/N 50385K72 and brass nut McMaster-Carr P/N 50385K62) for a short stretch of 1/4" tubing. This was expanded (Portland Valve Fitting P/N B-600-1-4) to match the larger 3/8" tubing of the rest of the water line.

There are three additional elements in the water line between the chiller and coils. First, just after leaving the chiller, there is a vibration damper that prevents vibrations created by the chiller from reaching the experiment. The damper is made of a long length of tubing that is coiled in 3 circles of about 1' diameter. The coils are inside of a plastic trashcan and the can was filled with cement. Second, there is a flowmeter (McMaster-Carr P/N 4351K37) attached to the water lines that lets us control the water flow between 0.3 gallon/minute and 3 gallons/minute. The water line then travels to the MOT coils, in series, before turning through the vibration damper. Lastly, the water runs through a low-flow switch (McMaster P/N 2371K4) that allows us to monitor the flow of water through the tubing. The water then returns to the chiller. The complete plumbing diagram for water cooling the MOT coils is shown in Figure 3.14.

To verify the coils will not over heat in our experiment, we analyzed the heating and cooling rates of the coils. This analysis is shown in C and reveals the temperature

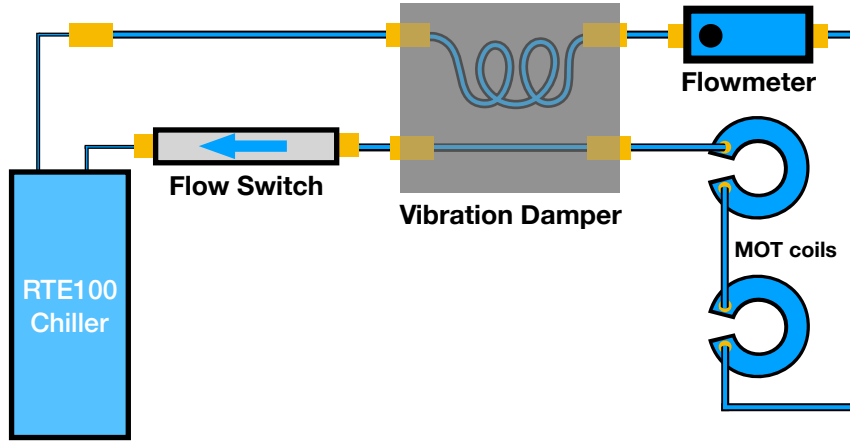


FIGURE 3.14. Plumbing Diagram for water cooling the MOT coils

of the coils as a function of time is

$$T(t) = \left(T_w + \frac{\beta}{\gamma} \right) e^{\gamma t} - \frac{\beta}{\gamma}, \quad (\text{C.10})$$

where T_w is the set-temperature of the water and parameters γ and β are complicated combinations of parameters given in Equations C.8 and C.9. To keep $\gamma < 0$, there is a maximum driving current (Equation C.11) that the coils can cool. For our coils, temperature settings, and chiller, (see Table C.1) this current is $I_{lim} = 61\text{A}$, well above our designed operating current. Because resistance is tied so closely to the coil temperature, the resistance will also raise as the temperature does according to the equation

$$R(t) = R'_0 [1 + R_m (1 - e^{-|\gamma|t})], \quad (\text{C.12})$$

where R'_0 is an effective initial resistance, R_m is a maximum resistance. This form is nice as it allows simple measurement of γ through monitoring the resistance of the coils. At current of 9A we measure $\gamma = -0.017 \pm 0.11/\text{s}$. Equation C.8 predicts a value of $\gamma = -0.23/\text{s}$ using experimental parameters in Table C.1.

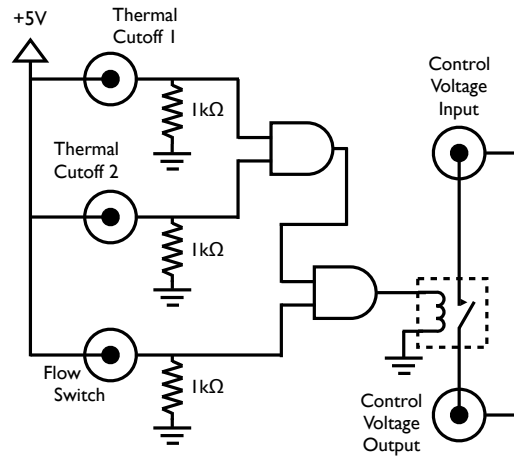


FIGURE 3.15. Water Cooled Coils Protection Circuit

The likely cause of this mismatch is over simplification in the calculation for the rate flows into the water from the coils. This derivation assumed the length of the cooling channel, L , is much larger than a characteristic channel diameter, D_H (see Appendix C.3). Our design has $L = 19D_H$, which is only sort of longer. As discussed in Appendix C.3, this means there is an inward temperature gradient from the surface of the cooling channel walls, reducing the efficiency of convection into the water from the walls of the channel. Even with this overestimate of the cooling, the coils remain cool to the touch even after operating at high currents for an extended period.

3.3.4 Protection

Because of the high power output of the MOT coils and the potential for over heating, we installed a temperature protection circuit as shown in Figure 3.15. This circuits uses TTL logic to trigger a relay (Mouser P/N 528-107-1) that allows the control voltage from the ZOINKS system to reach the coil power supply. The TTL signals run through three BNC outputs. Two these BNC connections are attached

to thermal cutoffs (Mouser P/N 667-EYP-2BN082) which can be attached to the top and bottom coils. The cutoffs act as fuses, blowing out if they, and therefore the coils, reach 82°C. The third is attached to the low-flow switch which is attached in-line for the MOT coils water chiller and gives an open circuit if the flow rate falls below 0.1 gallons/minute. These three guarantee the power supply will only run if the coils are being cooled and if the coils are not overheating.

Care is taken as to not leave the coils running without being monitored. The power supply and the water chiller are both turned off over night. We have had mistakes, however. At least once, the temperature control of the chiller was turned down well below room temperature and left on overnight. Water condensed on the cooled coils, which spread onto the experimental cell, dripping from above and wicking from below. The coils have also been left running at high currents for an extended period, allowing them to overheat. This caused a residue to form on the experimental cell. In both cases, removing the coils and carefully cleaning the experimental cell with acetone solved the problems.

3.3.5 Measuring Magnetic Fields

The Kepco power supply has a very obvious noise source of around 27 kHz. Eliminating this noise is done with an interchangeable capacitor to create a simple low-pass filter. This is the capacitor shown in Figure 3.16. Typically, a high voltage 1 μ F capacitor is used (Mouser P/N 5984-100V1-F). Forcing oscillations of the current necessitates careful monitoring of the current as the oscillation amplitudes will be heavily limited by the filter.

The current sent to the MOT trapping coils is monitored in 3 ways. Before going to the coils, the output current of the power supply is sent to the circuit shown

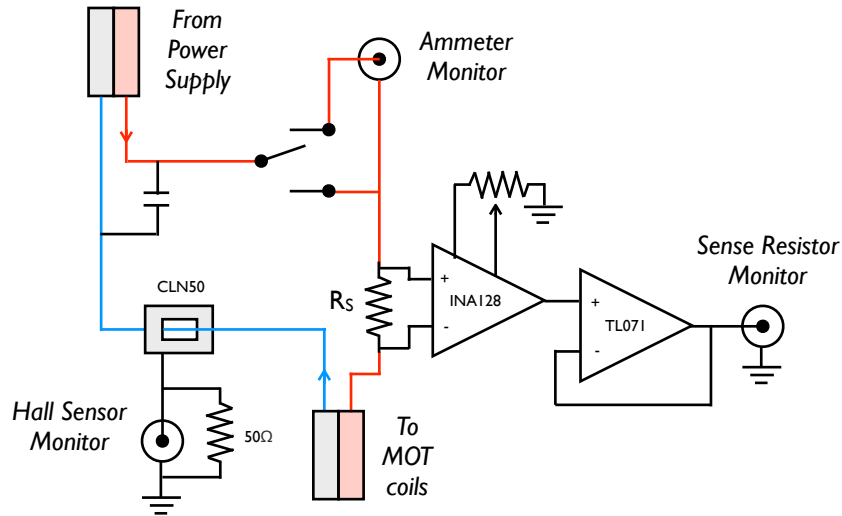


FIGURE 3.16. MOT Coils Current Monitoring Circuit. Red and blue coloring for the current labels the current path before reaching the MOT coils and after returning from the MOT coils, respectively.

in Figure 3.16. Before reaching the coils, the current passes through a dual-throw switch which allows for (or bypasses) a direct ammeter measurement. The current then travels through a 0.01Ω sense resistor (Mouser P/N 684-SR20-0.01), whose voltage output can be monitored. After traveling through the coils, the return current travels through a Hall sensor [101] (FW Bell CLN-50, Newark P/N 83F2355), before returning to the power supply.

3.3.6 Helmholtz Coils

The MOT theory in Section 2.5 reveals that the center of the trap is located where the magnetic field vanishes. Because of the Earth's magnetic field, this does not correspond to the mid-point between the anti-Helmholtz coils. This can be managed by using three sets of Helmholtz coils, a pair of matching coils separated by some distance with current running in the same direction, as sketched in Figure 3.17.

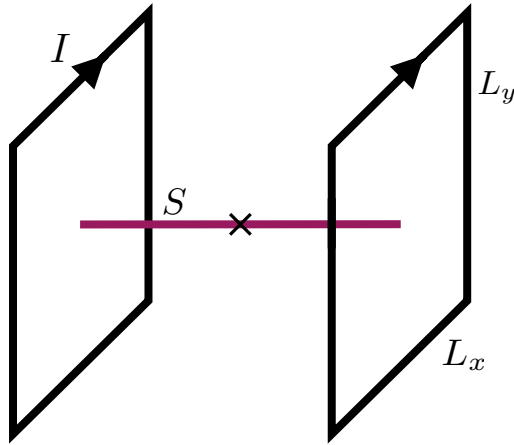


FIGURE 3.17. Helmholtz Coil Layout. This sketch shows the dimensions given in Equation 3.8 for the magnetic field at the center of the Helmholtz coils, marked by the x.

While the magnetic field cancels at the center of Helmholtz coils, the magnetic field along the axis of Helmholtz coils is (closer to) uniform. The Helmholtz coils can be arranged on the faces of a box centered around the midpoint of the anti-Helmholtz coils. Manipulating the current in each coil pair creates a (nearly) uniform magnetic field pointing in any direction, which can be used to cancel the Earth's magnetic field or move the center of the MOT away from the midpoint of the anti-Helmholtz coils.

The prior experiments built rectangular Helmholtz coils around each MOT. The coils for the second MOT are visible in 3.13b as the red and white wire structures built around the chamber. These coils are formed with loops of 10-strand ribbon cable connected so current runs through each strand in series. If one pair of matched coils having N turns and dimensions L_x and L_y are separated by distance S (as shown in Figure 3.17), the magnetic field (relative to the coil current, I) points along the at the center of the coils is given by

$$\frac{B_{\text{center}}}{I} = \frac{4\mu_0 N}{\pi} \frac{L_x L_y}{\sqrt{S^2 + L_x^2 + L_y^2}} \frac{2S^2 + L_x^2 + L_y^2}{(S^2 + L_x^2)(S^2 + L_y^2)} \quad (3.8)$$

Helmholtz Coil	L_x , in	L_y , in	S , in	N	B/I , G/A
First MOT, x-direction	13.4	13.4	8	6×10	1.7
First MOT, y-direction	12	9	6.5	3×10	1.7
First MOT, z-direction	12.4	10.8	6.2	3×10	2.6
Second MOT, x-direction	10	4.5	6	6×10	3.4
Second MOT, y-direction	5.5	7	10	10×10	2.6
Second MOT, z-direction	6	10	4.5	4×10	3.2

TABLE 3.2. Helmholtz Coil Field Gradients. Lengths and turn counts are from Schoene [73]. The turn number is written as the number of loops of ribbon cable with the number of wires in the cable. Field gradients calculated from 3.8. Note that for the first MOT, the directions labels are different from those defined by Schoene, who referenced directions relative to the axes for each set of anti-Helmholtz coils. Here, the directions are labeled universally, so that the first and second MOTs use the same direction. These directions are as labeled in 3.1. Translations between the two direction systems can be done by remapping the directions in figure 2.14 onto the directions as labeled in figure 2.21 from Schoene.

calculated simply using Ampere’s Law. The measurements and ribbon-cable loops numbers for the experiment are shown in Table 3.2 taken from Schoene [73]. These are repeated here because there is a disagreement with the magnetic field values found by Schoene for the second MOT.

The Helmholtz coils can be used to move the center of the MOT where where the magnetic field vanishes following Equation 2.81. By changing the current in the Helmholtz coils and imaging the location where the MOT loads, we are able to calculate the field generated by the coils. Because of our experimental geometry, we can only do this for the x- and z-direction (the y-direction is perpendicular to the camera imaging plane). Doing so gives that the Helmholtz coils in the x- and z-direction generate fields given by $B_x/I = 2.73 \pm 0.05$ G/A and $B_z/I = 2.91 \pm 0.17$ G/A. While still different from values calculated in Table 3.2, the results are closer to the values in Table 3.2 than the values given in [73].

3.4 Photon Collection

To detect single atoms, we built and implemented a single-photon counting system. The key component is a single-photon resolving avalanche-photodiode (APD). Light from atoms is collected by a series of lenses and fiber coupled to the APD. The photons measured by the APD are transmitted as TTL pulses to a field-programable gate array (FPGA) system which counts the arrived pulses. Photon counts, and time tagged photon arrival, were sent to lab computers over ethernet.

Later experiments to image the position of the atom require a single photon resolving CCD camera. After careful study by Jeremy Thorn [74], we purchased and installed a Hamamatsu C9100-13 Electron-multiplied CCD camera. An off-the-shelf Cannon lens is attached to the camera, although Matt Briel [102] designed a lens system for the camera to optimize off-axis position precision for future single-atom experiments.

The camera is installed along the axis of the APD's lens imaging system, but on the opposite side of the fused silica cell. In Figure 3.13b, the camera is visible at the top of the image and the tube housing the APD lenses is visible at the bottom. This camera and lens tube location allows careful positioning of the APD lenses. The camera is first moved as to focus on the MOT. Laser light is coupled backward through the lens system and shined it onto the camera, showing the focal spot of the lens system in the camera's imaging plane. The lenses can be moved with translation stages until the imaged focal spot overlaps the loading position of the MOT as imaged with the camera.

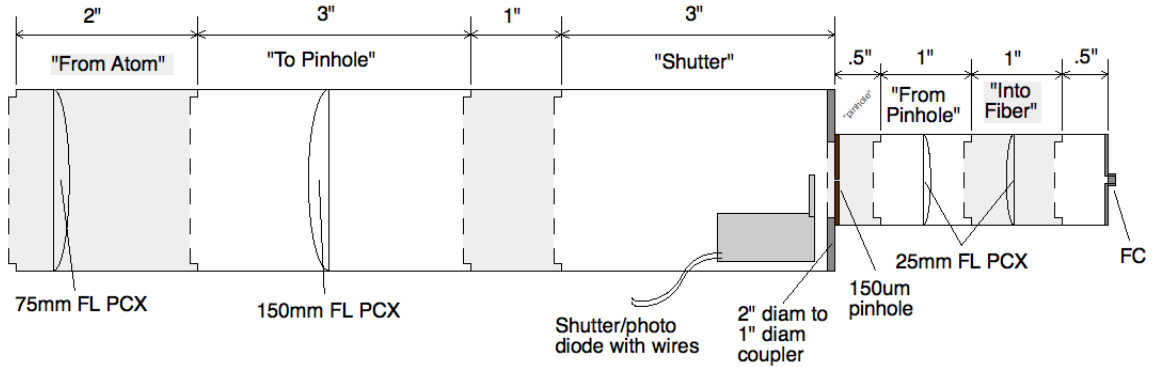


FIGURE 3.18. Single Photon Collect Lens System

3.4.1 APD

The APD (PerkinElmer P/N SPCM-AQRH-12-FC) used has a dark-count rate³ of <500 photons/sec (measured rate of 321 photons/sec). The APD ordered has an FC/PC fiber coupler attached.

Light from the atoms is collected by a system of lens shown in Figure 3.18. This lens system was based on a similar system in use at the University of Texas at Austin [103, 104] and originally designed by Wolfgang Alt [105, 106]. Our lens system lacked the complex aberration compensation of the Alt design but did attempt to match magnification ratios. Removing the aberration compensation just reduces the overall efficiency of the photon collection system.

Our lens system consists of a two 50 mm diameter lenses with focal lengths of 75 mm (Edmund Optics, P/N NT69-507) and 150 mm (Edmund Optics, P/N NT69-510). The 50 mm diameter is to increase the collection solid angle of the lens tube (0.388 steradian) and the focal lengths are to mimic the 2:1 magnification of the Alt

³A phone call with PerkinElmer revealed that all of their APDs are identical in fabrication. Dark count rates are measured after the APDs are built. The APDs are then classified and priced accordingly. There is no design or fabrication difference between APDs of different dark count rates.

design. The 150 μm pinhole (Thorlabs P/N P150s) is to limit background scatter. The matched 25 mm lens with focal lengths of 25 mm (Edmund Optics P/N NT65-524) create a 1:1 system to focus into the FC fiber coupler (Thorlabs P/N SM1FC) at the end of the lens system. The system is built into 1" and 2" Thorlab lens tubes (SM1 and SM2 product line). The 2" and 1" lens tube sections are joined with an adaptor (Thorlabs P/N SM2A6). The fiber used is a custom 105 μm diameter patch cable from Thorlabs (fiber P/N AFS105/125Y, double FC/APC couplers, 2 meters).

Because of the mismatch between lens tube diameter and lens diameter, each lens has a few narrow, thin (0.020" thickness for the 50 mm lenses and 0.012" thickness for the 25 mm lenses) brass sheets of around 1" in length between the lens and the tube. These shims were roughly equally spaced around the lens to limit their movement while securing the lens in place. I would not recommend using lenses and lens tubes with slightly different diameters.

Just prior to the pinhole, a small photodiode and relay are placed with wires leading outside the lens tube. The photodiode connects to the APD protection circuit (Section 3.4.3) to collect background light. The relay is also connected to the protection circuit and, when triggered, covers the pinhole in order to block light to the APD.

The light collection efficiency of each step between an atom and APD is shown in Table 3.3. Using the photon scatter rate for an atom (using Equations 2.28 and 2.27), with typical MOT parameters of detuning $\Delta \sim -\Gamma$, anti-Helmholtz coil current of 9A, and laser power of 1.1 mW , the photon count rate by the APD should be around 44,000 photons/sec. This falls far below measured values (a maximum of 6,5000 photons/sec). This mismatch between anticipated count rates and measured count rates is consistent with other single atom experiments [20, 77, 106].

Contribution	Efficiency
Spatial Collection	$0.3889/4\pi$
Transmission through experimental cell (reflection)	0.9325
Transmission through lens tube (reflection)	0.9900
Fiber Coupling	0.22
Transmission through fiber (reflection)	0.9329
Transmission to APD chip (reflections)	0.9176
APD Quantum Efficiency	0.66
Total Efficiency, e	3.551×10^{-3}

TABLE 3.3. Photon Collection Lens System Collection Efficiency

3.4.2 FPGA

The FPGA used in the experiment is a Terasic Cyclone II chip built into an Altera DE2 Development Board. The development board was chosen as it already contains many inputs and outputs, has an ethernet port, and can be configured with part of the FPGA operating as a NIOS II microprocessor [107]. The DE2 also has a large user base, providing a large selection of programs and uses that have been freely published online.

The DE2 board has two large banks of male header pins. We designed a small female plug that interfaced a few BNC plugs to the board's header. Each BNC input contained a 3/2 voltage divider shown in Figure 3.19 as the DE2 boards use a 3.3 V TTL logic. Shorting the 20Ω resistor and replacing the 30Ω resistor with a 50Ω resistor will give standard 50Ω terminated TTL inputs. The BNCs were used to connect FPGA to the APD and to the ZOINKS experiment control system. The board also contains a large selection of switches, which were configured to control timing for photon counting. The FPGA system does not have direct start and stop control. Instead, it has a run and reset trigger.

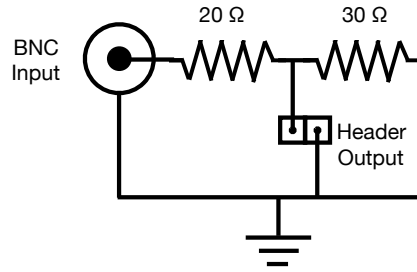


FIGURE 3.19. BNC-Header Adaptor for DE2 FPGA

Photon counting is simple input-pulse counting, implemented with very similar VHDL programming to the photon counting done by Mark Beck's group [108, 109], and data processing is done via the NIOS II microprocessor. This microprocessor is not a separate chip, but a portion of the FPGA chip that is configured to function as a microprocessor. The NIOS II, running code written in C, manages data from the photon counter and manually writes UDP ethernet packets for an onboard DM9000A ethernet chip. This chip routes the bare packets to our control computer.

We use two separate implementations of the FPGA board. The first simply counts photons for a predetermined time (set by switches), binning the photon count data. Timing is done with an onboard 50 MHz oscillator. After recording for the set time, data are sent to the computer. This occurs for a predetermined number of bins (set by switches). This schematic is shown in Figure 3.20. This implementation is used for the bayesian atom counting algorithm discussed in Chapter IV.

The second implementation does not count photons, but records the arrival time of photons (again, using the 50 MHz oscillator). This is done in VHDL and the arrival times are sent to the microprocessor. The microprocessor numbers the photons and stores the arrival times for successive photons. As the data is recored, ten of these arrival times are bundled together and written as one UDP packet before being set to the computer. The bundles are numbered to check for dropped packets and thus lost

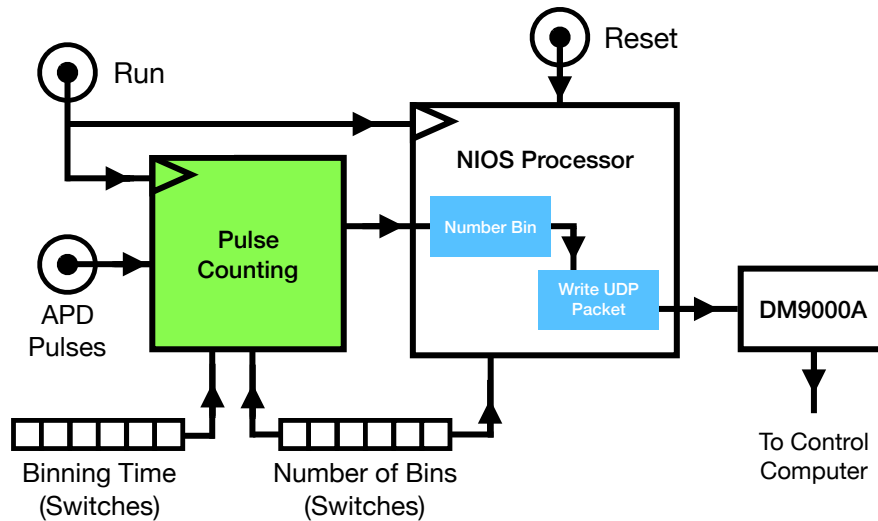


FIGURE 3.20. FPGA implementation for counting photons. Both the pulse counting and the NIOS processor are programmed onto the FPGA chip. The other elements are external connections on the DE2 board that interface with the FPGA. The “Number Bin” and “Write UDP Packet” blocks are segments of code written in C and running on the microprocessor.

photon data. Additionally, on the control-computer side of the experiment, a manual delay must be built in at the end of an experiment to check that all of the photon arrival data has arrived from the APD. With photon arrivals on the order of tens of thousands per second, an additional 30 s (after an experimental time of around 100 s) is needed so that the APD’s backlog of photon arrival times can be bundled and sent to the computer. The schematic for the APD implementation is shown in Figure 3.21. This implementation is used for the spectral experiments discussed in Chapter VI.

The DE2 board does have a dedicated clock input, so a higher speed oscillator could be used to record timing of photons [107]. Our APD has a maximum photon count rate of 20 MHz making the need for higher resolution on the FPGA unnecessary for our experiments. Additionally, rubidium has a decay rate of $\Gamma = 38.1$ MHz, so

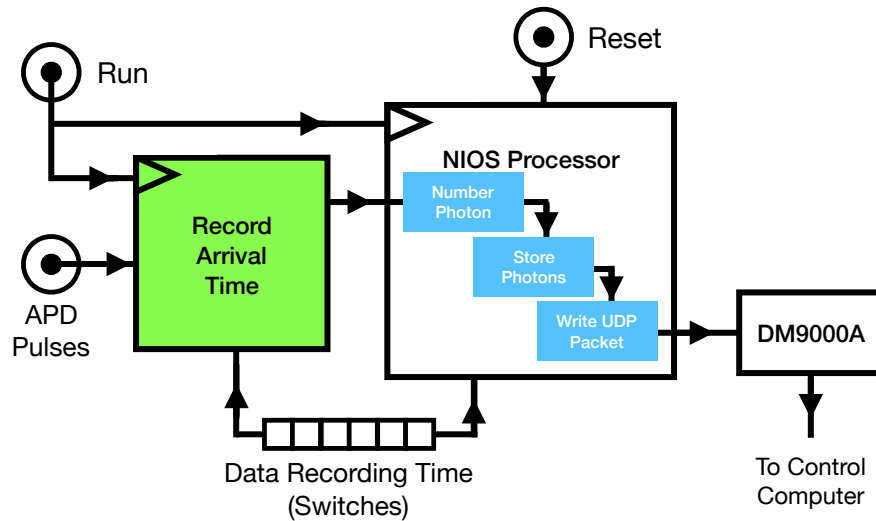


FIGURE 3.21. FPGA implementation for timing photons

when measuring light from a single atom, we should not see photon counts faster than this [62]. While testing the FPGA for our counting algorithms, it was able to function properly at rates up to 30 MHz using a function generator.

Because the ethernet packets are sent bare, there is no communication between the FPGA and the control computers. This allows for the possibility for dropped packets. Luckily at our lowish count rates (well under 100 kphotons/sec), we haven't noticed this occurring, but it is possible. Solving this could be done by designing a TCP/IP stack for the FPGA to deal with communications between the computer and FPGA. This would allow the computer to report back to the FPGA that it received the packet successfully. It could allow additional signals to be sent to the FPGA, such as timing settings (rather than using switches). Alternatively, there is an implementation of μ Linux that has been run on the NIOS II microprocessor. This contains its own TCP/IP stack that would handle the communication for us. We were unable to compile and execute this OS successfully. Instead, packets are numbered when being sent over ethernet and checking for dropped packets is done by making

sure all successive packets are received. Dropping a packet, then, can only be detected and not corrected. This occurs very rarely, but when it does the experimental run with lost data is thrown away.

3.4.3 APD Protection

Photon arrival rates higher than around 30 MHz risk damaging the APD. To prevent this a protection circuit was designed and built (not shown due to complexity). The circuit has two input measurement systems which trigger two safety measures. Once the protection mechanisms are triggered, the system can only be reset manually via a momentary switch. This requires a user to notice the problem and fix it before restarting an experiment.

Prior to the pinhole located in the APD's lens system, there is a photodiode and an electric relay as shown in Figures 3.18 and 3.22a. The photodiode measures light detected in the tube and is connected to the protection circuit. If the photodiode voltage output corresponds to measuring 30 Mphotons/second, it triggers the protection mechanisms. Because the photodiode is offset from the beam path of light focused to the APD, it can only detect broad, bright sources such as room lights.

The TTL output of the APD is also used as a protection mechanism. A copy of this data is put through a double-resistor RC circuit, shown in 3.22b. The double-resistor design allows voltage growth across the capacitor to have a much longer time constant than the voltage decay. Thus, the circuit behaves as an integrator for the TTL signal. Modeling the circuit, an input count rate of 18 Mcounts/sec gives an output voltage of 0.39 V after 1 ms. The circuit measures the voltage across the capacitor and triggers the protection mechanisms if the voltage is above 0.39 V. This circuit does cause some issues at count rates lower than this as the voltage across the

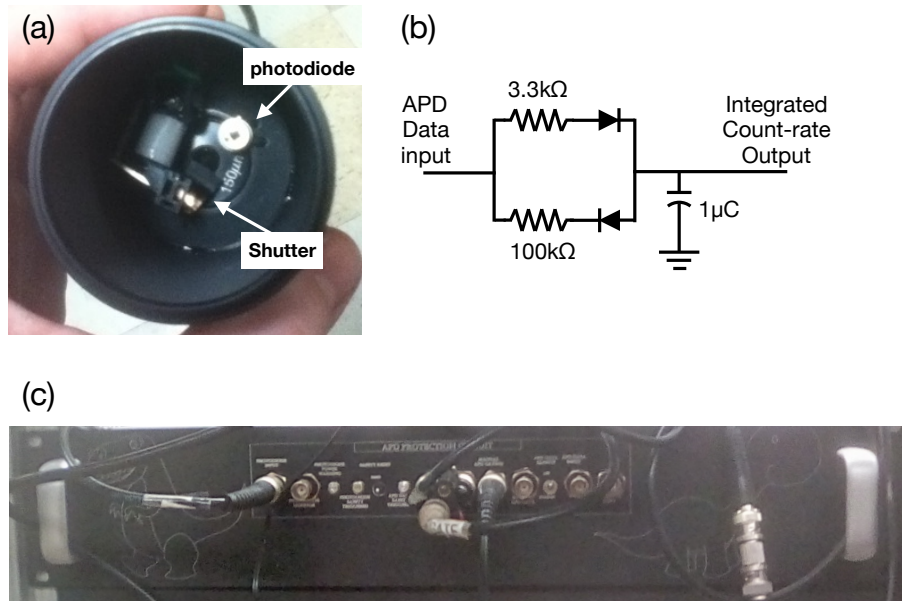


FIGURE 3.22. APD Protection Mechanisms. (a) Background light monitoring pinhole and protection shutter. (b) Integrating double-resistor RC circuit. (c) APD protection box

capacitor can eventually reach the cutoff voltage. For example, at 5 Mphotons/sec, the cutoff voltage is reached after 4.2 ms, at 1 Mphotons/sec the cutoff is reached after 23.5 ms. At 100 kphotons/sec, however, the voltage across the capacitor saturates to 0.22 V. Most of our experiments have photon count rates on just the order of 10 kphotons/sec, allowing the protection to only trigger if there is something a major issue. This circuit element protects against direct coupling of light into the APD. This could be triggered things such as by loading a large MOT of hundreds of thousands of atoms or misaligned or scattered MOT beams that could couple into the APD.

The APD is gated to turn on/off with a TTL input. One of the protection mechanism resets the TTL to turn off the APD. The ZOINKS system ideally controls the gating of the APD, but its control is routed through the protection circuit, allowing interruptions of the on signal. The protection circuit triggers this

interruption if the the APD count rate is too high or if the photodiode measures too much background light to safely use the APD. The second protection mechanism is a shutter installed along with the photodiode in the APD lens system, as was shown in Figure 3.22a. The shutter is a black-painted copper flag that moves in front of the pinhole. This blocks light from reaching the fiber coupler to the APD. The flag is attached to a T90 relay (Mouser P/N 655-T90N1D12-12) which triggers with a signal from the protection circuit.

CHAPTER IV

OUR SINGLE ATOM MOT

Single-atom MOTs typically rely on three mechanisms to greatly reduce the atomic loading rate to the single atom-level, all three of which have been used in our experiment.

1. Reducing the MOT beam diameter, typically on the scale of a few mm, reduces the volume of the optical molasses region from which atoms are trapped in the MOT [6, 110]. This was done simply with off-the-shelf irises in front of the MOT beam fiber launchers (see Section 3.2.2).
2. Reducing the background gas pressure for the atomic species to be trapped limits the number of atoms which can “wander” into the trapping region [6, 18, 77]. This is also beneficial to increase the lifetime of the trap as background atoms colliding with those in the trap is the major atomic loss mechanism. This was done originally by having the experiment’s rubidium source closed for years while continuing to pump the vacuum and, after rebaking the MOT, only leaving the rubidium source open for a short period after the rebake.
3. Increasing the magnetic field gradient reduces the radius of the trap (defined as the distance where the zeeman shift of the energy levels equals the laser detuning) [7, 11, 20]. This again limits the “volume” inside of which atoms can be trapped inside the MOT. We used both permanent and water-cooled electromagnets to create fields on order of 220 G/cm (see Section 3.3).

All these methods reduce MOT numbers strictly by reducing the probability of trapping atoms rather than any direct manipulation of atoms in the trap. These

methods can be used, however, to control the number of atoms in the MOT by increasing and decreasing loading rates as needed [10, 111].

This chapter looks more closely our single atom MOT, focusing on the detection methods to verify there is only a single atom. After detecting a single atom during an experimental run, we can trigger our system to reducing loading rates for atoms in the MOT and perform an experiment. To detect the single atom, we developed an algorithm based on bayesian statistics, discussed in the final section.

4.1 Detecting A Single Atom MOT

In large MOTs, the number of atoms is estimate from either the intensity of light emitted from the atoms [5] or by the reduction of light due to absorption of a light source that travels through the atoms [95, 96, 112]. With a small number of atoms, on the order of 10, it is possible to precisely measure the number based on the fluorescence from the atoms [7, 9, 20]. Each atom will emit photons at (nearly) the same rate, so fluorescence from the atoms should appear in discrete jumps corresponding to the number of atoms in the MOT. With a larger number of atoms, this technique is limited by factors such as the spatial extent of a larger MOT, motion of atoms within the MOT, and the large number photon counting limitations. With a very large number of atoms reabsorption of emitted photons by other atoms in the MOT [113, 114] is also an appreciable effect that prevents photon counting utility as a direct way to measure atom number.

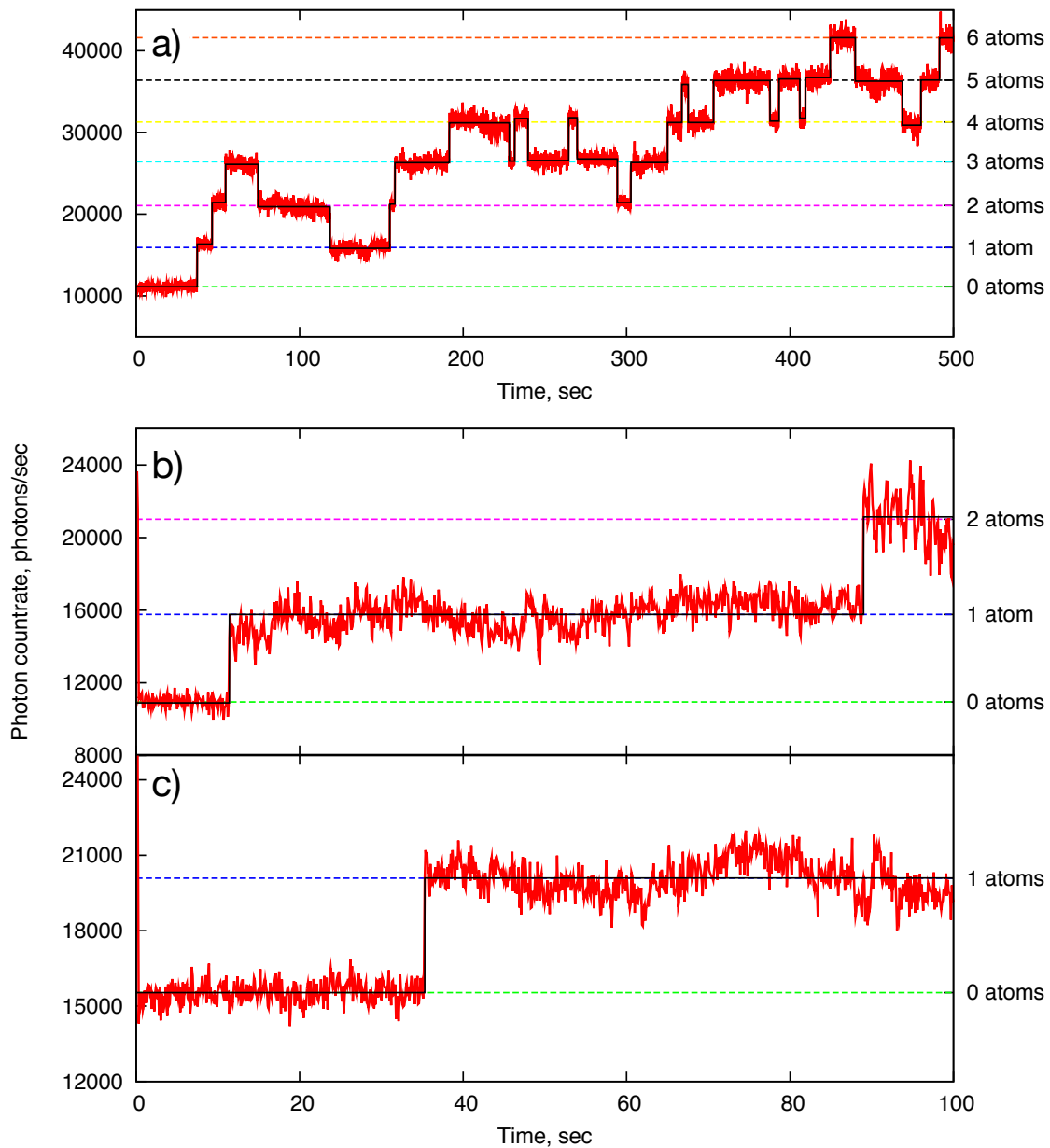


FIGURE 4.1. Sample Photon Collection Data. (a) Long data run recorded with permanent magnets. (b) Data run with anti-Helmholtz coils with 4 A current. (c) Data run with anti-Helmholtz coils with 9 A current. Graphs (b) and (c) share horizontal axes. Red line is recorded data, black line is linear estimate of fluorescence at a given atom number. Atom number dashed lines estimated from tracking jumps in data.

4.1.1 Detection : Fluorescence Jumps

For our small atom MOT, a few fluorescence records are shown in Figure 4.1. In each of these, and in general for the experiments discussed in this dissertation, the MOT lasers are shifted to frequencies above the atomic resonance to prevent loading atoms into the MOT for a few seconds. This gives a measure of the background fluorescence rate for an individual experimental run. This has two direct benefits. First, it gives a background level for the bayesian algorithm discussed in the next section. Second, it allows for estimation of the MOT beam power for an individual data run without measuring the power directly. While beam power is not measured directly, a set of data runs with known MOT beam powers can be done without loading atoms into the MOT to correlate background scatter rates measured from the APD to MOT beam powers. This is useful for modeling the behavior and temperature of atoms in the MOT (see Chapters VI). After the few seconds for background estimation, the laser detuning is reset to its desired value to allow atoms to load in the MOT. Sharp changes from the background are signals of atoms entering and leaving the MOT. These jumps are on the order of a few thousand photons/sec, generally counted for 100ms, which are the red curves in the three sample graphs. The jump size is impacted by MOT laser intensity and detuning as evident by the atomic fluorescence rate in Equations 2.27 and 2.28, but a much more significant impact on the jump size is alignment of the APD lens system with the MOT location.

Comparisons between the three graphs in Figure 4.1 show the direct influence of the first MOT. For the graph in Figure 4.1a, the first MOT is left on during the entire data run and this one data run has an atom loading rate of 0.034 atoms/s. For Figure 4.1b and Figure 4.1c, the first MOT is turned off once a single atom has

detected (using the bayesian algorithm triggering discussed in Section 4.2.7). In (b), there is a much weaker magnetic field in the second MOT (once one-atom has been detected in the MOT), but the loading rate is greatly reduced, just 1 atom in about seconds). In (c), the magnetic field of the second mot very closely matches that of the permanent magnet MOT in (a), but no additional atoms load into the MOT as they had in (a). This is directly the result of turning off the first MOT.

The discrete jumps in fluorescence are made more clear in histograms of the count rates, as commonly done in single atom experiments [6, 24, 115, 116]. The histograms for the graphs in Figure 4.1 are shown in Figure 4.2. In these graphs, the measured background rate has been subtracted from each data point before the histogram was created. The discrete separation between atom number counts is obvious here.

The broader width of the 1-atom peak in Figure 4.2b is tied to the weaker confinement of the atom. Because the MOT κ coefficient is proportional to the magnetic field gradient (Equation 2.78), the smaller current allows for a weaker trapping potential. This allows the atom to explore a larger region of space, altering the coupling between the atom and the APD's detector area. This is more obvious in the 2-atom peak where the motion of both particles greatly increases the width of the (tiny and hard to see) peak.

4.1.2 *Atom Counting by Fluorescence Jumps*

In the graphs of Figure 4.1, the the atomic number fluorescence levels (dashed lines) are calculated from the data after the experimental run completes. For these values, a running average and standard deviation for fluorescence rate is made until a subsequent data point differs from the running average by a threshold defined by a multiple of the standard deviation (typically $5 - 10\sigma$). This suggests a change

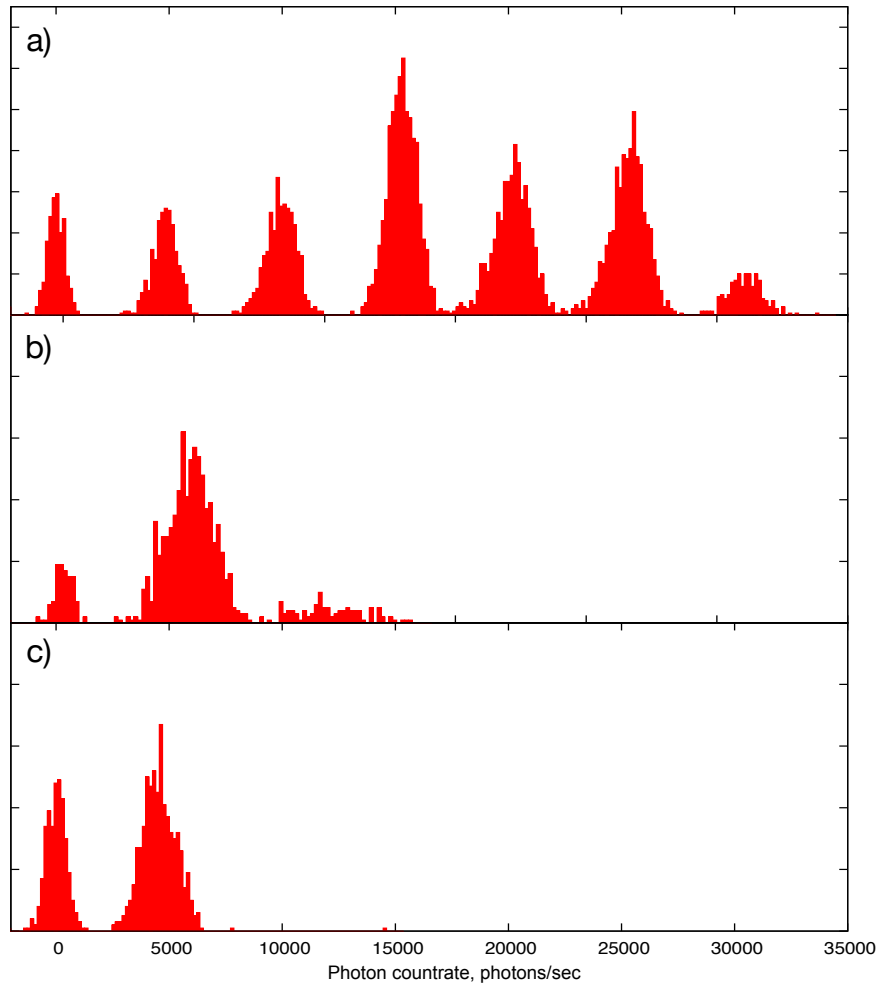


FIGURE 4.2. Histograms of sample photon collection data. Graphs correspond to data runs in Figure 4.1. Horizontal axis of each graph shifted by average zero atom fluorescence rate for that data run. All graphs share horizontal axes and fluorescence bin size of 150 photons/sec.

in atomic number at which point a new running average and standard deviation are made. These average values are the black horizontal lines plotted in the graphs and give an average fluorescence rate for the given number of atoms at that time. The average rates plotted as dashed lines in each graph are the average of correctly numbered black line averages. The number of atoms in the MOT is approximated by tracking the positive and negative jumps in fluorescence.

This atom counting method does have faults which are not present in the bayesian algorithm outlined in the next section. Drifts in fluorescence rate, especially with multiple atoms in the MOT, can also be interpreted as a spurious fluctuation in the atom number. Loading events with multiple atoms tends to result in very incorrect atom number approximations. For example, initially loading two atoms during a single fluorescence record only registers as a single atom. Subsequent individual atom losses from the trap result in an atom count of -1. Additionally, the counting algorithm does include the possibility for double-atom loss events, discussed briefly in Chapter I. This can cause similar misestimates of the atom number as a single-loss event could register as a double atom loss if the threshold for atoms loading and leaving the MOT is not carefully set. Even with these issues, the method gives a fair approximation of the atom number, especially for data runs with large jumps in fluorescence. This method is typically used to “seed” fluorescence rate estimates for subsequent data runs using the bayesian algorithm described below.

Evident in both Figures 4.1b and c, the initial count rates reported by the APD occasionally do not match the background levels. These levels, instead, more closely match the ending fluorescence levels from the prior data run. This is a result of the programming of the FPGA (see Section 3.4.2). Because the counting is done directly by the FPGA and controlling the number of binned data runs is done by software

running on the NIOS processor, there is a mismatch in when to count data. When the final data point of one run is fully counted, the FPGA immediately begins counting the next data point until the NIOS software tells it to stop. This results in occasional too-high count rates for the first data point of the next data run. This was a larger problem initially as the high count rate overlapped with multiple data points. Adding the “reset” signal to the FPGA (as shown in Figure 3.20), reduced this to just a single packet. This could be fixed by implementing the TCP/IP stack for the FPGA, but for the data recorded in this thesis, the very first data point is simply ignored when calculating the background fluorescence rate.

The atom number estimating method above produces standard deviations for the fluorescence level for each number of atoms. The variance of the fluorescence for each atom number in the graphs of Figure 4.1 is shown in Figure 4.3 where each data point corresponds to a different number of atoms. It is clear that the variance of these peaks grows faster than the average. The background is nearly poissonian (the initial point of each graph lies nearly on top of the black poissonian line). This is as expected since individual photon arrivals are un-related. For entirely single-atom sources, sub-poissonian photon statistics could be expected [117, 118], however the large background scatter swamps sub-Poisson statistics. On the other hand, super-Poisson statistics can be expected for single atoms [119, 120] when the driving laser detuning is larger than an atom’s decay rate. Our experiments use detunings close to the half-width-half-max, which would allow for Poisson fluorescence distributions to return, as noted by others [121]. In general, atomic motion tips the scales to expected Poisson statistics with a time-dependent average as the atomic motion will alter the coupling between the atom and the APD through the lens system. This effect should be more pronounced when there are multiple atoms which can move

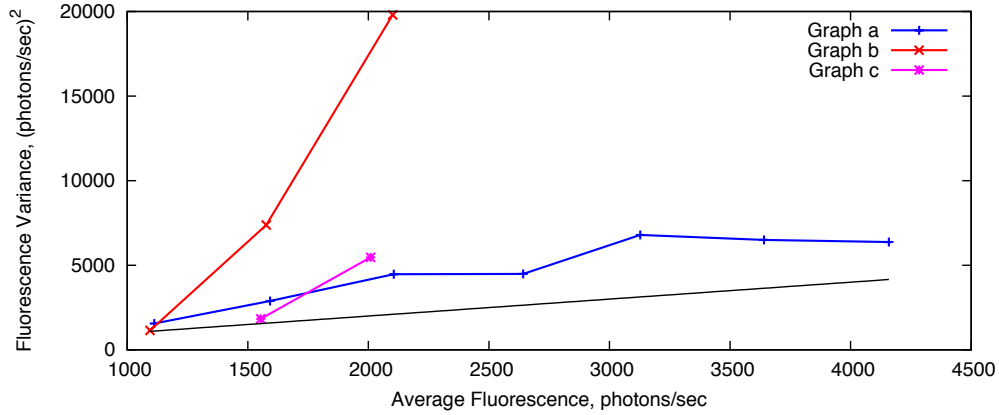


FIGURE 4.3. Variances of sample photon collection data. Graphs refer to those in Figure 4.1. Also plotted is a black line corresponding to a Poisson distribution.

around, which is what is observed as the graph of Figure 4.3b deviates from the black Poissonian line.

4.1.3 Detection : Atomic Pictures

Further evidence of small numbers of atoms is revealed when imaging the MOT with our CCD camera. Four data runs with varying numbers of atoms are shown in Figure 4.4. In each data run, a picture was taken at time $t=90$ s. As clear from the recorded APD data in graph (a), these four data runs had 0, 1, 2 and 3 atoms in the MOT at the time the picture was taken. These (background subtracted and cropped) images are shown as a series in (b), with outline colors corresponding to the graph colors in (a) and ordered in terms of increasing atom number. These pictures are gray-scale normalized such that the highest intensity pixel is white and the lowest intensity pixel is black. In the first image in series (b), the white dots correspond to random background fluctuations. The remained of these images show a clear bright spot where the MOT loads. Because each of these pictures are normalized

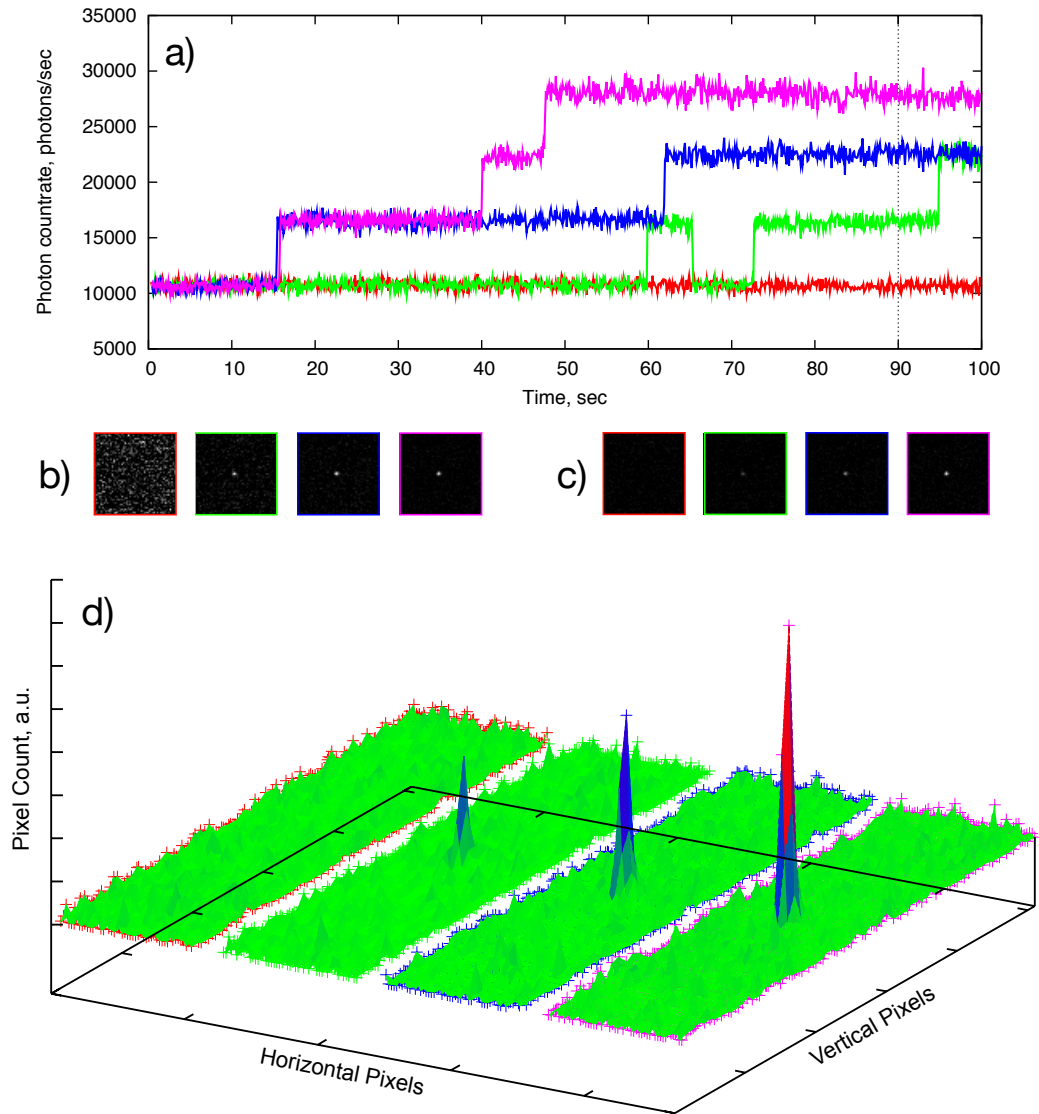


FIGURE 4.4. Atom counting with CCD camera. (a) Recorded fluorescence signal over 4 data runs. A picture of the MOT was taken at 90s for each data run. (b) Individually normalized MOT pictures. (c) Picture intensities normalized on same scale. (d) Raw picture pixel count data. Image and graph outline colors in b-d correspond to graphs with same color in a.

individually, it is hard to see much relation between them. In the series of pictures in (c). the four MOT pictures are normalized on the same scale. Clearly, increasing brightness occurs with higher number of atoms in the MOT. To further this, the background-subtracted, but un-normalized, pixel data is plotted in the graphs of (d). There is a clear increase in pixel intensity that corresponds to a larger number of atoms in the MOT. The large increase in pixel intensity is sufficient that it can be used, rather than fluorescence rates, by the bayesian algorithm discussed below.

4.2 Bayesian Algorithm

Many other single atom MOT experiments count atoms in the MOT by comparing the fluorescence level from the MOT to the known discrete steps in fluorescence contributed from each atom, very similar to the method described in Section 4.1.2. In many cases of these cases, including ours, the discrete steps are smaller than expected signaling unknown efficiency losses in their experiment [6, 20, 77, 106]. We have expanded on this approach implemented an atom counting algorithm based on bayesian estimation.

4.2.1 Atom-Number Probability Distribution

The probability for there to be n atoms in the MOT at time t_i is defined as $P^i(n)$. Of interest is how this probability will evolve as fluorescence measurements are made. Probability evolution follows Bayes' rule [122],

$$p(x|y) = \frac{p(x)p(y|x)}{\int_x p(x)p(y|x)dx}, \quad (4.1)$$

where $p(x)$ is the initial probability distribution for a parameter x , $p(x|y)$ is the probability distribution after measuring a value y for the parameter, and $p(y|x)$ tells the likelihood to have measured y when the parameter was actually valued as x . The experiment records a fluorescence measurement at time i from a prior fluorescence distribution and updates that distribution at time t_{i+1} . Comparing to the general form of Bayes' rule we can define $P^i(n) \equiv p(x)$ as the initial atom-number probability distribution of fluorescence before a measurement, $P(y_i|n) \equiv p(y|x)$ as the likelihood to have gotten measurement y with n -atoms in the MOT, and $P(y_i|n) \equiv p(y|x)$ as the updated atom-number probability distribution after fluorescence measurement result y . The integral over possible measurement values x becomes a sum over the number of atoms in the MOT. In this way, we have

$$P^{i+1}(n|y) = \frac{P^i(n)P(y_i|n)}{\sum_n P^i(n)P(y_i|n)},$$

or writing the evolution of $P^i(n)$ in terms of a differential change between times i and $i + 1$, $P^{i+1}(n) = P^i(n) + dP(n)$, we have

$$dP(n) = \left[\frac{P(y_i|n)}{\sum_n P^i(n)P(y_i|n)} - 1 \right] P^i(n). \quad (4.2)$$

With distributions $P^i(n)$ as being what is evolved in time, the most important term here is the likelihood function $P(y_i|n)$, which gives the likelihood that the photon measurement at time i came from a state with n atoms in the MOT.

4.2.2 Fluorescence Distribution

At a single time i , define the probability distribution for the fluorescence, x , from a MOT with n atoms as

$$Fl_n(x, r) = \frac{1}{\sqrt{2\pi\sigma_n^2}} \exp\left[\frac{-[x - (nr + B)]^2}{2\sigma_n^2}\right], \quad (4.3)$$

where r is the single atom fluorescence rate and B is the background fluorescence rate. Because photon arrivals are independent, the probability should be Poisson-distributed. The Poisson-distribution of the light arrival from an atom is further justified in Section 6.1 where the arrival rates of the atoms are important. However, looking at count rates, the noise isn't quite Poissonian as the atom is free to move slightly. This movement changes r . As seen in Figure 4.3, experimental measurements of σ_n for both $n = 0$ (i.e. for the background fluorescence) and $n > 0$ have variances a bit larger than the mean, justifying treating the count rates as Gaussian rather than strictly Poissonian. In practice, following the suggestion of Section 4.3, σ_n is treated as nearly Poissonian in the form $\sigma_n^2 = \langle nr + B \rangle (1 + \zeta_0 + n\zeta_n)$, where ζ_0 is a small non-Poissonian contribution to the background and ζ_n is a increase in variance due to atomic motion. Typically used values for the non-Poissonian contributions are $\zeta_0 = 0.08$ and $\zeta_n = 0.2$.

Motion of the atom changes coupling of atomic fluorescence into the APD, noise in laser power, magnetic fields, and polarization all change the photon emission rate. Thus, r is not constant, but is assumed to also have a gaussian probability distribution $P(r)$

$$Fl_{1-at}(r) = \frac{1}{\sqrt{2\pi\sigma_R^2}} \exp\left[\frac{-(r - R)^2}{2\sigma_R^2}\right], \quad (4.4)$$

where R is the average emission rate.

Combining these two probabilities gives the probability distribution for n atoms if we measure a photon rate of x with an average background rate, B , and average single-atom photon rate, R ,

$$\begin{aligned}
 Fl_n(x) &= \int_{-\infty}^{-\infty} Fl_n(x, r) Fl_{1\text{-at}}(r) dr \\
 &= \frac{1}{\sqrt{2\pi (n^2\sigma_r^2 + \sigma_n^2)}} \exp \left[\frac{-[x - (nR + B)]^2}{2(n^2\sigma_r^2 + \sigma_n^2)} \right]. \tag{4.5}
 \end{aligned}$$

A few plots of the fluorescence probability from n atoms in the MOT are plotted in Figure 4.5 with a single FPGA measured data run. Each peak along the y-axis is the distribution, $Fl_n(x)$, for atom numbers $n = 0$ to $n = 5$. The plotted probabilities are the final distributions calculated from the last measurement of the data run. The values for R , B , σ_R , and σ_n that make these distributions are calculated following the method in Section 4.2.6 from the data shown in the figure.

4.2.3 Noisy Measurements

The measurements take are noisy fluorescence measurements from the experiment. This noise is not fluctuations in the background signal or in the fluorescence rate from the atom, those are built into the fluorescence distributions $Fl_n(x)$. Instead, this noise is from measurement errors—dark counts from the APD and possible counting mistakes at the FPGA. Making a measurement, y , produces a sampled value x from the distribution $P_n^i(x)$ plus some noise, written as ζ (note that a noiseless measurement would then sample x values directly from $Fl_n(x)$). So the measurement outcome has a value

$$y = x + \zeta. \tag{4.6}$$

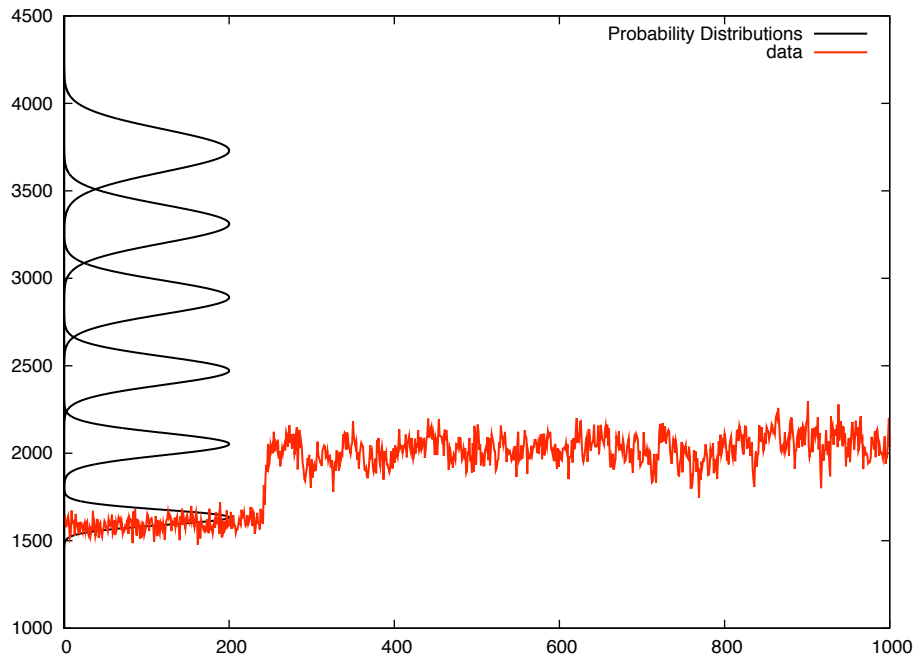


FIGURE 4.5. Sample data for bayesian fluorescence number estimation. Vertical axis is in units of photons/100 ms and horizontal axis is in units of recorded FPGA packets. Note the increasing distribution width for larger values of n . This comes from the factor of n^2 in the variance of Equation 4.5. This overlapping fluorescence distributions for n and $n + 1$ atoms shows the limitations of photon counting to estimate atom number at a large number of atoms.

To treat this noise, it is assumed that values for the noise follows a Gaussian distribution

$$p(\zeta) = \frac{1}{\sqrt{2\pi\sigma_\zeta^2}} \exp\left[\frac{-\zeta^2}{2\sigma_\zeta^2}\right], \quad (4.7)$$

so that the probability to have had a noise value of $\zeta = y - x$ is

$$p(\zeta = y - x) = \frac{1}{\sqrt{2\pi\sigma_\zeta^2}} \exp\left[\frac{-(y - x)^2}{2\sigma_\zeta^2}\right]. \quad (4.8)$$

The probability for the noise to take this value is the same as the probability to have measured y when the sampled fluorescence value is x .

For the Bayesian evolution, the likelihood to measure y with n atoms in the MOT is needed. This is the the probability for the noisy measurement to have sampled a value x and averaged over the probability for the fluorescence to have value x with n atoms in the MOT as below.

$$\begin{aligned} P(y_i|n) &= \int p(\zeta = y_i - x) Fl_n(x) dx \\ &= \frac{1}{\sqrt{2\pi (n^2\sigma_R^2 + \sigma_n^2 + \sigma_\zeta^2)}} \exp\left[\frac{-[y_i - (nR + B)]^2}{2(n^2\sigma_R^2 + \sigma_n^2 + \sigma_\zeta^2)}\right] \end{aligned} \quad (4.9)$$

This is the desired likelihood function for the bayesian estimation of the number of atoms in the MOT. It tells the probability that when a fluorescence rate y_i is measured, there are n atoms in the MOT, given that there is

1. an average photon emission rate per atom of R and with standard deviation of σ_R ,
2. average fluorescence background B ,

3. background (plus atomic motion) fluorescence rates with standard deviation σ_n , which are slightly super-Poissonian, and
4. systematic noise with variance σ_ζ .

4.2.4 Keeping $P(n) > 0$

From Bayes' rule, if $P_n^i(x) = 0$, for any time t_i , then for all later times, the probability to have n atoms in the MOT will always be zero. This can be resolved numerically one of two ways. First, manually setting $P_i(n) = \epsilon$ for some fixed small value ϵ at each time step if $P_i(n) < \epsilon$. Second, using a loading-rate method. This method includes, in the probability evolution, atomic loading and loss terms for the MOT. With the loading rate method, the probability to have n atoms in the MOT evolves as

$$\frac{dP^i(n)}{dt} = -n\Gamma P^i(n) + (n+1)\Gamma P^i(n+1) - LP^i(n) + LP^i(n-1), \quad (4.10)$$

where Γ is the rate that an atom is lost from MOT, and L is the loading rate of atoms into the MOT. The first term represents any one of the n atoms leaving the MOT. The 2nd term represents any one of the atom leaving a MOT that used to have $n+1$ atoms. The 3rd term represents at atom loading into the MOT from the background gas (to create a MOT with $n+1$ atoms). The 4th term represents an additional atom loading from a MOT with $n-1$ atoms. This loading-rate equation is identical to loading-rate model analysis done for small numbers of atoms in a MOT [20].

Using this method numerically requires a maximum number of atoms, N_{max} to be set. Doing this adds a cut-off term $\Theta(N_{max} - n)$ to the 3rd term so that an addition

atom “cannot” load if $n = N_{max}$. This definition also allows

$$\sum_{n=0}^{n=N_{max}} \frac{dP(n)}{dt} = 0,$$

so that the loading-rate method appropriately conserves probability.

Tests with both methods give the same predictions for $N(t)$ under a variety of other parameters. In practice, we use the loading-rate method with typical parameters $L = 0.006$, $\Gamma = 0.003$, and $N_{max} = 8$. These values are measured atomic loading and loss rates from the experiment.

4.2.5 Number Estimation

Combining the Bayesian evolution with the loading-rate differential gives an overall evolution for the atom-number probability

$$dP^{i+1}(n) = \left[-n\Gamma P^i(n) + (n+1)\Gamma P^i(n+1) - LP^i(n) + LP^i(n-1) \right] dt + \left[\frac{P(y_i|n)}{\sum_n P(y_i|n)} - 1 \right] P^i(n). \quad (4.11)$$

Again, this equation conserves probability when summed over n . It also solves the issues of any $P(n) \rightarrow 0$ as the probability for there to be n atoms in the MOT will be increased slightly by the loading rate portion (first term) of the differential. This probability evolution could be interpreted as a deterministic “Hamiltonian” like evolution at all times, punctuated with the noisy measurements at times t_i , similar to the stochastic evolution of a system in quantum measurement theory [123–125].

This algorithm is simple to implement in real time while we record fluorescence from the MOT and estimate the number of atoms in it. To determine the number of atoms in, we typically assume the n with the largest probability is the correct number of atoms in the MOT. This generally works well as often the average single-atom fluorescence rate is much larger than the width of its fluorescence distribution, $R \gg \sigma_R$.

In some cases, such as poor alignment of the APD lens system with the MOT center or cases where atomic position distributions are large, just taking the largest probability as the number of atoms in the MOT causes problems. The main error seen is constant fluctuations in the estimate of the number of atoms in the MOT as two values for $P_i(n)$ are close to 0.5 (typically for $n = 0$ and $n = 1$). In such cases, assume that states with $n > 1$ remain essentially unpopulated and initially $P^i(0) = 0.51$, so that there are believed to be no atoms in the MOT. Updating the probabilities after measurement could give $P^{i+1}(1) = 0.51$ so there is now believed to be one atom in the MOT. Another update gives $P^{i+2}(0) = 0.51$, so the state again returns to there being zero atoms in the MOT. This can repeat often if measurements of the fluorescence tend to stay in the “middle” between the peaks of the likelihood functions for zero atoms or one atom. This most often happens when the initial assumption about the single-atom fluorescence rate, R , is larger than the actual rate in the experiment.

Other than using a more realistic single-atom fluorescence rate, this can be solved via more complicated assumptions about when the number of atoms in the MOT changes. One method is to require the largest probability at t_{i+1} to be above some threshold value (larger than 0.5) before determining the atom number changed from time t_i . A second method could require the largest probability be above the 2nd largest probability by some determined factor, limiting jumps

between two states with probabilities close to 0.5. A third method would require that the maximum probability remain the maximum over a number of fluorescence measurements, avoiding the possibility of fast fluctuations in number. A final method is to reduce the possibility of such oscillations by updating the background and single-atom fluorescence rate as data were being recorded, described in detail below.

4.2.6 Background and single-atom fluorescence estimation

Mean values for single-atom fluorescence rates are often 5 or 6 times larger than the standard deviation of the background signal (this fact is occasionally used after data is recorded to locate times when a given number of atoms are in the MOT, as noted in the atom counting method in Section 4.1.2). Because of this, in many cases $P^i(n)$ is very close to unity. For example, for the data shown in Figure 4.1c, at times when $n=0$ gives the largest probability, the mean value of $P(0)$ is $0.9986 \pm 2.2 \times 10^{-4}$, and at times when $n=1$ is the largest probability, the mean value of $P(1)$ is $0.9979 \pm 1.4 \times 10^{-2}$. With good alignment of the imaging system with the MOT center, these are not uncommon values. With $P(n) \approx 1$ for some n , we can leave n fixed in Equation 4.5 and use the fluorescence measurements to update values for R or B rather than update predictions for n .

Taking $n = 0$, Equation 4.5 gives

$$Fl_0(x) = \frac{1}{\sqrt{2\pi\sigma_0^2}} \exp \left[\frac{-(x - B)^2}{2\sigma_n^2} \right].$$

Because the noise in a measurement is assumed to be Gaussian, updated values for the background mean value and variance after a measurement can be written analytically

[122]. Following this, a measurement of y_i allows updating of B and σ_0^2 as

$$\begin{aligned}
 B_{i+1} &= \frac{B_i \sigma_\zeta^2 + y_i \sigma_{0,i}^2}{\sigma_{0,i}^2 + \sigma_\zeta^2} \\
 \sigma_{0,i+1}^2 &= \frac{\sigma_{0,i}^2 \sigma_\zeta^2}{\sigma_{0,i}^2 + \sigma_\zeta^2},
 \end{aligned}
 \tag{4.12}$$

where, again, σ_ζ is systematic noise in the measurement. These updates are easy to make and include in subsequent measurements and probability calculations.

When there is an estimate of $n > 0$ atoms in the MOT, instead of updating the background and its variance, the atomic fluorescence rate and its variance is updated using the n -atom fluorescence probability Equation 4.5. The background level and its variance complicate the calculation for updating R and σ_R . This calculation is done in Appendix D and the conclusions are

$$\begin{aligned}
 R_{i+1} &= \frac{R_i \sigma_\zeta^2 + (y_i - B) n \sigma_{R,i}^2}{n^2 \sigma_{R,i}^2 + \sigma_\zeta^2} \\
 \sigma_{R,i+1}^2 &= \frac{\sigma_{R,i}^2 \sigma_\zeta^2}{n^2 \sigma_{R,i}^2 + \sigma_\zeta^2}.
 \end{aligned}
 \tag{D.3}$$

These two updating methods are effectively just a Bayesian filter [122] for the background (when $n = 0$) and for the fluorescence rate (when $n > 0$).

4.2.7 Bayesian Algorithm

The full Bayesian algorithm is sketched schematically in Figure 4.6. At each time step, t_i , a fluorescence rate, y_i , is measured. From this, calculate the likelihood functions for each atom number according to Equation 4.9. These are then used to update the atom-number probability distribution with Equation 4.2. The number of

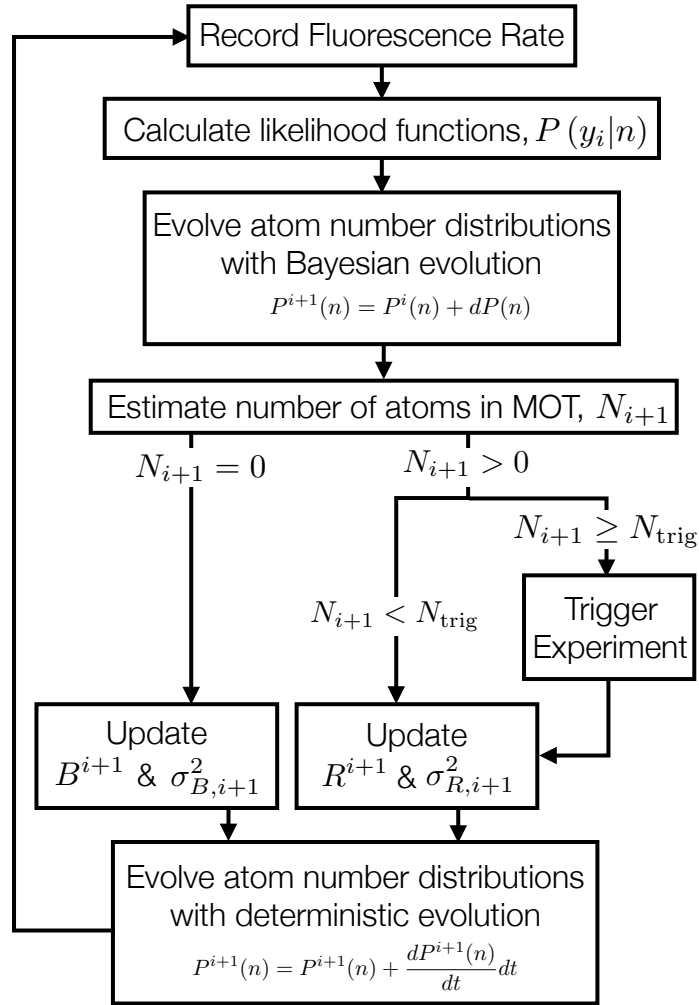


FIGURE 4.6. Bayesian algorithm flow chart. Initial background fluorescence measurement and algorithm ending elements are not shown.

atoms in the MOT is updated according to any of the methods discussed in Section 4.2.5.

If the algorithm is set to trigger an experiment based on atom number, this number is checked against the triggering atom number, N_{trig} . If the number of atoms meets or surpasses that value, whatever experiment is to be done is triggered. It is also possible to trigger an experiment manually after a given time. The experiment is a predetermined order of commands and runs “in the background” while the Bayesian algorithm continues.

Based on the predicted number of atoms in the MOT and the measured fluorescence, the background fluorescence parameters (with Equations 4.12) or the atomic fluorescence parameters (with Equations D.3) are updated. Because the atomic number estimate is made before updating rates, Equations D.3 should be modified to use the number of atoms assumed to be in the trap when the data was recorded. Thus the values N should become N_{i+1} in the equations. This completes the number probability update due to the measurement.

During the time before the *next* measurement, the probability is evolved according to the deterministic evolution of Equation 4.10. The time variable dt is the time between measurements. Alternatively, the probabilities could be checked as to not fall below the pre-determined minimum ϵ as described in Section 4.2.4. This prepares the probabilities for updating on the next measurement.

Starting and stopping of the algorithm are done based on the information from the FPGA. The algorithm does not start on the first data from the FPGA. Instead, all experiments are designed with a few second “dead time” where the MOT trapping laser detuning is shifted above resonance. This guarantees no atoms load in the MOT. The data recorded by the FPGA is only background fluorescence. The algorithm

knows when the dead time ends and once it receives photon data whose time stamp matches the end of the dead time, it can calculate initial background fluorescence and then begins the Bayesian evolution. The algorithm is ended once the FPGA transmits its final count rate. The final FPGA time-data packet is followed by a series of packets that just read "STOP" rather than photon data for this reason.

CHAPTER V

ATOMIC FORCES IN A MOT

In this chapter the MOT theory in Chapter II is expanded to more closely model the behavior of a real ^{87}Rb atom. The atom is expanded from the two-level or V-atom to the full D_2 level structure, in Figure 2.1. The magnetic and optical fields, along with the atom's position and velocity, are expanded to three dimensions, requiring 6 optical fields. The discussion in Section 5.1 briefly discusses modifications to the Hamiltonians in Chapter II to change to the full atom in 3D. Section 5.3 looks at these changes in the dynamics of the atom, but internally as the evolution of its density matrix and externally as the MOT trapping force on the atom. After laying the groundwork for the simulation, a discovered atomic loss mechanism is discussed along with a resolution to agree with established MOT theory.

5.1 3D and ^{87}Rb Hamiltonians

5.1.1 *Atomic Hamiltonian*

The free atomic Hamiltonian closely matches that of Equation 2.57 with a few small changes. The detuning is defined relative to the ground state energy rather than the excited state energies. This is done as a separate electric field is needed to excite atoms from each of the two ground states. The $|F_g = 2\rangle$ ground state is defined with (detuned) energy Δ_M and the $|F_g = 1\rangle$ ground state is defined with energy Δ_R . Here, the M subscript is in reference to the “MOT laser”—the laser field for the MOT trapping transition (see Section 3.2 and Figure 2.1). The R subscript

Energy Level	With Repump	Without Repump
$ F_e = 3\rangle$	0.35	5.6×10^{-7}
$ F_e = 2\rangle$	2.9×10^{-4}	4.6×10^{-10}
$ F_e = 1\rangle$	3.6×10^{-5}	5.8×10^{-11}
$ F_e = 0\rangle$	2.7×10^{-8}	2.6×10^{-14}
$ F_g = 2\rangle$	0.65	1.0×10^{-6}
$ F_g = 1\rangle$	8.3×10^{-4}	1

TABLE 5.1. Repumping field and populations of ^{87}Rb D₂ energy levels. Values are steady-state populations (summed over magnetic sublevels) for energy levels. Repump field powers, relative to trapping field power, are 10^{-1} and 10^{-10} . Values calculated with $\Delta_M = -\Gamma$, $\Delta_R = 0.5$ MHz, trapping beam intensity $10I_{\text{sat}}$, and without Zeeman shifts of the magnetic sublevels. These values were calculated as described in Section 5.3.1.

is in reference to the “repumping laser”. With these, the free atomic Hamiltonian is

$$\begin{aligned}
H_A = & \hbar \sum_{F_e=0}^3 \sum_{m_e=-F_e}^{F_e} \Delta_{F_e} |F_e; m_e\rangle \langle F_e; m_e| + \\
& \hbar \sum_{m_F=-2}^2 (\Delta_M + \Delta_{F_e=3}) |F_g = 2; m_F\rangle \langle F_g = 2; m_F| + \\
& \hbar \sum_{m_F=-1}^1 (\Delta_R + \Delta_{F_e=2}) |F_g = 1; m_F\rangle \langle F_g = 2; m_F|,
\end{aligned} \tag{5.1}$$

where the terms Δ_{F_e} give the (relative) energy differences between the various excited states. The two ground states also have different energies, but because their energy is defined relative to the excited state energy (through the detunings), the energy difference between the two grounds must match the energy shift of the excited state to which they are coupled. These energy differences are associated with the angular momenta of the atom and are defined in [48, Eq. 7.134].

For hyperfine splitting, transitions which do not change the total angular momentum are allowed, which makes excitations $|F_g = 2\rangle \rightarrow |F_e = 2\rangle$ possible. The likelihood of this excitation is small as it is detuned from the MOT trapping field

by 267 MHz (peak D in Figure 3.9). Even with such a large detuning, excitations that *do* occur can then decay to the $|G; F = 1\rangle$ ground state. Excitations out of this ground state are detuned by 6.8 GHz from the MOT trapping transition [62], effectively making this a dark (inescapable) state—atoms that fall into this state will remain there. The repumping field is thus required to excite atoms out of this state back into the MOT transition by coupling $|F_g = 1\rangle$ back to the $|F_e = 2\rangle$ (as shown in Figure 2.1). These atoms could then return to the $|F_g = 2\rangle$ state and the MOT transition. This result is shown numerically in Table 5.1. The values listed are the steady-state level populations (summed over magnetic m_F sublevels). Populations on the left are with a repump field (10% of the power of the trapping field) and values on the right are without the repump field. The decay of atoms into the inescapable $|F_g = 1\rangle$ state without a repumping field is clear.

5.1.2 Atom-Magnetic Field Hamiltonian

In one dimension, the magnetic field for the MOT was assumed to be linear with gradient $-B'_z$, which agrees with the magnetic field strength for permanent magnets in Figure 3.12 and for anti-Helmholtz electromagnets in Equation 3.6 near the center of the MOT. In a full 3D theory, the magnetic field at any point in space for anti-Helmholtz coils, with their axis defined as a z-axis, will be

$$\vec{B}(x, y, z) = \frac{\mu_0 I}{2\pi R} \int_0^{2\pi} d\theta \left[\begin{aligned} & \frac{\left(\frac{z+s/2}{R}\right) \cos \theta \hat{x} + \left(\frac{z+s/2}{R}\right) \sin \theta \hat{y} + \left(1 - \frac{x}{R} \cos \theta - \frac{y}{R} \sin \theta\right) \hat{z}}{\left(1 + \left(\frac{x}{R}\right)^2 + \left(\frac{y}{R}\right)^2 + \left(\frac{z+s/2}{R}\right)^2 - 2\frac{x}{R} \cos \theta - 2\frac{y}{R} \sin \theta\right)^{3/2}} \\ & - \frac{\left(\frac{z-s/2}{R}\right) \cos \theta \hat{x} + \left(\frac{z-s/2}{R}\right) \sin \theta \hat{y} + \left(1 - \frac{x}{R} \cos \theta - \frac{y}{R} \sin \theta\right) \hat{z}}{\left(1 + \left(\frac{x}{R}\right)^2 + \left(\frac{y}{R}\right)^2 + \left(\frac{z-s/2}{R}\right)^2 - 2\frac{x}{R} \cos \theta - 2\frac{y}{R} \sin \theta\right)^{3/2}} \end{aligned} \right], \quad (5.2)$$

where R is the radius of the coils, s is the separation between coils and the origin is along the axis exactly inbetween the two coils. As long as the atom stays close to the

origin, the magnetic field is nearly linear along the axis of the coils with a (negative) gradient of

$$B'_z \equiv - \left. \frac{\partial B_z}{\partial z} \right|_{\vec{r}=0} = \frac{3\mu_0 I s R^3}{[R^2 + (s/2)^2]^{5/2}}. \quad (5.3)$$

In order for the divergence of the magnetic field to vanish, the x - and y -direction contributions to the divergence must cancel the contribution from the z -direction. Additionally, the x - and y -direction magnitudes must be equal as the magnetic field should be symmetric around the z -axis. These, together with the linear assumption of the z -direction magnetic field, require that the magnetic field have the form

$$\vec{B}(\vec{r}) = B'_z \left(\frac{x}{2} \hat{x} + \frac{y}{2} \hat{y} - z \hat{z} \right). \quad (5.4)$$

This can be checked simply with the full form of the field in Equation 5.2. Looking at the field along the x -axis is

$$\vec{B}(x, y = 0, z = 0) = \frac{\mu_0 I}{2\pi R} \int_0^{2\pi} d\theta \frac{\frac{s}{R} \cos \theta \hat{x} + \frac{s}{R} \sin \theta \hat{y}}{\left(1 + \left(\frac{x}{R}\right)^2 + \left(\frac{s/2}{R}\right)^2 - 2\frac{x}{R} \cos \theta \right)^{3/2}} \quad (5.5)$$

The y -component clearly integrates to zero so that the field is just along the x -direction with magnitude

$$B_x(x) = \frac{\mu_0 I s}{\pi x} \left[\frac{(R^2 + x^2 + (s/2)^2) E \left[\frac{-4xR}{(x-R)^2 + (s/2)^2} \right]}{\sqrt{(x-R)^2 + (s/2)^2} ((x+R)^2 + (s/2)^2)} - \frac{K \left[\frac{-4xR}{(x-R)^2 + (s/2)^2} \right]}{\sqrt{(x-R)^2 + (s/2)^2}} \right], \quad (5.6)$$

where $K[k]$ and $E[k]$ are complete elliptical integrals. Near $x = 0$, the field is nearly linear with a slope of

$$B'_x = \lim_{x \rightarrow 0} \frac{dB_x}{dx} = \frac{3\mu_0 I s R^3}{2[R^2 + (s/2)^2]^{5/2}}, \quad (5.7)$$

which is half the z -direction gradient with the opposite sign. Thus the form of equation 5.4 is valid near the origin.

Do note, in our simulations, the z -direction gradient value, B'_z that is used is the measured value from the constructed water-cooled anti-Helmholtz coils. As noted in Section 3.3.1, this values was also numerically calculated, but must summed over many coil pairs with different radii R_i and separations s_i to account for many layered loops of wire in our coils.

In writing the form of the atom-magnetic field coupling Hamiltonian, Equation 2.49, it was assumed that the atomic dipole moment $\vec{\mu}$ stayed aligned with the magnetic field. This allowed the Hamiltonian to be written just as the Zeeman shifts of the energy levels. This assumption is kept here, giving the Hamiltonian

$$\hat{H}_z = \mu_B \frac{B'_z}{2} \sqrt{x^2 + y^2 + 4z^2} \left[\sum_{F_e} \sum_{m_e} g_{F_e} m_e |F_e; m_e\rangle \langle F_e; m_e| + g_{F_g} \sum_{F_g} \sum_{m_g} m_g |F_g; m_g\rangle \langle F_g; m_g| \right], \quad (5.8)$$

where the g_F values are as described in Section 2.3. When considering the motion of the atom, this assumption requires that the direction of the atomic dipole changes along with the magnetic field. This can be particularly burdensome when passing through the origin as the magnetic field direction changes abruptly (from $+\hat{z}$ to $-\hat{z}$ when traveling along the z -axis, for example). Allowing for the atom to do so also assumes that the motional times scale of the atom is much slower than the time

scale for the atomic dipole moment to precess and align with the magnetic field, the adiabatic limit [63].

5.1.3 Atom-Electric Field Hamiltonian

With the full level structure of rubidium, there are many transitions between the various magnetic sublevels. Rather than writing individual transitions independently, and with thoughts towards the polarization of the experimental light fields, they can be grouped by linear and circular transitions that change m_F by ± 1 or 0. In this way, the lowering operators are written as in

$$\hat{\Sigma}_q = \sum_{F_g, F_e, m_e} s(F_e, F_g, m_e) |J_g, m_e + q\rangle \langle J_e, m_e|, \quad (5.9)$$

with coefficients ([48, Eq . 7.407])

$$s(F_e, F_g, m_e) = (-1)^{F_e + J_g + 1 + I} \sqrt{(2F_e + 1)(2J_g + 1)} \times \langle F_g, m_e + q | F_e, m_e; 1, q \rangle \begin{Bmatrix} J_e & J_g & 1 \\ F_g & F_e & I \end{Bmatrix}, \quad (5.10)$$

where each term in the sum lowers the atom from the $|J_e, m_e\rangle$ state to the $|J_g, m_g = m_e + q\rangle$ state. Do note that under this definition, transitions with $q = +1$ increase the m_F sub-levels of the atom, which correspond to σ_- transitions as used in Chapter II. With these lowering operators, the atom-field interaction Hamiltonian can be defined in the same form as Equation 2.56, with appropriate care due to the $\sigma_{\pm, 0}$ and $\Sigma_{q=\mp 1, 0}$

Propagation direction	Polarization	Polarization Vector
$+z$	σ_-	$[1, -i, 0] / \sqrt{2}$
$-z$	σ_+	$[-1, -i, 0] / \sqrt{2}$
$+x$	σ_+	$[0, i, 1] / \sqrt{2}$
$-x$	σ_-	$[0, -i, 1] / \sqrt{2}$
$+y$	σ_+	$[-i, 0, 1] / \sqrt{2}$
$-y$	σ_-	$[i, 0, 1] / \sqrt{2}$

TABLE 5.2. MOT Beam Circular Polarizations. These are defined so atoms along an axis are pushed towards the origin as shown in Figure 1.1. Note the change flipping of polarizations between the x- and y-directions compared to the z-direction, which arises from the change in the sign of the magnetic field gradient in the x- and y-directions. The polarization vectors are in cartesian coordinates. Labels of σ_{\pm} are in reference to the polarization seen by the atom. In the frame propagating with each beam, the polarizations for opposing beams is identical (see Section 2.4).

relationship. This Hamiltonian is

$$\hat{H}_{\text{AF}} = \frac{\hbar}{2} \sum_q \left[\Omega_q^* \hat{\Sigma}_q + \Omega_q \hat{\Sigma}_q^\dagger \right]. \quad (5.11)$$

The optical field for the MOT is made of six lasers as described in Chapter I. A single beam has the form of Equation 2.14 with the \vec{E}^+ component (in the rotating atom frame) as

$$\vec{E}^+(\vec{r}) = \frac{E_0 \hat{e}}{2} e^{-i\phi} e^{i\vec{k} \cdot \vec{r}}, \quad (5.12)$$

where \vec{k} is the beam's propagation direction, \hat{e} is the beam polarization, and ϕ is the beam phase. In the MOT, the beam polarizations are circular and their direction is closely linked the magnetic field along an axis, as discussed in Section 2.5.1. The required polarizations are given in Table 5.2 in terms of their circular polarizations. These polarizations are defined so that atoms located along the beam axis feels a net force pushing them toward the origin.

The net electric field \vec{E}_T is the sum of the individual fields

$$\vec{E}_T^+(\vec{r}) = \sum_i \vec{E}_i^+(\vec{r}), \quad (5.13)$$

where the sum is over each MOT beam present in the trap. To sum the fields, the polarizations need to be written in a common (lab-based) Cartesian basis, which are the polarization vectors listed in the right column of Table 5.2. This gives the field in the cartesian basis, which then needs to be changed to the linear and circular basis as to write the field Hamiltonian as in Equation 5.11. In this basis, the Rabi frequencies are

$$\vec{\Omega}_z = \begin{bmatrix} \Omega_{q=-1} \\ \Omega_{q=0} \\ \Omega_{q=+1} \end{bmatrix} = \frac{\langle J_g = 1/2 | d | J_3 = 3/2 \rangle}{\hbar} \begin{bmatrix} -\frac{1}{\sqrt{2}} & \frac{i}{\sqrt{2}} & 0 \\ 0 & 0 & 1 \\ \frac{1}{\sqrt{2}} & \frac{i}{\sqrt{2}} & 0 \end{bmatrix} \vec{E}_T, \quad (5.14)$$

where $\langle J_g = 1/2 | d | J_3 = 3/2 \rangle$ is the D₂ dipole transition matrix element for ⁸⁷Rb [62].

This basis has the angular momentum quantization axis in the z -direction. To change to a basis where the quantization axis is along the magnetic field direction, the angular momentum vector must be rotated. From Rose [126], rotating an operator that changes total angular momentum by 1 to a basis with a different quantization

axis is done with a rotation operator⁴ whose matrix elements are

$$D_{m',m}^{(1)}(\alpha\beta\gamma) = e^{-im\gamma}e^{-im'\alpha} \sum_x \left[\frac{(-1)^x \sqrt{(1+m)!(1-m)!(1+m')!(1-m')!}}{(1-m'-x)!(1+m-x)!(x+m'-m)!x!} \times \left(\cos \frac{\beta}{2} \right)^{2+m-m'-2x} \left(-\sin \frac{\beta}{2} \right)^{m'-m+2x} \right], \quad (5.15)$$

where the angles α , β , and γ correspond to the standard Euler angles. Because only the direction of the z -axis is important to the rotation (the orientation of the x - and y - axis does not matter), we have $\gamma = 0$. With possible values $m = -1, 0, 1$, the (correctly indexed) rotation matrix is the 3×3 matrix :

$$R(\alpha, \beta) = \begin{pmatrix} \frac{1}{2}e^{i\alpha}(1 + \cos \beta) & -\frac{1}{\sqrt{2}}\sin \beta & \frac{1}{2}e^{-i\alpha}(1 - \cos \beta) \\ \frac{1}{\sqrt{2}}e^{i\alpha}\sin \beta & \cos \beta & -\frac{1}{\sqrt{2}}e^{-i\alpha}\sin \beta \\ \frac{1}{2}e^{i\alpha}(1 - \cos \beta) & \frac{1}{\sqrt{2}}\sin \beta & \frac{1}{2}e^{-i\alpha}(1 + \cos \beta) \end{pmatrix}. \quad (5.16)$$

This rotation matrix is identical to an operation that converts the circular basis polarizations to the Cartesian basis, rotates the Cartesian vectors with classical rotations around the z -axis by (polar) angle α and then around the y -axis by (azimuthal) angle β , then converts back to the circular basis.

For each position in the MOT, the magnetic field has spherical coordinate angles ϕ_B and θ_B (corresponding to azimuthal and polar angles respectively). With the

⁴This operator, based on historic derivation by Wigner, has indices ordered different from common matrix definitions. So the matrix elements are for the rotation operator, R , given by $R|1, m\rangle = \sum_{m'} D_{m',m}^{(1)}|1, m'\rangle$.

atom aligned to the magnetic field, it “sees” an electric field with polarization vector

$$\vec{\Omega}_B = R(\phi_B, \theta_B) \vec{\Omega}_z \quad (5.17)$$

The circular and linear components of this vector are the Rabi frequencies Ω_q used for the atom-field coupling Hamiltonian 5.11.

5.2 Matching Simulation to Experiments

Because of a lingering mismatch between experimental measurements and numeric results, the simulated MOT has had a large number of additional features included to better approximate the experiment. Some of these are discussed in brief here.

5.2.1 MOT Beam Power

The most obvious issue present in the MOT beams is imbalance in beam power, as noted in Section 3.2.2. This is corrected easily by providing each MOT beam its own field strength E_0 in Equation 5.12. In the simulation, a global laser beam power P (in milliwatts) is defined and each beam has a power ratio factor r_i relative to this power. With these, the field strength for each MOT beam is

$$E_0^i = \sqrt{\frac{2(P r_i)}{\pi w^2} \times \frac{20}{\epsilon_0 c}}, \quad (5.18)$$

where the first term is the central intensity for a Gaussian beam and the second term relates beam intensity to field strength [48]. In this equation, w is the MOT beam

waist (measured in cm) and the second term has an extra factor of 10 to convert from lab-measurement-units for beam intensity in mW/cm² to MKS units.

In our experiment, the MOT beams have a gaussian beam (intensity) profile rather than being pure plane waves as written above. The beam waist (measured as the 1/e² power radius) is 0.33 mm. For a single atom that remains within tens of microns of the MOT beams, the field intensity seen by the atom should be fairly uniform and close to the peak intensity. However, there is a small change in intensity which can be taken into account. For an atom located at \vec{r} and a MOT beam propagating in the direction \vec{k} and originating from position \vec{b}_0 , the (square of the) distance from the axis of the beam and the atomic position is

$$d^2 = \left| \lambda \vec{b}_0 - \vec{r} \right|^2 - \left[\left(\lambda \vec{b}_0 - \vec{r} \right) \cdot \vec{k} \right]^2, \quad (5.19)$$

where λ is the laser wavelength. This has been calculated by looking at two points along the MOT beam separated by one wavelength and basic point-line distance formulae. With this, the atom seems a field strength of

$$E_0^i \rightarrow E_0^i e^{-d^2/w^2}. \quad (5.20)$$

Note that this is the correct formula as the beam waist is the 1/e² radius (rather than its variance) and the field strength is proportional to the square root of the intensity.

MOT beam power measurements were done outside of vacuum (obviously), but the experimental cell was not anti-reflection coated. As such, the horizontal and vertical MOT beams inside the cell will have different powers. As seen in the vacuum system in Figure 3.1, the vertical beams enter the cell at nearly normal incidence, so that the beam is almost entirely polarized in the x - y plane, which is S-polarized

to the surface. However, if this beam is not exactly vertical, light polarized along the z -direction is P-polarized. For the horizontal beams (which enter the cell at nearly 45°), the light polarization component in the x - y plane is P-polarized and light polarized along the z -direction is S-polarized. For the appropriate wavelength and material, the field strength for each (Cartesian) polarization direction is reduced by a factor of either $\sqrt{1 - 2R_S}$ or $\sqrt{1 - R_P}$, where R_S and R_P are the S-polarization and P-polarization reflection coefficients, respectively. The factor of 2 accounts for reflections on the outer and inner surface of the experiment cell walls. In the case where $R_S \neq R_P$, this will shift the beams out of purely circular polarization inside the cell.

5.2.2 *MOT Beam Direction*

For an ideal MOT, the laser pairs are exactly counter-propagating and are normal to beams in other directions. This is, of course, not the case in physical MOTs. Instead, it is common while building a MOT to adjust the beam directions very slightly until the MOT “looks” good—that is to say it appears approximately round when imaged and there is a high atom number in the MOT. As discussed in great detail in Section 5.4 below, this adjusts the interference pattern of the lasers to minimize pathways for atoms to escape from the MOT. This is done numerically by rotating each beam’s propagation vector slightly with a classical rotation matrix. This rotation must also be applied to a MOT beam’s Cartesian polarization vector, although done with an angular momentum rotation matrix as above. Based on our experiment’s MOT beam alignment system, the misalignment of our MOT beams is no more than about half a degree, putting an upper limit on the angular displacement of a beam in the simulation.

Similarly, it is possible that an entire MOT beam is displaced from its ideal launching position. For example, a horizontal MOT beam could be a little too low, but angling its beam upward with a slight tilt would still have the beam strike the center of the MOT. This could still load a MOT without much difficulty. In the simulation then, each beam has a three dimensional positional offset vector to deal with this. It is important to note that this only comes into account when using a beam's gaussian profile, where the offset is the vector \vec{b}_0 discussed above. If the beams are plane waves there is no intensity dependence on the transverse dimension. Only a beam's propagation direction matters, not their displacement from ideal launching position.

5.2.3 MOT Beam Polarization

As discussed in Section 3.2.4, the experimental MOT beam polarizations are elliptical rather than circular. How much the beams are elliptical can be found by measuring the power (of the elliptical beam) through a polarizer. With perfectly circular light, the power through the polarizer will be constant for all angles through the polarizer. For elliptical light, the power will maximize at some angle and minimize at 90° from that angle.

For Cartesian axes a and b, normal to the beam propagation direction, the difference between the two powers in each polarization can be quantified as

$$\gamma_a = \cos^{-1} \left(\sqrt{\frac{P_a}{P_a + P_b}} \right), \quad (5.21)$$

where the angle is defined relative to the a-axis and the values P_a and P_b are the (measured) powers of the polarization in the two directions. Note that if the beam

is polarized completely along the a-direction, $P_b = 0$ and thus $\gamma = 0$. Similarly when the beam is linearly along the b-direction if $P_a = 0$ and $\gamma = \pi$. If the beams are balanced then $\gamma = \pi/2$. Incorporating this into the polarization vectors in Table 5.2, the $1/\sqrt{2}$ is replaced by $\cos \gamma_a$ for the polarization component the a-direction and $\sin \gamma_a$ for the polarization the b-direction. Each of the six beams will have its own value for γ_a and the direction a can be defined as either of the two directions normal the propagation direction.

5.2.4 Magnetic Fields

It is also possible to have a more complex formula for the magnetic field. Rather than the linearized form of Equation 5.4, a full form of the field at all positions from anti-Helmholtz coils could be used. Additionally, a background magnetic field \vec{B}_{back} could be present either from the Earth, the Helmholtz coils discussed in Section 3.3.6, miscellaneous equipment in the lab, or the lab next door. In this case, the magnetic field is

$$\vec{B}(\vec{r}) = B'_z \left(\frac{x}{2} \hat{x} + \frac{y}{2} \hat{y} - z \hat{z} \right) + \vec{B}_0, \quad (5.22)$$

where, as above, B'_z is the field gradient along the axis of the MOT magnetic field coils (or permanent magnets). Dealing with this magnetic field is straight forward as its magnitude is easily calculated for use in the atom-magnetic field Hamiltonian and the angles to use for the polarization rotation matrix in Equation 5.16 are calculated from this field.

The experiment sits on an optical table, whose top is a large conducting slab. As such, currents in the anti-Helmholtz coils will produce mirror images in the conductor. While this effect is small, it could play a larger role when magnetic field is modulated.

Including these effects just calls for including another term in the total magnetic field for another pair of anti-Helmholtz coils (with current in the opposite direction) whose placement is below the surface of the table a distance equal to the height of the real anti-Helmholtz coils above the table.

5.3 3D and ^{87}Rb Calculations

5.3.1 Atomic Equation of Motion

Spontaneous emission is handled identically to the $|F_g = 0\rangle \rightarrow |F_e = 0\rangle$ case with the appropriate forms of Σ_q as the lowering operators. That is, the differential equation governing the evolution of the atomic density matrix is

$$\frac{d}{dt}\rho = -\frac{i}{\hbar} \left[\hat{H}_A + \hat{H}_{AF} + \hat{H}_z, \rho \right] + \Gamma \mathcal{L} \left[\hat{\Sigma}_{q=-1} \right] \rho + \Gamma \mathcal{L} \left[\hat{\Sigma}_{q=0} \right] \rho + \Gamma \mathcal{L} \left[\hat{\Sigma}_{q=+1} \right] \rho \quad (5.23)$$

where the Hamiltonians are defined in Equations 5.1, 5.8, and 5.11, and the Lindblad superoperator was defined in Equation 2.6.

With the 24 magnetic sublevels of the D_2 transition for ^{87}Rb , the density matrix is 24×24 , probably not analytically solvable in 3D, but it can be done numerically. We implement this by reforming the density matrix into a 24×1 vector ρ_v and the Hamiltonian and Lindblad superoperators into an appropriate 24×24 matrix \mathcal{M} . With these, the equation of motion simply becomes

$$\frac{d}{dt}\rho = \mathcal{M}\rho_v. \quad (5.24)$$

Steady state solutions for this equation are found via LU decomposition to invert the matrix \mathcal{M} [127]. This is implemented through the LAPACK library [128].

The populations for the MOT trapping transition excited states are plotted in Figure 5.1a as a function of position from the origin in a 1D MOT. The preference for populating the outer most Zeeman sublevel is a result of these levels having only a single ground state to which they can decay. The growth (or much smaller decay) of the states with $m_e > 0$ states result from these states having their energy levels red shifted (recall $B(z > 0) < 0$ as shown in Figure 2.5). The rapid growth (or decay for $m_e < 0$) of populations in the outer most magnetic sublevels result from their having the largest Zeeman shifts, which most quickly moves these levels into (or out of) resonance with the electric fields. Additionally, as seen in other mutli-level atoms with ground state Zeeman shifts, at small magnetic detunings a two-photon process couples neighboring ground states [64].

As a test for success of the numeric simulation, the atom can be returned to the $|F_g = 0\rangle \rightarrow |F_e = 1\rangle$ model and the steady state populations were identical to the analytic results in Appendix A. For comparison between these two atomic models, the (MOT trapping) excited energy level steady state populations in a 1D MOT for the V-atom and the full rubidium atom are plotted in Figure 5.1b. For the rubidium atoms, the populations are summed over Zeeman sublevels for clarity in the graph.

5.3.2 Force Formalism

The force on the atom is calculated exactly as in Equation 2.29. The effect on the magnetic field Hamiltonian is exactly

$$\vec{\nabla} \hat{H}_z = \frac{\hat{H}_z}{x^2 + y^2 + 4z^2} [x\hat{x} + y\hat{y} + 4z\hat{z}]. \quad (5.25)$$

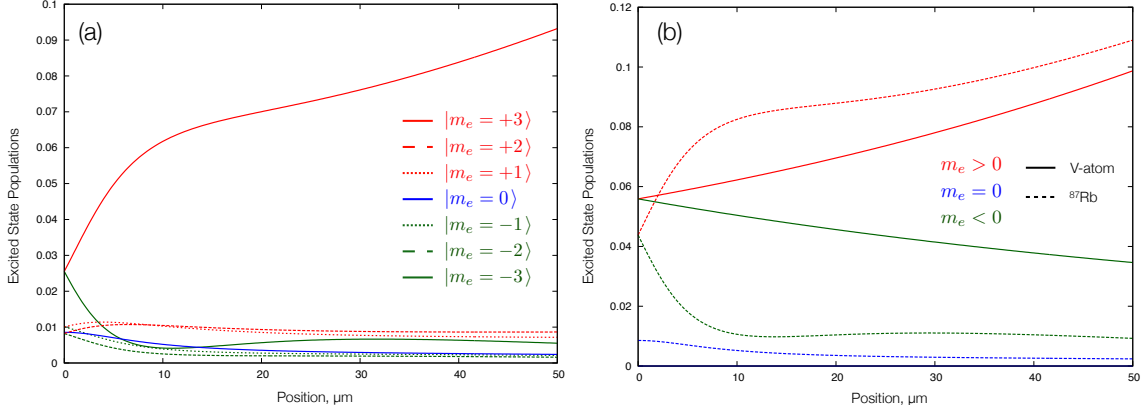


FIGURE 5.1. Excited state populations for ^{87}Rb and V-atom. Calculation done for a 1D MOT along the $+z$ -axis. (a) Populations for ^{87}Rb excited states. (b) Populations for both ^{87}Rb and V-atom model. The populations for ^{87}Rb are summed over magnetic sub-levels for clarity.

Noting that along the z -axis, the strength of H_z is twice as large as along the x - or y -axis, the force that results from this should also be twice as strong along the z -axis. This is expected as the magnetic field gradient is twice as large along the z -axis. If the system is treated as having no background magnetic field, this equation for the gradient of the atom-magnetic field Hamiltonian does not change.

The effect on the atom-field Hamiltonian follows the derivation of the optical molasses force. The gradient of Hamiltonian becomes just a gradient of the electric field propagation term $e^{-i\vec{k}\cdot\vec{r}}$, adding a factor $-i\vec{k}$ to each term in the sum of the total electric field in Equation 5.13. Because the electric field is already a vector, the gradient here is a tensor which is most clear when written in terms of individual directions. For the (pre-rotated) Rabi frequency vector of Equation 5.14, the gradient

in the ℓ direction is

$$\frac{\partial}{\partial \ell} \vec{\Omega}_z = \frac{\langle J_g = 1/2 | d | J_3 = 3/2 \rangle}{\hbar} \begin{bmatrix} -\frac{1}{\sqrt{2}} & \frac{i}{\sqrt{2}} & 0 \\ 0 & 0 & 1 \\ \frac{1}{\sqrt{2}} & \frac{i}{\sqrt{2}} & 0 \end{bmatrix} \left(-ik\vec{E}_{+\ell} + ik\vec{E}_{-\ell} \right). \quad (5.26)$$

This vector must then be rotated to the atomic dipole reference frame. In this view, the polarization rotation matrix is assumed to not change with position to first order. However, because the magnetic field changes with position, its direction will also change with position. This would change the rotation matrix as well, but this effect is ignored to first order, when the change in field orientation is small with respect to the change in the field polarization.

5.3.3 Steady State Force

To find the force in the s-direction for the atom located at position \vec{r} , calculate the steady state of the atomic density matrix, $\rho^{ss}(\vec{r})$, as above. The gradient of the Hamiltonian in the ℓ -direction is then calculated and is given by

$$\frac{\partial}{\partial \ell} \hat{H} = \frac{\partial}{\partial \ell} \hat{H}_z + R(\phi_B, \theta_B) \frac{\partial}{\partial \ell} \vec{\Omega}_\ell. \quad (5.27)$$

Calculating the expectation value of the force is done by tracing this operator over the steady state density matrix:

$$\langle F_\ell \rangle = \text{Tr} \left[\left(\frac{\partial}{\partial \ell} \hat{H} \right) \rho^{ss} \right]. \quad (5.28)$$

The form of Equation 5.27 does include both the purely magnetic trapping of Section 2.3.1 and the MOT magnetic confinement of Section 2.5.1. The magnetic trapping derived from the gradient of the magnetic Hamiltonian and the magnetic confinement derived from the gradient of the atom-field Hamiltonian. Both derive their the spatial dependence from the spacial dependence of ρ^{ss} .

For comparison, a one-dimensional force in steady state for the full ^{87}Rb atom and the V-atom is plotted in Figure 5.2 both with a trapping field gradient of 242G/cm (a current of 9A in our magnetic field coils). A few features are clear. First, near the center of the trap, the force on the full ^{87}Rb atom is larger. A linear fit of the force full rubidium force data near $z = 0$ gives a force of $\vec{F}_{\text{Rb}}(z) = -[3.68 \times 10^{-16}\text{N/m}] z\hat{z}$, an order of magnitude larger than the V-atom force $\vec{F}_{\text{V-at}}(z) = -[4.3 \times 10^{-17}\text{N/m}] z\hat{z}$ with the balanced restoring constant from Equation 2.84.

This enhancement to the trapping force is a result of having multiple ground state magnetic sublevels for the full atom [48]. For ground state sublevels where the energy is redshifted due to the magnetic field, a two-photon absorption process can couple neighboring ground state levels with slightly different detunings from resonance [64]. The effect is to enhance coupling to the MOT beam that the atom is closer to, leading to a larger force from this beam⁵. This effect “turns off” at larger Zeeman shifts when the ground state magnetic sublevels shift further apart in energy. This gives rise to a second feature, the change in slope of the force for the full ^{87}Rb atom around 20 μm for these parameters. In general, the width of the two-photon feature is

$$\delta_z = \frac{As\Gamma^2\hbar}{4\mu_B g F_g B'_z |\Delta|} \quad (5.29)$$

⁵For slowly moving atoms, a similar effect occurs in momentum-space (with Doppler shifts playing a similar role to the detuning) and is the polarization gradient cooling discussed in Section 2.5.3 [72].

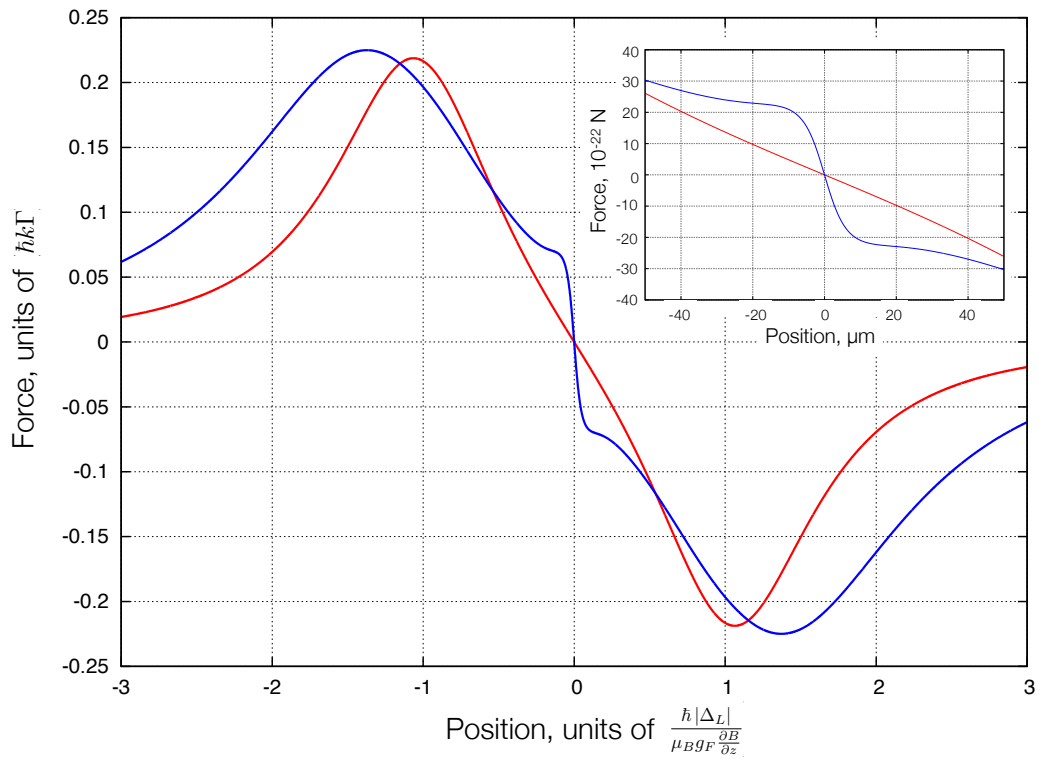


FIGURE 5.2. 1D forces on ^{87}Rb and V-atom. Red curves show V-atom results, blue curves show Full ^{87}Rb results. Inset shows forces in scaled to region near where the atom in the MOT is. Axes for main graph and inset are scaled identically to figures 2.4(a) and (c) respectively.

where s is the saturation parameter defined in Equation 2.38 and A is a numerical factor that depends on the structure of the atom [64].

The final feature is a larger trapping region for the complete ^{87}Rb atom. This results from the smaller Zeeman shifts of the inner magnetic sublevels. Once magnetic field grows to a large enough magnitude, the $|m_e = \pm 3\rangle$ energy levels are blue shifted out of resonance with the MOT lasers. However, the $|m_e < 3\rangle$ energy levels are still red-detuned of the electric field, letting them continue to interact with the beams. This extends the region where trapping can occur.

5.3.4 *Velocity*

The atomic velocity is not taken into account in our calculation, meaning that there is no doppler shifting of the MOT beams. This could be done, and requires restructuring the atomic hamiltonian of Equation 5.1, as each MOT beam will have a different detuning due to the atomic motion. recalculation as the detunings in must written separately for each beam. Without including velocity in the calculation, there are also no sub-doppler effects that may arise. The sub-Doppler effects on the atom can be taken into account simply by limiting the maximum energy (temperature) of the atom when calculating the probability distribution from the potential energy of the atom.

5.4 **Escape Channels**

Even the results graphed in Figure 5.1 is relatively simple as it represents a just a 1D system. Expanding to three dimensions as laid out above and can lead to an

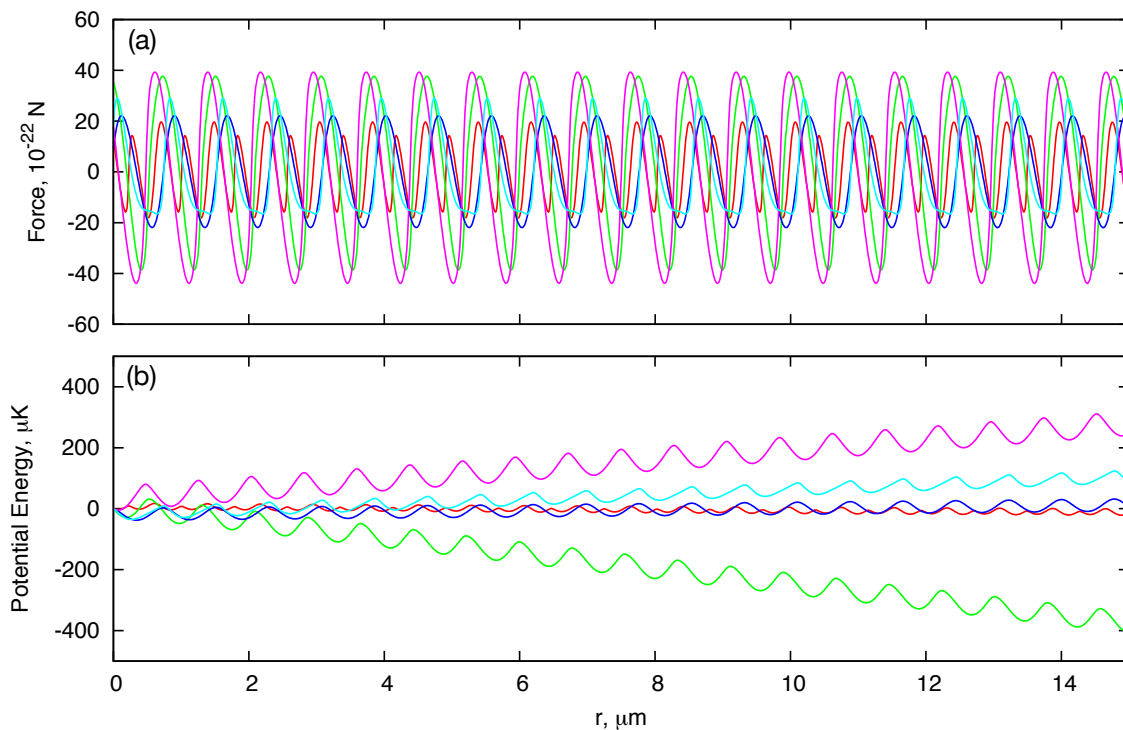


FIGURE 5.3. 3D MOT forces for an assortment of beam phases. Calculation done for a 3D MOT along the $+z$ -axis. Figure (a) shows the forces and figure (b) shows the resulting potential energy from these forces. The potential is found by numerically integrating the force along the positive z -axis.

unanticipated result. Figure 5.3 shows (a) the force and (b) the potential energy along the positive z -axis for a random selection of phases for the six 3-D MOT beams.

From the figure, it is clear that different arrangements of the MOT beam phases can greatly change the force on an atom. Mostly clearly, unlike in the 1D case, the force oscillates. This is a result of interference of the MOT beams creating an optical lattice inside the MOT (see the brief discussion in Section 1.3). Additionally, from the potential energy graphs, there are some phase arrangements where the force on an atom pushes it from the center of the trap. These are cases where the potential energies decrease as the atom travels outward from the center of the trap (the green

and red graphs). While not shown, in some of these cases the potential energy does eventually “turn around” becoming positive again. In such cases, this effectively just moves the “center” of the MOT away from the location where the magnetic field vanishes. This is similar to the beam imbalance or background magnetic field as discussed in Chapter II, both which also displace the center of the MOT.

In other cases, the potential does not “turn around” but instead continues to decrease. In these cases, atoms which found themselves along these paths could potentially escape from the trap. While shown below for just along the positive z -axis, these paths can arise in many directions and typically form narrow channels along which the force is not restorative. These channels are narrow, on the order of the light wavelength, and they grow wider further from the MOT center. Such non-restorative forces in MOTs [92, 129] have been observed before. In optical lattices, similar non-cooling forces can appear in momentum space [130]

The origin of these channels can be seen by more carefully consider the electric fields in the MOT. First, consider only the two z -beams. These beams have (positive-rotating) fields, as defined in Equation 5.12,

$$\vec{E}_{z-}^{(+)} = \frac{E_0}{2\sqrt{2}} \begin{bmatrix} -1 \\ -i \\ 0 \end{bmatrix} e^{-i\phi_{z-}} e^{+ikz} \quad \text{and} \quad \vec{E}_{z+}^{(+)} = \frac{E_0}{2\sqrt{2}} \begin{bmatrix} 1 \\ -i \\ 0 \end{bmatrix} e^{-i\phi_{z+}} e^{-ikz}. \quad (5.30)$$

Note that the field sub-scripts refer to the direction the beams come from, not the direction the beams propagate in. The total field is then

$$\vec{E}_T^{(+)} = \frac{E_0}{2\sqrt{2}} \begin{bmatrix} -e^{-i\phi_{z-}}e^{+ikz} + e^{-i\phi_{z+}}e^{-ikz} \\ -ie^{-i\phi_{z-}}e^{+ikz} - ie^{-i\phi_{z+}}e^{-ikz} \\ 0 \end{bmatrix},$$

and, with Equation 5.14, the Rabi frequency is

$$\vec{\Omega}_z = \frac{\langle d \rangle E_0}{2\hbar} \begin{bmatrix} e^{-i\phi_{z-}}e^{+ikz} \\ 0 \\ e^{-i\phi_{z+}}e^{-ikz} \end{bmatrix}.$$

Taking a position on the negative z -axis where $\vec{B} \parallel \hat{z}$ (for simplicity), the rotation matrix of Equation 5.16 is the identity, $R(\phi_B \theta_B) = 1$, so that $\vec{\Omega} = \vec{\Omega}_z$. The Rabi frequency vector has magnitude

$$|\vec{\Omega}| = \frac{\langle d \rangle E_0}{2\hbar} \begin{bmatrix} 1 \\ 0 \\ 1 \end{bmatrix}, \quad (5.31)$$

as is expected. The electric field (made by the two beams) is equal parts σ_- and σ_+ light. This is the normal assumption made when working with a 1-D MOT. When looking at forces, we need the negative gradient of each component of Ω :

$$-\vec{\nabla} \vec{\Omega} = \frac{\langle d \rangle E_0}{2\hbar} \begin{bmatrix} -ik (e^{-i\phi_{z-}}e^{+ikz}) \\ 0 \\ +ik (e^{-i\phi_{z+}}e^{-ikz}) \end{bmatrix} \hat{z}.$$

Since $\Omega_{q=-1}$ is associated with σ_+ polarization, this equation suggests σ_+ light is responsible for forces in the negative-z direction. This is exactly what was expected as defined in Table 5.2. Similarly, σ_- light (associated with $\Omega_{q=+1}$) is responsible for forces in the positive-z direction. Optical molasses, discussed in Section 2.4.1, takes advantage of these different force directions by increasing coupling to the beam that is counter-propagating to atomic motion in order to cool the atom. MOTs take advantage of this by using Zeeman shifts to increase coupling to the beam which will push the atom towards the center of the trap. The gradient equation above is exactly the situation plotted in Figure 5.2.

The phase dependence can be seen by adding just a single additional MOT beam. Say a beam propagating *in* the $-x$ direction (from the $+x$ direction). This beam has field

$$\vec{E}_{x+}^{(+)} = \frac{E_0}{2\sqrt{2}} \begin{bmatrix} 0 \\ i \\ -1 \end{bmatrix} e^{-i\phi_{x+}} e^{-ikx}.$$

With the two z-beams in Equation 5.30, the total field is

$$\vec{E}_T^{(+)} = \frac{E_0}{2\sqrt{2}} \begin{bmatrix} -e^{-i\phi_{z-}} e^{+ikz} + e^{-i\phi_{z+}} e^{-ikz} \\ -ie^{-i\phi_{z-}} e^{+ikz} - ie^{-i\phi_{z+}} e^{-ikz} + ie^{-i\phi_{x+}} e^{-ikx} \\ -e^{-i\phi_{x+}} e^{-ikx} \end{bmatrix}.$$

The Rabi frequency vector (with the magnetic field along z still) is

$$\vec{\Omega} = \frac{\langle d \rangle E_0}{2\hbar} \begin{bmatrix} e^{-i\phi_{z-}} e^{+ikz} - \frac{1}{2} e^{-i\phi_{x+}} e^{-ikx} \\ -\frac{1}{\sqrt{2}} e^{-i\phi_{x+}} e^{+ikx} \\ e^{-i\phi_{z+}} e^{-ikz} - \frac{1}{2} e^{-i\phi_{x+}} e^{-ikx} \end{bmatrix}.$$

Looking at this vector in terms of forces, we have gradient

$$-\vec{\nabla} \vec{\Omega} = \frac{\langle d \rangle E_0}{4\hbar} \begin{bmatrix} +ik (e^{-i\phi_{x+}} e^{-ikx}) \\ -i\sqrt{2}k (e^{-i\phi_{x+}} e^{-ikx}) \\ +ik (e^{-i\phi_{x+}} e^{-ikx}) \end{bmatrix} \hat{x} + \frac{\langle d \rangle E_0}{2\hbar} \begin{bmatrix} -ik (e^{-i\phi_{z-}} e^{+ikz}) \\ 0 \\ +ik (e^{-i\phi_{z+}} e^{-ikz}) \end{bmatrix} \hat{z} \quad (5.32)$$

The terms associated with forces in the z -direction do not change, which is good. The z -forces should still be controlled by the two z -beams. For the x -direction, forces arise from all three polarizations. This is to be expected as the field in the x -direction beam has a component of each polarization (in the circular basis). Note that the circular polarization components result in forces in the positive x -direction—opposite the propagation direction of the beam.

From the gradient, it appears that force in the z -direction should be the same as when there is no off-axis MOT beams. However, because $\vec{\Omega}$ is different, the steady-state atomic density matrix will be different. Thus the average force, as calculated from Equation 5.28, will be different. From Equations 2.27, A.1 and A.2, the excited state populations are generally proportional to the square of the exciting Rabi frequency component (just $|\Omega|^2$ for the two-level atom and $|\Omega_-|^2$ and $|\Omega_+|^2$ for the two excited states in the V-atom). Assuming this generally holds for the more

complex multi-level atom,⁶ we can look at the square of the Rabi vector:

$$|\vec{\Omega}|^2 = \frac{\langle d \rangle^2 E_0^2}{4\hbar^2} \begin{bmatrix} \frac{5}{4} + \cos[kz - kx - (\phi_{z-} + \phi_{x+})] \\ 1/2 \\ \frac{5}{4} + \cos[kz + kx + (\phi_{z+} + \phi_{x+})] \end{bmatrix}. \quad (5.33)$$

The linear component has a fixed value, but the two circular polarizations depend on position as well as the phase relationships between the various beams. This leads to a complicated force in the x - and z -direction as a function of position. Of specific interest, are locations where the oscillating terms have larger negative values. In these cases, the σ_+ or σ_- components can be less than their associated values in the two-beam case above, Equation 5.31. This would tend to decrease the excited state populations, and with the same form for the z -component of $-\vec{\nabla}\Omega$, and would reduce the overall force in the z -direction. Under some phase arrangements, this could change the sign of the force, resulting in a force that pushes the atom away from the center of the MOT, as seen in Figure 5.3.

As an illustrative example, the specific case for $\phi_{z-} = \phi_{z+} = \phi_{x+} = 0$ is shown in Figure 5.4. In this figure, the graphs for both the 1D two-vertical beam MOT and the 3-beam field arrangement just discussed is shown. Graphs (a) and (b), showing the (normalized) polarization components and the Rabi frequency magnitudes, agree with the calculations in Equation 5.33, where in all four sets of graphs the σ_- and σ_+ components are equal. In graph (d), which shows the components of the force on the atom, the total force in the x -direction is always negative as is expected because the beam is propagating in this direction.

⁶Looking at Equation 5.11, the average force is a sum over $\langle \hat{\Sigma}_q \rangle_{ss}$, weighted by the gradient of the appropriate component of $\vec{\Omega}$. For the analytically solved atoms, $\langle \hat{\Sigma}_q \rangle_{ss} = \rho_{qq}^{ss}$.

From graph (c), which shows the expectation values of the atomic lowering operators, the $\Sigma_{q=0}$ lowering operator always has a larger expectation value than either the $\Sigma_{q=-1}$ and $\Sigma_{q=+1}$ lowering operators. Compared to the forces in graph (d), $\langle \Sigma_{q=0} \rangle$ is minimized at positions where $F_x = 0$. These are also locations where the light is split evenly between circular and linear polarizations, as shown in graphs (a). This balance and cancel the two directions for the x-direction force as noted in Equation 5.32.

Because the two vertical beams essentially form a one-dimensional MOT, the force is (nearly) linear as expected and results in a quadratic potential. However, the addition of the third beam produces strong oscillations in z -direction force. The z -direction force does go to zero where $\langle \Sigma_{q=-1} \rangle = \langle \Sigma_{q=+1} \rangle$ (graph (c)), suggesting the atom experiences forces from the counter-propagating σ_+ and σ_- beams equally. While not clear from the z -direction force itself, the potential curve (calculated just from integrating the force) does show MOT trapping as from the 1D case, overlaid with deeper potential energy wells associated with the spatial polarization oscillations as shown in graphs (a). Detangling these two potentials is necessary for estimating the MOT temperature.

Adding additional beams further complicates the equation for Ω . The complex position relationship is not of specific interest as calculations for the temperature will integrate over position. However, the phase relationship between the six beams as evident above will greatly change the Rabi frequencies, the steady state populations and the force on the atom. This does include situations where the overall force is away from the center of the MOT as shown in Figure 5.3. In these cases, the polarization arrangement creates a state where one of the $\langle \Sigma \rangle_q$ values moves the atom away from the center of the MOT. For example, for the beam arrangement

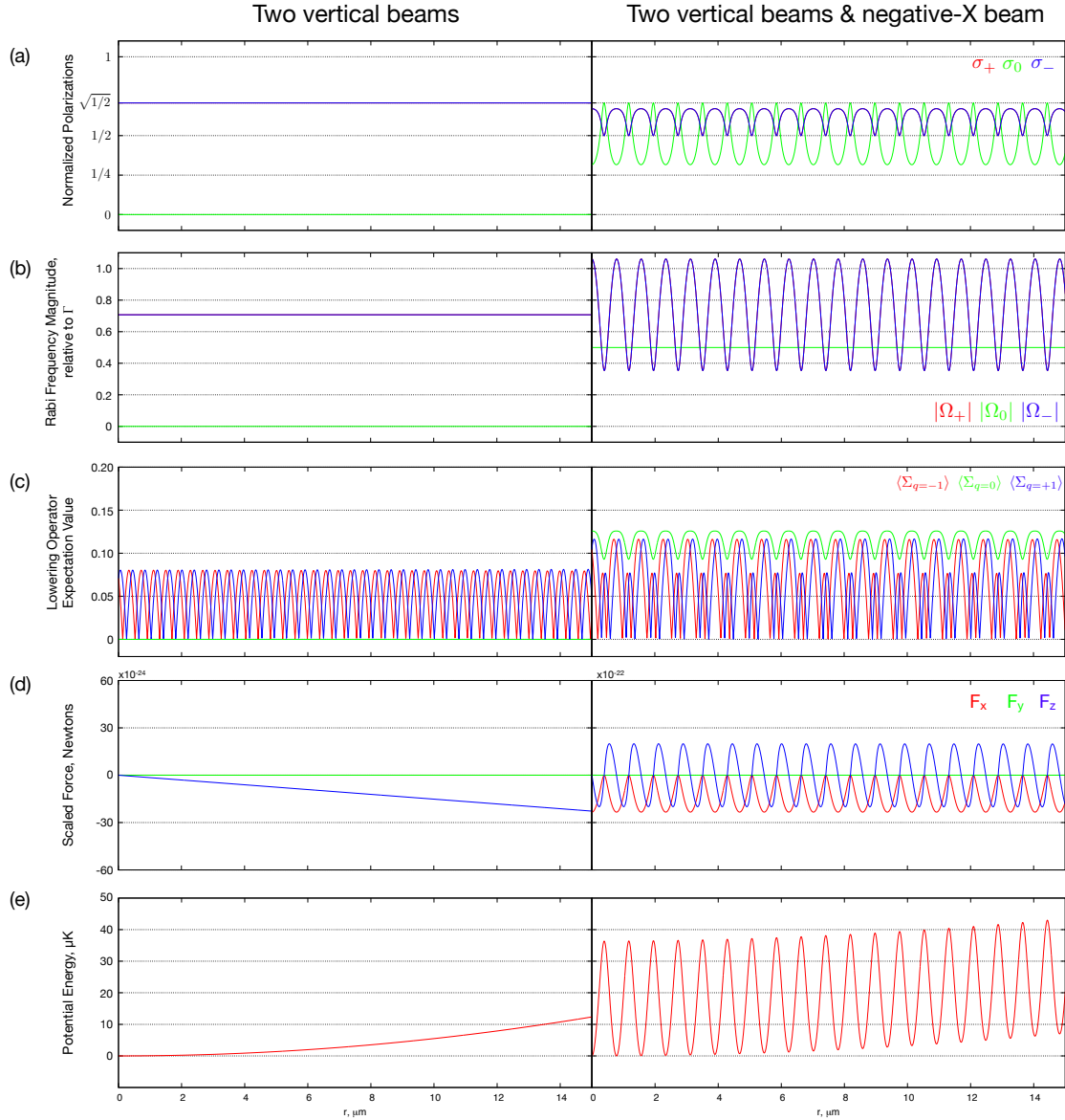


FIGURE 5.4. 3D MOT phase dependence. The left graphs show results for the MOT with just two vertical beams. The right graphs show the results for the MOT with an additional beam in the negative x-direction. In all graphs, the horizontal axis is positions along the positive-z axis. Calculations done with $\Omega = \Gamma/\sqrt{2}$ and $|B'_z| = 1$ G/cm. Graphs (a) and (b) show the normalized polarization components and Rabi frequency amplitude, respectively for the three circular polarizations as defined in equations 2.55. Figure (c) shows the three lowering operators' (Equation 5.9) expectation values in steady state. Figure (d) shows the force in the x-, y- and z-direction. Note that the two graphs have different scalings. Figure (e) shows the potential energy along the positive-z axis.

leading to Equation 5.32 if the beam phases (and possibly the MOT Zeeman shifts) are such that when $z > 0$ we have $\langle \hat{\Sigma}_- \rangle_{ss} > \langle \hat{\Sigma}_+ \rangle_{ss}$, then the resulting force along the z-direction would push the atom towards in the positive-z direction—away from the center of the MOT. These phase arrangements are the ones which lead to the anti-trapping forces in Figure 5.3.

5.5 Recovering Potential

In addition to anti-trapping, the force curves shown in Figure 5.3 have an additional problem. The forces, in general, are non-conservative. Integrating the force along another path (besides along the z-axis as calculated in Figure 5.3b) result in different values for the potential energy. In such a circumstance, it is impossible to define a potential energy of the form

$$\vec{F} = -\vec{\nabla}U. \quad (5.34)$$

Rectifying this can be done one of three ways. First, the Helmholtz theorem states any vector field, $\vec{v}(\vec{r})$, can be written as

$$\vec{v}(\vec{r}) = \vec{v}^{\parallel}(\vec{r}) + \vec{v}^{\perp}(\vec{r}), \quad (5.35)$$

where $\vec{\nabla} \times \vec{v}^{\parallel} = 0$ and $\vec{\nabla} \cdot \vec{v}^{\perp}(\vec{r}) = 0$. This first irrotational (curl-less) term is conservative, so that applying the Helmholtz theorem to the force we can define a potential as

$$U = - \int \vec{F}^{\parallel}(\vec{r}) \cdot d\vec{r}. \quad (5.36)$$

The α component of irrotational force can be computed directly from the full force [48] as

$$F_{\alpha}^{\parallel}(\vec{r}) = \int d^3 r' \left[\frac{1}{(2\pi)^3} \int d^3 k \frac{k_{\alpha} k_{\beta}}{k^2} e^{i\vec{k} \cdot (\vec{r} - \vec{r}')} \right] F_{\beta}(\vec{r}').$$

In a more numerically accessible form, this is

$$F_{\alpha}^{\parallel}(\vec{r}) = \mathcal{F}^{-1} \left[\frac{k_{\alpha}}{k^2} \mathcal{B} \right], \quad (5.37)$$

where

$$\mathcal{B} = \vec{k} \cdot \tilde{F}(\vec{k}),$$

and where

$$\tilde{F}(\vec{k}) = \mathcal{F}[F_x(\vec{r})] \hat{x} + \mathcal{F}[F_y(\vec{r})] \hat{y} + \mathcal{F}[F_z(\vec{r})] \hat{z}$$

is the Fourier transform of the force field.

These two transforms, to find the fourier transform of the force and the inverse transform to get the irrotational component, are three-dimensional. This requires numeric solutions for the force over a large grid that encompasses the region in which the atom exists. The region should be at least large enough such that the probability for an atom to be outside of the grid is small. Similarly, the position-space spacing of the grid should be smaller than the wavelength of the lasers to allow for oscillations in the results. For a fair sized MOT (approximate 50 μm in diameter) and square grid spacing $\lambda/10$, this is about 263 million grid points, each which has 3 components to the force. While the calculation for the irrotational force is not challenging, calculating the atomic density matrix in steady state at each point is numerically intensive (but definitely possible).

The second approach, much simpler numerically, is to calculate the force in a smaller region, or even in one dimension, for many phases of the six MOT beams. The forces are averaged together before calculating the potential energy. As our experimental lasers are not phase controlled, drift in phase, and potentially even change beam direction, an atom will see a variety of phase relationships between the beams. Averaging data over many data runs should approximate the numeric phase averaging.

The third approach, which we have not investigated numerically but mimics the experimental process to make “good” MOTs discussed above, is to adjust beam direction and phases until the escape channels vanish in the simulated results.

CHAPTER VI

POSITION AND TEMPERATURE MEASUREMENTS

Soon after loading a single atom MOT with our water-cooled electromagnetic anti-Helmholtz coils, pure curiosity lead us to check on the power spectrum of photons collected from our single atom. A very clear peak at around 21 kHz was visible and, soon after, an oscillation of the same frequency was seen in the anti-Helmholtz coil current. While it isn't revolutionary that an oscillation in one property (magnetic field strength) results in oscillations in properties that depend on it (atomic fluorescence rates through the Zeeman-shifted detuning), because the magnetic field strength varies with position, the strength of the field oscillation also has a positional dependence. This should encode some atomic position information about into the fluorescence oscillation strength, allowing us to learn about motion of the atom in the MOT, as well as its temperature, from the light that it emits.

The theory and data analysis technique are laid out at the beginning of the chapter. Following that, measurements of the atomic fluorescence oscillation in a variety of experimental contexts are shown and discussed. To close the chapter, two interesting additional effects are examined.

6.1 Theory

Following Equation 2.28, the rate that a multilevel atom scatters photons is

$$R = \Gamma \sum_i \rho_{e_i, e_i}, \quad (6.1)$$

where the sum is over all of the possible excited states of the atom. These excited state populations depend strongly on the detuning of the electric field from atomic

resonance. This is directly evident in the steady state equations for the two-level atom 2.27 or the V-atom excited states A.1 and A.2, which all depend on the detuning from resonance. For demonstration, the two-level population and the single-excitation field excited-state population for the V-atom (Equation 2.61), can be written in a generalized form as

$$\rho_{e,e} = \frac{|\tilde{\Omega}|^2}{1 + 4\delta^2 + 2|\tilde{\Omega}|^2} \quad (6.2)$$

where δ_i and $\tilde{\Omega}_i$ are the detuning from resonance and Rabi frequency for light coupled to the excited state, both scaled by the spontaneous decay rate Γ . Obviously, a smaller detuning from resonance results in a higher population. As was done in Chapter II, the detuning can be written in terms of the laser detuning plus a Zeeman shift (see Equations 2.76) as

$$\delta_i = \delta_{L,i} + m_i \delta_B,$$

where m_i is the magnetic quantum number for the excited state, and again the detunings are scaled by Γ , e.g. $\delta \equiv \Delta/\Gamma$. When the Zeeman detuning δ_B is much smaller than the laser detuning $\delta_{L,i}$, which is true for an atoms in a MOT as discussed in Section 2.5, the population can be expanded in terms of small Zeeman detuning. In one dimension, with Equation 2.75 defining the Zeeman shift's frequency, thus becomes

$$\rho_{e_i,e_i} = \frac{|\tilde{\Omega}_i|^2}{1 + 4\delta_{L,i}^2 + 2|\tilde{\Omega}_i|^2} + \frac{8\mu_B g_F m_i |\delta_{L,i}| |\tilde{\Omega}_i|^2}{\Gamma \hbar \left(1 + 4\delta_{L,i}^2 + 2|\tilde{\Omega}_i|^2\right)^2} B'_z z. \quad (6.3)$$

Interestingly, this form shows a clear breakdown of treating the atom in a MOT as either a two level atom or as the extended two-level atom described in Equation 2.4.1. For the two level atom's single excited state, $m = 0$ and there is no Zeeman

shift, and hence no position/magnetic field dependence in the fluorescence. For the extended two level atom, $m_{\pm} = \pm 1$ and when summing over both states to get a total scatter rate, the position and magnetic field dependence vanishes due to the linear dependence on m_i . Of course, an expansion to order δ_B^2 would return the position dependence as terms of m_i^2 would appear. Checking for linear or quadratic dependence of the fluorescence rate on the position/magnetic field would inform us as to if the extended-two level atom is a fair model for our experiment (hint: it is not, see below Section 6.3.1).

6.1.1 Fluorescence Oscillations

In any case, the magnetic field dependence of the excited state population is clear from Equation 6.3. As noted above, in a MOT, this dependence is weak and unlikely to be detectable in our MOT without much improved efficiency in photon collection. However, introducing oscillations, as done by accident above, should clearly reveal the dependence on the magnetic field. In one dimension again, an oscillation in the magnetic field of the MOT can be written as

$$\vec{B}(z, t) = -B'_z(1 + \epsilon \cos(2\pi ft))z \quad (6.4)$$

where ϵ is typically a small value, $\epsilon \lesssim 0.15$. To examine this analytically, we will turn to the V-atom model in Section 2.4 which had steady state populations⁷ given by Equations A.1, A.2, and A.3. With the magnetic field as defined above, the

⁷While it is true that the magnetic field is changing in time, steady state populations can still be used as the timescale for the internal evolution of the atom to the steady state is very different than the magnetic field oscillation period. The internal atomic dynamics timescale on the order of $1/\Gamma = 27$ ns [48] while the timescale for the field oscillations is on the order of 100 μ s or longer (frequencies for driving oscillations in the experiment are typically on the order of 100 Hz to 1 kHz). With the much longer time scale for the magnetic field, the atom basically sees a constant field

magnetic field detuning frequency (scaled by atomic decay rate) is

$$\delta_B(t) = \frac{\mu_B}{\hbar\Gamma} B'_z z [1 + \epsilon \cos(2\pi ft)] \quad (6.5)$$

(see the derivation of Equation 2.59). Here, we have imposed $|m_{\pm}| = 1$ and positive or negative shifts in frequency for the different excited state levels are written as $\delta_{\pm}(t) = \delta_L \pm \delta_B(t)$. With this, the fluorescence is (by expansion around small ϵ)

$$F \approx \langle Fl \rangle + dF \cos(2\pi ft), \quad (6.6)$$

with

$$\langle Fl \rangle = \Gamma \left(\rho_{+,+}^{ss} \Big|_{\epsilon=0} + \rho_{-,-}^{ss} \Big|_{\epsilon=0} \right) \text{ and} \quad (6.7)$$

$$dF = \left(\frac{\partial \rho_{+,+}^{ss}}{\partial \delta_B} \Big|_{\epsilon=0} + \frac{\partial \rho_{-,-}^{ss}}{\partial \delta_B} \Big|_{\epsilon=0} \right) \frac{\mu_B B'_z z \epsilon}{\hbar}. \quad (6.8)$$

Thus, the fluorescence oscillates with the same frequency and (unwritten) phase as the magnetic field, around an average value that matches the non-oscillating field value, and with an amplitude that is proportional to both position/magnetic field and the driving frequency. While the values for m_{\pm} have been suppressed here, it is clear from the form of δ_B that the linearity of dF with respect to ϵ requires linearity with respect to m_{\pm} . Then, when experimentally measuring values for dF , linear scaling with respect to ϵ will rule out the extended two-level atom model as noted above.

while evolving to steady state and we can assume the atom is always in its steady state value for the magnetic field at time t .

It is not particularly enlightening, but the derivatives of the excited state populations for the V-atom are given by

$$\begin{aligned}\frac{\partial \rho_{--}^{ss}}{\partial \delta_B} &= \frac{1}{N} \left[\rho'_{--} - \rho_{--}^{ss} \frac{\partial N}{\partial \delta_B} \right] \\ \frac{\partial \rho_{++}^{ss}}{\partial \delta_B} &= \frac{1}{N} \left[\rho'_{++} - \rho_{++}^{ss} \frac{\partial N}{\partial \delta_B} \right],\end{aligned}\tag{6.9}$$

with

$$\begin{aligned}\rho'_{--} &= \frac{s(1-w)}{2} \{16s(2\delta_{B,0} + \delta_L) + 64\delta_{B,0} [1 + 4\delta_{B,0}^2] + 32\delta_L [1 + 4\delta_{B,0}(3\delta_{B,0} + \delta_L)]\} \\ \rho'_{++} &= \frac{s(1+w)}{2} \{16s(2\delta_{B,0} - \delta_L) + 64\delta_{B,0} [1 + 4\delta_{B,0}^2] - 32\delta_L [1 + 4\delta_{B,0}(3\delta_{B,0} - \delta_L)]\} \\ \frac{\partial N}{\partial \delta_B} &= 8\delta_{B,0} (2 + s + 8\delta_{B,0}^2) [4 + 5s + 16\delta_{B,0}^2] - 24sw\delta_L [2 + s + 24\delta_{B,0}^2] + \\ &\quad 128\delta_L^2\delta_{B,0} [s - 16\delta_{B,0}^2] - 64\delta_L^3 [sw - 8\delta_L\delta_{B,0}]\end{aligned}$$

where $\delta_{B,0}$ is the scaled magnetic field detuning (Equation 6.5) with $\epsilon = 0$. In these equations, the two Rabi frequencies have been written in terms of beam imbalance ratio w (as defined in Equation 3.1), saturation parameter s as defined in Equation 2.38, and here s is calculated with the average power of the two beams). In these forms, the (decay rate scaled) Rabi frequencies are

$$\left| \tilde{\Omega}_{\pm} \right|^2 = \frac{s}{2} (1 \pm w),\tag{6.10}$$

which simplify the form of the steady state equations greatly.

There is another piece to note briefly here. The magnetic field underlies the mechanism that traps atoms in the MOT through a harmonic restoring force described in detail in Section 2.5.1. The restoring force strength κ , as shown in Equation 2.84, is proportional to the magnetic field gradient. Modulating the field gradient through

the current in the anti-Helmholtz coils then also modulates the value for κ . In doing so, it is possible to excite an additional resonance in the atomic motion, called a parametric resonance [131]. With a well damped atom, (i.e. large damping constant β), a small oscillation parameter ϵ , and driving the oscillations far from resonance (or rather far from twice the resonant frequency, see Appendix F), the influence of the field oscillations on the atomic motion is negligible and our theoretical framework is still valid. These resonances are discussed in much more detail in Section 6.5.

6.1.2 Position Averaging

The form of the equation for the fluorescence oscillation amplitude dF shows a dependence on position that is difficult to get at experimentally. Instead, it may be beneficial to look at spatially averaged values for this amplitude based on the temperature and potential energy seen by the atom. Following the damped harmonic oscillator formalism of Section 2.5.2, this potential will be

$$U(z) = \frac{1}{2}\kappa z^2, \quad (6.11)$$

where κ is the restoring force, given for the V-atom by Equation 2.84.

From this equation, it is clear that modulating the trapping strength will oscillate the potential energy of the atom. In doing so, it is possible to heat the atom and thus expand grow the position distribution for the atom [39]. At high frequencies (relative to a characteristic frequency $f_c = \kappa/2\pi\beta$, where β is the damping coefficient for that atomic motion), the oscillations are too fast for the atom to respond and it experiences the average non-modulated trap. At low frequencies, the particle's position variance grows by a factor of $(1 - \epsilon^2)^{-1/2}$ above its non-modulated value. The characteristic

frequency, with the form of the trapping strength of Equation 2.83 is

$$f_c = \frac{\mu_B g_F B'_z}{2\pi \hbar k},$$

where the only experimentally controlled value is the MOT magnetic field gradient B'_z . For our large field MOTs this frequency is on the order of tens of kHz. Experiments are typically modulated at frequencies of hundreds of Hz to a few kHz, putting the experiment deep into the low frequency range. Here, the modulation is slow enough to impact the motion of the atom and increase its positional variance. However, with small oscillation amplitudes, the growth is only on the order of a few percent of the non-oscillatory variance, which should not affect our calculations seriously.

In this “small” frequency limit, and defining an effective temperature value T' as just the variance of the position distribution as via the equipartition theorem, the average value for the fluorescence oscillation amplitude for the atom is

$$\langle dF \rangle = \sqrt{\frac{\kappa}{2\pi k_B T}} \int dF(z) \exp\left[-\frac{\kappa z^2}{2k_B T'}\right] dz. \quad (6.12)$$

Compared to the “true” temperature of the atom, the effective temperature is $T' = T/\sqrt{1 + \epsilon^2}$, just a few percent higher than the “true” temperature. This small difference will be ignored in the remainder of the calculations in this chapter. The form of $dF(z)$ in Equation 6.8 appears to be an odd function with respect to z (so that the average is just zero), but the derivatives of the excited state populations are also spatially dependent through the oscillation-free Zeeman detuning, $\delta_{B,0}$.

Looking ahead to extracting this oscillation from experimental data, the RMS oscillation amplitude is

$$dF_{RMS} = \left[\sqrt{\frac{\kappa}{2\pi k_B T'}} \int dF^2(z) \exp \left[-\frac{\kappa z^2}{2k_B T'} \right] dz \right]^{1/2}, \quad (6.13)$$

or, more generally,

$$dF_{RMS} = \left(A \int dF^2(z) \exp \left[-\frac{U(z)}{k_B T'} \right] dz \right)^{1/2}, \quad (6.14)$$

where A is some constant to normalize the position distribution. With the form of $dF(z)$ for the V-atom, both dF_{RMS} and $\langle dF \rangle$ should be proportional to $B'_z \epsilon$, the amplitude of the field oscillation.

Again, looking ahead to the measurement, rewriting the fluorescence of the atom as

$$F = \langle Fl \rangle [1 + m \cos(2\pi ft)], \quad (6.15)$$

then the dimensionless amplitude for the fluorescence oscillation can be calculated as either

$$\langle m \rangle = \frac{\langle dF \rangle}{\langle Fl \rangle} = \frac{A}{\langle Fl \rangle} \int dF(z) \exp \left[-\frac{U(z)}{k_B T'} \right] dz \text{ or} \quad (6.16)$$

$$m_{RMS} = \frac{dF_{RMS}}{\langle Fl \rangle} = \frac{A^{1/2}}{\langle Fl \rangle} \left[\int dF^2(z) \exp \left[-\frac{U(z)}{k_B T'} \right] dz \right]^{1/2}. \quad (6.17)$$

The dimensionless form for the fluorescence amplitude has at least two benefits. First, it is easily comparable to the similar dimensionless amplitude for the driving oscillations in the anti-Helmholtz coils, ϵ . Second, when comparing to experimental results, photon collection efficiency factors vanish. Rather than fitting data to

an exact number of photons per second for the oscillation amplitude, which is complicated by the unknown factor limiting collection efficiency (see Section 3.4.1), the fit is relative to the average count rate, which has the same unknown efficiency factor. The two collection factors multiply both photon rates (average and oscillation amplitude) and thus cancel in the final calculation.

6.1.3 Numeric Calculations

The RMS form of the dimensionless fluorescence amplitude, m , is written in a generic form so that any potential energy can be used, including for a three dimensional system with $z \rightarrow \vec{r}$ and $dz \rightarrow dV$. In the case of the one-dimensional V-atom, there is analytic form for the potential and for $dF(z)$ as described above, although it is (likely) there is no analytic form for the integral.

For the full rubidium atom calculation found discuss in Chapter V, there is no analytic form for the potential, but it is possible to numerically find a solution for a given temperature. The potential energy is found as done in Section 5.5—integrating the irrotational component of force (in one dimension, the entire force is irrotational) and the force is found as described in Section 5.3.3.

For $dF(z)$ (or $dF(\vec{r})$ if in three dimensions), there is also no closed form solution as there is for the the V-atom; rather, this can be done by assuming the fluorescence oscillates at a constant frequency and finding the amplitude from the difference in its extreme values, i.e. taking half the difference in the average fluorescence from when the magnetic field has its largest value ($B(z) = (1 + \epsilon)B'_z z$) and its smallest value ($B(z) = (1 - \epsilon)B'_z z$) :

$$dF_{Rb}(z) = \frac{Fl_{+\epsilon}(z) - Fl_{-\epsilon}(z)}{2}. \quad (6.18)$$

This is exactly equivalent to taking a numeric derivative of the fluorescence rate with respect to ϵ . In deriving Equation 6.6, the general form for the small ϵ expansion is

$$F(z) \approx F(z)|_{\epsilon=0} + \epsilon \left. \frac{dF(z)}{d\epsilon} \right|_{\epsilon=0}.$$

Ignoring the cosine term (remember that the atom is assumed to be in steady state at all times, so the cosine is effectively a constant and only its extremes are of interest for finding the amplitude), comparing to Equation 6.6 dF must be

$$dF = \epsilon \left. \frac{dF(z)}{d\epsilon} \right|_{\epsilon=0} = \epsilon \left(\frac{Fl_{+\epsilon}(z) - Fl_{-\epsilon}(z)}{2\epsilon} \right),$$

where the derivative is written numerically to first order in ϵ . This simplifies to exactly the form of dF_{Rb} in Equation 6.18.

The average fluorescence rate is found numerically exactly as in Equation 6.1—summing the steady state excited state populations and weighting by the atomic decay rate Γ .

These three numeric calculations for the potential (U_i), fluorescence rate ($\langle F \rangle_i$) and fluorescence oscillation amplitude (dF_i) can be done for all one dimensional positions z_i or for a multidimensional grid. Then, the two averages for the fluorescence

oscillation amplitude of Equations 6.16 and 6.17 are calculated as

$$\langle m \rangle(T) = \frac{\frac{1}{A} \sum_i \exp[-U_i/k_B T] dF_i \Delta z}{\frac{1}{A} \sum_i \exp[-U_i/k_B T] \langle Fl \rangle_i \Delta z} \quad (6.19)$$

$$m_{RMS}(T) = \frac{\sqrt{\frac{1}{A} \sum_i \exp[-U_i/k_B T] dF_i^2 \Delta z}}{\frac{1}{A} \sum_i \exp[-U_i/k_B T] \langle Fl \rangle_i \Delta z} \quad (6.20)$$

where Δz is the spacing of points in the numeric calculation and A is a factor to normalize the potential, $A = \sum_i \exp[-U_i/k_B T] \Delta z$. These equations are written fully, without simplification, because while it seems trivial to simplify factors of A and Δz , it is not always so clear while coding (lol!). In multiple dimensions, a similar form can be used most easily where the label i refers to points in a multi-dimensional grid, Δz factors are dropped, and A is recalculated appropriately (also without the spacing factor Δz).

Experimental measurements of either average, m_{RMS} or $\langle m \rangle$, can then be used to fit a temperature for an atom to these expressions, with an appropriate model to calculate U_i , dF_i^2 , and $\langle Fl \rangle_i$.

6.2 Analysis of Photon Arrivals

Extracting oscillation information can be done particularly well by looking at the spectrum of photon arrivals. The spectrum can be numerically calculated directly from the record of photon arrivals by an autocorrelation measurement of the photon arrivals as per the Wiener-Khinchin theorem [42]. It is numerically simpler to bin photon arrival data (creating a list of photon counts per timer) and calculate a power

spectrum directly with a fourier transform as is

$$S(f) = \frac{|\tilde{f}(f)|^2}{T_{max}}, \quad (6.21)$$

where $\tilde{f}(f)$ is the Fourier transform of the binned photon time data [48]. This is implemented, for this dissertation, via Octave to do the Fourier transforming. The Octave implementation returns both positive and negative frequency components of the spectrum, but in a non-intuitive order common in numeric Fourier transform algorithms. The code snippet below takes in photon count times in the array `data` and produces an appropriate power spectrum with the array indices ordered from most negative frequency to largest frequency for natural graphing of the power spectrum.

```
Spec=fftshift(fft(ifftshift(data))) * dt;
PowSpec=real(spec.*conj(Spec))./tMax;
```

In this code snippet, `dt` is the for one photon bin and `tMax` is the maximum time for the data. This clearly indicates two times must be defined. The first is a time to bin photon counts, Δt (`dt` in the code snippet). This sets a time step and gives a maximum frequency that will be calculated in the spectrum as $f_{max} = 1/2\Delta t$. Selecting a shorter bin time allows for higher frequencies to be revealed in the spectrum, but produces larger data sets to analyze impacting calculation time. Second is the maximum time to collect data, T_{max} (`tMax` in the code snippet). This gives a frequency spacing for the spectrum as $\Delta f = 1/2T_{max}$. Selecting a longer maximum time gives a higher resolution spectrum, but limits the number of spectra that can be calculated and averaged together to reduce noise.

In Figure 6.1a, one data run with 100 ms binned photon data (the binning time used to trigger the bayesian algorithm while collecting data) is shown. In Figure

6.1b, spectra for a few different maximum times are shown. In Figure 6.1c, spectra with a few different maximum frequencies (and thus different bin times) are shown for this same data. Figure 6.1d, the photon oscillation amplitudes for the spectra in (b) and (c) are shown, calculated using the method described below (Equation 6.28). In graphs (b-d) here, the spectra and oscillation amplitudes were calculated from the photon arrival time collected from the data run in (a).

In practice, the bin time is chosen to give maximum frequencies of 25 kHz to sample multiple harmonics (see Section 6.6) of the typical few kHz driving frequencies. With useable data collection times of around 90 s per experiment, maximum times for a spectra are typically around a 5 or 6 seconds to allow for many spectra to be averaged for a single photon's experimental lifetime.

6.2.1 Oscillation Calculation

From the spectra, information about the average fluorescence, amplitude of the oscillation and phase can be extracted. The measured fluorescence is assumed to be Poissonian distributed⁸. Defining the background average photon rate to be B and the atomic fluorescence rate to oscillate with frequency f_α

$$\alpha(t) = \alpha_0 [1 + m_\alpha \cos(2\pi f_\alpha t)], \quad (6.22)$$

so that the Poissonian sampled fluorescence signal is $Fl_m(t) = B + \alpha(t)$. As noted in Appendix E, the average rate of photon collections, $\langle Fl_m \rangle = B + \alpha_0$, (Equation E.2),

⁸As revealed in Figure 4.3, the fluorescence measured from the experiment is super-poissonian. The calculation in Appendix E there assumes a gaussian distribution a variance larger than the mean. The calculation there shows that even with the variance many times larger, there is little change in the power spectrum.

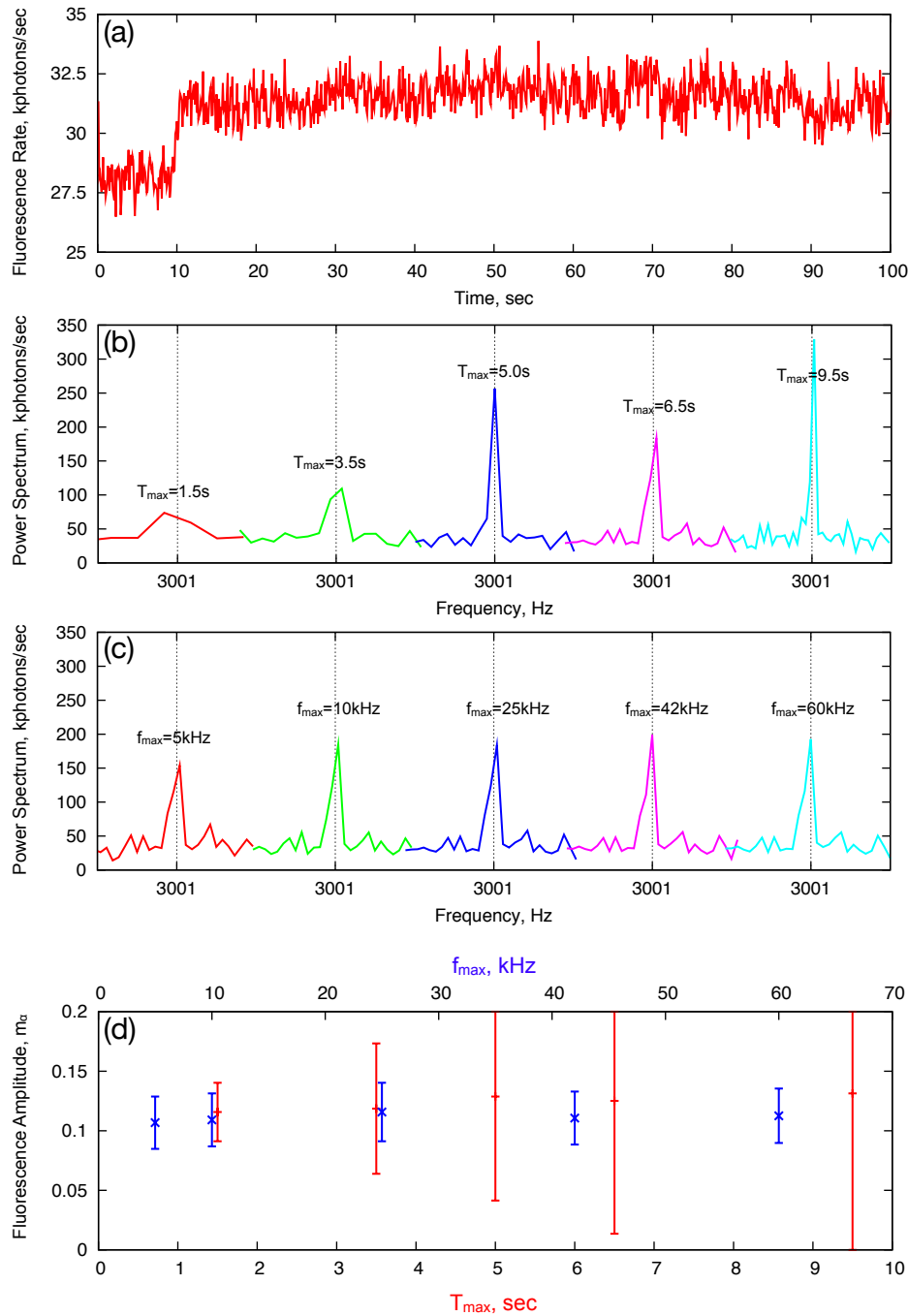


FIGURE 6.1. Sampled oscillation spectrum. (a) Fluorescence rate as a function of time. An atom appears in the MOT around 10seconds. (b) Averaged single atom spectra for a variety of maximum times. (c) Averaged single atom spectra for a variety of one photon bin times (or maximum spectrum frequencies). In both b and c, only ± 2 Hz is shown around the driving frequency, 3001 Hz. (d) Average values for unit-less oscillation amplitude m_α calculated from the spectra in (b) and (c). For this data run, the anti-Helmholtz current modulation amplitude was 0.058.

can be found from the tails of the power spectrum as

$$S(f \rightarrow \infty) = \langle Fl_m \rangle. \quad (6.23)$$

This appears clearly in the spectra shown in Figure 6.1(b) and (c), which all have similar backgrounds to the peak near 3001 Hz. When this is done numerically, an average of a power spectrum's tail is used rather than just the spectrum value for f_{max} . The average rate can also be gotten directly from the photon arrival data without needing to take a spectrum. With n_i photons in each time bin, the average rate is

$$\langle Fl_m \rangle = \frac{1}{T_{max}} \sum_i n_i. \quad (6.24)$$

This, of course, is the total background rather than just the single atom fluorescence rate. To get the single atom fluorescence rate, the background fluorescence rate just needs to be known. As was noted in the single-atom detection method Section 4.1, our experimental runs always begin with a few seconds with blue detuned laser frequencies so that no atoms can load into the MOT. Thus, we have a built in measurement of the no-atom fluorescence, B . Then the single atom fluorescence rate is $\alpha_0 = \langle Fl_m \rangle - B$. This rate can be measured entirely without a spectrum and is necessary for the Bayesian algorithm in Chapter IV.

For the oscillation amplitude, as calculated in E and in [132], there should be a peak in the power spectrum, calculated over a maximum time T_{max} , whose amplitude is

$$S(f_\alpha) = \langle Fl_m \rangle + \frac{\alpha_0^2 T_{max}}{4} m_\alpha^2 + \eta \frac{\alpha_0^2 m_\alpha^2}{4 \langle Fl \rangle}, \quad (E.12)$$

where η is defined in Equation E.3, a parameter that describes how much larger the standard deviation of the fluorescence is compared to the average fluorescence (i.e.

how close to Poissonian the signal is). The dependence of the peak height on T_{max} is revealed in the spectra in Figure 6.1b, with a few qualifications. First, the spacing of the spectral points changes with T_{max} . With wider spacing, the peak gets spread out which over emphasizes the peak height visually. Second, with T_{max} being integer seconds, there are spectral points that align exactly with integer frequencies, as such as the peak at $T_{max} = 5$ s in the figure. This peak appears higher than the peak at $T_{max} = 6.5$ s because the peak is shifted over a bit and widened to align with the spectral points. This lowers the peak heights when the maximum time is not an integer. The lowering is compensated for by the integration method described below for calculating the peak height (see Equation 6.26) and does not have an impact the calculation of the oscillation amplitude as shown in Figure 6.1d.

Assuming a perfectly Poissonian distribution or ($\eta = 0$), as noted in Appendix E, when there is a large background fluorescence ($\langle Fl_m \rangle \gg \eta$), the amplitude of the oscillation is then

$$m_\alpha = \frac{2}{\langle Fl_m \rangle - B} \sqrt{\frac{S(f_\alpha) - \langle Fl_m \rangle}{T_{max}}}. \quad (6.25)$$

In this form, all values are directly measurable. The peak height, or as we'll see the area under the peak height, is $S(f_\alpha)$. The background fluorescence rate, B , is measured from the data run before any atoms were loaded into the trap. The measured, experimental fluorescence rate, $\langle Fl_m \rangle$, can either come from the tails of the spectrum (as noted in Appendix E) or just from the raw photon arrival data (Equation 6.24).

The power spectral height of Equation E.12 assumed that we had $f = f_\alpha$, the externally driven magnetic field frequency. This is an implicit delta function in the general spectrum, however the experimental data are certainly not a delta function, see Figures 6.1b and c. Instead, due to the numeric calculation, the delta

function is spread over many frequencies. To get the original peak height back, we can numerically integrate over the peak. This produces

$$S(f_\alpha) = \int S(f)\delta(f - f_\alpha)df \approx \sum_{k=-N}^{k=N} S(f_\alpha + k\Delta f)\Delta f, \quad (6.26)$$

where the value N is a defined window size to integrate over, typically done so that the window around the peak is ± 1 Hz, i.e. $N = 1/\Delta f$. In this numeric language then, directly from the power spectrum it is possible to calculate the square of the fluorescence modulation amplitude as

$$dF_m^2 = \alpha_0^2 m_\alpha^2 = \frac{4}{T_{max} dt^2} \sum_{k=-N}^{k=N} [S(f_\alpha + k\Delta f) - S(f = \infty)]. \quad (6.27)$$

Note that a factor of Δf has been lost here in order to return the integrated area of Equation 6.26 to a delta-function peak height. There is an additional factor of $1/dt^2$ present in this equation. The spectrum is calculated from data are in raw photon count numbers, so that the amplitude measured is in terms of just photon number². The factor is to return the amplitude to units of photons/s. This is done to compare directly to the atomic fluorescence rate defined in Equations 6.1, which is given in terms of the atomic decay rate Γ . Additionally, rescaling amplitudes to photons/s gives a systematic unit for comparison between analysis with different values of dt (the blue data in Figure 6.1d). Because the value for dF_m^2 can be pulled directly out of the experimental data, this implies that the RMS form of the analytic fluorescence amplitude (m_{RMS} of Equation 6.20) should be used to for calculating the temperature of the atom. For this comparison, the measured dimensionless oscillation amplitude is then

$$m_\alpha = \frac{\sqrt{dF_m^2}}{\alpha_0} = \frac{\sqrt{dF_m^2}}{\langle Fl_m \rangle - B} \quad (6.28)$$

where again α_0 is the average fluorescence rate from the atom (which can/must be found separately as noted above).

The phase for the fluorescence oscillation comes directly from the spectra as well. Take, for example, the cosine function with frequency f_0 and phase ϕ . The Fourier transform is

$$\tilde{f}(f) = \frac{1}{2} [e^{-i\phi}\delta(f + f_0) + e^{+i\phi}\delta(f - f_0)] \quad (6.29)$$

Taking the tangent of the real and imaginary parts of this wave gives

$$\tan\left(\frac{\text{Im}[\tilde{f}]}{\text{Re}[\tilde{f}]}\right) = \frac{\sin\phi[-\delta(f + f_0) + \delta(f - f_0)]}{\cos\phi[\delta(f + f_0) + \delta(f - f_0)]} = \tan\phi \quad (6.30)$$

when evaluated at $f = f_0$. Then, if the complex Fourier transform of an oscillating time signal is written as

$$\tilde{f}(f) = |\tilde{f}(f)| e^{i\phi}, \quad (6.31)$$

the phase ϕ corresponds to the phase of the underlying oscillation and can be found just by taking the inverse tangent of the real and imaginary parts of the transformed function. Doing this numerically with the binned photon data returns the appropriate phase, offset by factors of π that are related to the total time and spacing between bins.

As noted above, choosing shorter segments of time to create power spectra from limits the resolution of the spectra, but it allows for more averaging of data for a clearer signal. This averaging is particularly important in light of Equations 6.25 and 6.27 as the background fluorescence is subtracted. For individual data runs, particularly those with small MOT coil current amplitudes, ϵ , small peaks in a spectrum or a noisy background and produce negative values for dF^2 and thus imaginary amplitudes for the fluorescence oscillation, m_α . This is resolved by taking

just the real part of the calculated dF^2 and averaging it over many spectra before calculating the fluorescence amplitude. The averages are calculated as below.

1. Photon arrival times are recorded with the FGPA system described in Section 3.4.2.
2. Using the bayesian algorithm to predict times when a single atom was in the MOT (see Section 4.2), photons collected during these times are counted in bins of time length Δt , as above. The size of the bin is determined by the maximum desired frequency of the spectrum.
3. For a defined maximum collection time, T_{max} , the appropriate number of bins ($N_{bin} = T_{max}/\Delta t$) are spliced out of the data.
4. The spliced data are used to calculate a spectrum. Total background fluorescence $\langle Fl_m \rangle$ (Equations 6.24 or 6.23), the square of the fluorescence oscillation amplitude dF_m^2 (Equation 6.27) and oscillation phase ϕ (Equation 6.30) are calculated from the spectrum, or photon counts, for a number of harmonics of the known driving frequency of the MOT coils.
5. Splicing and calculations are done with consecutive numbers of bins until remaining number of bins is smaller than N_{bin} .
6. Average spectra, fluorescence background and square of the fluorescence oscillation amplitudes together. Note that averaging the square of the fluorescence oscillation amplitude and taking a square root calculates exactly the RMS of the fluorescence oscillation amplitude.

Together with a measurement of the non-atom background, B , from each data run, the three measured averaged values for $\overline{dF_m^2}$, $\overline{\langle Fl_m \rangle}$ and \overline{B} calculate the

dimensionless oscillation amplitude of Equation 6.28. When these three measured values have error σ_{dF} , σ_{Fl} , and σ_B , respectively, the error in the calculated oscillation amplitude σ_m is

$$\sigma_m^2 = \frac{\sigma_{dF}^2}{4 \left(\langle Fl_m \rangle - \bar{B} \right)^2 \overline{dF_m^2}} + \frac{\overline{dF_m^2} (\sigma_{Fl}^2 + \sigma_B^2)}{\left(\langle Fl_m \rangle - \bar{B} \right)^4}. \quad (6.32)$$

This can be done for individual data runs and thus specific atoms, as was done for the data in Figure 6.1. With a particular MOT model, these data can be fit to Equation 6.17 or Equation 6.20 to find a temperature of the atom while it is still in the MOT, as is done in other atomic temperature measurements [133]. The individual atom, then, can be used for other experiments.

It is also possible to average the spectra and amplitudes for many data runs together with specific MOT system parameters. This does produce an approximate atomic temperature for an atom in the MOT with those system parameters, rather than an in-situ measure of the temperature of a specific atom. However, as is done with the other temperature measurements discussed in Chapter I, it is assumed that atomic temperatures are primarily a function of the MOT system parameters.

6.3 Measurements

Fluorescence measurements were previewed briefly in Figure 6.1, which showed the fluorescence peak in a spectrum measured from a single atom. Some complete spectra are shown in Figure 6.2 for a variety of driving frequencies, but all with a driving anti-Helmholtz current modulation amplitude of $\epsilon = 0.025$. Some clear features can be noted about these spectra that are universal to single-atom fluorescence spectra measured in our experiments. The tail of the low-frequency peak

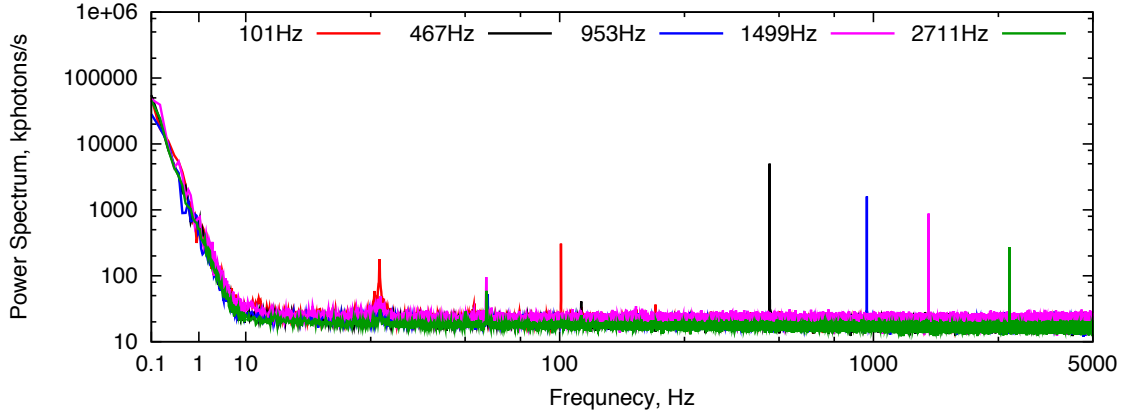


FIGURE 6.2. Assorted measured spectra. Single-atom fluorescence spectra with a variety of driving frequencies. All spectra done with a driving current amplitude of $\epsilon = 0.025$.

scales as $1/f^2$, which is not surprising. There is a wide peak in the spectra around 27 Hz. This peak originates from an unknown magnetic field oscillation that appears ubiquitous in the building around the lab. It can be seen even on simple loops of wire connected to a spectrum analyzer. The frequency is not fixed, but drifts slightly causing the widened peak in the spectrum. There are peaks at 60 Hz because of course there are. As calculated in Appendix E, the spectral tails equal the average measured fluorescence rate. Finally, although the current modulation amplitude is the same for all the peaks in Figure 6.2, the peak heights, and thus the fluorescence oscillation magnitudes, change with frequency. This fact is analyzed in more detail in Section 6.3.2 below.

To check the developed temperature measurement technique, comparisons to known methods should be done. Figure 6.3 shows temperature measurements for a single atom in our high gradient MOT with the release-recapture method described in Section 1.4 [4, 16]. In the figure, two sets of data and three simulations with different atomic temperatures is shown. The red data are done with the magnetic field turned

off with the MOT lasers, while the blue data leaves the magnetic field on during the test. At short times (below about 6 ms) the recapture rate is quite similar in both cases. This is due to slow ramp down of the anti-Helmholtz coil current while turning off the field.⁹ The field persists during this time and magnetically traps the atom (see Section 2.3.1). At long times, the two cases diverge as the field is no longer trapping atoms. With the influence of the magnetic field taken into account, the long-time tail for the recapture rate should be used to estimate the temperature. Thus, the atom is likely around 160 μK , surprisingly above the Doppler temperature. From the data and simulation, it is expected that the atom has temperatures around 160 μK , which should be the “target” for verifying our temperature measure technique. The measurements and simulations in Figure 6.3 may be discussed in more detail in the dissertation of Erickson [134], but serve as a fine comparison for this work.

6.3.1 *The Linearity of Fluorescence Amplitude*

The most pressing measurement is verifying the scaling of the fluorescence oscillation amplitude to the driving current modulation amplitude. As noted in Section 6.1, linear scaling of the fluorescence amplitude would rule out the extended two-level model to describe the atom in the MOT, as this model would predict fluorescence modulation only at higher orders of the current modulation amplitude.

The measured fluorescence amplitude as a function of current oscillation magnitude for two different driving frequencies are shown in Figure 6.4. Red data

⁹This ramp-down is not caused by the RC circuit created by the anti-Helmholtz coil and the filtering capacitor discussed in Section 3.3.5. These have an RC time constant of $\tau=4.6 \mu\text{s}$, much faster than the ramp-down time. This is also much slower than the ramp-down time due to internal capacitors in the current supply, which have capacitance 1.5 μF as programmed for our power supply [100]. This time delay, instead, may be a result of self-inductance in our MOT coils or eddy currents in the various conducting elements around the experiment.

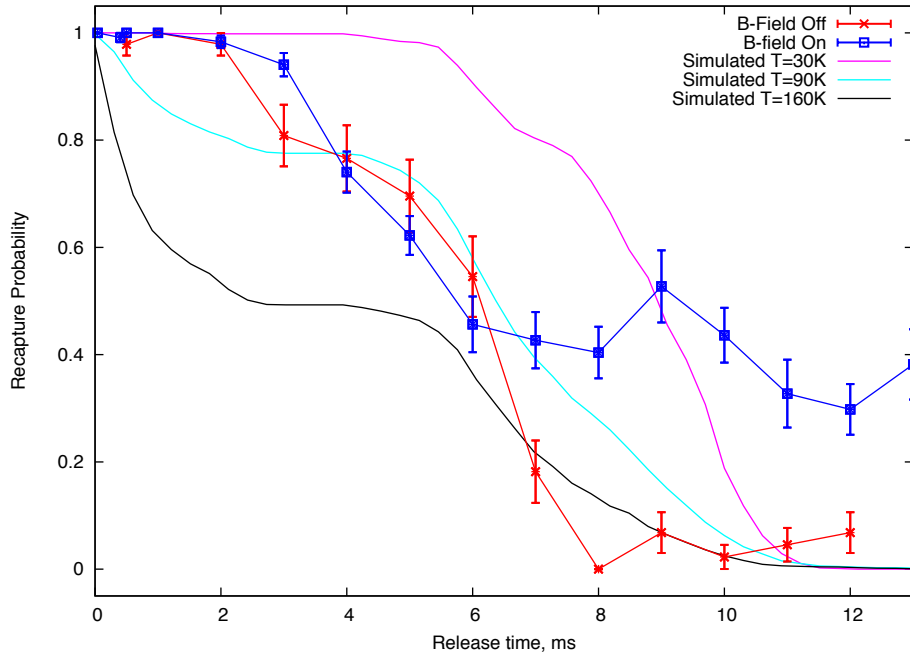


FIGURE 6.3. Single-atom temperatures with release-recapture method. Measured data in red done while ramping down MOT magnetic field on release. Data in blue have the MOT magnetic field left on during the measurements.

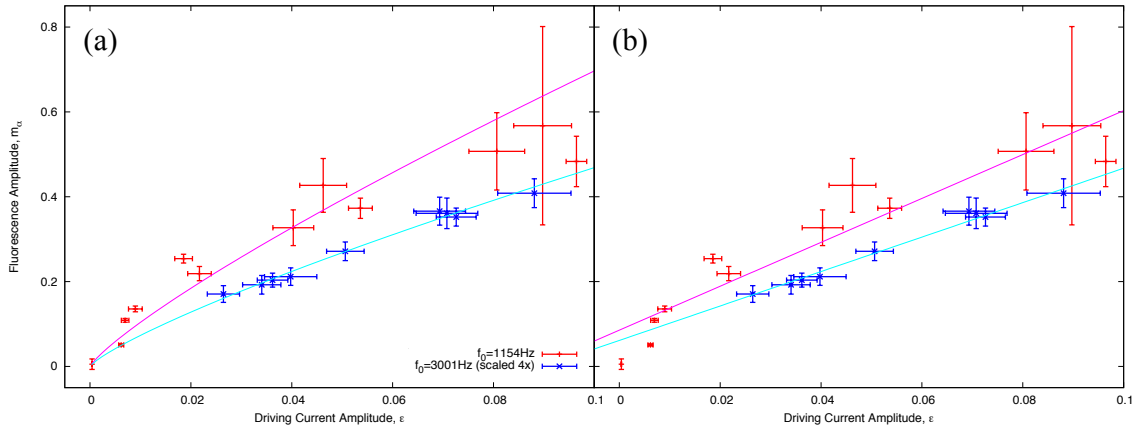


FIGURE 6.4. Fluorescence amplitude scaling with current amplitude. The same data appear in both graphs, but is fit (the curves in each graph) with a power law in (a) and linearly in (b).

are recorded at a frequency of 1154 Hz and the blue data are recorded at a frequency of 3001 Hz. It is important to note that the blue data have been (vertically) scaled by a factor of 4 so that its behavior is clear on the graph. In Figure 6.4a, the lines are power law fits. The low frequency data scales as $m_\alpha \propto \epsilon^{0.82 \pm 0.05}$ and the high frequency data scales as $m_\alpha \propto \epsilon^{0.81 \pm 0.03}$. While not quite linear, the scaling is still far from ϵ^2 . Thus we can rule out the extended two-level atom as a model for our experiment. Linear fits to the data are shown in Figure 6.4. Here, the lower frequency data have a slope of 5.2 ± 0.55 and the higher frequency data have an unscaled slope of 1.0 ± 0.03 .

The large difference in slope (and larger fluorescence amplitude in general) for the two measurements in Figure 6.4 corresponds to the different frequencies of the two data sets. This is analyzed in Section 6.3.2 in more detail, but we'll note here that the higher frequency measurement is a better model to calculate temperature. The lower frequency data can excite mechanical resonances in the atom causing additional motion in the atom, as noted in Section 6.1.1. The higher frequency oscillations avoid these resonances and should reveal the behavior of the atom without influence of the magnetic field oscillations.

Figure 6.5 shows simulated results for the slope of the fluorescence amplitude compared to the magnetic field modulation amplitude for a variety of models. Here, the slope is plotted as a function of atomic temperature following Equation 6.20. In Figure 6.5a, the three lines are all calculations for a 1D MOT for the V-atom, full ^{87}Rb atom, and a $J_g = 1 \rightarrow J_e = 2$ atom (referred to as $J_{1 \rightarrow 2}$ through the rest of this work). The $J_{1 \rightarrow 2}$ atom was used in some of our simulations for comparison to an analytic derivation of the spring constant for this atom in the MOT [92]. The MOT

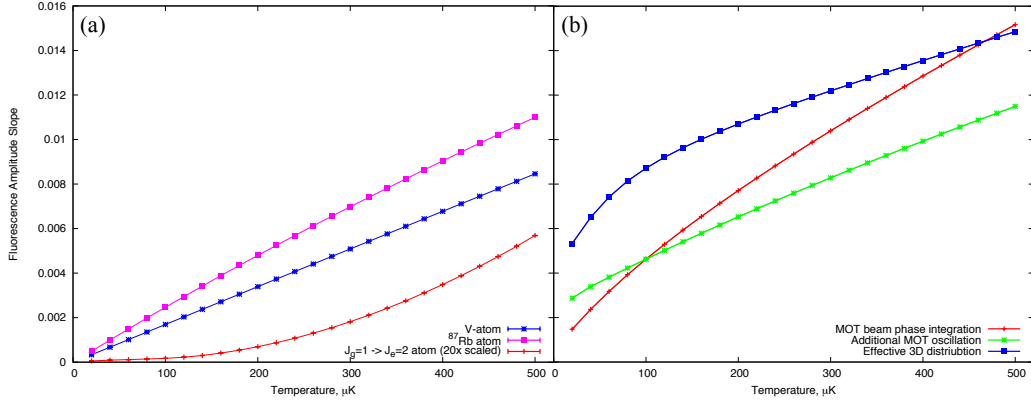


FIGURE 6.5. Simulated 1D modulation slopes. Values are slopes of fluorescence amplitudes to driving current modulation amplitudes (i.e., the slopes of the linear fits in Figure 6.4). The two graphs have the same vertical scale.

spring constant in our simulation does match this analytic form and thus this atom model has been used to examine some results of our simulation.

With the larger total angular momentum of the excited state for the $J_{1 \rightarrow 2}$ atom larger than the V-atom's, the outermost excited state energy level for the $J_{1 \rightarrow 2}$ has a larger Zeeman splitting than that of the V-atom. This would imply the $J_{1 \rightarrow 2}$ atom should have a larger amplitude in the fluorescence modulation, as it is driven by oscillations in the Zeeman shift of the atoms energy levels. However, in calculating the fluorescence amplitude for the V-atom, the simulation added an additional factor of 3 to its excited state Zeeman splitting by changing g_F to $3g_F$. This was to better mimic the behavior of the outmost energy levels of the full ^{87}Rb atom and leads the larger fluorescence amplitude for the V-atom compared to the $J_{1 \rightarrow 2}$ atom in Figure 6.5a.

All three of these 1D simulations clearly show slopes that are significantly less than the slope of order 1 from the data in Figure 6.4. Thus in Figure 6.5b, simulations are of the 3D MOT with the full ^{87}Rb atom as described in Chapter V. For all of

these, as noted in Section 5.5, the calculation is averaged over many phases of the MOT beams. This direct averaging is the red curve in figure (b). While its results are larger than the 1D results, and particularly true for low (reasonable experimental) temperatures, they are still much less than the measured slopes .

Recalling the effective temperature discussed in Section 6.1.2 and with prior knowledge of additional atomic motion as seen in Section 6.5, we can add an additional “forced” modulation of the atom to our calculation. This is done by assuming that the atom’s entire position distribution oscillates around the peak position with amplitude, A . This amplitude is small enough to not change the coupling of light from the atom into the APD detection system (unlike the oscillations observed in Section 6.4). With this “forced” oscillation model, it is assumed that the modulation frequency of the magnetic field is much faster than this oscillation frequency of the atom in the trap. This is generally true for most of our measurements and certainly for the data in Figure 6.4, where the relevant position oscillations are on the order of 100 Hz (see section 6.3.2). With this slow position oscillation, the atom would then see the full modulation of the magnetic field at each position, so that the average fluorescence amplitude (and thus its slope) would just be its value at each position averaged over one period of the atom’s motion. For a fluorescence amplitude that depends on position, $m_\alpha(a)$, then the average rate is

$$\langle m_\alpha \rangle = \int_{-A}^A m_\alpha(a)P(a)da \tag{6.33}$$

where $P(a)$ is the probability to be at position a for an object oscillating with amplitude A :

$$P(a) = \frac{1}{\pi} \sqrt{\frac{1}{A^2 - a^2}}. \tag{6.34}$$

The results of these slow atomic oscillations are shown as the green data of Figure 6.5b.

While the calculations above for the “3D” MOT are only looking at the forces (and thus the potential energy) along one axis, the larger 3D environment can be modeled more directly with an effective 3D distribution. A majority of our calculations, and indeed all of those seen above in this section, have been done along one MOT beam axis. This gives a position distribution along one axis rather than a true 3D distribution. If we assume that the atom’s position distribution is small in the other directions (a fair assumption with a strong confining force due to the high-gradient fields), we can map an effective 3D solution onto our 1D calculation. With a well confined atom (and exactly true for a 1D MOT), the field strength largely dictates the probability to be at each position along an axis. With the 3D mapping, we re-weight the 1D position probabilities by the number of points in the 3D with the same magnetic field magnitude. As points in the 3D move away from the axis, the field magnitude grows and thus the higher magnetic-field tails of the distribution are move heavily weighted. This effectively turns the 1D position distribution into a (local) magnetic field magnitude distribution for the atom. Renormalizing this distribution with its heavier tails should result in a higher fluorescence oscillation as the field oscillation is also higher in the tails. While this seems artificial, it does mimic the behavior of the 3D atom. The atom explores regions off-axis that have a stronger magnetic field and stronger oscillation in the field than points on the axis. This numeric mapping method takes these into account without calculating the (potentially non-conservative) force off-axis. The blue data in Figure 6.5b shows this effective 3D distribution with a off-axis grid size of $15 \mu\text{m}$.

It is still evident that simulations are not matching the measured experimental results. Thus, calculations for approximate MOT temperatures will be dropped from the remaining calculations and functional behavior will be the focus.

6.3.2 Frequency Dependence of Fluorescence Amplitude

As revealed in Figures 6.2 and 6.4, the amplitude of fluorescence oscillations changes with frequency. In Figure 6.6, the amplitude as a function of driving frequency is plotted. Here all the driving currents have modulation amplitude¹⁰ $\epsilon = 0.025$. In this graph, also shown are fits to the low frequency response ($f < 500$) and the high frequency response ($f > 700$). The low frequency signal scales as a power law $f^{0.55 \pm 0.02}$. The high frequency tails scale with a power law as $f^{-1.51 \pm 0.11}$ (or with exponential decay that has decay constant $(8.30 \pm 0.36) \times 10^{-4} \text{ Hz}^{-1}$).

These two power law scalings closely match the scaling of a Lorentzian distribution weighted by $f^{1/2}$. For a particle with a small modulation to its trapping frequency ω_0 , its position variance should have a Lorentzian shape as a function of the driving frequency [39, 135]. Since the fluorescence amplitude depends closely on this position variance (see Section 6.1.2), it is expected that the fluorescence amplitude follows this same shape at high frequencies. As discussed above, for a fast modulation of the fluorescence rate, at all positions the atom sees the whole range of fluorescence rate values so that its fluorescence rate can just be averaged

¹⁰As a practical note, the modulation in anti-Helmholtz coil current was introduced by adding a signal from a function generator to the control signal that went to the coil power supply. Due to both the MOT coil low-pass filtering capacitor and the power supply's own frequency response, a number of amplitudes for the function generator signal have to be tested and the current response in the coils measured with a Hall probe for each frequency. The amplitude of the coil current, A , was calculated by comparisons to the measured current variance σ^2 , which are related by $A^2 = 2\sigma^2$ for a sinusoidal oscillation (Table 6.2 gives the relationship between amplitude and variance for different waveforms). The amplitudes for the function generator signal were adjusted until the measured current amplitude reached the desired value.

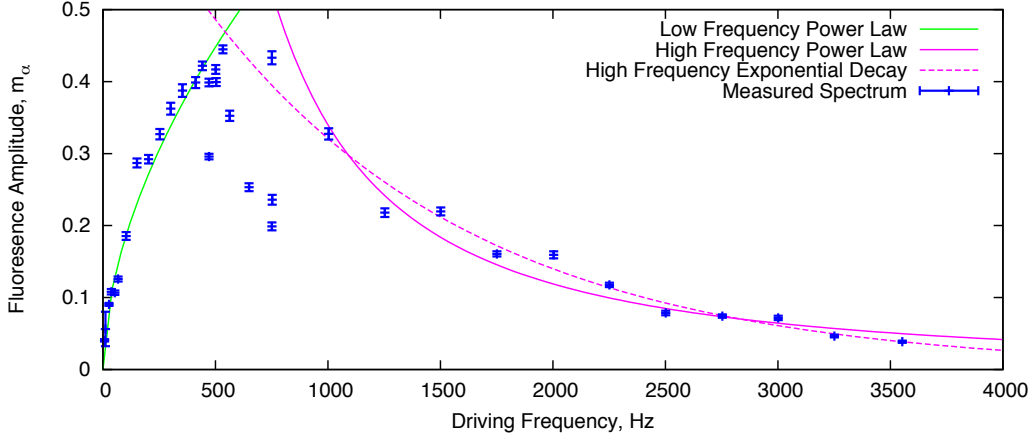


FIGURE 6.6. Fluorescence amplitude spectrum. Along with the data (blue) low-frequency and high-frequency fits to the data are shown.

over positions—producing the same frequency distribution for the fluorescence. At lower frequencies, the spectrum is weighted by $f^{1/2}$. Therefore, the spectrum can then be written as

$$S(f) = \frac{a\sqrt{f}/\pi\Gamma}{(f - 2f_z)^2 + \Gamma^2/4}, \quad (6.35)$$

where Γ is the (Lorentzian) FWHM, a is a scaling factor, and $2f_z$ is the (Lorentzian) peak frequency, which is twice the frequency of the (undamped) atomic motion in the MOT [39, 136]. The atomic motion has frequency $2\pi f_z = \omega_{0,MOT} = \sqrt{\kappa/m}$ where κ is the MOT spring constant.

There is an additional trapping constant associated with magnetic trapping in the MOT. As discussed in Section 2.5.1, the magnetic trapping force is of the form

$$\vec{F}_{mag} = -\kappa_{mag}z\hat{z}, \quad (6.36)$$

with

$$\kappa_{mag} = \frac{\mu_B g_f B'_z}{\hbar k \Gamma} \kappa_{MOT}. \quad (6.37)$$

With this, the magnetic trapping frequency is

$$\omega_{0,mag} = \sqrt{\frac{\mu_B g_F B'_z}{\hbar k}} \omega_{0,MOT}. \quad (6.38)$$

The data shown in the spectrum of Figure 6.6 were recorded with MOT laser detuning $\Delta_L = -4.8$ MHz, magnetic field gradient $B'_z = 215$ G/cm, and laser Rabi frequency $|\Omega| = 0.575\Gamma$, where Γ is the atomic decay rate. With the (laser power balanced) V-atom solutions for κ and β in Equations 2.84 and 2.71, the MOT has a trapping frequency of $f_{0,V-at, MOT} = 1056$ Hz and the magnetic trap has frequency $f_{0,V-at, Mag} = 77$ Hz. It is also good to look at the frequency for the full ^{87}Rb atom calculation, as the spring constant for the full atom had a much stronger trapping force. Using the scaling between the full atom and the V-atom confinement forces from fitting the simulated data in Figure 5.2, the MOT has a trapping frequency of $f_{0,^{87}\text{Rb-MOT}} = 3094$ Hz and the magnetic-trapping frequency is $F_{0,^{87}\text{Rb-Mag}} = 228$ Hz. All of these values, of course, are for the vertical axis of the MOT. In the horizontal direction, the magnetic field and thus the trapping strength, is reduced by half. These, then, give an additional frequencies scaled by $\sqrt{2}$ compared to the z -axis frequencies.

In principle, then, the spectrum of Figure 6.6 could be made of four Lorentzian peaks, all scaled by \sqrt{f} . However, due to the high MOT frequencies, it is more likely that the magnetic trapping results in the peaks shown in Figure 6.6. This gives a spectrum of the form

$$S(f) = a\sqrt{f} \left[\frac{\Gamma_z/2\pi}{(f - 2f_z)^2 + \Gamma_z^2/4} + \frac{\Gamma_{xy}/2\pi}{(f - 2\sqrt{2}f_z)^2 + \Gamma_{xy}^2/4} \right]. \quad (6.39)$$

The two spectrum formulae of Equations 6.35 and 6.39 are plotted along with the fluorescence data in Figure 6.7. The green curve in the figure is a fit to the the single

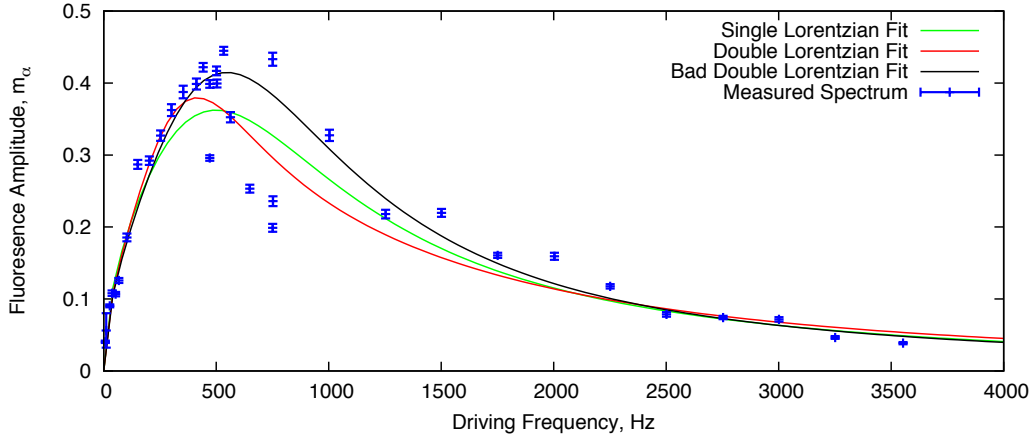


FIGURE 6.7. Lorentzian fluorescence amplitude spectrum. The green curve is a fit to the single Lorentzian spectrum of Equation 6.35 and the red curve is a fit to the double Lorentzian spectrum of Equation 6.39. The black curve is a fit to the double Lorentzian spectrum without the group of 5 “low” values on the interior of the curve, hence its “Bad” labeling.

Lorentzian spectrum of Equation 6.35 with fit values $a = 42 \pm 0.3$, $\Gamma = 1442 \pm 11$, and $f_z = 100 \pm 3$ Hz. The red curve is a fit to the double Lorentzian spectrum of Equation 6.39 with fit values $a = 20 \pm 0.1$, $\Gamma_z = 2608 \pm 68$, $\Gamma_{xy} = 834 \pm 14$, and $f_z = 94 \pm 1$ Hz. The black curve, which should be treated as suspect, is a fit of the double Lorentzian spectrum without the 5 “low” data points in the interior of the spectrum. Without these, the fit parameters are $a = 21 \pm 0.2$, $\Gamma_z = 1153 \pm 88$, $\Gamma_{xy} = 1500 \pm 105$, and $f_z = 143 \pm 5$ Hz. While this is not an appropriate way to analyze data, it does show that the spectrum equation is pretty spot-on to (most of) the data. All of these frequencies are the appropriate order for the magnetic trapping frequency.

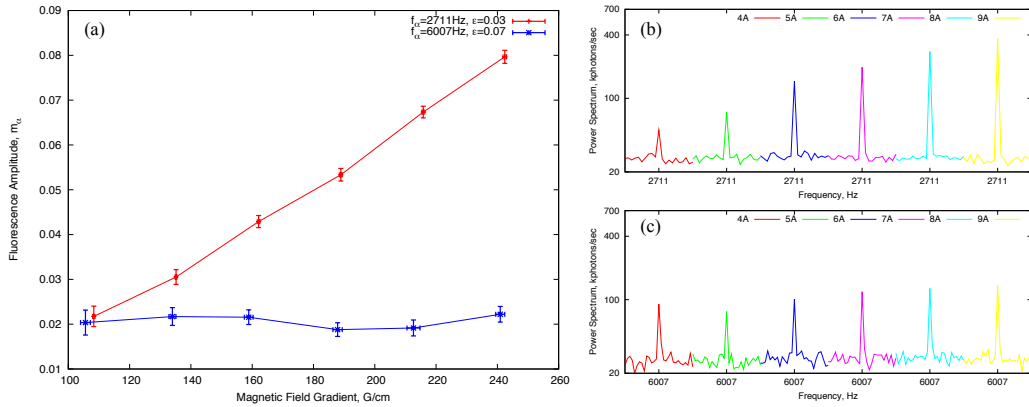


FIGURE 6.8. Fluorescence amplitude scaling with field gradient. (a) Calculated fluorescence amplitudes. (b) Low-frequency (red data) fluorescence spectra. (c) High frequency (blue data) fluorescence spectra. In both spectra (b) and (c), graphs are labeled as their desired anti-Helmholtz currents while horizontal positions in (a) are in terms of measured field gradients.

6.3.3 MOT Size: Trapping Strength

The “size” of the MOT can be scaled by changing the trapping strength, κ for the MOT. This is done easily by changing the anti-Helmholtz coil gradient. This is done for two data runs in Figure 6.8. In Figure 6.8a, two very different relationships are seen. The blue data shows clear independence of the fluorescence amplitude at different DC field gradients. This could be expected as the current amplitude ϵ is constant for all field gradients. With the weaker trapping of the field, the atom may explore further distances from the center of the trap, but the (relative to DC) size of the oscillation is the same everywhere.

The red data in Figure 6.8a show a linear relationship between the gradient and the fluorescence. This could be expected as at every position the total oscillation of the magnetic field magnitude (in Gauss) is larger for the higher field gradient. So

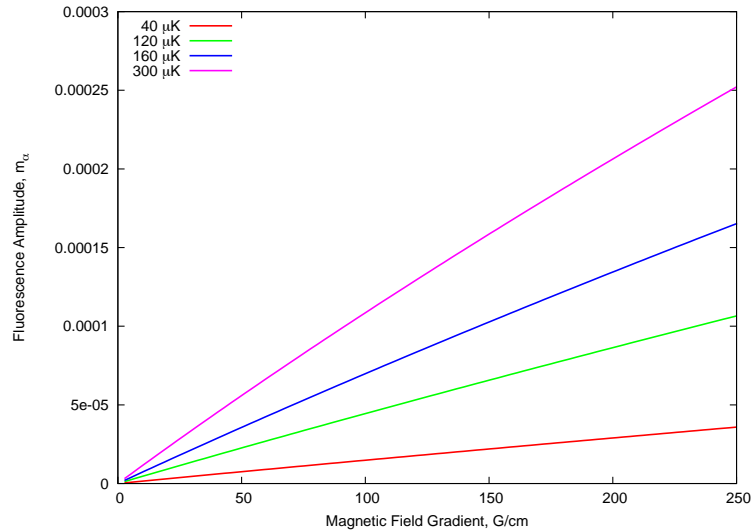


FIGURE 6.9. Simulated fluorescence amplitude scaling with field gradient. They are linear.

even while the atom explores shorter distances from the center of the trap with the higher gradient, the change in magnetic field strength is larger in these regions.

These two different scalings is also reflected directly in the spectra of Figures 6.8b and 6.8c. In Figure 6.8b, the peak heights clearly grow with increasing DC current, while in 6.8c, they are relatively constant. So which is correct? Apparently the linear results. In Figure 6.9, a simulation for the 1D ^{87}Rb atom shows the fluorescence amplitude as a function of the DC anti-Helmholtz current at a variety of temperatures in μK . Clearly the results are linear. The two experiments shown in Figure 6.8 have similar MOT parameters—their only clear difference is the frequency of the oscillations. It is unclear why the two give very different results.

6.3.4 MOT Size: Detuning

It is also possible to scale the size of the MOT through the detuning of the lasers. As can be seen from the “traditional” view of the atomic Zeeman shifts in the MOT of Figure 2.5, there is some distance from the center of the MOT where the Zeeman shifts cause the lasers become blue detuned. From Equation 2.75, this happens at a z -direction “radius”

$$z_{\text{rad}} = \frac{\hbar\Delta_L}{\mu_B g_F m_F B'_z} \quad (6.40)$$

and twice this distance from the MOT center for the x - and y - directions (due to the halved magnetic field gradient in these directions). This blue detuning as a function of position is also responsible for the “turn off” of the enhanced trapping of the atoms with multiple ground states discussed in Section 5.3.3. For our high magnetic field gradient MOT, $B'_z = 215$ G/cm (an anti-Helmholtz current of 8 A to match the data in Figure 6.10) and lasers detuned by $\Delta_L = -\Gamma$ and the outer most excite state for the ^{87}Rb atom ($m_F = \pm 3$), this radius is $48 \mu\text{m}$, which is significantly larger than an atom’s position distribution at MOT temperatures, as seen both in simulations and images of the atom (see the single-atom fluorescence profile in Figure 6.15a, which has standard deviation of around $15 \mu\text{m}$).

This is examined in two ways in Figure 6.10. The red data shows the fluorescence oscillation strength as a function of laser detuning with a fixed magnetic field gradient of 215 G/cm. The blue data show the fluorescence amplitude as a function of detuning with a constant MOT radius as defined in Equation 6.40. Figure 6.10a shows measured experimental data and Figure 6.10b shows simulated results. A few things are noticeable. First, the vertical scale is very different between the two, but that is understandable based on the discussion in Section 6.3.1. Second, while the shape

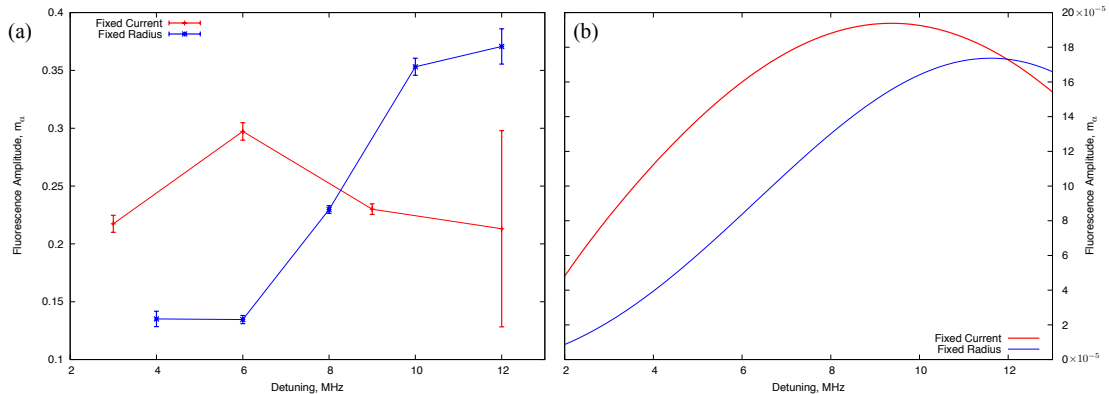


FIGURE 6.10. Fluorescence amplitude as a function of laser detuning. (a) Measured Data and (b) 1D simulated data for ^{87}Rb with a temperature of $190 \mu\text{K}$. Red data in both graphs changes detuning with keeping the anti-Helmholtz current fixed. The blue data in both graphs changes the anti-Helmholtz current along with the detuning to keep the MOT “radius” in the z -direction constant as in Equation 6.40.

of the fixed radius graphs roughly agree, the fixed current graphs are quite different. Third, the strong dependence of the amplitude on the detuning near $\Delta_L = -\Gamma$ could play an important role in noisy signals. Our experiments are done with detunings right around $-\Gamma$. As seen in Equation 3.2, the detuning of the laser light is controlled by the frequency of 3 AOMs. Poor calibration between the experimental control system and the AOM’s output frequency could cause systematic errors in the detuning.

6.3.5 Position Changes: Background Fields

Another clear check on the positional dependence of the fluorescence oscillations can be done by shifting the center of the MOT (defined as where $\vec{B} = 0$) using a background magnetic field. In being shifted away from the center of the anti-Helmholtz coils, the atom should see higher total magnetic field modulations. This agrees with the measured and simulated results of Section 6.3.3 which showed the higher field gradient gave larger fluorescence amplitudes. Here, rather than higher

gradients producing larger total fields for the atom to see, shifting the center of the MOT with a uniform background field puts the atom at locations with a higher field gradient.

Doing this test requires a change to the Bayesian algorithm as described in Section 4.2.7. Rather than triggering the experiment based on measuring a single atom, the experiment must be triggered manually after some set time. Because there is a background field, increasing the magnetic field gradient (to limit loading in the MOT) causes the “center” of the MOT to shift, as discussed in Section 2.5.1. Thus, to collect light from the single atom, the APD must be focused on the location where the atom will appear after the gradient is increased, rather than the location where the atom started (when there were low magnetic field gradients). Without the APD focused on the center of the MOT, an average loading time must be “guessed” to ramp up the magnetic fields and hope that a single atom has arrived in the trap. Normally, a time of 10-20 s works well for just a single atom to load into the MOT. This matches well with the loading rate of 0.006 atoms/100ms used in the Bayesian algorithm (see Section 4.2.4).

In Figure 6.11a, the slope of the fluorescence oscillation amplitude (compared to the current amplitude) is plotted as a function of the DC background magnetic field. This field was applied along the lab x -axis (parallel to the face of the imaging camera). Here, the slope of the fluorescence amplitude was chosen to limit noise that may arise in individual dI settings. The shape of the graph is not too surprising. It is symmetric, which is to be expected as the anti-Helmholtz magnetic field magnitude is symmetric. It is a little surprising that the graph is not centered on $B = 0$, but this can be easily explained as a result of an additional background field and/or an

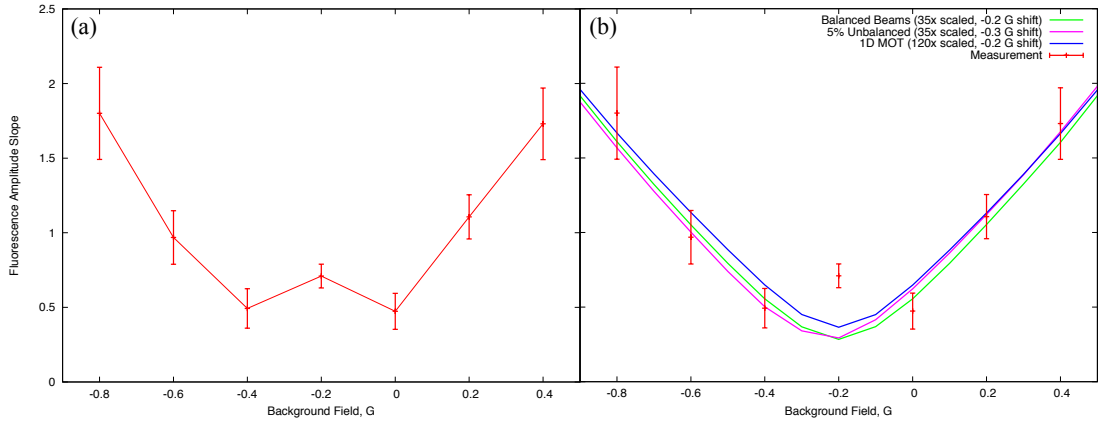


FIGURE 6.11. Fluorescence amplitude with background magnetic fields (a) Measured Data. (b) Scaled and shifted simulations for different models for the MOT.

imbalance in the MOT beams. While considerable effort is put into canceling these (see Section 3.2.4 in particular), the cancelation must not have been complete.

In Figure 6.11b, three MOT models have been used to attempt to match the measured data, with varying success. Each model, however, still requires a large overall scaling factor as well as a manual shift of data center to match the experimental data. The scalings and shifts are given in the figure key. The 3D theory matches the experimental results as closely as possible. It does use all six MOT beams and calculates the force along an axis that is in between the beams, rather than along the axis of a beam. As discussed in Section 5.2.1, the beams enter the experimental cell at 45° while the camera images the MOT along the length of the cell. Thus when moving the atoms horizontally, they do not move down the axis of a beam. All six MOT beams are used in the 3D calculations, with MOT beam phases averaged over. The 3D calculations do include an addition atom position oscillation of $5 \mu\text{m}$, but does not include the off-axis 3D probability estimation. Because the this estimator maps 3D position onto the magnetic field magnitude, the large background field quickly swamps the change in field magnitude for atoms that are off-axis. In fact, this tends

to narrow the atomic distribution rather than broaden it, which was the goal of implementing the 3D mapping.

From the theory graphs in Figure 6.11b, there is still a numeric factor of 35 between the measured experimental data and the best theory we have developed. The increasingly complex simulations discussed in Section 6.3.1 have reduced this scaling factor from around 350 between the data in Figure 6.4 and the 1-D V-atom simulation in Figure 6.5 (at 190 μK) to “just” 35 here, but this gap persists.

There is also a large background field offset that does not match well with the experiment. In the experimental data, the “minimum” of the slope graph is around -0.2 G, but is still close to zero for the simulated data. In Figure 6.11b, the simulation results are shifted manually by 0.2G to 0.38G to have them overlap with the measured data. These additional shifts could be explained by imbalance in the experimental MOT beam powers. Despite careful balancing of their beam powers with the new fiber launcher systems discussed in Section 3.2.4, a lasting power imbalance of 5% is reasonable (although still quite large). This imbalance is simulated as the pink curve in Figure 6.11b, but only shifts the MOT center by around 0.1G. An imbalance of 10-20% could result in the observed shift in the data, but this imbalance is much larger than in the experiment.

A lingering background magnetic field would also be a surprise source for the central shift, as the “default” currents for the Earth canceling Helmholtz coils are set by keeping the atom in one place when ramping the MOT coil magnetic field. This ensures any Earth or lab based background field is canceled, prior to adding a known background field for the experiment. While this technique to cancel background fields could also impose a background field that cancels the MOT beam power imbalances

(see Equation 2.82), such a large imposed field of the order 0.2G as seen in the data would require the same 10-20% imbalance as discussed previously.

6.4 Multiple Atom Fluorescence Amplitudes

Another reasonable experiment would be to look at the modulation from more than one atom. In this case, there are n atoms that are emitting fluorescence at the modulated rate. These should all have the same phase as the current modulation, but would have different amplitudes based on the position of the different atoms in the MOT. For n atoms in the MOT, the spectrum calculation of Appendix E would change in Equations E.1 where the measured average fluorescence rate and its variance would become

$$\begin{aligned} fl(t) &= \langle Fl \rangle [1 + [(\sum_i \epsilon_i) \cos(2\pi f_\alpha t)]] \\ \sigma^2 &= \sigma_B^2 + n\sigma_\alpha^2, \end{aligned} \tag{6.41}$$

where $\langle Fl \rangle$ is the average fluorescence rate, ϵ_i is the oscillation amplitude for MOT atom i , σ_B^2 is the background fluorescence variance and σ_α^2 is the fluorescence variance for one atom. As shown in Figure 4.3, the deviation from a Poisson distribution is small for multiple atoms in the tightly confined MOT. So with a large fluorescence rate, it is still valid to assume the fluorescence is Poisson distributed just as discussed for a single atom in the appendix and Section 6.2.1. Then the only difference between the single-atom calculation the multiple atom calculation is an effective fluorescence amplitude

$$\epsilon'(\vec{r}, t) = \sum_i \epsilon_i(\vec{r}, t), \tag{6.42}$$

where their specific time and position dependence is shown here. With a single atom, the time dependence is managed by averaging over data runs and the spatial dependence is what provided for the position and temperature measurements. With

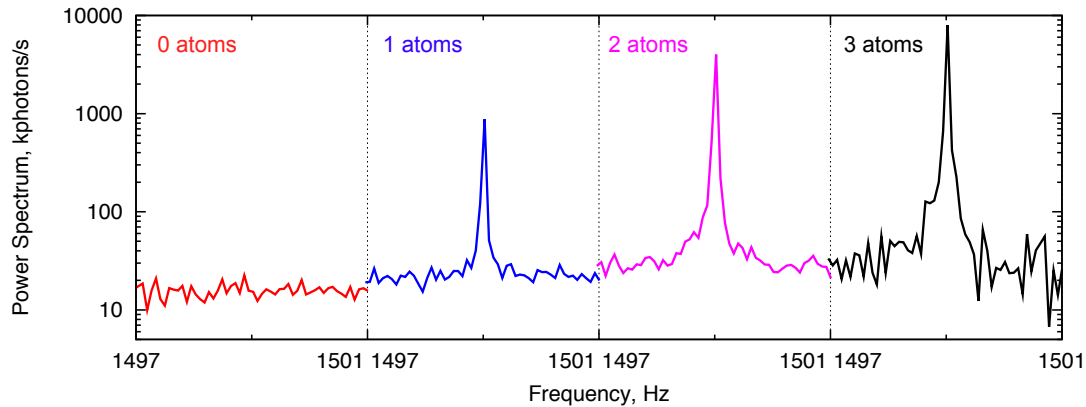


FIGURE 6.12. Spectra of multiple atoms in a MOT. Magnetic field driven at 1499 Hz with modulation amplitude $\epsilon = 0.025$.

multiple atoms, these averages are challenging as the atoms move independently and possibly interact (although the interaction cross-section for a few atoms in the MOT is small [15]). Even if the averaging was straightforward, it would be impossible to distinguish between photons from each atom so their overall oscillation amplitude would still appear as just one amplitude. With this, the amplitude from multiple atoms does not appear as a useful tool for measuring temperatures. Despite its lack of utility, spectral peaks from multiple numbers of atoms are graphed in Figure 6.12.

6.5 Parametric Resonances

As we've seen in Chapter II, atoms in MOTs and objects confined by dipole forces behave as damped, harmonic oscillators. In such systems, modulating the strength of the restoring force can bring about new resonances as noted in Section 6.1. These resonances can be caused by forces oscillating at twice the natural frequency of the system, called parametric oscillations and have been studied some in optical systems for atoms in large MOTs [136–138] and for beads in a dipole trap [39].

Under parametric oscillation, the equation of motion for the location of an atom in the MOT (in 1D) is given by

$$m\ddot{z} = -\beta\dot{z} - \kappa [1 + \epsilon \cos(\omega t)] z, \quad (6.43)$$

where ϵ is the “strength” of the oscillation and ω is a parametric driving frequency, not necessarily the same as the natural frequency of the oscillator, $\omega_0 = \sqrt{\kappa/m}$. As calculated in Appendix F, additional excitation modes of the oscillator can be induced if the oscillator strength is above a threshold strength given by

$$\epsilon_{\text{TH}}^2 = \frac{4\beta^2}{m^2\omega_0^2} = \frac{4\beta^2}{m\kappa}, \quad (F.8)$$

and the parametric frequency occurs in the region

$$2\omega_0 - \frac{\omega_0}{2} \sqrt{\epsilon^2 - \epsilon_{\text{TH}}^2} < \omega < 2\omega_0 + \frac{\omega_0}{2} \sqrt{\epsilon^2 - \epsilon_{\text{TH}}^2}. \quad (F.7)$$

Comparing the equation for ϵ_{TH} to the known MOT relationship between κ and β in Equation 2.83, it simplifies to

$$\epsilon_{\text{TH, MOT}}^2 = \frac{4\beta\hbar k}{mg_F\mu_B B'_z}. \quad (6.44)$$

Additionally, we could look for parametric excitation in the magnetic trapping force. As discussed above the magnetic trapping force has a trapping strength related to the MOT strength according to Equation 6.37. With this the magnetic trapping could

	Natural Frequency, $\omega_0/2\pi$	Threshold Strength
MOT (V-atom)	897 Hz	0.051
Magnetic Trapping (V-atom)	70 Hz	0.65
MOT (^{87}Rb)	2624 Hz	0.017
Magnetic Trapping (^{87}Rb)	205 Hz	0.22

TABLE 6.1. High-gradient MOT parametric resonance conditions. Experimental parameters have typical MOT values as noted in the text.

also experience parametric excitation with threshold strength

$$\epsilon_{\text{TH, mag}}^2 = \frac{4\beta\hbar^2 k^2 \Gamma}{mg_F^2 \mu_B^2 (B'_z)^2}. \quad (6.45)$$

For both MOT magnetic confinement and magnetic trapping, the natural frequency and threshold strengths are given in Table 6.1 using typical (high-gradient) MOT values $\tilde{\delta}_L = -1$, $|\Omega| = 0.5\Gamma$ and $B'_z = 242$ G/cm. This table also shows approximate values for the full ^{87}Rb atom, using the the scaling between the full atom and V-atom MOT confinement force from fitting the simulated data in Figure 5.2.

While the solution to Equation 6.43 predicts exponential growth of the atomic position, including higher order terms of the position and velocity (z^3 and v^3) in the expansion for the force Equations 2.77 and 2.68, allows for stable oscillations

$$z(t) = R \cos(\omega t + \phi), \quad (6.46)$$

where the amplitude is given by

$$R^2 = \frac{16}{3A(4 + \epsilon_{\text{TH}}^2)^2} \left[4 \left(\frac{2\omega}{\omega_0} - 2 \right) - \epsilon_{\text{TH}}^2 + \sqrt{\epsilon^2 (4 + \epsilon_{\text{TH}}^2) - 4\epsilon_{\text{TH}}^2 \left(\frac{2\omega}{\omega_0} - 1 \right)^2} \right] \quad (6.47)$$

and $A\kappa/m$ is the coefficient for the force term proportional to $-z^3$ [138].

These oscillations are clear when looking at pictures of the atom, such as those in Figure 6.13a. These pictures are the average of a number of data runs with one atom and were taken with an exposure time of 150 ms. The magnetic fields had a parametric frequency of 1154 Hz, so that the pictures reveal the atom's position distribution over 173 oscillation periods. The pictures clearly show the double-peaks as would be expected for the position distribution of an oscillating particle. Even without averaging over many pictures the double-peak shape appears, as shown in Figure 6.16a. The graphs in Figure 6.13b were found by summing pixel intensity across the rows of the pictures in (a). The slight tilt, around 4° was ignored for the integration. These figures clearly show the double-peaks as would be expected for the position distribution of an oscillating particle. The oscillation amplitudes measured in Figure 6.13c compare the distance between peaks.

As discussed in Section 2.5.1, the center of a MOT tracks the location where the magnetic field vanishes. If there is a background magnetic field, B_0 , in 1D, the field is given by Equation 2.80. If the magnetic field gradient oscillates, the location where the magnetic field vanishes also oscillates according to

$$z_0(t) = \frac{-B_0}{B'_z [1 + \epsilon \cos(\omega t)]} \approx \frac{-B_0}{B'_z} + \frac{B_0}{B'_z} \epsilon \cos(\omega t) \quad (6.48)$$

by solving Equation 2.81 in the equal laser field strength regime. If the oscillations present in Figure 6.13a were due to the movement of the center of the MOT, a linear fit of the graph in Figure 6.13b would correspond to the ratio B_0/B'_z . This fit gives a value of $B_0/B'_z = 551 \pm 53 \mu\text{m}$. This data was recorded with a magnetic field gradient of 219 G/cm, which would require a background field of $B_0 = 12 \pm 1$ G. This is much larger than the actual background field. Such large oscillations are best explained, then, by a parametric resonance.

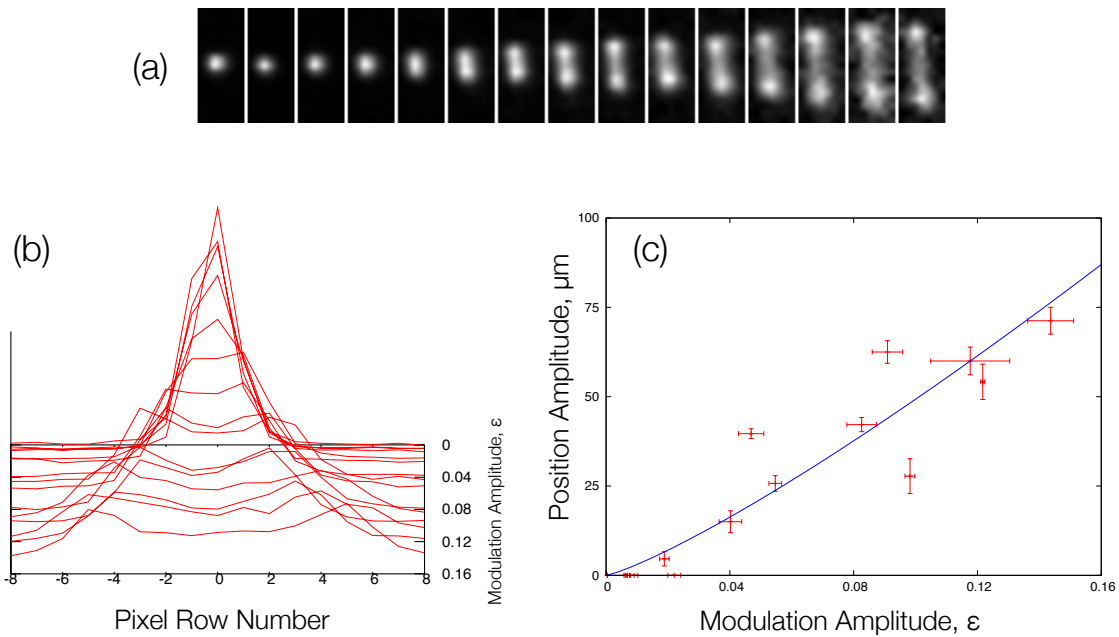


FIGURE 6.13. Images of Single Atom Parametric Resonance. (a) CCD exposures of one atom in a parametric MOT with increase modulator strength. (b) Pixel intensity of images integrated across a row (normalized to a position distribution). (c) Oscillation amplitudes of an atom oscillating in a parametric MOT. The curve is a power law fit to the data: $A_p = 796\epsilon^{1.21}$.

For a particle oscillating with amplitude A , the probability to be at a position a is given by Equation 6.34). We can assume our camera sees a gaussian distribution for light detected from a single atom located at position a . The variance of this distribution, σ^2 , is largely to displacement of the atom from the camera's focal plane, but there is also a contribution due to atom motion during an exposure. If the exposure time is much longer than the period of oscillation for the atom, the light distribution seen by the atom is given by

$$L(z) = \frac{1}{\pi\sqrt{2\pi\sigma^2}} \int_{-A}^A \exp\left[\frac{-(z-a)^2}{2\sigma^2}\right] \frac{da}{\sqrt{A^2-a^2}} \quad (6.49)$$

or in dimensionless variables relative to σ , we have

$$L(z') = \frac{1}{\pi\sqrt{2\pi\sigma^2}} \int_{-1}^1 \exp\left[\frac{-(z'-A'a')^2}{2}\right] \frac{da'}{\sqrt{1-a'^2}}. \quad (6.50)$$

This does not have an analytic form, but is plotted in Figure 6.14. If the oscillation amplitude is small relative to the standard deviation, the resulting distribution looks like a single peak. At larger amplitudes, distinct peaks at the edges of the oscillation can be resolved. These are both observable in Figure 6.13b.

Making one additional change, we can fit Equation 6.49 using the data from 6.13b. This change adds an offset to the integrable value a :

$$L(z) = \frac{1}{\pi\sqrt{2\pi\sigma^2}} \int_{-A}^A \exp\left[\frac{-(z-(a-a_0))^2}{2\sigma^2}\right] \frac{da}{\sqrt{A^2-(a-a_0)^2}}. \quad (6.51)$$

We can fit this equation for for values of σ , A , and a_0 using the distributions in Figure 6.13b. The data to fit is pixel data, which is the integrated fluorescence over region of size $15 \mu\text{m}$. To fit this appropriately, the fitting algorithm integrates a high-resolution

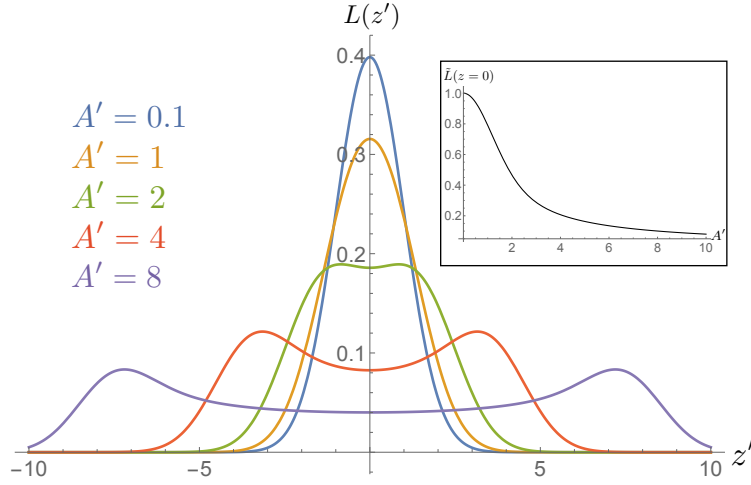


FIGURE 6.14. Light Distribution for Parametric Oscillating Atom. Numeric solutions for Equation 6.50 with listed values for the scaled oscillation amplitudes $A' = A/\sigma$. Inset shows plots of Equation 6.53, the normalized light amplitude at the center of the MOT. Both graphs have unit variance.

position spacing, then sums over a 15μ region to generate information for effective pixels before comparing to the data. A few plots of the fitted (higher-resolution) distributions for some atom images are reproduced in Figure 6.15 along with graphs of the resulting fitted values for the data in Figure 6.13.

The fit for the detected light distribution standard deviation σ (Figure 6.15d) is consistently between $15 \mu\text{m}$ and $30 \mu\text{m}$, which corresponds to a width of 1 and 2 pixels. This is consistent with single-atom photographs being a few pixels in size.

In Figure 6.15e, the oscillating atom's position amplitude grows as the modulation amplitude increases, which is expected. The values are also close to the values measured amplitudes in Figure 6.13c, but a little larger. This is expected from the graphs in Figure 6.14, where the oscillation amplitudes A' (which were measured in Figure 6.15e) are larger than the peak of the light distribution (which

were measured in 6.14c). This is due to the hard cutoff of the oscillation probability distribution above $a = \pm A$ in Equation 6.34.

The center offsets in Figure 6.15f are all much smaller than a pixel, which is expected from the images. The large noise in the fit data for small oscillations are a result of the widening oscillation amplitude closely mimicking an increase of the detected light distribution variance. The shared impact on the resulting light distribution makes fitting the two values difficult.

At the center of the oscillation, Equation 6.50 does have an analytic solution given by

$$L(z' = 0) = \frac{I_0\left(\frac{A'^2}{4}\right)}{\sqrt{2\pi\sigma^2}} \exp\left[\frac{-A'^2}{4}\right] \quad (6.52)$$

where I_0 is the 0-th order modified Bessel function of the first kind [139]. We can normalize this to the condition of no oscillation ($A = 0$) to give a useful equation

$$\tilde{L}(z' = 0) = I_0\left(\frac{A'^2}{4}\right) \exp\left[\frac{-A'^2}{4}\right], \quad (6.53)$$

which just represents the center intensity (relative to no oscillations) for the atom. This equation is plotted as a function the oscillation amplitude in the inset of Figure 6.14. This is an expected shape as the atom spends less of its time close to the center of the MOT when there is a large oscillation amplitude. We can verify this one of two ways. First, by examining the light intensity in the center pixel for each atom image in Figure 6.13a. Here, equation 6.51 is integrated over the size of one pixel. This is shown in Figure 6.16a.

The second way is by looking at the average fluorescence for a single atom from the APD data. This fluorescence is shown in Figure 6.16b. This graph shows the drop of intensity directly. At around $t = 31$ s, there is a spike in fluorescence as the

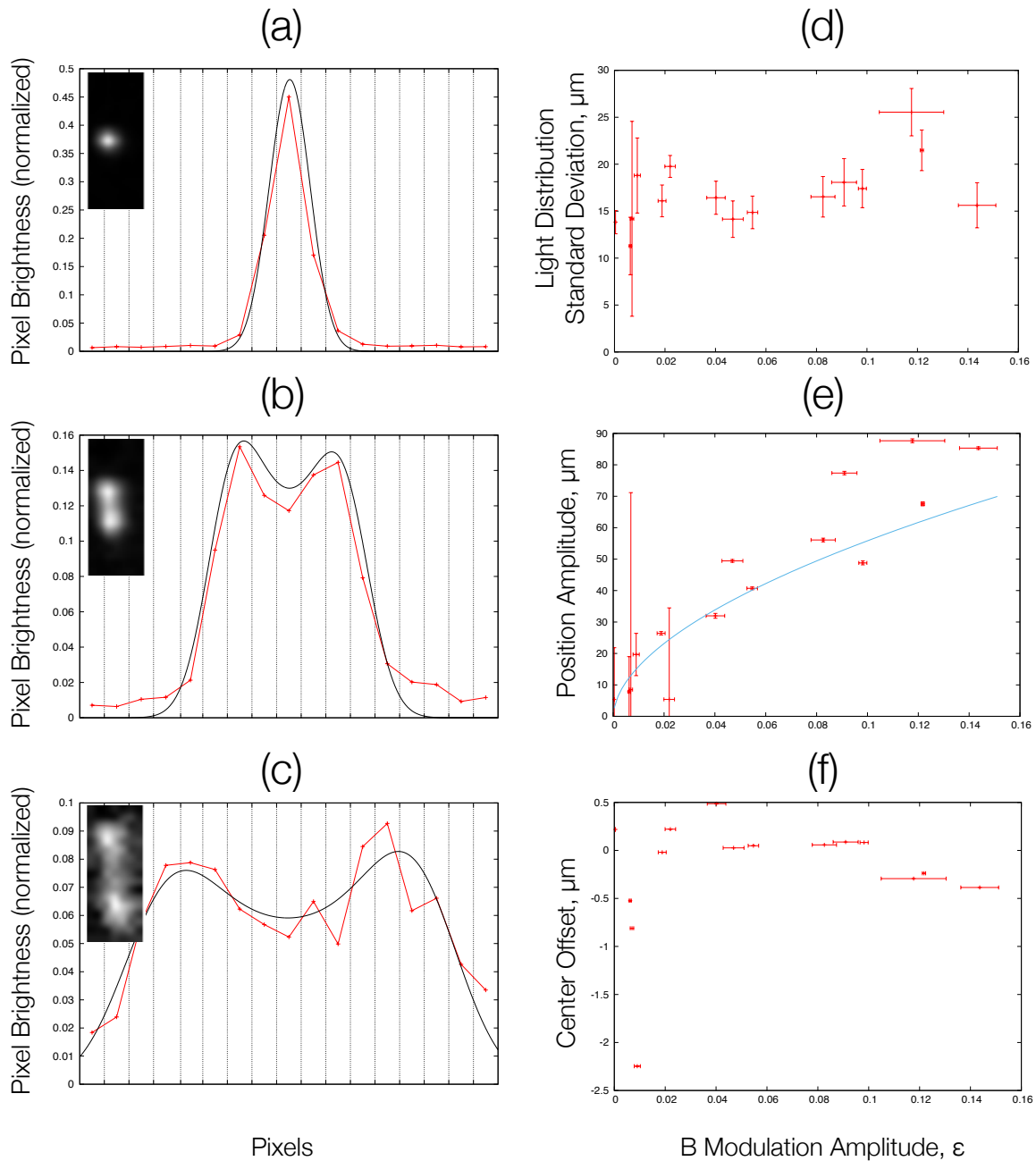


FIGURE 6.15. Fitted Light Distributions for Parametric Oscillating Atoms. All graphs are results fits for Equation 6.51 (a-c) Plots of fitted pixel data for modulation amplitudes $\epsilon = 0.0062, 0.055, 0.12$ respectively. Vertical lines show the "boundaries" of pixels. Black lines are fits, red lines are data. (d) Fitted values for light distribution standard deviation for data in Figure 6.13. (e) Fitted values for position amplitude for data in Figure 6.13. Line is a power law fit : $A = 196\epsilon^{0.546}$. (f) Fitted values for center offset for data in Figure 6.13. Graphs (d-f) share a common horizontal scale.

atom enters the MOT. This triggers the bayesian algorithm to reduce the trapping region and introduce the magnetic field oscillation. Immediately, the atom beings oscillating and the fluorecence drops as the atom spends less time in the focus of the APD lens system. This graph is representative of each data run that produced the single atom images in Figure 6.13a. Here, the intensity is plotted as a function of A/σ , the position oscillation amplitude relative to the light distribution standard deviation. Also shown is a plot of Equation 6.54 using average values from the prior fits ($\sigma = 16.9 \mu\text{m}$ and $a_0 = -0.22 \mu\text{m}$) for comparison.

Equation 6.53 looks at just the value at $z' = 0$, which we cannot measure. Instead, the values in Figure 6.16c are from a region of space equal to the focus size of the APD lens system. To calculate this accurate, we integrate Equation 6.51 over some small region, again normalizing to the case of no oscillations. This gives equation

$$\tilde{F}l = \frac{\sqrt{2/\pi^3}}{\left(\text{Erf}\left[\frac{s+a_0}{\sqrt{2}\sigma}\right] + \text{Erf}\left[\frac{s-a_0}{\sqrt{2}\sigma}\right]\right)} \int_{-s}^s dz \int_{-A}^A da \frac{\exp\left[\frac{-(z-(a-a_0))^2}{2\sigma^2}\right]}{\sqrt{A^2 - (a - a_0)^2}}, \quad (6.54)$$

where the integration region represents the width of the APD lens system focus. The error functions appear from the normalization, an integral from $-s \rightarrow s$ over a gaussian of variance σ and centered at $a - a_0$.

This APD measured signal is plotted in Figure 6.16c, with the integration region defined as the radius of the APD lens system focal spot size. Represents a fit of the Equation 6.54. The longer tail in the APD data compared to the pixel intensity arises from the larger focal size compared to pixel size.

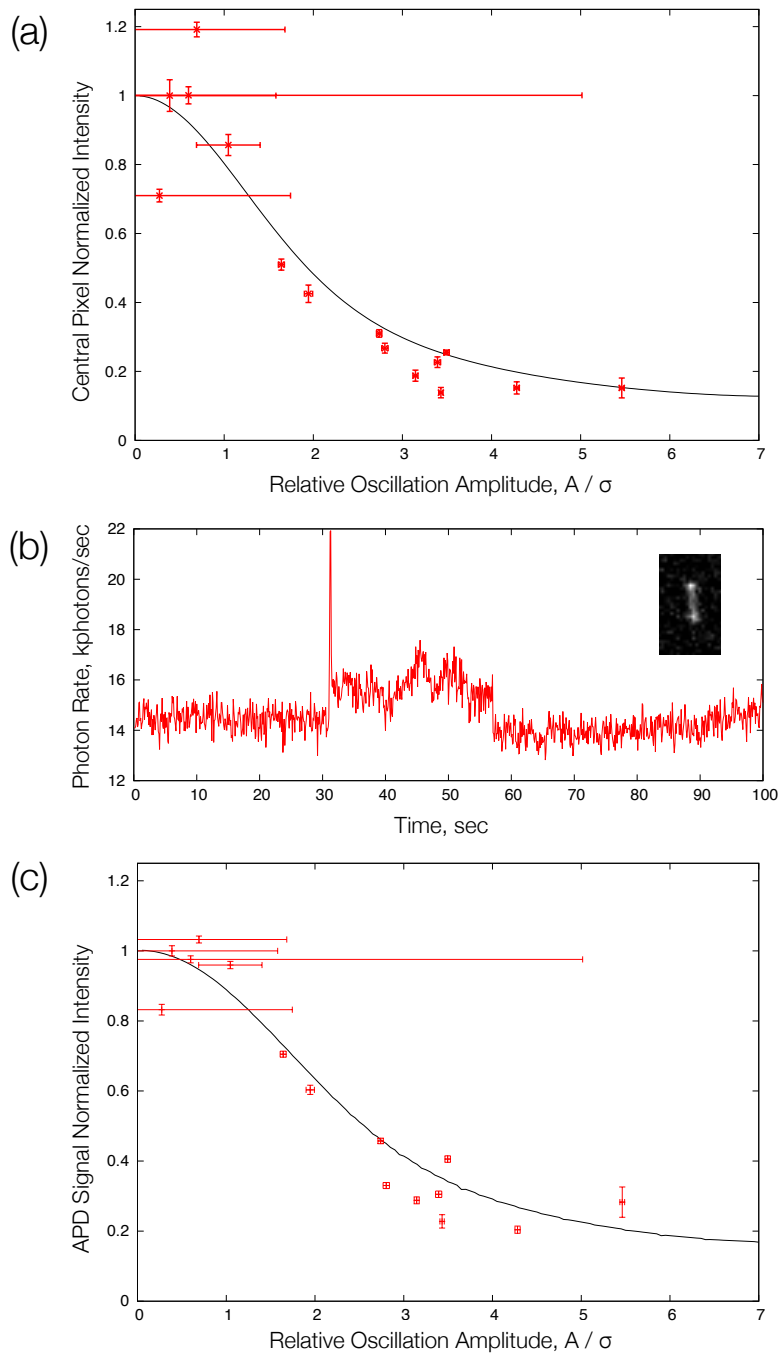


FIGURE 6.16. Light intensity loss due to parametric oscillations. (a) Normalized intensity of center pixel for parametrically oscillating atom. (b) Graph of APD measured intensity for one data run with magnetic field modulation amplitude $\epsilon = 0.149$. A single picture of this atom is also shown. (c) Normalized intensity of APD signal for a parametrically oscillating atom. Lines are calculation of Equation 6.54 with average fit values for A , σ , and a_0 .

3-Dimensional Parametric Resonances

As discussed in Section 5.1.2, the magnetic field created by the anti-Helmholtz coils have the form

$$\vec{B}(\vec{r}) = B'_z \left(\frac{x}{2} \hat{x} + \frac{y}{2} \hat{y} - z \hat{z} \right), \quad (5.4)$$

where B'_z is the magnitude of the linear gradient along the MOT axis. Recalling Equation 2.78, the restoring spring-constant, κ along some axis in a MOT is proportional to the magnetic field gradient along that axis. From these two, we must have that the restoring spring-constant along the x - and y -directions in the MOT is half that of along the z -direction. Writing the equation of motion for an atom in a MOT, we then have

$$m\ddot{\vec{r}} = -\beta\dot{\vec{r}} - \kappa z \hat{z} - \frac{\kappa}{2} x \hat{x} - \frac{\kappa}{2} y \hat{y} \quad (6.55)$$

where κ is defined as in Equation 2.78 for the V-atom or from the potential recovery method in Section 5.5. In prior parametric resonance experiments for atoms in a MOT, the z -direction MOT trapping beams were modulated to cause parametric oscillations for just piece of this equation [136–138]. However, modulating the MOT magnetic field also imposes parametric conditions on the x - and y -directions:

$$m\ddot{\vec{r}} = -\beta\dot{\vec{r}} - \kappa [1 + \epsilon \cos(\omega t)] z \hat{z} - \frac{\kappa}{2} [1 + \epsilon \cos(\omega t)] x \hat{x} - \frac{\kappa}{2} [1 + \epsilon \cos(\omega t)] y \hat{y} \quad (6.56)$$

The parametric oscillations along the z -direction were discussed and observed above. However, because of the differing strength of the restoring spring-constant along the x - and y -directions, there will be additional resonances that can appear which can cause large oscillations perpendicular to the anti-Helmholtz coil axis. Because these occurs

in a plane that is normal to the camera's imaging plane, these will be challenging to image.

The parametric oscillations in x - and y -direction can be analyzed using the same method as outlined for the 1D parametric resonance in Appendix F with a simple change to Equations F.3 to make them

$$\begin{aligned}\omega &\rightarrow \sqrt{2}\omega_0 + \zeta \\ \nu &\rightarrow \frac{1}{\sqrt{2}}\omega_0 + \frac{1}{2}\zeta,\end{aligned}\tag{6.57}$$

where ω_0 is the oscillation frequency along the z -direction (i.e., $\omega_0 = \sqrt{\kappa/m}$). The resulting parametric resonance region is given by

$$\sqrt{2}\omega_0 - \frac{\omega_0}{\sqrt{2}}\sqrt{\epsilon^2 - \epsilon_{\perp H}^2} < \omega < \sqrt{2}\omega_0 + \frac{\omega_0}{\sqrt{2}}\sqrt{\epsilon^2 - \epsilon_{\perp H}^2},\tag{6.58}$$

where the threshold strength to excite x - and y -direction oscillations is

$$\epsilon_{\perp H}^2 = \frac{2\beta^2}{\omega_0^2 m^2}.\tag{6.59}$$

This formalism reveals that the additional excitations in the x - y plane should appear at a different frequency from the excitation along the z -direction and at a smaller threshold strength. It is instructive look at these in terms of x - and y - frequencies:

$$2\omega_{xy} - \omega_{xy}\sqrt{\epsilon^2 - \epsilon_{\perp H}^2} < \omega < 2\omega_{xy} + \omega_{xy}\sqrt{\epsilon^2 - \epsilon_{\perp H}^2}\tag{6.60}$$

and

$$\epsilon_{\perp H}^2 = \frac{\beta^2}{\omega_{x,y}^2 m^2}.\tag{6.61}$$

From this form, the parametric resonance region is still centered on twice the natural frequency in the x - y plane—which would be expected. Comparing to the threshold strength along the z -axis, ϵ_{TH} of Equation F.8, in the x - y plane the threshold strength is half as large. This is easily explained by noting that the weaker restoring force in the x - y plane requires a smaller perturbing strength (ϵ) to overcome. Additionally, the width of the parametric resonance region in the x - y plane is twice that of the z -axis as revealed in Equation F.7. This is also easily explained by the weaker restoring force allowing parametric excitation over a wider range of frequencies. This last piece could help explain the broad peak of the spectrum in Figure 6.6.

6.6 Non-Sinusoidal Waveforms

The oscillation measurements described above focus on sinusoidal modulations. The same analysis should hold for any periodic modulation of the MOT magnetic field. Focusing on three common waveforms, all with fundamental frequency f_1 and amplitude A , the Fourier series for

- square waves contain only odd harmonics with amplitudes A/n ,
- triangle waves contain only odd harmonics with amplitudes A/n^2 , and
- sawtooth waves contain all harmonics with amplitudes A/n ,

where n denotes the index of the harmonic [140]. If the current in the anti-Helmholtz coils is modulated with different waveforms, evidence of it should be present in fluorescence spectra of a single atom.

Figure 6.17 shows the power spectra from an atom for a sine wave and the three waveforms above. In each of these, the driving frequency was 401 Hz and the anti-Helmholtz current modulation amplitude was 0.04. Some things stand out clearly in

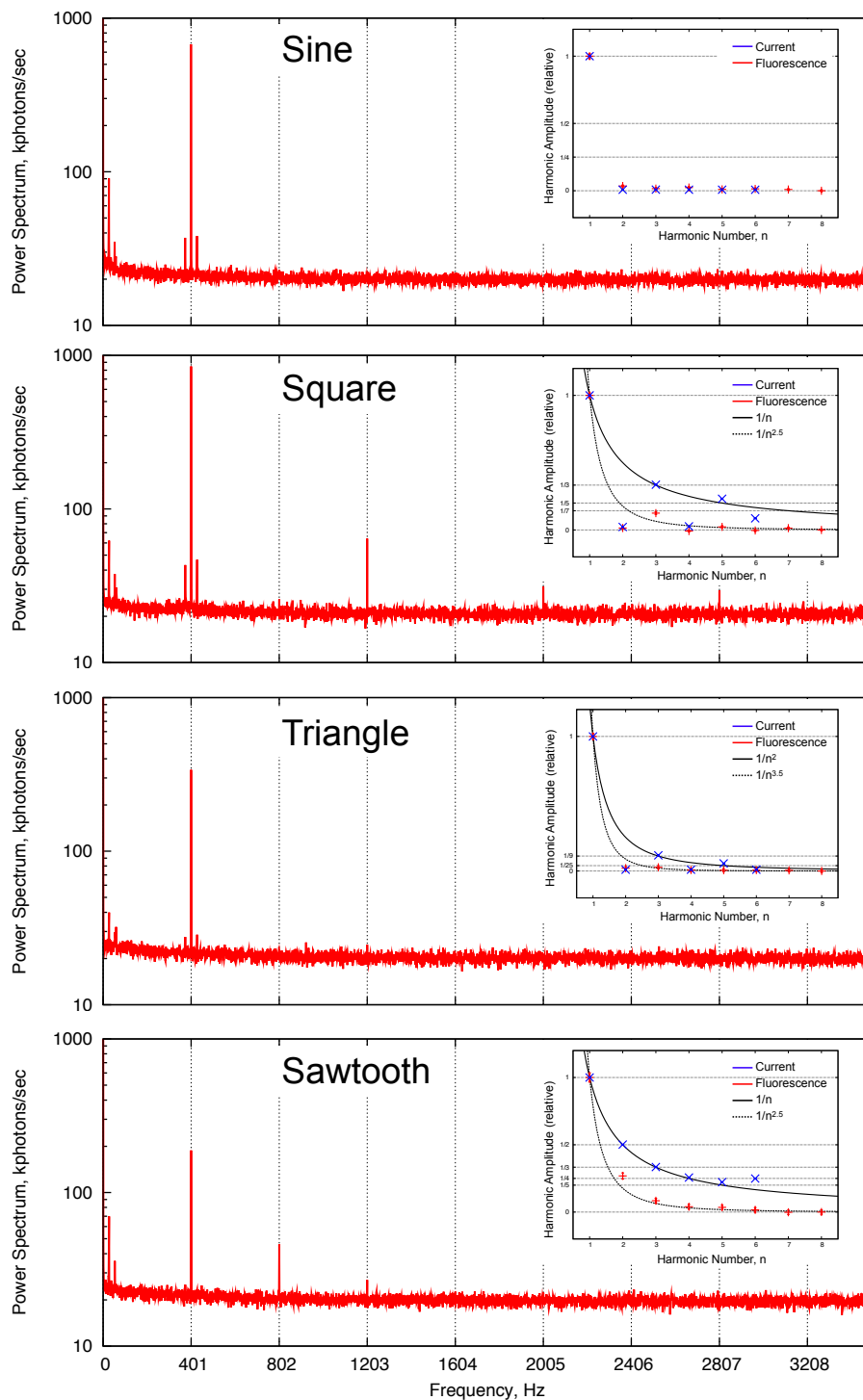


FIGURE 6.17. Power spectra for different waveforms. Inset graphs show the amplitudes of peaks at each harmonic, relative to the first. Solid lines show the expected Fourier series amplitude and dashed line show the expected amplitude scaled by a factor of the harmonic number, $n^{-3/2}$.

these. First, the spectra do generally show the correct harmonics for each waveform. Second, the fundamentals in some of the graphs show sidebands who differ from the peak by around ± 27 Hz. This results from mixing with the unknown 27 Hz magnetic field oscillation. Lastly, the triangle wave shows almost no harmonics above the first, although willful examination of the spectra may show a peak at the third harmonic frequency. The lack of higher harmonic peaks for the triangle wave is directly related its much faster amplitude decay, n^{-2} .

The inset graph for each waveform in Figure 6.17 shows the amplitude for the first 8 harmonics calculated from the power spectra for the fluorescence (red data) and the first 6 harmonics from a power spectrum of the anti-Helmholtz current (blue data). The current signal is measured with an oscilloscope and the CLN-50 Hall sensor (see Section 3.3.5), so the maximum harmonic measurable for the current is limited by the time resolution of the oscilloscope. For clarity, these have been scaled to the amplitude of the fundamental. The solid black line shows the appropriate scaling of the Fourier series amplitudes as a function of the harmonic number n and the dashed black line shows the appropriate scaling with an additional factor of $n^{-3/2}$.

The amplitudes for the current modulation are close to their “correct” scaling. For the square wave, the amplitudes of the odd harmonics scale as $n^{-0.92 \pm 0.06}$. For the triangle wave, the amplitudes of the odd harmonics scale as $n^{-1.81 \pm 0.12}$. For the sawtooth wave, the amplitudes of the harmonics scale as $n^{-0.84 \pm 0.09}$.

On the other hand, the fluorescence modulation amplitudes scale closer to the values when an additional factor for $n^{-3/2}$ is included. This factor arises from the non-uniform frequency response of the fluorescence as shown in the power spectrum of Figure 6.6, as its high frequency tail went as $f^{-3/2}$. For the square wave, the

Waveform	Function (one period)	Variance
Sinusoid	$y(t) = A \sin\left(\frac{2\pi t}{T}\right)$	$\sigma^2 = A^2/2$
Square	$y(t) = -A\Theta(-t) + A\theta(t)$	$\sigma^2 = A^2$
Sawtooth	$y(t) = \frac{2A}{T}t$	$\sigma^2 = A^2/3$
Triangle	$y(t) = \frac{4A}{T} \left[\left(t + \frac{T}{4}\right) \Theta(-t) - \left(t - \frac{T}{4}\right) \Theta(t) \right]$	$\sigma^2 = A^2/3$

TABLE 6.2. Variance compared to amplitude for common waveforms. Each waveform has a period T and amplitude A .

odd harmonics scale as $n^{-2.27 \pm 0.19}$. For the triangle wave, the odd harmonics scale as $n^{2.89 \pm 0.29}$. For the sawtooth wave, the harmonics scale as $n^{-2.27 \pm 0.13}$.

The calculations for the current amplitudes from their (unshown) spectra do not derive from Equation 6.28, which applies only for the oscillating average of a Poissonian sampled fluorescence. The current is measured directly as noted above and should follow the function

$$I(t) = I_0 [1 + \epsilon \sin(2\pi f_\alpha t + \phi)]. \quad (6.62)$$

This gives rise to Equation 6.4, as the magnetic field gradient is directly proportional to the current. The power spectrum of this current is

$$P_I(f) = I_0^2 \delta(f) + \frac{I_0^2 \epsilon^2}{4} \delta(f - f_\alpha) + \frac{I_0^2 \epsilon^2}{4} \delta(f + f_\alpha). \quad (6.63)$$

When calculating the spectrum numerically, the amplitudes of the two delta functions are found with with the same area-under the curve calculation as in Equation 6.26. Doing this for the peak corresponding to each harmonic n gives the current harmonic amplitudes ϵ_n for the inset graphs in Figure 6.17.

The overall oscillation amplitude for these different waveforms can also be calculated directly from the current measurement via its the variance, as was done for the sinusoidal waves in Section 6.3.2. For the four waveforms of interest, the variance, σ^2 , as a function of the amplitude A is given in Table 6.2. Each of these waveforms, $y(t)$, have an average value of zero when averaged over a period, so calculating the variance is given by

$$\sigma^2 = \int_{-T/2}^{T/2} y^2(t) dt. \quad (6.64)$$

This method, of course, cannot extract the amplitudes of the Fourier series for the waves, but it can easily find the overall wave amplitude, particularly useful for calibrating amplitudes at different modulation frequencies.

CHAPTER VII

CONCLUSIONS

As discussed in Section 6.3.5, there remains a disagreement between experimental measurements and theoretical predictions for the amplitude of fluorescence modulations. At temperatures similar to the measured atomic temperature of $160 \mu\text{K}$ using the release-recapture method, our MOT model predicts fluorescence amplitudes around 35 times smaller than our measured results. As noted in Section 6.1.3, selecting an appropriate model for the atom in the MOT is important for our measurement. The measurement results were sensitive enough to rule out the extended two-level atom model that is common in the literature [25]. Our best model, a full D_2 level structure for ^{87}Rb in a 3D MOT with both added small oscillations and off-axis atomic probabilities, still fell short of the measured predictions but is a noticeable improvement over simpler models of both the atom and its environment.

The disagreement could, of course, be from either the data analysis rather than the model. The analysis has been thoroughly checked against simulated fluorescence signals with a known modulation amplitude, m_α , and has been shown to correctly extract its value via Equations 6.27 and 6.28. This fluorescence simulation randomly sampled photon arrivals from an oscillating average fluorescence rate, producing data that closely mimics the experimental data without any reference to a source of photons. It did not simulate the behavior of the atom and tie that to fluorescence measurements. This check was purely to verify the analysis of Section 6.2 was appropriate. With confidence that our analysis measures fluorescence amplitudes appropriately, the disagreement must lie in the theoretical model.

The continued improvement of the theoretical model to approach the measured result (see, for example, Figure 6.5) gives a hint that there is potentially a missing

complication of the MOT that has yet to be included in the simulation. Based on the magnetic field offset between measured amplitudes and theoretical ones seen in Figure 6.11, one potential route is to more closely model the magnetic field of the coils. At the most basic level this would require using the full magnetic field of Equation 5.2. We have exclusively used the linear description in Equation 5.4 which should be very accurate near the center of the MOT coils. Shifting the MOT further from the center, with either a background field or imbalanced MOT lasers, could move the atom to a location where this description breaks down. However, the full field equation and the linearized field differ in magnitude by less than 1.5% out to $500 \mu\text{m}$ from the center of the trap in the z -direction and around half that for displacements in the x - y plane. This should comfortably cover the range of positions the atom would explore even with large background fields.

Along a similar and potentially more valuable addition would take into account known defects in the MOT coils. In the process of building the water cooled MOT coils, one coil became tilted a few degrees so that the two are not perfectly coaxial. This is largely responsible for the 4° tilt of the atom's oscillations seen in Figure 6.13. While the effect does not prevent the MOT from loading, it could be partially responsible for added noise in fluorescence from a single atom seen in Figure 4.3. The blue data in this figure was recorded with the (second generation) permanent magnets while the others are done with the electromagnets (without added modulation). The permanent magnet MOT shows very close to Poissonian growth of the variance with atom number while the two data sets for the electromagnets show added noise in the fluorescence variance. This appears as a general feature of our single atom electromagnet MOT—the variance in the fluorescence signal from a single atom is larger than for its permanent magnet equivalent. This could arise from a more

complex magnetic field arrangement from the electromagnet coils due to their tilt. We have investigated solving this tilt by manually rotating the coil to compensate for the tilt (although this still causes the coils to have parallel axes rather than be coaxial), but it did not have a noticeable impact on the fluorescence amplitudes. Additionally, preliminary theoretical investigations of the coil defect has done just by rotating the magnetic field of one coil slightly, which these showed very little impact on the theoretical results. This test was done just along one MOT axis and with an otherwise idealized MOT. How these defects interplay with other magnetic fields, induced currents, or non-ideal MOT beams could explain some, but likely not all, of the gap between experiments and the MOT model.

As mentioned briefly in Section 5.2.4, the presence of conducting materials around our experiment could create image currents that impact the magnetic field seen by the atom. With an oscillating magnetic field as in our experiments, causes additional issues as the changing magnetic field will induce currents in the surrounding material. The eddy currents would then add a time-dependent background field to the atom, shifting the center the MOT, as shown in Equation 2.81. Of particular note, the Helmholtz coils around experiment which help cancel the Earth's magnetic field will have oscillating currents induced in them. Because the induced currents act to oppose the change in field, their impact would be to lessen the modulation in the magnetic field and thus reduce the fluorescence oscillation. While the induced currents are small, they have been measured directly by monitoring the voltage across the coils during experimental runs. While these currents should be equal and opposite for opposing Helmholtz coils, the induced current measured in one of the Helmholtz coils was significantly lower than the current in the coil opposite it. This coil is the closest to the vacuum system and has the vacuum flange that mounts the experiment

cell in its interior. Because there is this second conducting path for an induced current (around the flange), the oscillating magnetic flux through the coils is reduced and thus its induced current is smaller. The magnetic field this makes, then, does not cancel the field from its opposite coil and leaves some residual induced field. This field will be much smaller than the field from the MOT trapping coils, but does have a spatial dependence and would impact the magnetic oscillations seen by the atom as it moves around the trap. While this effect from the Helmholtz coils will likely be insignificant, the measurable influence of eddy currents in the flange hints that they do influence the system and may cause added motion to the atom.

Most experimental measurements have been done in the regime of fast magnetic field modulation—where its frequency is must larger than the motional frequency of atoms in the MOT.¹¹ In this regime it was possible to ignore the motion of the atom in the trap as discussed in Section 6.1.2 and even outside this regime the impact on the position distribution of the atom is small [39]. As discussed Section 6.3.2 there are multiple relevant frequency scales (around hundreds of hertz for magnetic trapping and kilohertz for the MOT) which complicate this high frequency regime. The importance of the magnetic trapping to the shape of the amplitude-frequency spectrum in Figure 6.7 as well as the parametric resonances seen in Section 6.5 further suggest that motion of the atom in the trap may play a more significant role than the present theoretical model assumes.

Extra motion of the atom has only been analyzed in our experiment through the “forced” oscillations of the atom’s position (see Section 6.3.1). More careful analysis of the motion of the atom could be done in a few ways. The numeric methods of

¹¹The key exceptions to this being the frequency response measurements in Section 6.3.2 and the non-sinusoidal waveform measurements in Section 6.6, where a lower frequency was needed so that multiple higher harmonics would be visible in the spectra.

Chapter V could be altered to include velocity of the atom. To do so, the detuning of each laser must be modified with a doppler shift so that the detuning for the i laser field become

$$\Delta_{L,i} \rightarrow \Delta_{L,i} + \vec{k}_i \cdot \vec{v}, \quad (7.1)$$

where \vec{k}_i is the propagation direction of the field. This change would have to be implemented for each beam and for both the trapping and repumping laser fields. In this way, the wavefunction would be for both position and momentum and more thorough analysis of motional dependence could be done. Similarly, the theory could be reformed into a Wigner function formalism which reflects both position and momentum distributions. This has been for many atomic models (in one dimension) to examine sub-doppler cooling for atoms with many energy levels in a MOT [64, 72]. Doing so could reveal an overlooked physical mechanism for the measured, larger than anticipated, fluorescence amplitude, much as Sisyphus and polarization gradient cooling were unpredicted prior to the first MOT temperature measurements [71].

APPENDIX A

HOW A $F_G = 0 \rightarrow F_E = 1$ ATOM BECOMES A V-ATOM

The derivation for the equations of motion for the $F_g = 0 \rightarrow F_e = 1$ atom is sketched in Section 2.5. The equation of motion for the evolution of the atom's density matrix is given in Equation 2.60. The individual element equations are in Section A.2.

If there is no electric field which couples the ground state to an excited state, then the Rabi frequency for that state is zero. For the atom discussed in Section 2.5, there is no field coupling $|0\rangle$ to $|g\rangle$, which gives $\Omega_0 = 0$.

These equations will be analyzed in the steady state. Taking a peak forward with that in mind, Equation A.5c drives $\rho_{0,0} \rightarrow 0$ when $\Omega_0 = 0$. With this, combining Equations A.5f, A.5a, and A.5g produce $\rho_{g,0} = \rho_{-,0} = \rho_{+,0} = 0$ and combining Equations A.5b, A.5d, and A.5e produce $\rho_{g,0} = \rho_{-,0} = \rho_{+,0} = 0$. Thus, in the steady state all density matrix elements associated with the $|E; m = 0\rangle$ state go to zero in the steady state.

This effectively decouples this state from the rest of the atom, making the atom behave as a V-atom: an atom with a ground state and two excited states. A level diagram for such an atom is shown in Figure 2.2c. The internal dynamics of this atom then evolve under the equations in Section A.1, where we've also let $\Delta_0 \rightarrow 0$ for the nonexistent field's detuning. In the steady state, the V-atom equations produce excited state populations

$$\rho_{-,-}^{ss} = \frac{|\Omega_-|^2}{N} \left[(|\Omega_-|^2 + |\Omega_+|^2)^2 + 4(|\Omega_-|^2 + |\Omega_+|^2) + 16|\Omega_+|^2 (\delta_- - \delta_+)^2 + 8(|\Omega_-|^2 \delta_+ - |\Omega_+|^2 \delta_-) (\delta_- - \delta_+) + 4(1 + 4\delta_+^2) (1 + (\delta_- - \delta_+)^2) \right] \quad (\text{A.1})$$

and

$$\rho_{+,+}^{ss} = \frac{|\Omega_+|^2}{N} \left[(|\Omega_-|^2 + |\Omega_+|^2)^2 + 4(|\Omega_-|^2 + |\Omega_+|^2) + 16|\Omega_-|^2 (\delta_- - \delta_+)^2 + 8(|\Omega_-|^2 \delta_+ - |\Omega_+|^2 \delta_-) (\delta_- - \delta_+) + 4(1 + 4\delta_-^2) (1 + (\delta_- - \delta_+)^2) \right], \quad (\text{A.2})$$

where $\tilde{\Omega}_\pm = \Omega_\pm / \Gamma$, $\delta_\pm = \Delta_\pm / \Gamma$, and the normalization factor is

$$\begin{aligned} N = & 2(|\Omega_-|^2 + |\Omega_+|^2)^3 + (|\Omega_-|^2 + |\Omega_+|^2)^2 [9 + 4(\delta_- + \delta_+)^2] \\ & + 4(|\Omega_-|^2 + |\Omega_+|^2) [1 + (\delta_- - \delta_+)^2] + \\ & 4|\Omega_+|^2 [2 - 4\delta_- (2\delta_+ - \delta_-) (\delta_-^2 - \delta_+^2) + 3(\delta_-^2 + \delta_+^2) + 2\delta_+^2] + \\ & 4|\Omega_-|^2 [2 + 4\delta_+ (2\delta_- - \delta_+) (\delta_-^2 - \delta_+^2) + 3(\delta_-^2 + \delta_+^2) + 2\delta_-^2] + \\ & -20 [|\Omega_+|^2 \delta_- + |\Omega_-|^2 \delta_+]^2 + 20|\Omega_+|^2 |\Omega_-|^2 [\delta_- - \delta_+]^2 + \\ & 8 [|\Omega_-|^2 \delta_- + |\Omega_+|^2 \delta_+] [|\Omega_-|^2 \delta_+ + |\Omega_+|^2 \delta_-] + \\ & 16 [1 + (\delta_- - \delta_+)^2] [|\Omega_+|^2 \delta_-^2 + |\Omega_-|^2 \delta_+^2] + \\ & 4 [1 + 4\delta_-^2] [1 + 4\delta_+^2] [1 + (\delta_- - \delta_+)^2] \end{aligned} \quad (\text{A.3})$$

The ground state population is given by $\rho_{g,g}^{ss} = 1 - \rho_{+,+}^{ss} - \rho_{-,-}^{ss}$.

A.1 V-atom Equation of Motion

$$\begin{aligned}
\dot{\rho}_{-,-} &= -\Gamma\rho_{-,-} - \frac{i}{2}(\Omega_-\rho_{g,-} - \Omega_-^*\rho_{-,g}) \\
\dot{\rho}_{-,+} &= -[\Gamma + i(\Delta_- - \Delta_+ - 2\Delta_B)]\rho_{-,+} - \frac{i}{2}(\Omega_-\rho_{g,+} - \Omega_+^*\rho_{-,g}) \\
\dot{\rho}_{-,g} &= -\left[\frac{\Gamma}{2} + i(\Delta_- - \Delta_B)\right]\rho_{-,g} + \frac{i}{2}\Omega_+\rho_{-,+} + \frac{i\Omega_-}{2}(\rho_{-,-} - \rho_{g,g}) \\
\dot{\rho}_{+,-} &= -[\Gamma - i(\Delta_- - \Delta_+ - 2\Delta_B)]\rho_{+,-} + \frac{i}{2}(\Omega_-^*\rho_{+,g} - \Omega_+\rho_{g,-}) \\
\dot{\rho}_{+,+} &= -\Gamma\rho_{+,+} - \frac{i}{2}(\Omega_+\rho_{g,+} - \Omega_+^*\rho_{+,g}) \\
\dot{\rho}_{+,g} &= -\left[\frac{\Gamma}{2} + i(\Delta_+ + \Delta_B)\right]\rho_{+,g} + \frac{i}{2}\Omega_-\rho_{+,-} + \frac{i\Omega_+}{2}(\rho_{+,+} - \rho_{g,g}) \\
\dot{\rho}_{g,+} &= -\left[\frac{\Gamma}{2} - i(\Delta_+ + \Delta_B)\right]\rho_{g,+} - \frac{i}{2}\Omega_-^*\rho_{-,+} - \frac{i\Omega_+^*}{2}(\rho_{+,+} - \rho_{g,g}) \\
\dot{\rho}_{g,-} &= -\left[\frac{\Gamma}{2} - i(\Delta_- - \Delta_B)\right]\rho_{g,-} - \frac{i}{2}\Omega_+^*\rho_{+,-} - \frac{i\Omega_-^*}{2}(\rho_{-,-} - \rho_{g,g}) \\
\dot{\rho}_{g,g} &= \Gamma(\rho_{-,-} + \rho_{+,+}) + \frac{i}{2}(\Omega_-\rho_{g,-} - \Omega_-^*\rho_{-,g}) + \frac{i}{2}(\Omega_+\rho_{g,+} - \Omega_+^*\rho_{+,g})
\end{aligned} \tag{A.4}$$

A.2 $J_g = 0 \rightarrow J_e = 1$ Equation of Motion

$$\begin{aligned}\dot{\rho}_{-,-} &= -\Gamma\rho_{-,-} - \frac{i}{2}(\Omega_-\rho_{g,-} - \Omega_-^*\rho_{-,g}) \\ \dot{\rho}_{-,0} &= -[\Gamma + i(\Delta_- - \Delta_B - \Delta_0)]\rho_{-,0} - \frac{i}{2}\Omega_-\rho_{g,0} + \frac{i}{2}\Omega_0^*\rho_{-,g}\end{aligned}\quad (\text{A.5a})$$

$$\begin{aligned}\dot{\rho}_{-,+} &= -[\Gamma + i(\Delta_- - \Delta_+ - 2\Delta_B)]\rho_{-,+} - \frac{i}{2}(\Omega_-\rho_{g,+} - \Omega_+^*\rho_{-,g}) \\ \dot{\rho}_{-,g} &= -\left[\frac{\Gamma}{2} + i(\Delta_- - \Delta_B)\right]\rho_{-,g} + \frac{i}{2}\Omega_+\rho_{-,+} + \frac{i}{2}\Omega_0\rho_{-,0} + \frac{i\Omega_-}{2}(\rho_{-,-} - \rho_{g,g}) \\ \dot{\rho}_{0,-} &= -[\Gamma + i(\Delta_0 - \Delta_- + \Delta_B)]\rho_{0,-} + \frac{i}{2}\Omega_-^*\rho_{0,g} - \frac{i}{2}\Omega_0\rho_{g,-}\end{aligned}\quad (\text{A.5b})$$

$$\dot{\rho}_{0,0} = -\Gamma\rho_{0,0} - \frac{i}{2}(\Omega_0\rho_{g,0} - \Omega_0^*\rho_{0,g}) \quad (\text{A.5c})$$

$$\dot{\rho}_{0,+} = -[\Gamma + i(\Delta_0 - \Delta_+ - \Delta_B)]\rho_{0,+} + \frac{i}{2}\Omega_+^*\rho_{0,g} - \frac{i}{2}\Omega_0\rho_{g,+} \quad (\text{A.5d})$$

$$\dot{\rho}_{0,g} = -\left[\frac{\Gamma}{2} + i\Delta_0\right]\rho_{0,g} + \frac{i}{2}\Omega_-\rho_{0,-} + \frac{i}{2}\Omega_+\rho_{0,+} - \frac{i\Omega_0}{2}(\rho_{g,g} - \rho_{0,0}) \quad (\text{A.5e})$$

$$\begin{aligned}\dot{\rho}_{+,-} &= -[\Gamma - i(\Delta_- - \Delta_+ - 2\Delta_B)]\rho_{+,-} - \frac{i}{2}\Omega_+\rho_{g,-} + \frac{i}{2}\Omega_-^*\rho_{+,g} \\ \dot{\rho}_{+,0} &= -[\Gamma + i(\Delta_+ + \Delta_B - \Delta_0)]\rho_{+,0} - \frac{i}{2}\Omega_+\rho_{g,0} + \frac{i}{2}\Omega_0^*\rho_{+,g}\end{aligned}\quad (\text{A.5f})$$

$$\begin{aligned}\dot{\rho}_{+,+} &= -\Gamma\rho_{+,+} - \frac{i}{2}(\Omega_+\rho_{g,+} - \Omega_+^*\rho_{+,g}) \\ \dot{\rho}_{+,g} &= -\left[\frac{\Gamma}{2} + i(\Delta_+ + \Delta_B)\right]\rho_{+,g} + \frac{i}{2}\Omega_-\rho_{+,-} + \frac{i}{2}\Omega_0\rho_{+,0} - \frac{i\Omega_+}{2}(\rho_{g,g} - \rho_{+,+}) \\ \dot{\rho}_{g,0} &= -\left[\frac{\Gamma}{2} - i\Delta_0\right]\rho_{g,0} - \frac{i}{2}\Omega_-^*\rho_{-,0} - \frac{i}{2}\Omega_+^*\rho_{+,0} + \frac{i\Omega_0^*}{2}(\rho_{g,g} - \rho_{0,0})\end{aligned}\quad (\text{A.5g})$$

$$\dot{\rho}_{g,+} = -\left[\frac{\Gamma}{2} - i(\Delta_+ + \Delta_B)\right]\rho_{g,+} - \frac{i}{2}\Omega_-^*\rho_{-,+} - \frac{i}{2}\Omega_0^*\rho_{0,+} + \frac{i\Omega_+^*}{2}(\rho_{g,g} - \rho_{+,+})$$

$$\dot{\rho}_{g,-} = -\left[\frac{\Gamma}{2} - i(\Delta_- - \Delta_B)\right]\rho_{g,-} - \frac{i}{2}\Omega_+^*\rho_{+,-} - \frac{i}{2}\Omega_0^*\rho_{0,-} + \frac{i\Omega_-^*}{2}(\rho_{g,g} - \rho_{-,-})$$

$$\begin{aligned}\dot{\rho}_{g,g} &= \Gamma(\rho_{0,0} + \rho_{-,-} + \rho_{+,+}) - \frac{i}{2}(\Omega_-^*\rho_{-,g} - \Omega_-\rho_{g,-}) + \\ &\quad - \frac{i}{2}(\Omega_+^*\rho_{+,g} - \Omega_+\rho_{g,+}) - \frac{i}{2}(\Omega_0^*\rho_{0,g} - \Omega_0\rho_{g,0})\end{aligned}$$

APPENDIX B

DUAL POLARIZER NOISE REDUCTION

Let the output of the fiber have electric field $\vec{E} = E\hat{E}$ with polarization angle $\alpha + \delta_n(t)$ where $\delta_n(t)$ is a small amount of noise (on the order of a few degrees). This field, along with its relation to polarizers are shown in Figure B.1.

B.1 One Polarizer

As shown in Figure B.1a, one polarizer has polarization vector \hat{D}_{out} at angle γ . After passing through this polarizer, the electric field becomes

$$\vec{E}_{out} = \left(\vec{E} \cdot \hat{D}_{out} \right) \hat{D}_{out} = E \cos [\gamma - \alpha - \delta_n(t)] \hat{D}_{out}.$$

The power output is then

$$P_{out} = P_{in} \cos^2 [\gamma - \alpha - \delta_n(t)].$$

Doing a series expansion around small angles $\delta_n(t) \approx 0$, the power output is

$$P_{out}^{1 \text{ pol}} = P_{in} \cos^2 [\gamma - \alpha] + 2P_{in} \cos(\gamma - \alpha) \sin(\gamma - \alpha) \delta_n(t) + P_{in} [\sin^2(\gamma - \alpha) - \cos^2(\gamma - \alpha)] \delta_n^2(t).$$

In general, the noise in the power output of the beam is of order $\delta_n(t)$, except in limiting cases where $\gamma - \alpha = \frac{n\pi}{2}$.

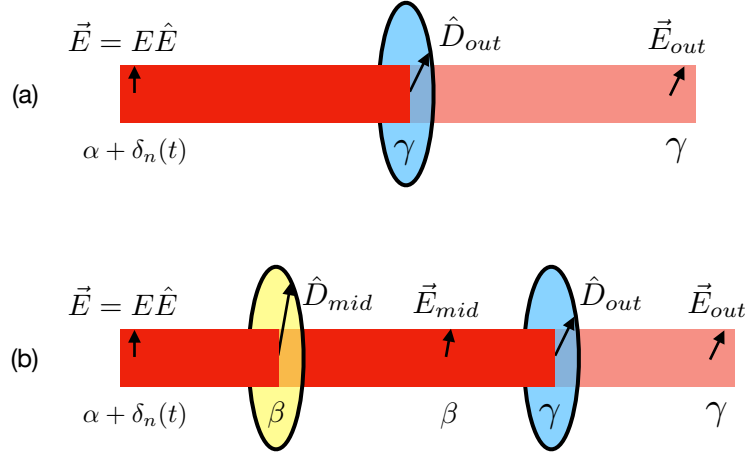


FIGURE B.1. Laser power control with polarizers. (a) Electric field names (above beam) and field polarization directions (below beams) before and after one polarizer. (b) Electric field names and field directions before, between, and after two polarizer.

B.2 Two Polarizers

As shown in Figure B.1b, assume there is a middle polarizer between the fiber and output polarizer. The middle polarizer has polarization vector \hat{D}_{mid} at angle β . Then after the middle polarizer the electric field is

$$\vec{E}_{mid} = (\vec{E} \cdot \hat{D}_{mid}) \hat{D}_{mid} = E \cos[\beta - \alpha - \delta_n(t)] \hat{D}_{mid}.$$

After the output polarizer, the electric field is

$$\vec{E}_{out} = (\vec{E}_{mid} \cdot \hat{D}_{out}) \hat{D}_{out} = E \cos[\beta - \alpha - \delta_n(t)] \cos[\gamma - \beta] \hat{D}_{out}.$$

where, again, γ is the angle of the output polarization vector \hat{D}_{out} . The power output is

$$P_{out} = P_{in} \cos^2[\beta - \alpha - \delta_n(t)] \cos^2[\gamma - \beta].$$

Doing another expansion for small noise, the power is

$$P_{out} = P_{in} \cos^2 [\beta - \alpha] \cos^2 [\gamma - \beta] + 2P_{in} \cos(\beta - \alpha) \sin(\beta - \alpha) \cos^2 [\gamma - \beta] \delta_n(t) + P_{in} \cos^2 [\gamma - \beta] [\sin^2(\beta - \alpha) - \cos^2(\beta - \alpha)] \delta_n^2(t).$$

If the middle polarizer is aligned with the ideal polarization axis of the fiber $\beta = \alpha$, this becomes

$$P_{out}^{\text{pol}} = P_{in} \cos^2 [\gamma - \alpha] - P_{in} \cos^2 [\gamma - \alpha] \delta_n^2(t).$$

Therefore, for the 2 polarization setup, the noise is reduced to order $\delta_n^2(t)$.

APPENDIX C

MOT COIL WATER COOLING RATE

Due to large current used in the experimental anti-Helmholtz coils, they are designed to be water-cooled to prevent overheating. This cooling method is analyzed in detail here.

C.1 Heat Equation

In considering the heating of the coils, the only input source of energy is the power dissipated by the current, $P = I^2 R$. This heating is dissipated by 5 mechanisms:

- Heating the water via conduction, Q_{water}
- Power radiated from coils, P_{rad}
- Heating the aluminum coil mount, Q_{Al}
- Heating the copper wires, Q_{Cu}
- Heating the air around the coils via conduction, Q_{air}

Equating the input and output powers gives,

$$I^2 R = \frac{d}{dt} Q_{water} + P_{rad} + \frac{d}{dt} Q_{Al} + \frac{d}{dt} Q_{Cu} + \frac{d}{dt} Q_{air} \quad (C.1)$$

A few simplifications should be made. Assume the copper and aluminum of the coils have the same temperature. Both the convection to the air and the radiated power are much smaller than the convection to the water and heating of the coils, so both of these terms can be dropped¹². The heating rate to the water, Q_{water} , is derived below

¹²Including conduction to the air changes the growth rate of the temperature, the variable γ in as defined in equation C.8, by less than 1%. The radiative power dissipated, even though it scales as T^4 , is a few orders of magnitude less than other loss mechanisms.

in Section C.2. The heating of the aluminum and copper follows from introductory thermodynamics as

$$Q_{\text{Al}} = m_{\text{Al}}C_{\text{Al}}\Delta T \quad (\text{C.2})$$

$$Q_{\text{Cu}} = m_{\text{Cu}}C_{\text{Cu}}\Delta T, \quad (\text{C.3})$$

respectively. Additionally, the resistance of the coils will change as the coils change temperature as,

$$R(T) = R_0 [1 + \alpha(T - T_0)] \quad (\text{C.4})$$

where R_0 and T_0 are a reference resistance and temperature respectively.

Combing these equations with C.1 gives

$$I^2 R_0 [1 + \alpha(T - T_0)] = \dot{m}_w C_w (T - T_w) \left(1 - \exp \left[\frac{-h_c A}{\dot{m}_w C_w} \right] \right) + (mC)_{eff} \frac{\partial T}{\partial t}, \quad (\text{C.5})$$

where \dot{m}_w is the water mass flow rate through the cooling channel and $(mC)_{eff}$ is an effective value for the combined heating of the aluminum mount and copper wires. If they have the same temperature at all times, then this equals

$$(mC)_{eff} = m_{\text{Al}}C_{\text{Al}} + m_{\text{Cu}}C_{\text{Cu}}. \quad (\text{C.6})$$

Because of the large contact area between the wires and mount and their relatively small volume, it is safe to make this equal-temperature assumption.

The power equation has the form

$$\frac{\partial T}{\partial t} = \gamma T + \beta \quad (\text{C.7})$$

with

$$\gamma = \frac{I^2 R_0 \alpha - \dot{m} C_w \left(1 - \exp\left[\frac{-h_c A}{\dot{m} C_w}\right]\right)}{(mC)_{eff}} \quad (\text{C.8})$$

$$\beta = \frac{I^2 R_0 (1 - \alpha T_0) + \dot{m} C_w T_w \left(1 - \exp\left[\frac{-h_c A}{\dot{m} C_w}\right]\right)}{(mC)_{eff}} \quad (\text{C.9})$$

The differential equation is solved by

$$T(t) = \left(T_w + \frac{\beta}{\gamma}\right) e^{\gamma t} - \frac{\beta}{\gamma} \quad (\text{C.10})$$

This result is problematic if $\gamma > 0$. The limiting case where $\gamma = 0$ (i.e. when the heating just balances the cooling) gives a steady state temperature of T_w when the current is

$$I_{\text{lim}} = \sqrt{\frac{\dot{m} C_w}{R_0 \alpha} \left(1 - \exp\left[\frac{-h_c A}{\dot{m} C_w}\right]\right)}. \quad (\text{C.11})$$

Currents above this will heat the coils indefinitely ($\gamma > 0$) according to the model. This indefinitely heating results from ignoring radiative and thermal conduction to the air. Currents below I_{lim} will result in a steady temperature of $T_f = \beta/|\gamma|$. As noted in the text, currents used in the experiment are far below I_{lim} .

With the solution for $T(t)$, the resistance of the wires as a function of time becomes

$$R(t) = R'_0 \left[1 + R_m \left(1 - e^{-|\gamma|t}\right)\right], \quad (\text{C.12})$$

where R'_0 is the chilled coil resistance

$$R'_0 = R_0 [1 - \alpha(T_0 - T_w)] \quad (\text{C.13})$$

Parameter	Value
Aluminum support volume	$3.52 \times 10^{-5} \text{ m}^3$
Copper wire volume	$1.73 \times 10^{-5} \text{ m}^3$
Water flow rate, \dot{m}_w [141] ¹³	3.43 litre / min = 0.217 kg / s
Water chiller set temperature, T_w	15°C
Cooling channel Length, L	$9.7 \times 10^{-2} \text{ m}$
Cooling channel surface area, A	$3.29 \times 10^{-2} \text{ m}^2$

TABLE C.1. Water-cooled MOT coil parameters. Variable names reference equations C.2, C.3, and C.5.

T_0 is a reference temperature used in defining the “normal” resistance of the wires, R_0 , and R_m is a maximum change of resistance

$$R_m = \frac{I^2 R_0}{|\gamma| (mC)_{eff}} = \left| \alpha - \frac{\dot{m} C_w}{I^2 R} \left(1 - \exp \left[\frac{-h_c A}{\dot{m} C_w} \right] \right) \right|^{-1}. \quad (\text{C.14})$$

As noted in the text, measuring the resistance of the anti-Helmholtz coils as a function of time is straightforward and provides a clear method to find a value for γ .

C.2 Water Cooling Rate Derivation

A closed channel through which water flows can be used to regulate the temperature of the bulk medium. The rate that heat flows from the bulk into the water and leaves the medium is calculated here, following the general formalism of [142].

Divide the length of the channel into a small segment dx , as shown in figure C.1. The mass of water, dm , that flows through this channel in time dt will absorb heat,

¹³We cannot locate a manual for our chiller, RTE100. The RTE101 has the same specifications as our chiller and the plumbing and circuit diagrams match the innards of our chiller, leading us to trust the RTE101 manual.

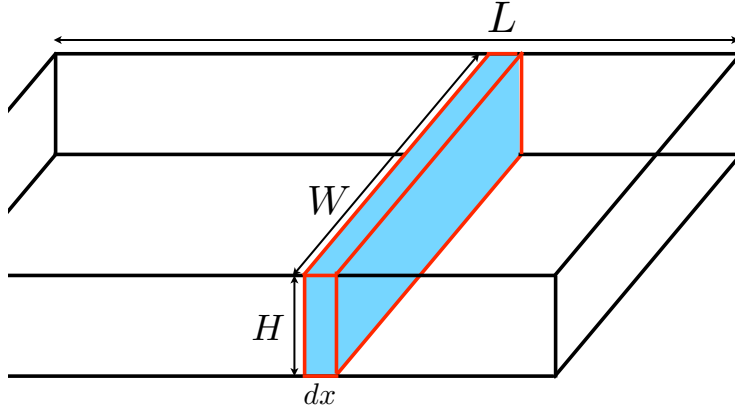


FIGURE C.1. Water cooling channel dimensions

dq , from the walls of the channel according to

$$dq = \dot{q}dt, \quad (\text{C.15})$$

where \dot{q} is the rate of heat transfer. This rate is from conduction from the walls into the fluid, which follows

$$\dot{q} = h_c(T_s - T_f)dA, \quad (\text{C.16})$$

where dA is the surface area of the fluid that is in contact with walls of the channel, h_c is the conduction coefficient (discussed below in Section C.3), and T_s is the (fixed) temperature of the walls of the channel and T_f is the temperature of the fluid. If the perimeter of the volume of water has length P , then the surface area is just $dA = Pdx$.

Assume the heat is absorbed uniformly throughout the fluid (there is no temperature gradient from the surface into the bulk of the liquid), so that the absorbed heat will warm the water by an amount dT as

$$dq = dmCdT_f, \quad (\text{C.17})$$

where C is the specific heat of the water. Combining equations C.15 through C.17 gives

$$h_c(T_s - T_f)Pdx = \frac{dm}{dt}CdT_f. \quad (\text{C.18})$$

In this equation dm/dt is just the mass flow rate through the fluid, \dot{m} . The total change in the temperature from the input, T_{in} , to the output, T_{out} , is found by integrating along the total length of the channel, L .

$$\begin{aligned} \frac{h_c P}{\dot{m} C} \int_0^L dx &= \int_{T_{input}}^{T_{output}} \frac{dT_f}{T_s - T_f} \\ \exp\left[\frac{-h_c P L}{\dot{m} C}\right] &= \frac{T_s - T_{out}}{T_s - T_{in}} \end{aligned} \quad (\text{C.19})$$

Now, consider the total heat absorbed by the water in the channel,

$$Q = mC(T_{out} - T_{in}). \quad (\text{C.20})$$

This occurs at a rate

$$\dot{Q} = \dot{m}C(T_s - T_{in}) \left[1 - \frac{T_s - T_{out}}{T_s - T_{in}}\right]. \quad (\text{C.21})$$

Using the result of equation C.19 gives an equation for the rate that heat is absorbed into the water from the bulk of

$$\dot{Q} = \dot{m}C(T_s - T_{in}) \left[1 - \exp\left[\frac{-h_c A}{\dot{m} C}\right]\right], \quad (\text{C.22})$$

where $A = PL$ is the total surface area of the water-flow channel and T_s is the temperature of the walls of the water-flow channel.

C.3 Conduction Coefficient

The conduction coefficient, h_c can be related to the Nusselt Number, N_u a ratio between the thermal conduction of heat from surface into fluid and the thermal convection of heat into into the fluid. This is,

$$N_u = \frac{h_c L_c}{k} \quad (\text{C.23})$$

where L_c is a characteristic length of a flow and k is the thermal conductivity of the fluid. For a long rectangular channel with a width that is 4-times the height and a uniform temperature of the channel, the Nusselt number is 4.439 [142]. The characteristic length for a flow through a long tube is

$$L_c = 4 \frac{\text{cross-sectional area}}{\text{perimeter of cross-sectional area}} = \frac{2HW}{H + W} \quad (\text{C.24})$$

where H and W are as shown in figure C.1. This gives a conduction coefficient of

$$h_c = \frac{k N_u (H + W)}{HW} \quad (\text{C.25})$$

Relating this to our experiment, for water, $k = 0.6098 \text{ W / mK}$ [143], and our channel has $H = 1/8''$ and $W = 1/2''$. These give the conduction coefficient $h_c = 5.3 \times 10^2 \text{ W / K m}^2$.

APPENDIX D

BAYESIAN EVOLUTION DERIVATION

Equation 4.4 gives the probability distribution for fluorescence rate (variable x) from a single atom, $Fl_{1\text{-at}}(x)$. With a known number of atoms in the MOT, the measurement of the fluorescence from n atoms in the MOT can be used to update information about the fluorescence rate average, R , and standard deviation, σ_R , from one atom with Bayes theorem.

With a noisy measurement, y as in section 4.2.3, the noise in a measurement must have value

$$\zeta = y - (B + nr), \quad (\text{D.1})$$

where B is the (assumed constant) background fluorescence rate, n the number of atoms in a MOT, and r is the single-atom fluorescence rate. The probability for the noise to have this value is

$$p(\zeta = y - B + nr) = \frac{1}{\sqrt{2\pi\sigma_\zeta^2}} \exp\left[-\frac{(y - (B + nr))^2}{2\sigma_\zeta^2}\right],$$

which is similar to Equation 4.8 with multiple atoms in the MOT. Then, Bayes' theorem just says that the single atom signal fluorescence evolves according to

$$Fl_{1\text{-at}}(r) \rightarrow \frac{Fl_{1\text{-at}}(r)p(\zeta = y - B + nr)}{\int_{-\infty}^{\infty} Fl_{1\text{-at}}(r)p(\zeta = y - B + nr) dr}$$

The normalization function is

$$\int_{-\infty}^{\infty} Fl_{1\text{-at}}(r)p(\zeta = y - B + nr) dr = \frac{1}{2\pi\sigma_R\sigma_{zeta}} \times \int_{-\infty}^{\infty} \exp\left[\frac{-(r-R)^2}{2\sigma_R^2}\right] \exp\left[\frac{-(y-(B+Nr))^2}{2\sigma_{\zeta}^2}\right] dr,$$

which integrates to

$$\frac{1}{\sqrt{2\pi(\sigma_R^2 N^2 + \sigma_{\zeta}^2)}} \exp\left[\frac{-(y-(B+NR))^2}{2(\sigma_R^2 N^2 + \sigma_{\zeta}^2)}\right]. \quad (\text{D.2})$$

Thus, the single-atom fluorescence probability evolves according to

$$\begin{aligned} Fl_{1\text{-at}}(r) &\rightarrow \frac{1}{\sqrt{2\pi\frac{\sigma_R^2\sigma_{\zeta}^2}{(\sigma_R^2 n^2 + \sigma_{\zeta}^2)}}} \exp\left[\frac{-(r-R)^2}{2\sigma_R^2}\right] \exp\left[\frac{-(y-(B+nr))^2}{2\sigma_{\zeta}^2}\right] \times \\ &\quad \exp\left[\frac{-(y-(B+nR))^2}{2(\sigma_R^2 n^2 + \sigma_{\zeta}^2)}\right] \\ &= \frac{1}{\sqrt{2\pi}\sqrt{\frac{\sigma_R^2\sigma_{\zeta}^2}{n^2\sigma_R^2 + \sigma_{\zeta}^2}}} \times \exp\left[\frac{-\left[r - \frac{(R\sigma_{\zeta}^2 + y n \sigma_R^2 - B n \sigma_R^2)}{n^2\sigma_R^2 + \sigma_{\zeta}^2}\right]^2}{2\frac{\sigma_R^2\sigma_{\zeta}^2}{n^2\sigma_R^2 + \sigma_{\zeta}^2}}\right]. \end{aligned}$$

This is, of course, just a Gaussian. Starting at i , and evolving to $i+1$ while measuring data point y_{i+1} , the average and variance evolve as:

$$\begin{aligned} R_{i+1} &= \frac{R_i\sigma_{\zeta}^2 + (y_i - B)n\sigma_{R,i}^2}{n^2\sigma_{R,i}^2 + \sigma_{\zeta}^2} \\ \sigma_{R,i+1}^2 &= \frac{\sigma_{R,i}^2\sigma_{\zeta}^2}{n^2\sigma_{R,i}^2 + \sigma_{\zeta}^2}. \end{aligned} \quad (\text{D.3})$$

It is good to note that if $n = 0$, then $R_{i+1} = R_i$ and $\sigma_{R,i+1}^2 = \sigma_{R,i}^2$. This should be the case as with no atoms in the MOT, no information can be gained about the

fluorescence rate from a single atom. For this reason, when there are no atoms in the MOT, our algorithm instead updates the background fluorescence rate average and standard deviation as discussed in Section 4.2.6.

APPENDIX E

GAUSSIAN SAMPLED OSCILLATION AMPLITUDE

Photons are measured by the APD as both a background rate, β , which is Gaussian-distributed with average rate B and a fluorescence rate from the atom, α which is Gaussian distributed with variance σ_α and whose average oscillates in time as described in the text:

$$\alpha(t) = \alpha_0 [1 + m_\alpha \cos(2\pi f_\alpha t)]. \quad (6.22)$$

These two random values are sampled together, so that their total rate f and rate variance σ^2 are just the sum of the two,

$$\begin{aligned} fl(t) &= \langle Fl \rangle [1 + \epsilon \cos(2\pi f_\alpha t)] \\ \sigma^2 &= \sigma_B^2 + \sigma_\alpha^2, \end{aligned} \quad (E.1)$$

with average total background fluorescence and (dimensionless) total fluorescence oscillation amplitude defined as

$$\begin{aligned} \langle Fl \rangle &= B + \alpha_0, \text{ and} \\ \epsilon &= \alpha_0 m_\alpha / (B + \alpha_0). \end{aligned} \quad (E.2)$$

For single-atom fluorescence, as shown in Figure 4.3, the fluorescence is relatively close to a Poisson distribution and can be written after time T as

$$\sigma^2(T) = \langle fl(T) \rangle (1 + \eta), \quad (E.3)$$

where η is a parameter that compares the variance to the mean rate. Because of the Gaussian assumption for the photon rates, as time progresses both the variance and the mean for the fluorescence distribution grows linearly. Thus, the parameter η is constant over all times. The variances as measured in Figure 4.3 should then hold for estimates of the oscillation parameter (m) for the atom. Photon arrivals between time $t = 0$ and $t = T$ produce a pulse chain,

$$p(t) = \sum_i \delta(t - t_i) \quad (\text{E.4})$$

which has a power spectrum [132]

$$S(f) = \frac{1}{T} [\langle fl(T) \rangle + \{ \langle fl^2(T) \rangle - \langle fl(T) \rangle \} \langle e^{i2\pi f(t_c - t_{c'})} \rangle], \quad (\text{E.5})$$

where the brackets donate statistical averages and the exponentials result from Fourier transforms of the photon arrivals [144]. With a variance defined relative to the average rate, it is possible to write

$$\langle fl^2 \rangle = \sigma^2 - \langle fl \rangle^2 = \langle fl \rangle + \langle fl \rangle \eta - \langle fl \rangle^2, \quad (\text{E.6})$$

which simplifies the power spectrum to

$$S(f) = \frac{1}{T} [\langle fl(T) \rangle + \{ \langle fl(T) \rangle^2 + \eta \langle fl(T) \rangle \} \langle e^{i2\pi f(t_c - t_{c'})} \rangle]. \quad (\text{E.7})$$

To calculate the statistical average of the exponential, integrate over both t_c and $t_{c'}$ with both exponentials normalized by average photon rate. This produces

$$\langle e^{i2\pi f(t_c - t_{c'})} \rangle = \frac{1}{\langle f(T) \rangle^2} \left| \int_0^T f(t) e^{-i2\pi ft} dt \right|^2, \quad (\text{E.8})$$

so that the spectrum becomes

$$S(f) = \frac{1}{T} \left[\langle f(T) \rangle + \left| \int_0^T f(t) e^{-i2\pi ft} dt \right|^2 \right] + \frac{\eta}{T} \frac{\left| \int_0^T f(t) e^{-i2\pi ft} dt \right|^2}{\langle f(T) \rangle}. \quad (\text{E.9})$$

The first term is identical to the Poisson-distributed rate calculated by Matzner and Bar-Gad [132], while the second term corresponds to the Gaussian modification made here. The added noise from the Gaussian-distributed fluorescence then increases the spectral power over the Poisson-distributed signal. The average fluorescence is given by

$$\langle f(T) \rangle = \int_0^T f(t) dt = \langle Fl \rangle T [1 + \epsilon \text{sinc}(2\pi f_\alpha T)]. \quad (\text{E.10})$$

In the limit of small ϵ and at $f = f_\alpha$, the last term is

$$\begin{aligned} \frac{\eta}{T} \frac{\left| \int_0^T fl(t) e^{-i2\pi ft} dt \right|^2}{\langle fl(T) \rangle} &= \eta \langle Fl \rangle \times \left[\frac{\epsilon^2}{4} + \text{sinc}(\pi f_\alpha T) + \epsilon \text{sinc}(\pi f_\alpha T) + \right. \\ &\quad \left. \frac{\epsilon^2}{4} \text{sinc}(2\pi f_\alpha T) \{1 + 4 \text{sinc}(\pi f_\alpha T) + \text{sinc}(2\pi f_\alpha T)\} \right]. \end{aligned} \quad (\text{E.11})$$

All of the oscillating terms decay rapidly at high frequencies (or long times), so they can be dropped. Inserting the Poisson-distributed spectrum, gives a final form for the power spectrum at $f = f_\alpha$

$$S(f = f_\alpha) = \langle Fl \rangle + \frac{\langle Fl \rangle^2 T \epsilon^2}{4} + \eta \frac{\epsilon^2 \langle Fl \rangle}{4}. \quad (\text{E.12})$$

Similarly, far from the driving frequency, f_α , the spectrum becomes just

$$S(f \rightarrow \infty) = \langle Fl \rangle, \quad (\text{E.13})$$

which is just the average measured fluorescence rate (from the background and an atom). Now, from the power spectrum from the APD, the oscillation amplitude can be measured as

$$\epsilon = \sqrt{\frac{4[S(f = f_\alpha) - \langle Fl \rangle]}{\langle Fl \rangle^2 T + \eta \langle Fl \rangle}} \quad (\text{E.14})$$

Just setting $\eta = 0$ returns the Poisson-distributed result of Matzner and Bar-Gad [132] for the oscillation parameter m_p . Comparing these results gives

$$\epsilon = \sqrt{\frac{\langle Fl \rangle T}{\langle Fl \rangle T + \eta}} m_p. \quad (\text{E.15})$$

The quantity $\langle Fl \rangle T$ is the total number of photons counted in time T without any oscillations. This value should be much larger than the added super-Poissonian noise, η . Using the simpler Poisson result of Matzner and Bar-Gad is justified.

The atom's fluorescence is responsible for the oscillations. Then writing the Poisson form of ϵ (setting $\eta = 0$) in terms of the atomic oscillation amplitude gives

$$m_\alpha = \frac{2}{\alpha_0} \sqrt{\frac{S(f = f_\alpha) - (B + \alpha_0)}{T}}. \quad (\text{E.16})$$

APPENDIX F

PARAMETRIC RESONANCE DERIVATION

A parametric resonator is one where the value for the restoring spring constant oscillates [131]. This means that the resonant frequency also oscillates. . Taking the simplest equation for a damped, harmonic oscillator and allowing it to become parametric gives the differential equation for its position, z

$$\ddot{z} + \frac{\beta}{m}\dot{z} + \frac{\kappa}{m}z[1 + \cos(\omega t)] = 0 \quad (\text{F.1})$$

where m is the mass of the oscillator, κ is the restoring force spring constant, β is the damping coefficient, and ω is the oscillation frequency of the parametric spring constant. This frequency is not necessarily the same as the constant oscillation frequency, $\omega_0 = \sqrt{\kappa/m}$. Assume that the differential equation can be solved by an equation $z(t)$ given by

$$\begin{aligned} z(t) &= a(t) \cos(\nu t) + b(t) \sin(\nu t) \\ \dot{z}(t) &= [\dot{a}(t) + \nu b(t)] \cos(\nu t) + [\dot{b}(t) - \nu a(t)] \sin(\nu t) \\ \ddot{z}(t) &= [\ddot{a}(t) + 2\nu\dot{b}(t) - \nu^2 a(t)] \cos(\nu t) + [\ddot{b}(t) - 2\nu\dot{a}(t) - \nu^2 b(t)] \sin(\nu t) \end{aligned} \quad (\text{F.2})$$

for some frequency ν . Putting these equations into the differential equation F.1 gives

$$\begin{aligned} 0 &= \left[\ddot{a} + 2\nu\dot{b} - \nu^2 a + \frac{\beta}{m}\dot{a} + \omega_0^2 \nu b + \omega_0^2 a + \omega_0^2 a \epsilon \cos \omega t \right] \cos(\nu t) + \\ &\quad \left[\ddot{b} - 2\nu\dot{a} - \nu^2 b + \frac{\beta}{m}\dot{b} - \frac{\beta}{m}\nu a + \omega_0^2 b + \omega_0^2 b \epsilon \cos \omega t \right] \sin(\nu t). \end{aligned}$$

Replacing the two frequencies with the natural frequency of the oscillator and a small deviation frequency ζ :

$$\begin{aligned}\omega &\rightarrow 2\omega_0 + \zeta \\ \nu &\rightarrow \omega_0 + \frac{1}{2}\zeta,\end{aligned}\tag{F.3}$$

and noting that

$$\begin{aligned}\cos(\omega t) \cos(\nu t) &= \cos [(\omega + \nu)t] + \cos [(\omega - \nu)t] = \cos [3\nu t] + \cos [\nu t] \\ \cos(\omega t) \sin(\nu t) &= \sin [(\omega + \nu)t] - \sin [(\omega - \nu)t] = \sin [3\nu t] - \sin [\nu t],\end{aligned}$$

the differential equation becomes

$$\begin{aligned}0 &= \left[\ddot{a} + 2\nu\dot{b} - \nu^2 a + \frac{\beta}{m}\dot{a} + \frac{\beta}{m}\nu b + \omega_0^2 a + \omega_0^2 a\epsilon \right] \cos(\nu t) + \\ &\quad \left[\ddot{b} - 2\nu\dot{a} - \nu^2 b + \frac{\beta}{m}\dot{b} - \frac{\beta}{m}\nu a + \omega_0^2 b - \omega_0^2 b\epsilon \right] \sin(\nu t),\end{aligned}$$

after dropping the quickly rotating 3ν terms. Further, assume that

$$\begin{aligned}\dot{a} &\sim \zeta a \\ \dot{b} &\sim \zeta b\end{aligned}\tag{F.4}$$

Dropping terms that scale as the very small ζ^2 , the following changes are made to the differential equations:

$$\begin{aligned}\ddot{a} &\approx 0 \\ \ddot{b} &\approx 0 \\ \nu^2 &\approx \omega_0(\omega_0 + \zeta) \\ \nu\dot{a} &\approx \omega_0\dot{a} \\ \nu\dot{b} &\approx \omega_0\dot{b}.\end{aligned}$$

These changes give a final differential equation of the form

$$\begin{aligned}0 = & \left[2\dot{b} - \zeta a + \omega_0 \frac{\epsilon a}{2} + \frac{\beta \dot{a}}{\omega_0 m} + \frac{\beta \nu b}{\omega_0 m} \right] \cos(\nu t) + \\ & - \left[2\dot{a} + \zeta b + \omega_0 \frac{\epsilon b}{2} + \frac{\beta \nu a}{\omega_0 m} - \frac{\beta \dot{b}}{\omega_0 m} \right] \sin(\nu t).\end{aligned}$$

Under the assumption of small damping, $\beta \sim \zeta$, the differential equation can be simplified to

$$\begin{aligned}0 = & \left[2\dot{b} - \zeta a + \omega_0 \frac{\epsilon a}{2} + \frac{\beta}{m} b \right] \cos(\nu t) + \\ & - \left[2\dot{a} + \zeta b + \omega_0 \frac{\epsilon b}{2} + \frac{\beta}{m} a \right] \sin(\nu t).\end{aligned}$$

This is solved only when the coefficients for both $\cos(\nu t)$ and $\sin(\nu t)$ vanish. Forcing both to vanish produces coupled differential equations for \dot{a} and \dot{b} that follow the

vector equation

$$\frac{d}{dt} \begin{bmatrix} a \\ b \end{bmatrix} = - \begin{bmatrix} \frac{\beta}{2m} & (\frac{1}{4}\epsilon\omega_0 + \frac{\zeta}{2}) \\ (\frac{1}{4}\epsilon\omega_0 - \frac{\zeta}{2}) & \frac{\beta}{2m} \end{bmatrix} \begin{bmatrix} a \\ b \end{bmatrix}. \quad (\text{F.5})$$

Assuming an eigenvalue solution, the equations of motion are

$$a(t) = a_0 e^{-\lambda t}$$

$$b(t) = b_0 e^{-\lambda t}$$

with eigenvalue

$$\lambda = \frac{\beta}{2m} \mp \sqrt{\frac{1}{16}\epsilon^2\omega_0^2 - \frac{\zeta^2}{4}}. \quad (\text{F.6})$$

A non-parametric resonator will be damped to $z = 0$. This solution will behave similarly unless $\lambda < 0$. This exponential growth of the oscillator amplitude occurs if

$$\zeta^2 < \frac{1}{4}\epsilon^2\omega_0^2 - \frac{\beta^2}{m^2}.$$

In terms of the frequencies, this parametric resonance is excited for frequencies

$$2\omega_0 - \frac{\omega_0}{2}\sqrt{\epsilon^2 - \epsilon_{\text{TH}}^2} < \omega < 2\omega_0 + \frac{\omega_0}{2}\sqrt{\epsilon^2 - \epsilon_{\text{TH}}^2} \quad (\text{F.7})$$

if the parametric strength is above a threshold strength

$$\epsilon_{\text{TH}}^2 = \frac{4\beta^2}{m^2\omega_0^2}. \quad (\text{F.8})$$

REFERENCES CITED

- [1] T. Hänsch and A. Schawlow, *Optics Communications* **13**, 68 (1975).
- [2] V. S. Letokhov, V. G. Minogin, and B. D. Pavlik, *Journal of Experimental and Theoretical Physics* **45**, 698 (1977).
- [3] S. Chu, L. Hollberg, J. E. Bjorkholm, A. Cable, and A. Ashkin, *Phys. Rev. Lett.* **55**, 48 (1985).
- [4] E. L. Raab, M. Prentiss, A. Cable, S. Chu, and D. E. Pritchard, *Phys. Rev. Lett.* **59**, 2631 (1987).
- [5] A. Höpe, D. Haubrich, G. Müller, W. G. Kaenders, and D. Meschede, *Europhysics Letters* **22**, 669 (1993).
- [6] Z. Hu and H. J. Kimble, *Optics Letters* **19**, 1888 (1994).
- [7] S. B. Hill and J. J. McClelland, *Applied Physics Letters* **82**, 3128 (2003).
- [8] K. M. Fortier, S. Y. Kim, M. J. Gibbons, P. Ahmadi, and M. S. Chapman, *Physical Review Letters* **98** (2007).
- [9] M. J. Gibbons, C. D. Hamley, C.-Y. Shih, and M. S. Chapman, *Phys. Rev. Lett.* **106**, 133002 (2011).
- [10] L. Förster, W. Alt, I. Dotsenko, M. Khudaverdyan, D. Meschede, Y. Miroshnychenko, S. Reick, and A. Rauschenbeutel, *New Journal of Physics* **8**, 259 (2006).
- [11] Z. Zuo, M. Fukusen, Y. Tamaki, T. Watanabe, Y. Nakagawa, and K. Nakagawa, *Opt. Express* **17**, 22898 (2009).
- [12] D. Schrader, I. Dotsenko, M. Khudaverdyan, Y. Miroshnychenko, A. Rauschenbeutel, and D. Meschede, *Phys. Rev. Lett.* **93**, 150501 (2004).
- [13] Y. Miroshnychenko, D. Schrader, S. Kuhr, W. Alt, I. Dotsenko, M. Khudaverdyan, A. Rauschenbeutel, and D. Meschede, *Opt. Express* **11**, 3498 (2003).
- [14] D. B. Hume, I. Stroescu, M. Joos, W. Muessel, H. Strobel, and M. K. Oberthaler, *Phys. Rev. Lett.* **111**, 253001 (2013).
- [15] B. Ueberholz, S. Kuhr, D. Frese, V. Gomer, and D. Meschede, *Journal of Physics B* **35** (2002).

- [16] N. Spethmann, F. Kindermann, S. John, C. Weber, D. Meschede, and A. Widera, *Phys. Rev. Lett.* **109**, 235301 (2012).
- [17] F. Schmidt, D. Mayer, T. Lausch, D. Adam, Q. Bouton, M. Hohmann, F. Kindermann, J. Koch, J. Nettersheim, and A. Widera, *Physica Status Solidi B Early View*, 1800710.
- [18] C. Y. Chen, Y. M. Li, K. Bailey, T. P. O'Connor, L. Young, and Z.-T. Lu, *Science* **286** (1999).
- [19] J. Welte, F. Ritterbusch, I. Steinke, M. Henrich, W. Aeschbach-Hertig, and M. K. Oberthaler, *New Journal of Physics* **12**, 065031 (2010).
- [20] F. Ruschewitz, D. Bettermann, J. L. Peng, and W. Ertmer, *Europhysics Letters* **34**, 651 (1996).
- [21] Y. Choi, S. Yoon, S. Kang, W. Kim, J.-H. Lee, and K. An, *Phys. Rev. A* **76**, 013402 (2007).
- [22] J. Weiner, V. S. Bagnato, S. Zilio, and P. S. Julienne, *Rev. Mod. Phys.* **71**, 1 (1999).
- [23] V. Gomer, F. Strauch, B. Ueberholz, S. Knappe, and D. Meschede, *Phys. Rev. A* **58**, R1657 (1998).
- [24] V. Gomer, B. Ueberholz, S. Knappe, F. Strauch, D. Frese, and D. Meschede, *Applied Physics B* **67**, 689 (1998).
- [25] H. J. Metcalf and P. van der Straten, *Laser Cooling and Trapping* (Springer-Verlag, New York, 1999).
- [26] P. Kohns, P. Buch, W. Sptitz, C. Csambal, and W. Ertmer, *Europhysics Letters* **22**, 517 (1993).
- [27] A. M. Steane and C. J. Foot, *Europhysics Letters* **14**, 231 (1991).
- [28] C. Tuchendler, A. M. Lance, A. Browaeys, Y. R. P. Sortais, and P. Grangier, *Phys. Rev. A* **78**, 033425 (2008).
- [29] A. Fuhrmanek, A. M. Lance, C. Tuchendler, P. Grangier, Y. R. P. Sortais, and A. Browaeys, *New Journal of Physics* **12**, 053028 (2010).
- [30] P. D. Lett, R. N. Watts, C. I. Westbrook, W. D. Phillips, P. L. Gould, and H. J. Metcalf, *Phys. Rev. Lett.* **61**, 169 (1988).
- [31] A. Kastberg, W. D. Phillips, S. L. Rolston, R. J. C. Spreeuw, and P. S. Jessen, *Phys. Rev. Lett.* **74**, 1542 (1995).

- [32] W. Alt, D. Schrader, S. Kuhr, M. Müller, V. Gomer, and D. Meschede, *Phys. Rev. A* **67**, 033403 (2003).
- [33] W. Ketterle and N. V. Druten, *Advances In Atomic, Molecular, and Optical Physics* **37**, 181 (1996).
- [34] R. Grimm, M. Weidemüller, and Y. B. Ovchinnikov, *Advances In Atomic, Molecular, and Optical Physics* **42**, 95 (2000).
- [35] M. Weber, J. Volz, K. Saucke, C. Kurtsiefer, and H. Weinfurter, *Phys. Rev. A* **73**, 043406 (2006).
- [36] F. M. V. Gheorghe and G. Werth, *Charged Particle Traps* (Springer-Verlag, Heidelberg, 2005).
- [37] J. C. Bergquist, W. M. Itano, and D. J. Wineland, *Phys. Rev. A* **36**, 428 (1987).
- [38] A. D. Ludlow, M. M. Boyd, T. Zelevinsky, S. M. Foreman, S. Blatt, M. Notcutt, T. Ido, and J. Ye, *Phys. Rev. Lett.* **96**, 033003 (2006).
- [39] J. B. Yi Deng and N. R. Forde, *Journal of Optics A: Pure and Applied Optics* **9**, S256 (2007).
- [40] S. Friebel, C. D’Andrea, J. Walz, M. Weitz, and T. W. Hänsch, *Phys. Rev. A* **57**, R20 (1998).
- [41] A. Görlitz, M. Weidemüller, T. W. Hänsch, and A. Hemmerich, *Phys. Rev. Lett.* **78**, 2096 (1997).
- [42] R. Loudon, *The Quantum Theory of Light*, 3rd ed. (Oxford University Press, New York, 2008).
- [43] M. A. Nielsen and I. L. Chuang, *Quantum Computation and Quantum Information*, ninth ed. (Cambridge University Press, 2007).
- [44] W. K. Wootters, *Phys. Rev. Lett.* **80**, 2245 (1998).
- [45] R. Wagner and J. P. Clemens, *Phys. Rev. A* **79**, 042322 (2009).
- [46] R. Wagner and J. P. Clemens, *J. Opt. Soc. Am. B* **27**, A73 (2010).
- [47] H.J.Carmichael and K. Kim, *Optics Communications* **179**, 417 (2000).
- [48] D. A. Steck, *Quantum and atom optics* (2017), [Online; accessed February, 6 2018. <http://steck.us/teaching>].
- [49] R. Shankar, *Principles of Quantum Mechanis*, 2nd ed. (Springer, New York, 1994).

- [50] Y. Kaluzny, P. Goy, M. Gross, J. M. Raimond, and S. Haroche, Phys. Rev. Lett. **51**, 1175 (1983).
- [51] T. H. Stievater, X. Li, D. G. Steel, D. Gammon, D. S. Katzer, D. Park, C. Piermarocchi, and L. J. Sham, Phys. Rev. Lett. **87**, 133603 (2001).
- [52] E. Cook, *Laser Cooling and Trapping of Neutral Strontium for Spectroscopic Measurements of Casimir-Polder Potentials*, Ph.D. thesis, University of Oregon (2017).
- [53] J. B. Mackrory, T. Bhattacharya, and D. A. Steck, Phys. Rev. A **94**, 042508 (2016).
- [54] P. W. Milonni, *The Quantum Vacuum* (Academic Press, Inc., San Diego, 1994).
- [55] G. K. Campbell and W. D. Phillips, Philosophical Transactions of the Royal Society A **369**, 4078 (2011).
- [56] G. Santarelli, P. Laurent, P. Lemonde, A. Clairon, A. G. Mann, S. Chang, A. N. Luiten, and C. Salomon, Phys. Rev. Lett. **82**, 4619 (1999).
- [57] O. Arcizet, P. F. Cohadon, T. Briant, M. Pinard, and A. Heidmann, Nature **444**, 71 (2006).
- [58] S. Gigan, H. R. Böhm, M. Paternostro, F. Blaser, G. Langer, J. B. Hertzberg, K. C. Schwab, D. Bäuerle, M. Aspelmeyer, and A. Zeilinger, Nature **444**, 67 (2006).
- [59] J. A. E. A. (JAXA), Small solar power sail demonstrator 'ikaros' confirmation of photon acceleration (2010), [Press Release] Last accessed Aug. 2018. Originally available at http://global.jaxa.jp/press/2010/07/20100709_ikaros_e.html.
- [60] Y. Tsuda, O. Mori, R. Funase, H. Sawada, T. Yamamoto, T. Saiki, T. Endo, K. Yonekura, H. Hoshino, and J. Kawaguchi, Acta Astronautica **82**, 183 (2013).
- [61] P. W. Milonni and J. H. Eberly, *Lasers* (Wiley-Interscience., New York, 1988).
- [62] D. A. Steck, Rubidium 87 d line data (2001), [Online; accessed December, 2 2017. <http://steck.us/alkalidata>].
- [63] D. M. Brink and C. V. Sukumar, Phys. Rev. A **74**, 035401 (2006).
- [64] J. W. Jun, S. Chang, T. Y. Kwon, H. S. Lee, and V. G. Minogin, Phys. Rev. A **60**, 3960 (1999).
- [65] A. L. Migdall, J. V. Prodan, W. D. Phillips, T. H. Bergeman, and H. J. Metcalf, Phys. Rev. Lett. **54**, 2596 (1985).

- [66] W. Petrich, M. H. Anderson, J. R. Ensher, and E. A. Cornell, *Phys. Rev. Lett.* **74**, 3352 (1995).
- [67] M. H. Anderson, J. R. Ensher, M. R. Matthews, C. E. Wieman, and E. A. Cornell, *Science* **269**, 198 (1995).
- [68] W. W. Erickson and D. S. Steck, In preparation (2019).
- [69] T. Bergeman, G. Erez, and H. J. Metcalf, *Phys. Rev. A* **35**, 1535 (1987).
- [70] Y. Shevy, D. S. Weiss, P. J. Ungar, and S. Chu, *Phys. Rev. Lett.* **62**, 1118 (1989).
- [71] J. Dalibard and C. Cohen-Tannoudji, *J. Opt. Soc. Am. B* **6**, 2023 (1989).
- [72] S. Chang, T. Yong Kwon, H. Seong Lee, and V. Minogin, *Phys. Rev. A* **60**, 2308 (1999).
- [73] E. A. Schoene, *Cold Atom Control with an Optical One-way Barrier*, Ph.D. thesis, University of Oregon (2010).
- [74] J. Thorn, *Dissipative Control and Imaging of Cold Atoms*, Ph.D. thesis, University of Oregon (2012).
- [75] T. Li, *Manipulation of Cold Atoms using an Optical One-way Barrier*, Ph.D. thesis, University of Oregon (2008).
- [76] M. Fuchs, *Development of a High power Stabilized Diode Laser System*, Master's thesis, University of Oregon (2006).
- [77] D. Haubrich, H. Schadwinkel, F. Strauch, B. Ueberholz, R. Wynands, and D. Meschede, *Europhysics Letters* **34**, 663 (1996).
- [78] M. Meucci, E. Mariotti, P. Bicchi, C. Marinelli, and L. Moi, *Europhysics Letters* **25**, 639 (1994).
- [79] A. Gozzini, F. Mango, J. H. Xu, G. Alzetta, F. Maccarrone, and R. A. Bernheim, *Il Nuovo Cimento D* **15**, 709 (1993).
- [80] C. Marinelli, A. Burchianti, A. Bogi, F. Della Valle, G. Bevilacqua, E. Mariotti, S. Veronesi, and L. Moi, *The European Physical Journal D - Atomic, Molecular, Optical and Plasma Physics* **37**, 319 (2006).
- [81] C. Klempt, T. van Zoest, T. Henninger, O. Topic, E. Rasel, W. Ertmer, and J. Arlt, *Phys. Rev. A* **73**, 013410 (2006).
- [82] J. H. Xu, A. Gozzini, F. Mango, G. Alzetta, and R. A. Bernheim, *Phys. Rev. A* **54**, 3146 (1996).

- [83] B. P. Anderson and M. A. Kasevich, *Phys. Rev. A* **63**, 023404 (2001).
- [84] M. H. T. Extavour, L. J. LeBlanc, T. Schumm, B. Cieslak, S. Myrskog, A. Stummer, S. Aubin, and J. H. Thywissen, *AIP Conference Proceedings* **869**, 241 (2006).
- [85] G. Telles, T. Ishikawa, M. Gibbs, and C. Raman, *Phys. Rev. A* **81**, 032710 (2010).
- [86] S. N. Atutov, R. Calabrese, V. Guidi, B. Mai, A. G. Rudavets, E. Scansani, L. Tomassetti, V. Biancalana, A. Burchianti, C. Marinelli, E. Mariotti, L. Moi, and S. Veronesi, *Phys. Rev. A* **67**, 053401 (2003).
- [87] E. Mimoun, L. D. Sarlo, D. Jacob, J. Dalibard, and F. Gerbier, *Phys. Rev. A* **81**, 023631 (2010).
- [88] K. M. Birnbaum, *Ultra high vacuum chambers* (2005), [Online; Last access unknown. Originally available at http://www.its.caltech.edu/qoptics/Vacuum/UHV_chambers.pdf].
- [89] Z. T. Lu, K. L. Corwin, M. J. Renn, M. H. Anderson, E. A. Cornell, and C. E. Wieman, *Phys. Rev. Lett.* **77**, 3331 (1996).
- [90] C. Y. Park, M. S. Jun, and D. Cho, *J. Opt. Soc. Am. B* **16**, 994 (1999).
- [91] C. D. Wallace, T. P. Dinneen, K. Y. N. Tan, A. Kumarakrishnan, P. L. Gould, and J. Javanainen, *J. Opt. Soc. Am. B* **11**, 703 (1994).
- [92] A. M. Steane, M. Chowdhury, and C. J. Foot, *J. Opt. Soc. Am. B* **9**, 2142 (1992).
- [93] P. G. Pappas, M. M. Burns, D. D. Hinshelwood, M. S. Feld, and D. E. Murnick, *Phys. Rev. A* **21**, 1955 (1980).
- [94] P. E. Gaskell, J. J. Thorn, S. Alba, and D. A. Steck, *Review of Scientific Instruments* **80**, 115103 (2009), <https://doi.org/10.1063/1.3250825> .
- [95] J. J. Thorn, E. A. Schoene, T. Li, and D. A. Steck, *Phys. Rev. Lett.* **100**, 240407 (2008).
- [96] E. A. Schoene, J. J. Thorn, and D. A. Steck, *Phys. Rev. A* **82**, 023419 (2010).
- [97] J. D. Jackson, *Classical Electrodynamics*, 3rd ed. (John Wiley & Sons, Inc., New York, 1999).
- [98] J. H. Moore, C. C. Davis, M. A. Coplan, and S. C. Greer, *Building Scientific Apparatus*, 4th ed. (Cambridge University Press, New York, 2009).

- [99] P. C. D. Hobbs, *Building Electro-optical Systems*, 2nd ed. (John Wiley & Sons, Inc., Hoboken, New Jersey, 2009).
- [100] K. Inc., Ate full rack power supply operator's manual (2010).
- [101] E. H. Hall, *American Journal of Mathematics* **2**, 287 (1879).
- [102] M. Briel, *Design and Characterization of a Custom Aspheric Lens System for Single Atom Imaging*, Master's thesis, University of Oregon (2012).
- [103] C.-S. Chuu, *Direct Study of Quantum Statistics in a Degenerate Bose Gas*, Ph.D. thesis, The University of Texas at Austin (2006).
- [104] J. L. Hanssen, *Controlling Atomic Motion: From Single Particle Classical Mechanics to Many Body Quantum Dynamics*, Ph.D. thesis, The University of Texas at Austin (2004).
- [105] W. Alt, *Optik - International Journal for Light and Electron Optics* **113**, 142 (2002).
- [106] W. Alt, *Optical control of single neutral atoms*, Ph.D. thesis, University of Bonn (2004).
- [107] Altera, De2 development and education board user manual (2012).
- [108] D. Branning, S. Bhandari, and M. Beck, *American Journal of Physics* **77**, 667 (2009), <https://doi.org/10.1119/1.3116803> .
- [109] M. Beck, Coincidence counting units (ccus) (2014), [Online; accessed December 2, 2017. <http://people.whitman.edu/~beckmk/QM/circuit/circuit.html>].
- [110] S. Kuhr, *A controlled quantum system of individual neutral atoms*, Ph.D. thesis, University of Bonn (2004).
- [111] S. Yoon, Y. Choi, S. Park, J. Kim, J.-H. Lee, and K. An, *Applied Physics Letters* **88**, 211104 (2006).
- [112] W. Ketterle, K. B. Davis, M. A. Joffe, A. Martin, and D. E. Pritchard, *Phys. Rev. Lett.* **70**, 2253 (1993).
- [113] G. Labeyrie, F. Michaud, and R. Kaiser, *Phys. Rev. Lett.* **96**, 023003 (2006).
- [114] T. Walker, D. Sesko, and C. Wieman, *Phys. Rev. Lett.* **64**, 408 (1990).
- [115] N. Schlosser, G. Reymond, I. Protsenko, and P. Grangier, *Nature* **411**, 1024 (2001).
- [116] S. Yoon, Y. Choi, S. Park, W. Ji, J.-H. Lee, and K. An, *Journal of Physics: Conference Series* **80**, 012046 (2007).

- [117] L. Mandel, *Opt. Lett.* **4**, 205 (1979).
- [118] R. Short and L. Mandel, *Phys. Rev. Lett.* **51**, 384 (1983).
- [119] T. W. Hodapp, G. W. Greenlees, M. A. Finn, and D. A. Lewis, *Phys. Rev. A* **41**, 2698 (1990).
- [120] R. J. Cook, *Optics Communications* **35**, 347 (1980).
- [121] Z. Hu, *Quantum Optics with Cold Atoms – Nonlinear Spectroscopy and Road towards Single-Atom Trap*, Ph.D. thesis, Californian Institute of Technology (1995).
- [122] O. Jacobs, *Introduction to control theory* (Oxford University Press, London, 1974).
- [123] T. Bhattacharya, S. Habib, and K. Jacobs, *Physical Review Letters* **85** (2000).
- [124] G. Milburn, *Quantum Semiclassical Optics* **8** (1996).
- [125] K. Jacobs and D. A. Steck, *Contemporary Physics* **47** (2006).
- [126] M. E. Rose, *Elementary theory of angular momentum* (Wiley, New York, 1957).
- [127] J. H. Wilkinson and C. Reinsch, *Handbook for Automatic Computation : Volume II: Linear Algebra*, 1st ed. (Springer-Verlag, Berlin Heidelberg, 1971).
- [128] L. Team, Lapack-linear algebra package (2017), [Online; Last access Aug. 2018. Available at <http://www.netlib.org/lapack/>].
- [129] E. Raab, *Trapping Sodium with Light*, Ph.D. thesis, Massachusetts Institute of Technology (1988).
- [130] S. Marksteiner, K. Ellinger, and P. Zoller, *Phys. Rev. A* **53**, 3409 (1996).
- [131] L. Landua and E. Lifshitz, *Mechanics*, 2nd ed. (Peramon Press, Oxford, 1969).
- [132] M. A. and B.-G. I., *PLoS Computational Biology* **11**, e1004252 (2015).
- [133] M. Hohmann, F. Kindermann, T. Lausch, D. Mayer, F. Schmidt, and A. Widera, *Phys. Rev. A* **93**, 043607 (2016).
- [134] W. W. Erickson, *In Preparation*, Ph.D. thesis, University of Oregon (2020).
- [135] L. Pedersen and H. Flyvbjerg, *Phys. Rev. Lett.* **98**, 189801 (2007).
- [136] K. Kim, H.-R. Noh, Y.-H. Yeon, and W. Jhe, *Phys. Rev. A* **68**, 031403 (2003).
- [137] K. Kim, H.-R. Noh, H.-J. Ha, and W. Jhe, *Phys. Rev. A* **69**, 033406 (2004).

- [138] K. Kim, H.-R. Noh, and W. Jhe, *Optics Communications* **236**, 349 (2004).
- [139] G. B. Arfken, H. J. Webber, and F. E. Harris, *Mathematica Methods for Physicists*, seventh ed. (Academic Press, Waltham, MA, 2013).
- [140] R. E. Berg. and D. G. Stork, *The Physics of Sound*, 3rd ed. (Pearson Education, San Francisco, 2005).
- [141] T. NESLAB, Rte-101 bath circulator - installation, operation and service manual (2000).
- [142] F. Kreith and M. S. Bohn, *Principles of Heat Transfer* (Harper and Row, New York, 1986).
- [143] C. N. de Castro, S. Li, A. Nagashime, R. Trengove, and W. Wakeham, *Journal of Physical and Chemical Reference Data* **15**, 1073 (1986).
- [144] Y. Pinhasi and Y. Lurie, *Phys. Rev. E* **65**, 026501 (2002)